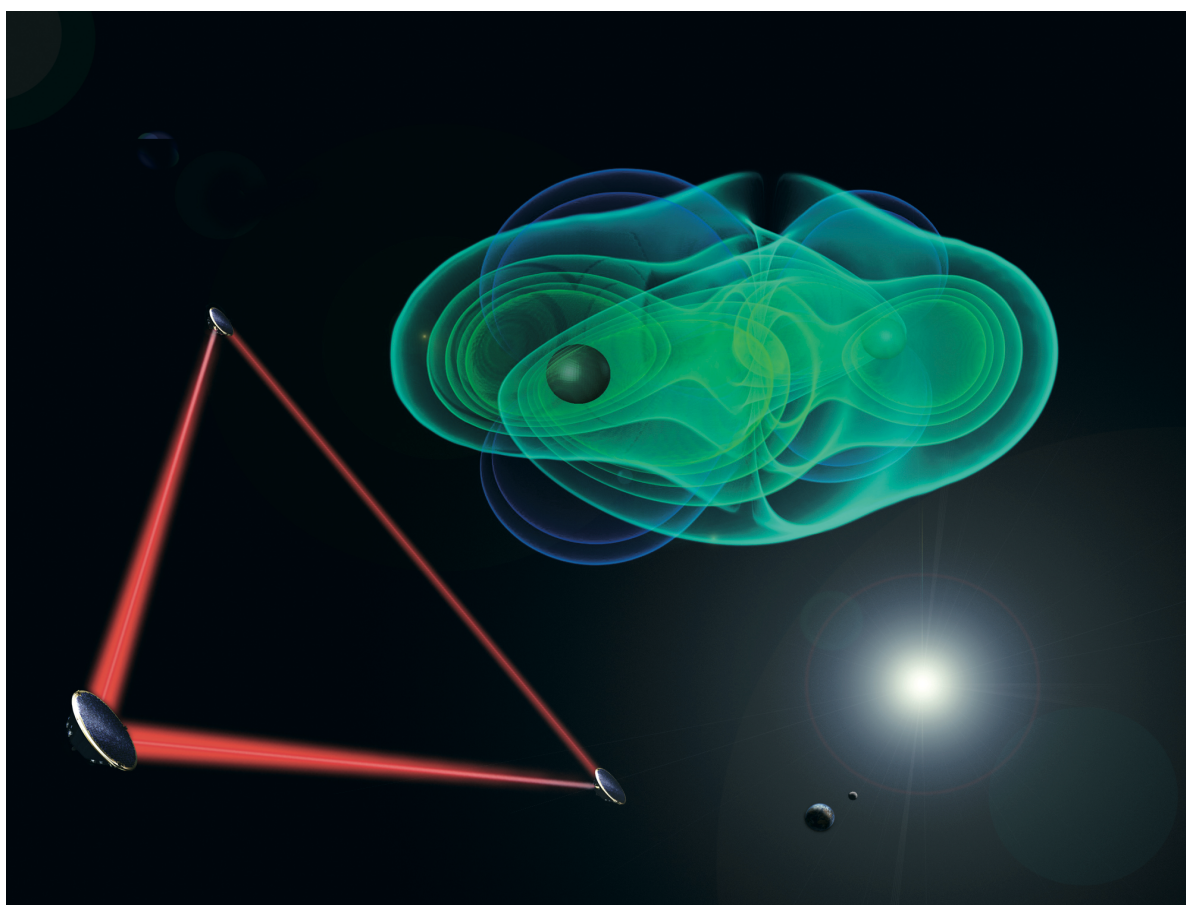


LISA

Unveiling a hidden Universe



Assessment Study Report

Cover page graphics

Numerical simulation of merging black holes: The search for gravitational waves requires detailed knowledge of the expected signals. Scientists of the Albert Einstein Institute's numerical relativity group simulate collisions of black holes and neutron stars on supercomputers using sophisticated codes developed at the institute. These simulations provide insights into the possible structure of gravitational wave signals. Gravitational waves are so weak that these computations significantly increase the probability of identifying gravitational waves in the data acquired by the detectors.

Numerical simulation: C. Reisswig, L. Rezzolla (Max Planck Institute for Gravitational Physics (Albert Einstein Institute))

Scientific visualisation: M. Koppitz (Zuse Institute Berlin)

Satellite visualisation: Milde Marketing Science Communication

Mission Description

Science Objectives

- Trace the formation, growth, and merger history of massive black holes
 - Explore stellar populations and dynamics in galactic nuclei
 - Survey compact stellar-mass binaries and study the structure of the Galaxy
 - Confront General Relativity with observations
 - Probe new physics and cosmology with gravitational waves
 - Search for unforeseen sources of gravitational waves
-

Event Rates and Event Numbers

| | |
|------------------------------|--|
| Frequency band | 1×10^{-4} Hz to 1 Hz, (3×10^{-5} Hz to 1 Hz as a goal) |
| Massive black hole mergers | 1 yr^{-1} to 1000 yr^{-1} |
| Extreme mass ratio inspirals | 1 yr^{-1} to 1000 yr^{-1} |
| Galactic Binaries | $\sim 30\,000$ resolvable out of a total of $\sim 30 \times 10^6$ in the LISA band |

Mission

| | |
|----------------------|---|
| Duration | 5 years science orbit, (~ 7 years including transfer and commissioning) |
| Orbits | Three drag-free satellites in heliocentric orbits, semimajor axis ≈ 1 AU, eccentricity $e \approx 0.0096$, inclination $i \approx 0.96^\circ$ |
| Spacecraft bus | Provides power, communication, and AOCS on science orbit. Micronewton propulsion system, magnetically and gravitationally controlled design, power supply from solar cells |
| AOCS | Derived from test mass position and received laser, star tracker as backup |
| <i>Pointing</i> | Spacecraft attitude jitter $< 10 \text{ nrad}/\sqrt{\text{Hz}}$ |
| <i>Mass</i> | Mass (three spacecraft incl. payload): 865 kg |
| <i>Power</i> | Science mode: 493 W |
| Propulsion module | Used during transfer, chemical propulsion |
| <i>Mass</i> | Dry mass (three modules): 1509 kg |
| <i>Power</i> | Transfer phase: 147 W maximum |
| Constellation | Equilateral triangle, 5×10^6 km armlength, trailing Earth by 20° , inclined by 60° with respect to the ecliptic. Armlength variation $< 1\%$, angular variation $\pm 0.8^\circ$, rel. velocity between S/C < 20 m/s |
| Communications | Data generation rate 11 kbps per S/C , downlink via DSN 70 m, X-band, downlink data rate 217 kbps during 8 hours contact. Contact schedule: every 48 hours to one of the spacecraft (S/C), max. 6 days latency, max. 12 hour latency during preferred periods. |
| Total Mass | Including margin, launch adapter and propellant: 6155 kg |
| Power per S/C | Including margin and conversion losses: 1006 W maximum (Science mode) |
| Launcher | Atlas V 541 |

Payload

| | |
|----------------|--|
| Laser | 2 per S/C , 2 W output power (EOL), wavelength 1064 nm, frequency stability (pre-stabilised) $282 \text{ Hz}/\sqrt{\text{Hz}}$, fractional power stability $10^{-3}/\sqrt{\text{Hz}}$ |
| Optical bench | 2 per S/C , low- CTE material (Zerodur), monolithic construction (hydroxy-catalysis bonding) |
| Interferometry | heterodyne interferometry, $18 \text{ pm}/\sqrt{\text{Hz}}$ requirement. Inter- S/C ranging to ~ 1 m, clock tone transfer |
| GRS | $46 \text{ mm} \times 46 \text{ mm} \times 46 \text{ mm}$ test mass made from AuPt alloy (73:27), electrostatically controlled, optical readout, residual acceleration $3 \times 10^{-15} \text{ m/s}^2/\sqrt{\text{Hz}}$ (10^{-9} m/s^2 at DC) |
| Telescope | 2 per S/C , 40 cm off-axis telescope. Changing inter- S/C angle compensated by telescope movement. |
| <i>Mass</i> | Net mass per payload: 282 kg, total payload mass 846 kg |
| <i>Power</i> | Science mode: 277 W per payload |

Foreword

The first mission concept studies for a space-borne gravitational wave observatory can be traced back to activities in the 1980s at the **Joint Institute for Laboratory Astrophysics** (JILA) leading to a first full description of a mission comprising three drag-free spacecraft in a heliocentric orbit, then named Laser Antenna for Gravitational-radiation Observation in Space (LAGOS). In the early 1990s, LISA was proposed to ESA, first to the then M3-cycle, later as a cornerstone to the “Horizon 2000 Plus” programme, as captured in the first “Yellow Book” of 1996. At this time LISA still consisted of six spacecraft, but showed already the key features of today’s LISA: Interferometric measurement of distances, long baselines (5×10^6 km), drag-free spacecraft based on inertial sensors, and the familiar LISA “cartwheel”-orbits. The number of spacecraft was reduced to the current three in a series of cost-reduction exercises in 1996 and 1997, resulting in an update of the first Yellow Book in 1998. As well in 1997, the then study team and ESA’s Fundamental Physics Advisory Group (FPAG) recommended to carry out LISA in collaboration with NASA, laying the grounds for the present days’ collaboration.

The first industrial study on LISA published its final report in July 2000 (the so called *System and Technology Study Report*), proposing a mission design for LISA that has in essence survived till today – three spacecraft, a separation of spacecraft and propulsion module, single launch, and a measurement principle that had been refined, but saw little change in the underlying principles. In 2001, the current science team was formed. In the spirit of a collaborative mission, the two science teams (ESA and NASA) formed a single, joint **LISA International Science Team** (LIST) that is since meeting regularly (typically twice a year) and makes scientific recommendations to support the formulation study. The LIST is co-chaired by K. Danzmann (for the ESA Science Team) and Tom Prince (for the NASA Science Team) and consists of 14 members on each side.

Equally in 2001, LISA became part of the Beyond Einstein programme of NASA as one of the great observatories. In 2003, LISA underwent a first of a series of US reviews aimed at technology readiness that culminated with LISA being identified as the mission with the highest readiness in NASA’s Beyond Einstein programme.

The current industrial study started in 2005 as a “Formulation” study after an agreement between ESA and NASA on roles and responsibilities during a formulation study. It was agreed that the ESA study will cover the whole mission, although with a stronger emphasis on the potential European contributions, while the US project conducted independent studies on their share of the payload, the spacecraft, the avionics, the launcher and the ground segment. During that time both agencies ran their own technology development activities in a coordinated fashion, so that critical technology areas saw activities by both agencies for risk reduction.

When ESA formulated the Cosmic Vision 2015–2025 programme in 2005, and started the assessment phase in 2007, LISA was identified early on as one of the potential candidates for the L1 launch slot due to the relative maturity of the concept and the proceeding industrial study.

This report summarises the design of the mission and the payload that are the result of the recent industrial study together with many contributions from technology development activities, either sponsored by ESA or undertaken by laboratories and institutes in the US and Europe on national funding. The mission design and the measurement principle have withstood the intense scrutiny of past and ongoing reviews and demands – the current design is a product of more than twenty years of refinement and optimisation.

Over the last decade, the scientific objectives and requirements for LISA underwent many refinements, described in this report and captured in the Science Requirements Document this report summarises. Today, computational tools are available to assess the impact of changes in the sensitivity on the science output, leading to science requirements that are traceable to the scientific objectives. Furthermore, the scientific community rose to the challenge of demonstrating the feasibility of the LISA Data Analysis, closing the loop between science objectives and science output.

Authors

This report has been authored by the members of the **LISA International Science Team (LIST)**:

| | | |
|---|-----------------------------|-------------|
| Karsten Danzmann (co-chair) | AEI Hannover | Germany |
| Thomas A Prince (co-chair) | JPL | USA |
| Pierre Binetruy | APC Paris | France |
| Peter Bender | JILA | USA |
| Sasha Buchman | Stanford University | USA |
| Joan Centrella | NASA GFSC | USA |
| Massimo Cerdonio | INFN Padua | Italy |
| Neil Cornish | Montana State University | USA |
| Mike Cruise | University of Birmingham | UK |
| Curt J Cutler | JPL | USA |
| Lee Sam Finn | PennState University | USA |
| Jens Gundlach | University of Washington | USA |
| Craig Hogan | Fermilab | USA |
| Jim Hough | University of Glasgow | UK |
| Scott A. Hughes | MIT | USA |
| Oliver Jennrich (ESA Project Scientist) | ESA | Netherlands |
| Philippe Jetzer | University of Zurich | Switzerland |
| Alberto Lobo | IEEC Barcelona | Spain |
| Piero Madau | UC Santa Cruz | USA |
| Yannick Mellier | IAP | Paris |
| Sterl Phinney | Caltech | USA |
| Douglas O. Richstone | University of Michigan | USA |
| Bernard Schutz | AEI Potsdam | Germany |
| Robin Stebbins (NASA Project Scientist) | NASA GSFC | USA |
| Tim Sumner | Imperial College | UK |
| Kip Thorne | Caltech | USA |
| Jean-Yves Vinet | Observatoire de Côte d'Azur | France |
| Stefano Vitale | University of Trento | Italy |

Acknowledgements

The ESA Formulation study was led by A. Gianolio (ESA Project Manager), O. Jennrich (ESA Project Scientist), M. Sallusti (ESA System Engineer), and L. d'Arcio (ESA Optical Engineer) with the support of B. Johlander, L. Scalamiero, and Z. Sodnik. The ESA Formulation Study was conducted by EADS Astrium with contributions of TNO.

The US Formulation Study was led by A. Mansoor (US Project Manager, GSFC), M. Pniel (US Project Manager, JPL), R. Stebbins (US Project Scientist) with the support of T. Hyde, N. Jedrich, S. Merkwowitz, J. Livas, I. Thorpe, and J. Baker (all GFSC), M. Vallisneri, W. Klipstein, R. Spero, and D. Shaddock (all JPL).

Much scientific support was given to LISA from scientists that were not members of the **LIST** but served in one of its working groups or contributed in other ways to this report (in alphabetical order):

Berangere Argence (APC), Stuart Aston (Birmingham), Gerard Auger (APC), Stas Babak (AEI), Simon Barke (AEI), Iouri Bykov (AEI), Martin Caldwell (RAL), Jordan Camp (NASA GSFC), John Conklin (Stanford), Dan deBra (Stanford), Luciano Di Fiore (Naples), Gudrun Diederichs (AEI), Christian Diekmann (AEI), Juan Jose Esteban Delgado (AEI), Roland Fleddermann (AEI), Antonio Garcia (AEI), Catia Grmani (Urbino) Felipe Guzman (AEI/GSFC), Hubert Halloin

(APC), Ian Harris (JPL), Gerhard Heinzel (AEI), Martin Hewitson (AEI) Steven Hochman (U Florida), Daniel Hollington (Imperial College), Mac Keiser (Stanford), Christian Killow (Glasgow), Joachim Kullmann (AEI), Jeffrey Livas (GSFC), Kirk McKenzie (JPL), Paul McNamara (ESA), Shawn Mitryk (U 2Florida), Anneke Monsky (AEI), Guido Müller (U Florida), Gijs Nelemans (U Nijmegen), Miquel Nofrarias (AEI), Kenji Numata (GSFC), Eric Plagnol (APC), Scott Pollack (University of Washington), Ed Porter (APC), Alix Preston (U Florida), Alix Preston (UF), Volker Quetschke (UTB), Dave Robertson (Glasgow), Albrecht Rüdiger (AEI), Josep Sanjuan (IEEC Barcelona), B. Sathyaprakash (U Cardiff), Alberto Sesana (AEI), Diana Shaul (Imperial College), Ben Sheard (AEI), Frank Steier (AEI), Ke-Xun Sun (Stanford), Dylan Sweeney (U Florida), David Tanner (UF), Michael Troebs (AEI), Glenn de Vine (JPL), Marta Volonteri (University of Michigan), Vinzenz Wand (AEI), Harry Ward (U Glasgow), Brent Ware (JPL), Peter Wass (U Trento/Imperial College), Bill Weber (U Trento), Yinan Yu (U Florida), Alberto Vecchio (U Birmingham), Andreas Zoellner (Stanford)

Contact

Please direct all comments and questions to [O. Jennrich](#).

Contents

| | |
|---|------------|
| Mission Description | i |
| Foreword | iii |
| Authors | v |
| 1. Executive Summary | 1 |
| 2. Scientific Objectives | 5 |
| 2.1. Gravitational Waves – An Overview | 5 |
| 2.1.1. What are gravitational waves? | 5 |
| 2.1.2. How are gravitational waves detected? | 7 |
| 2.1.3. The gravitational wave Universe in the LISA band | 8 |
| 2.2. Survey of LISA Science | 10 |
| 2.3. Black Hole Astrophysics: Massive Black Holes in Galactic Nuclei | 13 |
| 2.3.1. Evidence for supermassive black holes in galactic nuclei | 13 |
| 2.3.2. Growth and merger history of massive black holes | 16 |
| 2.3.3. Black hole Spins | 18 |
| 2.3.4. Stellar captures and the dynamics of galactic nuclei | 20 |
| 2.4. Confronting General Relativity with Precision Measurements of Strong Gravity | 23 |
| 2.4.1. Setting the stage | 23 |
| 2.4.2. Testing strong-field gravity: The inspiral, merger, and ringdown of MBH binaries | 24 |
| 2.4.3. Extreme mass ratio inspirals: precision probes of Kerr spacetime | 27 |
| 2.4.4. The mass of the graviton | 29 |
| 2.5. Ultra-Compact Binaries | 30 |
| 2.5.1. Summary | 30 |
| 2.5.2. LISA as a workhorse: thousands of new binaries | 31 |
| 2.5.3. Instrument verification | 32 |
| 2.5.4. Studying the astrophysics of compact binaries using LISA | 33 |
| 2.5.5. New studies of galactic structure with LISA | 36 |
| 2.6. Precision Cosmology | 38 |
| 2.6.1. Absolute cosmology with black hole binaries | 39 |
| 2.7. New Physics and the Early Universe | 43 |
| 2.7.1. Backgrounds, bursts, and harmonic notes from cosmic strings | 45 |
| 3. Scientific Requirements | 47 |
| 3.1. Science Requirements Overview | 47 |
| 3.2. The LISA concept | 47 |
| 3.2.1. LISA design concept | 48 |
| 3.2.2. Science requirements rationale | 50 |
| 3.3. Observation Requirements | 51 |
| 3.4. Instrument Sensitivity Model | 53 |
| 3.4.1. ISM Description | 53 |
| 3.4.2. Instrument sensitivity function | 54 |
| 3.4.3. Instrument Noise Model | 55 |
| 3.4.4. ISM Validation | 56 |

| | |
|--|-----------|
| 3.4.5. Noise Model validation | 57 |
| 3.5. Performance Requirements | 59 |
| 4. Payload | 61 |
| 4.1. Optical System | 62 |
| 4.1.1. Optical bench | 62 |
| 4.1.2. Telescope | 67 |
| 4.1.3. Optical assembly tracking mechanism | 69 |
| 4.2. Laser System | 69 |
| 4.2.1. Laser frequency noise suppression | 70 |
| 4.3. Phase measurement | 74 |
| 4.3.1. Clock noise removal | 74 |
| 4.4. Disturbance Reduction System | 75 |
| 4.4.1. Principle of operation | 77 |
| 4.4.2. Environmental requirements | 77 |
| 4.4.3. Gravitational Reference Sensor | 78 |
| 4.4.4. Micro-newton thrusters | 81 |
| 5. Mission Design | 83 |
| 5.1. Overview | 83 |
| 5.2. Spacecraft Design | 83 |
| 5.3. Propulsion module design | 85 |
| 5.3.1. Structural Concept | 85 |
| 5.3.2. Separation Subsystem | 86 |
| 5.4. Mission Analysis | 87 |
| 5.4.1. Overview | 87 |
| 5.4.2. Launch and Early Operations Phase | 87 |
| 5.4.3. Transfer | 88 |
| 5.4.4. Separation from Propulsion Module | 88 |
| 5.4.5. Science orbit | 88 |
| 5.5. Mission budgets | 90 |
| 5.5.1. Mass budget | 90 |
| 5.5.2. Propellant budget | 92 |
| 5.5.3. Power budget | 92 |
| 5.5.4. RF link budgets | 94 |
| 6. Mission Operations | 95 |
| 6.1. Introduction | 95 |
| 6.2. Mission Phases | 96 |
| 6.2.1. Launch and Early Operations Phase | 97 |
| 6.2.2. Cruise Phase | 97 |
| 6.2.3. Commissioning Phase | 98 |
| 6.2.4. Calibration phase | 99 |
| 6.2.5. Science Operations Phase | 99 |
| 6.2.6. Post-operations Phase | 100 |
| 6.3. Mission Operations Elements | 100 |
| 6.3.1. Deep Space Network | 100 |
| 6.3.2. Flight Operations | 100 |
| 6.4. Science Operations Elements | 101 |
| 6.4.1. Science Operation Centre | 101 |
| 6.4.2. Data centres | 102 |
| 6.4.3. Data Archive | 103 |

| | |
|---|------------|
| 6.5. Data Analysis | 103 |
| 6.5.1. General principles | 103 |
| 6.5.2. Templates | 104 |
| 6.5.3. Algorithms | 105 |
| 6.5.4. Mock LISA Data Challenge | 105 |
| 7. Management | 107 |
| 7.1. Procurement strategy | 107 |
| A. Cosmic Vision Science Questions | 109 |
| B. LISA Science Objectives | 111 |
| Acronyms | 113 |
| Bibliography | 115 |

1. Executive Summary

Einstein's theory of spacetime and gravity, general relativity, predicts that suitably accelerated masses produce propagating vibrations that travel through spacetime at the speed of light. These gravitational waves (as the vibrations are called) are produced abundantly in the Universe and permeate all of space. Measuring them will add an altogether new way to explore what is happening in the Universe: rather than studying the propagation and transformation of conventional particles and fields in spacetime, as all science has done up to now, LISA will sense vibrations of the fabric of spacetime itself. Studying these signals will convey rich new information about the behaviour, structure, and history of the physical universe, and about physics itself. When gravitational waves become observable they will provide a new and uniquely powerful probe of the extremes of spacetime, from the Big Bang to black holes, to address the deep questions that have emerged in mankind's never-ending quest to understand the cosmos: what powered the Big Bang, what happens to space and time in black holes and what is the mysterious dark energy accelerating the expansion of the Universe?

LISA is a space mission designed to measure gravitational radiation over a broad band at low frequencies, from about 0.1 mHz to 100 mHz, a band where the Universe is richly populated by strong sources of gravitational waves. It measures signals from a wide range of different sources that are of strong interest to the astrophysics of black hole and galaxy formation, and also to tests of general relativity and to cosmology: massive black holes merging in galaxies at all distances; massive black holes consuming smaller compact objects; known binary compact stars and stellar remnants; members of known populations of more distant binaries; and probably other sources, possibly including relics of the extremely early Big Bang, which are as yet unknown. These strong signals convey detailed information addressing a wide range of science, addressing scientific questions raised by ESA's Cosmic Vision programme (see appendix A), such as "What are the fundamental laws of the Universe?" and "How did the Universe originate and what is it made of?"

LISA will directly determine how massive black holes present in most galactic nuclei today have formed and grown over cosmic time. Signals from the merger of early intermediate-mass black holes reveal the mass of each black hole and its spin as a function of the redshift z . The distribution of masses observed in merging binary black holes allows a clear distinction between formation scenarios for massive black holes.

LISA will trace the interaction of galaxy growth and massive black hole growth over the entire history of galaxy formation. Observing the masses of the massive black holes involved in binary mergers as a function of redshift, LISA will provide a strong constraint on the way in which black hole masses in the galactic centre evolved over time.

LISA will explore the populations of stellar-mass compact objects in galactic nuclei and their dynamics. Orbits of stellar objects captured by the black hole at the galactic centre evolve by gravitational radiation, providing information on the space density of those objects.

LISA will study in detail the signals from thousands of stellar-mass close binaries in the Galaxy and give information on the extreme endpoints of stellar evolution and Galactic structure using Galactic binaries. LISA provides distances and detailed orbital and mass parameters for hundreds of the most compact binaries, a rich trove of information for detailed mapping and reconstruction of the history of stars in our galaxy, and a source of information about tidal and non-gravitational influences on orbits associated with the internal physics of the compact remnants themselves.

LISA will observe highly relativistic mergers of black hole binaries and provide exceptionally strong tests of the predictions of **General Theory of Relativity**. Dynamical tests are based on mergers of two massive black holes where maximally warped vacuum spacetimes travelling at near the speed of light interacting strongly with each other, allowing to test the full nonlinear dynamics of gravitational theory.

LISA will probe new physics and cosmology with gravitational waves, and search for unforeseen sources of gravitational waves. The LISA frequency band in the relativistic early Universe corresponds to horizon scales where phase transitions of new forces of nature or extra dimensions of space may have caused catastrophic,

explosive bubble growth and efficient gravitational wave production. LISA is capable of detecting a stochastic background from such events from about 100 GeV to about 1000 TeV, if gravitational waves in the LISA band were produced with sufficient efficiency.

Although gravitational waves have never been directly detected, the existence of gravitational waves is in little doubt as their effects have been measured precisely, if indirectly. Any theory of gravity consistent with special relativity will exhibit gravitational waves, and the predictions of general relativity should be quantitatively reliable for LISA because the long-standing best evidence for gravitational waves is the orbital decay of the Hulse-Taylor binary pulsar, which radiates at frequencies only marginally below LISA's operating band. Therefore LISA will be able to detect the gravitational waves predicted by any reasonable theory of gravity.

In the same way that electromagnetic radiation accompanies acceleration of electric charges, gravitational radiation accompanies quadrupolar acceleration of any kind of mass or energy, perturbing spacetime with a dimensionless metric-strain amplitude. LISA senses this by monitoring the changes in the distances between inertial test masses. LISA uses precision laser interferometry across 5×10^6 km of space to compare separations between test masses that are protected by the spacecraft from non-gravitational disturbances. LISA coherently measures spacetime strain variations, including frequency, phase, and polarisation, all of which reflect large-scale properties of the systems that produce them and are therefore direct traces of the motions of distant matter.

LISA is an astronomical observatory of unprecedented versatility and range. Its all-sky field of view ensures that it can observe every source of gravitational waves, without having to compromise between observations. Its coherent mode of observing allows it to resolve and distinguish overlapping signals and locate them on the sky. Its unparalleled sensitivity allows it to study sources within the Galaxy and out to the edge of the Universe. Finally, LISA's wide frequency band (more than three decades in frequency) allows it to study similar sources of widely different masses and cosmological redshifts. Because gravitational waves penetrate all regions of time and space with almost no attenuation, LISA can sense waves from the densest regions of matter, the earliest stages of the Big Bang, and the most extreme warpings of spacetime near black holes.

The key components of the LISA mission concept are the interferometric measurement of the changes of a large baseline (5×10^6 km), free-falling test masses that define the endpoints of the baseline, suitable orbits of the spacecraft to avoid orbit maintenance (and hence disturbances on the test masses) and a mission lifetime of five years. With this mission concept and an instrument sensitivity model (ISM) that captures the anticipated sensitivity of the measurement the science performance of LISA can be demonstrated: enough sources with sufficient signal-to-noise ratio (SNR) are detected in the mission lifetime to fulfil the science objectives.

The classical distinction between spacecraft and payload doesn't fit LISA very well, as the spacecraft is not just providing the infrastructure for the instruments, but must be designed and built with the gravitational requirements of the free-falling test masses in mind. The usual structural and thermal analysis of the spacecraft has therefore been extended to include gravitational effects as well to ensure that the requirements on gravity gradient at the position of the test masses is fully met. In addition, the payload controls the position of the spacecraft during science operations, rendering the spacecraft effectively a part of the instrument. The importance of the co-design (and the co-operation) of spacecraft and payload is captured in the term "sciencecraft". The core features of the payload have been stable since more than a decade – the interferometric measurement system, the telescope, the gravitational reference sensor, and the micropropulsion system. Their design has evolved and over the time has now reached considerable maturity – many of the design features of, *e.g.*, the optical bench have been shown in laboratory prototypes, during testing of the **LISA Pathfinder** (LPF), and will finally be demonstrated on orbit during **LPF** operations. The disturbance reduction system (DRS) for LISA is identical to the one that is being built as the flight model for **LPF**, the micropropulsion system enjoys full heritage from **LPF** as well. Other critical components of LISA that are not needed for **LPF** have been demonstrated experimentally to fully meet the requirements of LISA, such as the phasemeter post-processing techniques to remove the residual laser phase noise (**TDI**) and the mechanism to compensate for the angle between send and receive beam.

Data analysis, the extraction of the science from the LISA data, had been conjectured to be a problem in the past. The community rose to the challenge of proving that not only the instrument can deliver data that in principle allow to assess the science questions, but that the techniques and concepts to extract the source parameters from the data streams are available and can be applied. A key component for that demonstration are the ability to create high-fidelity waveforms for the sources, having a well-understood signal simulator for the

mission, and being able to extract the source parameters from the simulated signals, which has been developed by the LISA project. The community-organised **Mock LISA Data Challenge** (MLDC) can be given credit to demonstrate the feasibility of the LISA data analysis. Having started in 2005, the **MLDC** is based on blind challenges of increasing complexity – from a few sources in the first challenge to the full combination of all likely sources in the data stream in the most recent fourth challenge. Scientific research groups from all over the world developed, tested and implemented a wide variety of techniques, so that we are now in the position to assert that LISA data analysis is not only feasible, but that a proof-of-concept for the actual data analysis is at hand.

LISA is a joint study since August 2004, when an agreement between ESA and NASA was signed, establishing the roles and responsibilities during the jointly conducted formulation phase. Operation is planned to be under joint responsibility, where the agency responsible for the launch will be responsible for the mission operation as well. The science operation will be conducted through a jointly staffed Science Operation Centre (SOC) that takes the responsibility for the science products of the mission. The data analysis will be conducted by two (or more) data centres that will work in close collaboration with the **SOC** to ensure the highest possible quality of the data products. The data products will be fully and freely available to the public after a short period required to ensure data quality. As transient events, such as mergers of super-massive black holes (SMBHs) are of high interest to the astronomy and astrophysics community, transient event alerts will be issued as soon as they become evident to allow electro-magnetic observations of the event.

2. Scientific Objectives

2.1. Gravitational Waves – An Overview

Almost everything we know about the Universe we have learned from light: since ancient times, electromagnetic waves have been messengers from the cosmos to our eyes, and later to our telescopes and our antennas. More recently, we have begun to parse the messages of more exotic carriers such as the elusive neutrinos from the Sun and beyond. We are now ready to add an altogether new modality to science: sensing vibrations of the very fabric of spacetime. Gravitational waves will add a many-voiced soundtrack to the rich imagery of the cosmos (see Hogan, 2006a).

In Einstein’s 1915 General Theory of Relativity (GR), the geometry of spacetime is not a passive setting for the dynamics of matter and energy, but an equally dynamic player. Matter and energy cause spacetime curvature, which in its turn guides the free fall of matter and energy. Remarkably, spacetime can support curvature without any matter: black holes, the densest masses in the Universe, are objects of pure spacetime wrapped around itself; gravitational waves are self-sustaining, undulatory excitations of spacetime, carrying energy and travelling at the speed of light. Unlike electromagnetic radiation (but much like neutrinos) gravitational waves interact very weakly with matter, and can penetrate anything almost without losing intensity. This makes them powerful probes of faraway regions and extreme conditions, but it also makes them very hard to detect. Only recently has technology advanced to the point of building apparatus sensitive enough to measure the minute effects of gravitational waves on matter.

Gravitational waves will reveal the most violent events in the Universe, the collision and coalescence of two black holes. During the final orbits before the merger, the power radiated in gravitational waves reaches 10^{49} W, independent of the involved masses (the energy, however, depends on the masses), a thousand times more luminous than all the stars in all the galaxies in the visible Universe put together. These mergers will allow us to test how well Einstein’s equations work in such extreme conditions, offering us insight into the strongest and most violently dynamic spacetimes Nature has produced since the Big Bang.

2.1.1. What are gravitational waves?

Electromagnetic waves are self-sustaining oscillations of the electric and magnetic fields, propagating through spacetime. By contrast, gravitational waves are oscillations of spacetime itself (see Thorne, 1987; and Flanagan and Hughes, 2005, for reviews). Einstein predicted gravitational waves shortly after developing GR, but the first experimental verification of their existence had to wait over 60 years, until the binary pulsar observations by Hulse and Taylor starting in 1974 (Hulse and Taylor, 1974).

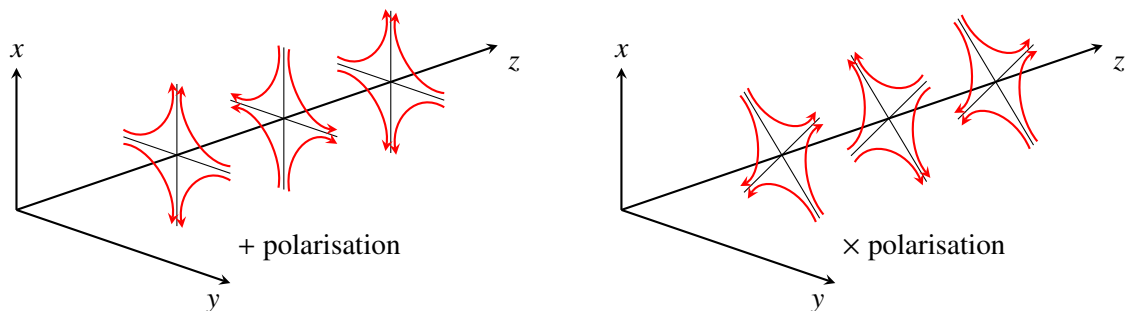


Figure 2.1.: Gravitational waves propagating along the z axis act in the x - y -plane. The two different polarisations (“+” and “ \times ”) exert different forces (red arrows).

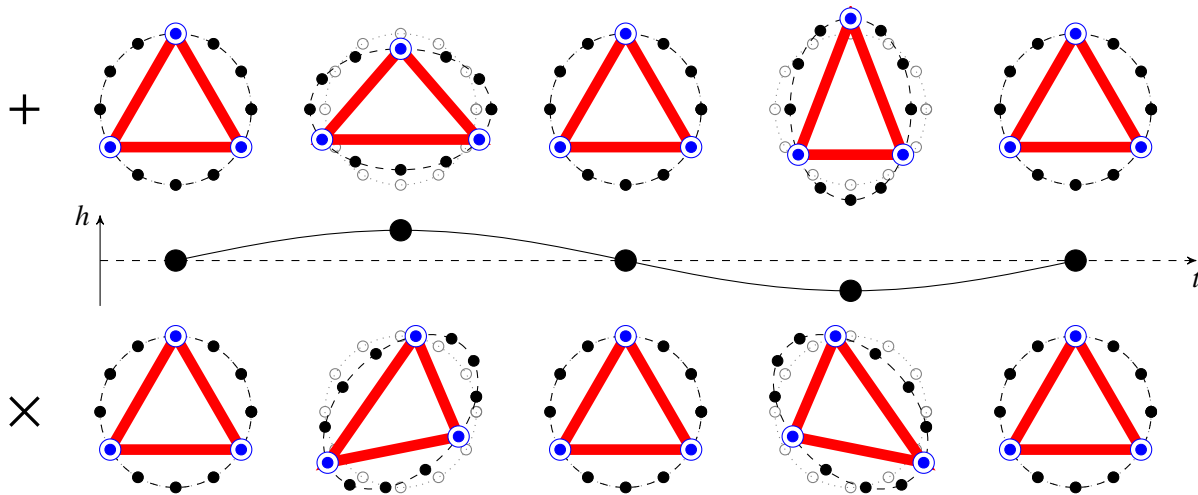


Figure 2.2.: A cartoon illustrating the passage of a gravitational wave through a ring of masses. Four phases of one cycle of the spatial distortion by a wave normal to the plane of the figure are shown both for the plus (“+”, upper row) and cross (“×”, lower row) polarisations. Three of the masses in the ring are used to represent the three LISA spacecraft, and the time-varying changes in the red arms show what the LISA interferometer would measure.

According to **GR**, gravitational waves propagate at the speed of light, acting tidally by stretching and squeezing any extended distribution of matter or energy through which they pass. This warping action is transverse to the direction of wave propagation. Gravitational waves contain two dynamical degrees of freedom, which can be identified with the “+” (plus) and “×” (cross) polarisations, corresponding to the axes associated with the stretching and squeezing (see figure 2.1). A pure “+” polarisation squeezes along the x -axis and stretches along the y -axis, and then the other way round one half-cycle later (figure 2.2). It is a particular property of **GR** that gravitational waves come in only two polarisations. Other theories of gravity predict as many as five different polarisations and the absence (or indeed presence) of such polarisations will serve as a further test of **GR** (Eardley et al., 1973).

Just as electromagnetic waves are generated by accelerated charges, gravitational waves are generated by accelerated masses. Because of charge conservation, an oscillating charge dipole is the lowest-order time dependent distribution that can produce electromagnetic waves; because of mass and momentum (*i.e.*, mass dipole) conservation, a variable mass *quadrupole* is needed to produce gravitational waves – technically it is the second time derivative of the transverse-traceless part of the quadrupole moment that generates gravitational waves.

Electromagnetic waves arise from the interactions of atoms, nuclei, or other particles within astrophysical sources and they are typically generated in numerous individual emitting volumes, much smaller than the astrophysical object of interest, so the wavelength of radiation is also much smaller than the object. For this reason, electromagnetic waves permit us to image the object if it is close enough or big enough. But the short wavelength has a disadvantage: typically, we receive an incoherent superposition of radiation from many independent regions in the source. If the source is not close enough to be resolved, then it is often a difficult and uncertain job to model the emission process well enough to go from the information we get about many different wavelength-scale regions up to the much larger scale of the entire astrophysical system.

By contrast, gravitational waves are generated by the bulk mass distribution of the objects, so their wavelength is typically comparable to or larger than the size of the entire emitting region, *e.g.* for two black holes orbiting each other and losing energy by gravitational radiation, the wavelength of the gravitational waves is 10 to 20 times the radius of the orbit. Thus, gravitational wave observations do not generally allow imaging, and the extraction of information from waveforms proceeds, *e.g.*, with audio-like methods such as time-frequency analysis or matched filtering. Because gravitational waves are emitted coherently from the entirety of the astrophysical object, they provide direct information about the object’s large-scale structure. Moreover, observations of gravitational waves allow us to extract information from the phase of the wave as well as its amplitude or

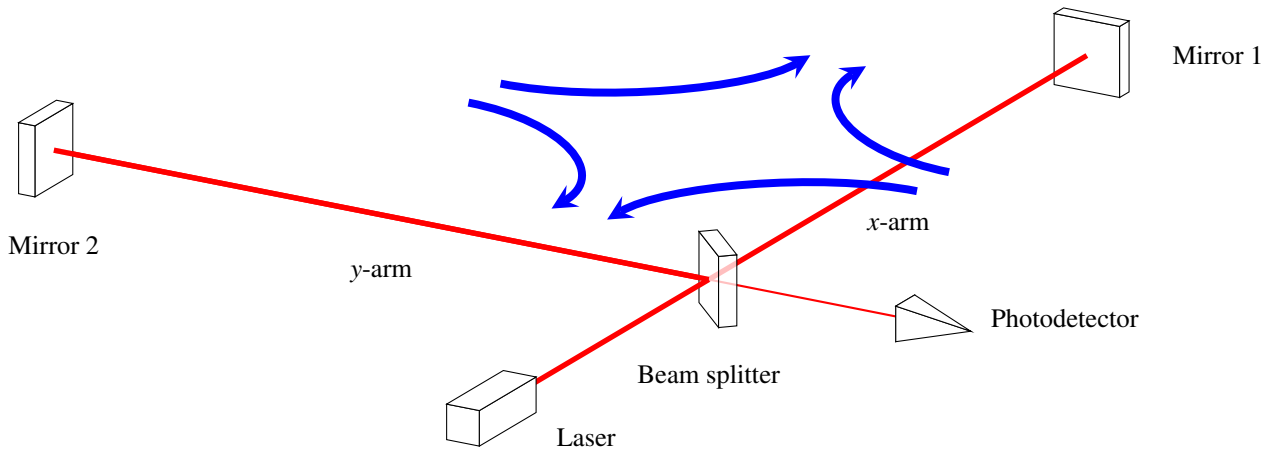


Figure 2.3.: *Idealised Michelson interferometer with laser, beam splitter, end mirrors, and photodetector at the exit port. The blue arrows represent a perpendicularly propagating, linearly polarised gravitational wave.*

intensity. The phase evolution often carries more information about the detailed dynamics of the emitter than the amplitude does.

2.1.2. How are gravitational waves detected?

Einstein’s great epiphany was that gravity is the manifestation of the curvature of spacetime, the background for all the interactions of matter and energy. Freely falling test bodies (small compared to the spacetime curvature and undisturbed by other forces) thread spacetime along geodesics, the straightest paths possible through this curved arena. Nearby, approximately parallel geodesics are pushed together and pulled apart by spacetime curvature. Gravitational waves are waves of spacetime curvature and are experienced by test bodies as an oscillating change in their relative distance.

To understand how this principle is used to detect gravitational waves, it is useful to visualise an idealised Michelson laser interferometer (see figure 2.3) whose components are floating freely in space, at rest with each other, and far removed from any gravitating bodies. The power measured by a photodetector at the exit port of the interferometer is a simple function of the phase difference of the two light beams that are divided at the beamsplitter, propagated along the two arms, and recombined at the exit port. Incoming gravitational waves (consider for simplicity a plane gravitational wave, propagating perpendicularly to the plane of the interferometer, with “+” polarisation aligned with the two arms) alternately increase the distance experienced by light travelling along one arm and decrease the distance along the other, creating oscillations in the power measured at the exit port. This is the basic principle of ground-based interferometric detectors such as LIGO and Virgo.

LISA brings the Michelson measurement concept to the grander scale and much quieter environment of space. While ground-based detectors are naturally limited by the Earth’s curvature to kilometre armlengths, LISA is more than a million times larger. As gravitational waves cause a *strain*, *i.e.* a fractional length change, longer arms undergo bigger changes, so LISA can achieve 10^{-22} strain resolution by measuring displacements of the order of fractions of a picometer. Combining this with the absence of seismic and gravity-gradient noise, LISA achieves sensitivity to the low-frequency gravitational waves emitted by large massive systems. Thus, while advanced ground-based detectors may observe neutron stars or stellar-mass black holes coalescing out to distances of hundreds of megaparsecs, LISA will be sensitive to massive black hole (MBH) coalescences out to redshifts of $z \sim 10$, allowing it to fathom the earliest stages of galaxy formation.

While LISA can be thought of as a “Michelson interferometer in space”, its actual implementation is quite different from a conventional Michelson interferometer. The experimental approach is closer to that of spacecraft Doppler tracking, in which the observed quantity is the frequency change in the signal from a distant spacecraft. In LISA, each spacecraft sends a beam of laser light to each of the other two distant spacecraft, and in turn receives a beam from each of them. The received laser light is coherently combined at a photodetector with the light from an on-board reference laser, and the frequency difference is recorded as a beat signal. The beat signals

recorded at each of the three spacecraft are delayed in time and recombined in a technique called time-delay interferometry (TDI) (Tinto and Larson, 2005) which essentially creates three virtual Michelson interferometers whose output signals represent the basic LISA science data stream.

LISA as an astronomical observatory for gravitational waves has some characteristics that are different from observatories of electromagnetic radiation. It will help to understand the range and versatility of LISA's observations as described in this document if we make some of these differences explicit below.

First, LISA has a large intrinsic dynamic range: it could in principle measure accurately signals over an amplitude range of 10^5 or an energy range of 10^{10} . This is because it measures tiny changes in separations between the test masses and therefore always operates in a linear regime. LISA is designed to study signals well below its mean noise level (extracting them by matched filtering) up to the strongest expected sources in the Universe.

Second, LISA has a very large frequency range, spanning four decades, limited at high frequencies by its size and at low frequencies by the difficulty of isolating the test masses. This means that, unlike optical, ultraviolet, or infrared observatories, LISA is less likely to miss distant sources because they are cosmologically red-shifted to lower frequencies: indeed, it will be able to study the populations of objects out to the highest redshifts.

Third, LISA has all-sky acceptance of signals; it sweeps three different quadrupolar antenna patterns across the sky as it orbits the Sun, so that its sensitivity for all but the shortest transient sources is fairly isotropic. Unlike any imaging electromagnetic observatory, LISA is not pointed, so it does not miss any signals once they are above its noise level. This property is particularly important as it allows LISA to detect strong transient events such as black hole coalescences without having to point at the source; the strongest events in the Universe are necessarily transient, because they radiate far too much energy to be sustained in a steady state. Although LISA is an all-sky detector, it can nevertheless reconstruct event positions through its data analysis, by analysing phase modulation (Doppler effects) and amplitude modulation of the signals, which are available thanks to the detector's coherent observations. LISA can also separate thousands of simultaneously superimposed signals because it uses phase information to resolve them, so its all-sky acceptance does not lead to confusion except where there are very large numbers of sources.

Finally, LISA is not troubled by absorption, scattering, or obscuration in any of its observations, as gravitational waves interact very weakly with matter. The best illustration of this is in searching for a cosmological background of radiation from inflation: LISA can in principle see right back to the end of the inflationary epoch, through all stages of decoupling, symmetry breaking, and particle creation. Gravitational waves will also give us our deepest views of the interiors of very dense environments, our only direct information about black holes, leading to their unequivocal identification, and to our first chance to observe any possible structures in the electrically neutral dark matter in the Universe.

We also note that LISA (as all interferometric gravitational wave detectors) observes the *amplitude* of the gravitational wave (or wave strain) h , *i.e.* the fractional amount of the stretching and squeezing discussed above. As the amplitude h falls off only as $1/r$, strong sources of gravitational waves (such as the binary inspirals of massive black holes, which LISA will see with amplitude signal-to-noise ratio (SNR) of more than 1000 at a redshift $z = 1$), can essentially be detected out to arbitrarily large redshifts. A further consequence of measuring the amplitude is the practise to express the sensitivity as an amplitude spectral density, *i.e.*, the square root of the more commonplace power spectral density, as the amplitude spectral density relates more closely to the measurement. As strain is a dimensionless quantity, strain amplitude spectral density has the peculiar units of inverse square root of hertz.

The distinctive characteristics of gravitational waves ensure that they will provide a unique new channel to study the Universe, complementing information gathered over decades from electro-magnetic (EM) channels, and probing previously inaccessible dense and dark regions of the Universe. The potential for discovery and surprise is great.

2.1.3. The gravitational wave Universe in the LISA band

Although gravitational waves have not been detected directly yet, we know enough about the contents of the Universe to make reasonably accurate assessments about some of their sources that LISA will observe (see Hughes, 2003; Hughes, 2006, for reviews). As discussed earlier, in the same way that accelerated electric charges

generate electromagnetic radiation, accelerated mass and energy generate gravitational radiation. The periodic motion of a system of mass M and size R at a (luminosity) distance D creates gravitational waves with a strain amplitude of about $h \sim (GM/(Rc^2))^2(R/D)$, with a frequency determined by the frequency of the motion. The shapes and strengths of the observed waves give us details about the structure and behaviour of the system that produced them.

The strongest waves are generated by systems with the largest gravitational fields GM/R , which correspond to large masses and small sizes and are generated by the interactions of black holes, which have $GM/(Rc^2) \approx 1$. The lightest black holes (remnants of single stars, with about ten times the mass of the Sun) emit at the highest frequencies, in the 100 Hz band, accessible to ground-based detectors.

By contrast, the strongest sources in the far lower LISA band (between 0.1 mHz to 100 mHz) are the **MBHs** at the centres of galaxies; these are the remnants of the process of galaxy formation, with about 10^4 to 10^7 times the mass of the Sun (M_\odot). Optical, radio, and X-ray astronomy have produced abundant evidence that nearly all galaxies have massive black holes in their central nucleus, and that some of them even have two.

Mergers of **MBHs** happen frequently: galaxies are continually forming, in a hierarchical fashion, starting from the mergers of smaller galaxies, and whenever two galaxies merge their central black holes sink to the centre and find each other. **MBH** mergers are so powerful that LISA can detect them out to a wide range of redshifts, extending back to the first protogalaxies at $z \sim 15$. Estimates from standard galaxy formation theory suggest that LISA will detect **MBH** mergers about once or twice every week (Volonteri, 2006), but predictions are very uncertain at the high-redshift end, which is beyond the reach of electromagnetic observations. LISA will lift the veil of these cosmic “dark ages”, providing a direct record of the history of galaxy formation and central black hole growth in the observable Universe.

Smaller galactic objects can also be captured (and eventually consumed) by the central black hole. Compact objects such as degenerate dwarfs, neutron stars, and black holes sometimes will be driven by chance encounters into a close orbit around the **MBH**: a dance of death that they will repeat for many revolutions until they finally plunge into the black hole’s event horizon. The gravitational waves from these extreme mass-ratio inspirals (EMRIs) encode a detailed map of spacetime geometry around the **MBH**. The history and environment of the black hole leave no imprint on this geometry, which is a very pure and beautiful solution (the Kerr metric) of the equations of **GR**. Thus, **EMRI** signals will test Einstein’s theory by probing the most accurately predicted structures in all of astrophysics.

In addition to black holes, many other known systems in our Universe can produce gravitational waves in LISA’s frequency band. Soon after it is turned on, LISA will quickly detect a handful of nearby verification binary stars, which have known periods and positions (and even assigned names), and which will appear in the LISA data with predictable, distinctive signatures.

A large Galactic population of undiscovered degenerate-dwarf binaries will be observed all across the LISA band; we know from electromagnetic observations that such objects exist in our vicinity, but LISA will detect thousands of individual binaries throughout the Galaxy. At low frequencies millions more binaries from across the Galaxy will blend together into a confusion background in the LISA data, which will nevertheless teach us about the statistics of their population. At higher frequencies, the binaries have more powerful signals, and are farther apart in frequency space, allowing LISA to characterise each individually. At high frequencies, LISA may also detect the background signal from the degenerate binaries in other distant galaxies, allowing us to place constraints on cosmic star formation rates.

Given that all forms of matter and energy couple to gravity, it seems likely that the Universe will treat LISA to yet other gravitational wave sources that we cannot anticipate on the basis of our electromagnetic observations. This is especially true for observations at very high redshifts, where LISA may give us the very first clues to the unknown conditions of matter and energy in the very early Universe.

In the relativistic early Universe, the LISA frequency band corresponds to the Terascale frontier, where the phase transitions of exotic fields or extra spatial dimensions may have caused catastrophic and explosive bubble growth, with efficient gravitational wave production. LISA will also probe superstrings, relics of the early Universe predicted in some versions of string theory. These exotic structures, which are completely invisible except for the gravitational waves they emit, could produce strong, distinctive LISA signatures; they could provide direct evidence that all forms of matter and energy, and possibly even spacetime itself, are ultimately

made of quantum strings.

2.2. Survey of LISA Science

This section provides a brief survey of the key scientific measurements that LISA will perform. These measurements address the basic scientific goals of the LISA mission, which are captured formally in the *LISA Science Requirements Document* (LISA-ScRD-066) and given for reference in appendix B. The scientific background for the LISA science measurements and objectives is discussed extensively in the following sections of this chapter.

LISA directly determines whether intermediate mass black holes formed at early times, and grew over cosmic time to generate the massive black holes present in most galactic nuclei today.

Optical, radio and X-ray astronomy have produced abundant evidence that nearly all galaxies have massive black holes in their central nuclei (and indeed that some recently merged galaxies even have two black holes). For most galaxies, where the massive black holes today are smaller than roughly $10^8 M_{\odot}$, growth from intermediate-mass black holes (IMBHs) seeds that formed very early appears to be quite feasible. In standard concordance cosmology, the first IMBHs naturally arose from the very first, supermassive stars. In this scenario, IMBHs began to form at high redshift, $z \sim 20$, and then grew in the galaxies that started to be assembled by a series of (hundreds to thousands of) hierarchical mergers of smaller protogalaxies. When two galaxies merge into one, their central black holes sink to the centre of the new galaxy, usually find each other, form binaries, inspiral, and merge. The IMBHs grow mostly by accretion, but a substantial number of inspiral events are likely to be observed by LISA each year, giving the mass of each black hole and its spin as a function of the redshift z . Estimates based on standard galaxy formation theory suggest that LISA will detect a merger event about once a week from a wide range of redshifts extending back to early protogalaxies at $z \sim 15$. Some events at early times with one mass as low as $300 M_{\odot}$ are expected.

There also are other scenarios for the growth of present massive black holes from IMBHs that formed in different ways. In addition, it is possible that massive black holes of $10^4 M_{\odot}$ or higher mass formed directly from the collapse of large gas clouds that managed to lose their angular momentum and cool before fragmenting to form stars. In this case, the distribution of masses observed in merging binary black holes would be quite different, so that a clear resolution of the issue of how most present massive black holes formed is expected.

LISA traces the interaction of galaxy growth and massive black hole growth over the entire history of galaxy formation.

There is strong evidence for a fundamental relationship between the growth of massive black holes in the centres of galaxies and the growth of the galaxies themselves. This evidence is based on the close relationship that has been observed between the black hole mass and both the stellar mass and the velocity dispersion of the stars of the galaxy the black hole is in. However, although a number of possible mechanisms for establishing the close relationship have been investigated, there is no clear consensus on the explanation yet.

By observing the masses of the massive black holes involved in binary mergers as a function of redshift, LISA will provide a strong constraint on the way in which black hole masses in the galactic centre evolved over time. These observations, when coupled with new near-infrared observations of the evolution of the galactic masses, will help in understanding the relationship between the growth processes. Other types of observations give information on the black hole masses in the relatively nearby universe, and quasar measurements do the same for supermassive black holes at early times. However, gravitational wave observations of mergers appear to be the best approach for determining the growth history at moderate to large redshifts for intermediate mass and up to perhaps $10^7 M_{\odot}$ black holes.

LISA explores the populations of stellar-mass compact objects in galactic nuclei and their dynamics.

There are expected to be quite large populations of stellar-mass black holes, neutron stars, and white dwarf stars in galactic nuclei. For such stellar-mass compact objects, some will have nearly radial orbits and be scattered in

close enough to the massive black hole at the galactic centre to be captured. The resulting binaries with very small mass ratios will evolve by gravitational radiation and later merge in what are called **EMRI** events. The resulting signals will be observed by LISA at redshifts out to $z \sim 1$.

The time over which such signals can be followed by LISA is roughly a year. The strongest signals will come from stellar-mass black holes, which are expected to be concentrated near the galactic centre by mass segregation processes. Such events will give extremely strong tests of the predictions of general relativity, as discussed later. However, the frequencies of **EMRI** events for the different types of stellar-mass compact objects will give unique information on their space density and on the dynamics of their orbits in the neighbourhoods of galactic centre massive black holes.

LISA will study in detail the signals from thousands of stellar-mass close binaries in the Galaxy and also give information on the Galactic structure.

LISA can detect many stellar-mass binary systems in our Galaxy, mostly very compact remnants of normal stars, called white dwarfs. Very soon after turning on, LISA will detect a handful of already identified nearby binary compact stars. These “verification binaries” provide sources with known positions and periods ensuring particular, predictable LISA signals. Signals are also certain to appear from populations in our galaxy of numerous and various remnants, including white dwarfs and neutron stars, which are known to exist from others that emit electromagnetically. Simple extrapolation of known nearby samples to the whole Galaxy predicts that LISA will detect tens of thousands of binaries. The most compact binaries (those at high frequency) will be measured in detail as individual sources from across the Galaxy, while at lower frequencies only the nearby ones will be individually distinguished; millions of others from across the Galaxy will blend together into a confusion foreground. LISA provides distances and detailed orbital and mass parameters for hundreds of the most compact binaries, a rich trove of information for detailed mapping and reconstruction of the history of stars in our galaxy, and a source of information about tidal and non-gravitational influences on orbits associated with the internal physics of the compact remnants themselves. LISA may also detect at high frequencies the background signal from compact binaries in distant galaxies.

LISA will observe highly relativistic mergers of black hole binaries, and provide exceptionally strong tests of the predictions of general relativity.

LISA can provide two different types of tests of gravitational theories. The first type is dynamical tests based on mergers of two massive black holes of similar mass, with masses of up to about $10^7 M_{\odot}$. In the last hours or minutes before mergers the **SNR** grows very high, sometimes to several thousands, depending on the redshift. At its peak luminosity, around the moment of merger, a massive black hole binary is the most extreme transformer of mass into energy of any kind in the Universe, radiating a power of about 10^{49} W for a few wave cycles. With the two masses being maximally warped vacuum spacetimes travelling at near the speed of light and interacting strongly with each other, the full nonlinear dynamics of gravitational theory will be tested.

The second type of test involves roughly $10 M_{\odot}$ black holes spiralling in toward massive black holes and merging with them. In this case roughly 10^5 cycles of the motion will be observable over about a year before merger, and the speed for the lower mass black hole near periastron will be roughly half the speed of light. For such **EMRIs**, because the eccentricities of the orbits will be very high initially and will stay roughly in the range of 0.3 to 0.7 until just before merger, there will be periastron precession at almost the orbital motion rate, and probably rapid Lense-Thirring precession as well. If the phase of the observed gravitational wave signal agrees with the predictions of general relativity to a small fraction of a cycle over the whole observing period, this will provide exceptionally strong support for the theory under the most extreme conditions.

LISA will probe new physics and cosmology with gravitational waves, and search for unforeseen sources of gravitational waves.

The LISA frequency band in the relativistic early Universe corresponds to horizon scales at the Terascale frontier, where phase transitions of new forces of nature or extra dimensions of space may have caused catastrophic,

explosive bubble growth and efficient gravitational wave production. LISA is capable of detecting a stochastic background from such events from about 100 GeV to about 1000 TeV, if gravitational waves in the LISA band were produced with an overall efficiency of more than about 10^{-7} , a typical estimate from a moderately strong relativistic first-order phase transition. This corresponds to times about 3×10^{-18} to 3×10^{-10} seconds after the start of the Big Bang, a period not directly accessible with any other technique. Reaching much further still beyond the range of any particle accelerator, LISA also deeply probes possible new forms of energy such as cosmic superstrings, relics of the early Universe predicted in some versions of string theory, that are invisible in all ways except by the gravitational waves they emit. In principle, their signature could provide direct evidence for new ideas unifying all forms of mass and energy, and possibly even spacetime itself.

2.3. Black Hole Astrophysics: Massive Black Holes in Galactic Nuclei

LISA science objectives and investigations relevant to this section

1. Trace the formation, growth, and merger history of massive black holes
 - 1.1 Trace the formation, growth, and merger history of **IMBHs** and **MBHs** out to redshift $z = 15$
 - 1.2 Determine the merger history of **MBHs** with masses of $10^4 M_\odot - 3 \times 10^5 M_\odot$ from the era of the earliest known quasars, $z \sim 6$
 - 1.3 Determine the merger history of **MBHs** with masses between $3 \times 10^5 M_\odot$ and $10^7 M_\odot$ at later epochs, $z < 6$
2. Explore stellar populations and dynamics in galactic nuclei
 - 2.1 Characterise the immediate environment of **MBHs** in $z < 1$ galactic nuclei from **EMRI** capture signals
 - 2.2 Study intermediate-mass black holes from their capture signals
 - 2.3 Improve our understanding of stars and gas in the vicinity of Galactic black holes using coordinated gravitational and electromagnetic observations

Cosmic Vision scientific questions addressed by this section

- 3.3 Matter under extreme conditions

Probe gravity theory in the very strong field environment of black holes and other compact objects, and the state of matter at supra-nuclear energies in neutron stars
- 4.2 The Universe taking shape

Find the very first gravitationally-bound structures that were assembled in the Universe – precursors to today’s galaxies, groups and clusters of galaxies – and trace their evolution to the current epoch
- 4.3 The evolving violent Universe

Trace the formation and evolution of the supermassive black holes at galaxy centres – in relation to galaxy and star formation – and trace the life cycles of matter in the Universe along its history

The LISA Science Objectives are given in appendix B, the Cosmic Vision scientific questions in appendix A.

There is now abundant evidence that nearly all galaxies have massive black holes in their central nuclei. These nuclear black holes can have profound effects on galaxy formation, releasing huge amounts of thermal and kinetic energy into the galaxy via accretion-powered outflows and jets. The formation of this population of massive black holes is thought to be associated with a multistage process of binary inspiral and merger, together with accretion. LISA will detect the merger events directly, thus tracing the growth and merger history of massive black holes and their host galaxies. LISA will search for a population of seed black holes at early epochs and use precision measurements of black hole spins to help determine the relative importance of black-hole growth mechanisms. LISA will also probe the rich astrophysics in the nuclei of normal galaxies by observing the inspiral of compact objects into the massive black holes in their centres.

2.3.1. Evidence for supermassive black holes in galactic nuclei

Supermassive black holes accreting gas in galactic nuclei were first proposed in the 1960s (Salpeter, 1964; Zel’dovich and Novikov, 1964) to explain the enormous luminosities of the newly discovered quasars. Refinements of this idea have become the generally accepted explanation for the electromagnetic and matter emissions from all active galactic nuclei (AGN) (see, *e.g.*, Krolik, 1999).

The disks of gas around accreting black holes (mass M_\bullet) in active galaxies are inferred to have luminosities approaching the Eddington limit L_{Edd} at which radiation pressure on the Thomson cross section σ_T of electrons balances the gravitational attraction on them and the protons from which they were stripped:

$$L_{\text{Edd}} = 4\pi \frac{GcM_\bullet m_p}{\sigma_T} = 10^{39} \text{ W} \left(\frac{M_\bullet}{10^8 M_\odot} \right) . \quad (2.1)$$

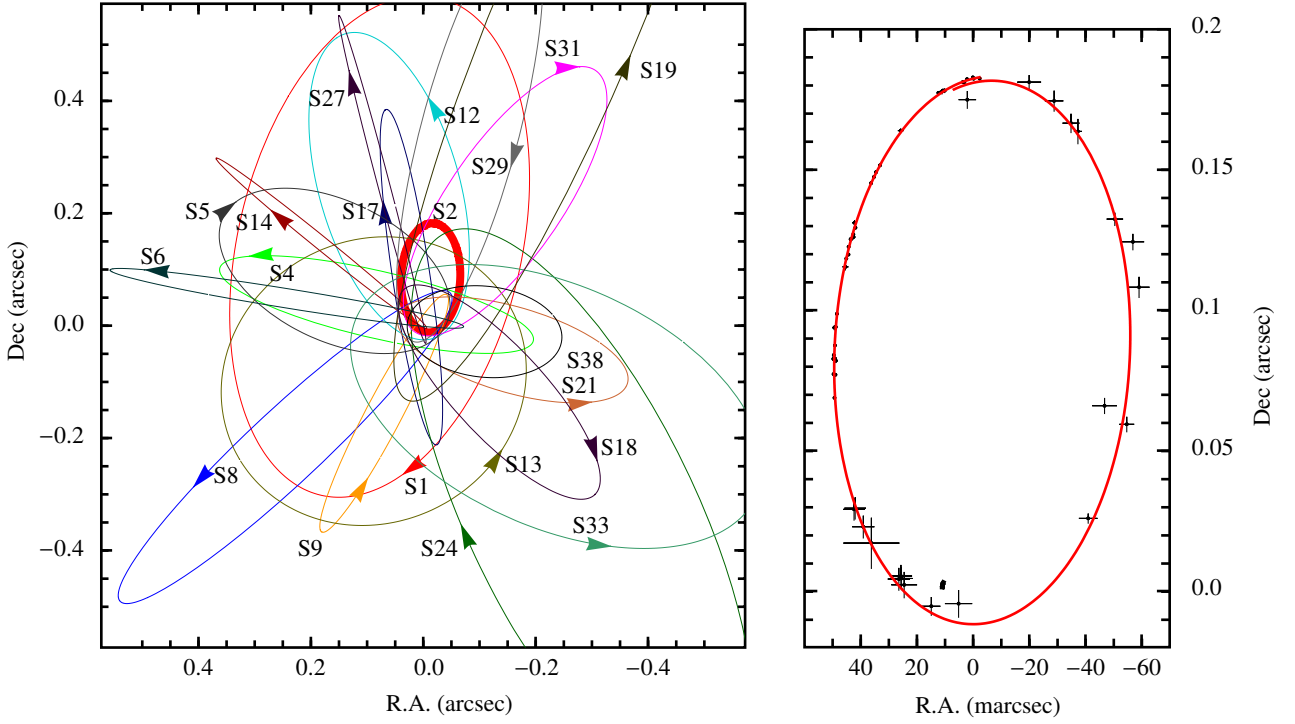


Figure 2.5.: Left panel: *Orbits of stars around the central point mass in the Milky Way with the orbit of S2 in bold red.* Right panel: *Detailed orbit and measurements for S2.* Both adapted from Gillessen et al. (2009)

radius of the inferred black hole, so other astrophysical models (*e.g.*, dense clusters of stellar-mass black holes) are not conclusively ruled out. In the notable case of our own Milky Way, the orbits of stars passing as close as 1300 Schwarzschild radii from the $(4.31 \pm 0.06 \pm 0.36)M_{\odot}$ central mass (Ghez et al., 2008a; Gillessen et al., 2009, see also figure 2.5) can be observed, and even contrived astrophysical alternatives to black holes (Maoz, 1998) can be ruled out, leaving only exotic models such as soliton stars with radii of less than a few Schwarzschild radii.

The black hole mass estimates derived from the kinematics of stars and gas in the nuclei of nearby representative galaxies also allow one to estimate the space density of local black holes ρ_{\bullet} . These estimates give

$$\rho_{\bullet} = 2 \times 10^5 - 5 \times 10^5 M_{\odot}/\text{Mpc}^3 \quad (2.3)$$

(for $H_0 = 70 \text{ km}/(\text{s Mpc})$; Aller and Richstone, 2002; Marconi et al., 2004). The uncertainty in ρ_{\bullet} results principally from uncertainties and dispersion in the correlations between black hole mass and galaxy luminosity or between black hole mass and velocity dispersion (Lauer et al., 2007; Tundo et al., 2007).

The density ρ_{\bullet} can be compared to the total increase in the mass density of black holes derived from the total radiation density emitted by AGN, an argument suggested by Soltan in 1982. If the total radiation density emitted by AGN were produced by accretion onto black holes with an efficiency ϵ of converting accreted rest-mass to radiation, then it must have increased the mass-density of supermassive black holes by

$$\Delta\rho_{\bullet} \approx 3.5 \times 10^5 \frac{M_{\odot}}{\epsilon_{0.1} \text{Mpc}^3} \quad (2.4)$$

(Marconi et al., 2004; Soltan, 1982). Most of this radiation comes from AGN with redshifts between $z = 0.5$ and $z = 3$. There is probably a 50 % uncertainty in $\Delta\rho_{\bullet}$ due to uncertainties in the bolometric corrections and in corrections for obscured AGN and faint high-redshift AGN (Gilli et al., 2007).

The estimates for the growth in black hole mass, $\Delta\rho_{\bullet}$, can be compared to the estimate for the local density of black holes. Most of the contribution to the local black hole mass density comes from black holes with masses between $10^8 M_{\odot}$ and $10^9 M_{\odot}$. Similarly, the main contribution to $\Delta\rho_{\bullet}$ comes from black holes in the same mass

range at $z = 2-3$ (Merloni, 2004). Since these black holes have grown in mass mainly through accretion, by a few orders of magnitude from $z = 3$ to now, the high-redshift Universe must have been dominated by black holes of a smaller variety, $10^6 M_{\odot}-10^7 M_{\odot}$. The contribution of mergers to the growth of these smaller black holes is uncertain but can be determined with LISA, which will detect any merger of mass $10^5 M_{\odot}-10^7 M_{\odot}$ with high SNR (Baker et al., 2007a; Cornish and Littenberg, 2007; Hughes, 2002) out to redshift $z = 20$ or higher.

2.3.2. Growth and merger history of massive black holes

Expected merger rates

There is a simple argument bounding the number of mergers of massive black holes that LISA is likely to see. HST observes more than 10^{10} galaxies. Most bright local galaxies contain central supermassive black holes. Fossil evidence for mergers among local galaxies implies that about 70 % of these have undergone a merger during the 8 Gyr since redshift $z = 1$ (Bell et al., 2006; Toomre, 1977). Therefore, the galaxy merger rate at $z < 1$ must be close to one per year, and if the black holes in merging galaxies merge in turn, the merger rate of massive and supermassive black holes should also be at least one per year.

Observations show that our Universe is dominated by cold dark matter (CDM), and that its initial spectrum of perturbations was such that the first objects to collapse under their self-gravity were tiny systems the size of dwarf galaxies. These then fell into each other to create larger ones. Present-day galaxies like our Milky Way grew by the merger of more than 1000 subunits, which started forming already at redshift higher than 20. If each of these subunits initially contained a seed black hole of $10^4 M_{\odot}$, the merger rate seen by LISA could be as high as one thousand per year.

These elementary arguments suggest strongly that the merger rate of binary black holes that LISA will see lies in the range $1 \text{ yr}^{-1}-1000 \text{ yr}^{-1}$ (see figure 2.6). The actual rate is proportional to the fraction of proto-galactic fragments that contain seed black holes massive enough for LISA to detect their mergers, multiplied by the fraction of galaxy mergers that lead to black hole mergers. Our theoretical understanding of these fractions is limited and neither is well constrained observationally. LISA's measurements offer our best hope of determining them.

Seed black holes

The number densities and masses of seed black holes largely determine the merger history of galaxies. The similarity between ρ_{\bullet} (the current best estimate for the mass density in black holes) and $\Delta\rho_{\bullet}$ (the density of rest mass that must have been accreted in order to produce the observed AGN) lends itself to at least two possible scenarios. In one, accretion does play a large part in the building of supermassive black holes from small ($1 M_{\odot}$ to $100 M_{\odot}$) seed black holes. In another scenario a significant fraction of the present black hole mass density is already present as black hole “seeds” by $z = 10-20$ (Koushiappas et al., 2004). In this scenario only a few of the seeds have grown through accretion to $10^9 M_{\odot}$ which then make up most of the mass we detect in supermassive black holes today and explain most of the accretion luminosity. Thus, mergers would provide a larger contribution to the mass-growth of today's black holes. LISA's direct observations of gravitational waves emitted by these mergers will be able to distinguish between the different scenarios.

Several scenarios have been proposed for the seed black hole formation and their initial mass function (IMF): seeds with masses of a few $100 M_{\odot}$ can form as remnants of metal free (PopIII) stars at redshift $z \leq 20$ (Abel et al., 2002; Bromm and Larson, 2004; Bromm et al., 2002; Madau and Rees, 2001; Volonteri et al., 2003) while intermediate-mass seeds with masses about $10^5 M_{\odot}$ can be the end product of the dynamical instabilities arising in massive gaseous protogalactic disks in the redshift range $10 < z < 15$ (Begelman et al., 2006; Koushiappas et al., 2004; Volonteri and Begelman, 2010) or by direct collapse of radiation-dominated massive star-like objects (Bond et al., 1984; Rees, 1978).

Observational evidence for low-mass black holes that possibly retain some information of the original seed mass is difficult to obtain with electromagnetic observations except for nearby ($z < 0.2$) low-mass AGN (Barth et al., 2005; Greene and Ho, 2007). Seed black holes might power “mini-quasars” at high redshift, but if the mass

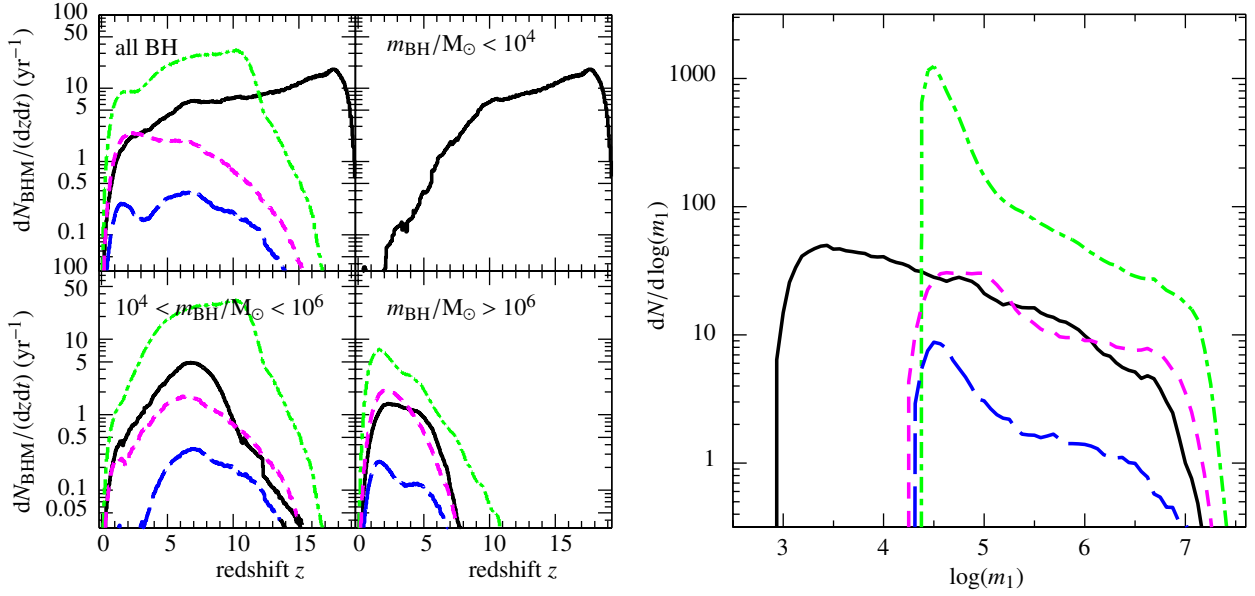


Figure 2.6.: Left panel: number of massive black hole binary (MBHB) coalescences per observed year at $z = 0$, per unit redshift, in different $m_{\text{BH}} = m_1 + m_2$ mass intervals. Black (Solid lines): seeds with masses of a few $100 M_{\odot}$ (Volonteri et al., 2003, see); green (short–long dashed lines): seeds with $10^5 M_{\odot}$ (Koushiappas et al., 2004, see) model; purple (short–dashed lines): seeds with $10^5 M_{\odot}$, slow metal enrichment; blue (long–dashed lines): seeds with $10^5 M_{\odot}$, rapid metal enrichment (both Begelman et al., 2006). Right panel: Mass function of the more massive member of massive black hole binaries resolved with $S/N > 5$ by LISA in a 3-year mission. Line style as in left panel. All curves are normalised such that the integral in $d\log(m_1)$ gives the number of detected events. Both panels adapted from Sesana et al. (2009).

of the seeds is below about $10^6 M_{\odot}$, the large formation redshifts ($z \sim 10\text{--}30$) and the ensuing large luminosity distance D_L will make the electromagnetic signals too weak to be detectable by today’s telescopes.

Observing their gravitational radiation allows us to identify seeds with masses of about $10^4 M_{\odot}$ during their mergers, which may play a much more important role in the higher-redshift Universe than at lower redshifts. Not only is the merger rate at $z > 5$ not limited by Soltan-type arguments that constrain the mass growth of black holes that can occur through mergers, but constraints the number of mergers at $z < 3$, but constraints derived from the X-ray background limit the overall growth by accretion for black holes at $z > 6$ (Volonteri et al., 2006).

The different types of IMFs for the seeds give rise to distinctive features in the rates and masses observed by LISA. Detectable mergers with masses below $10^4 M_{\odot}$ are a unique feature of the models favouring light seeds (e.g. Volonteri et al., 2003); the rate of mergers in the mass range of $10^4 M_{\odot} < M(1+z) < 10^5 M_{\odot}$ discriminates between different models with intermediate mass seeds (see figure 2.6 and Sesana et al., 2007, 2009).

The role of massive black holes in the evolution of early cosmic structure.

AGN powered by supermassive black holes keep the Universe ionised at $z < 4$, structure the inter-galactic medium (IGM), and probably regulate star formation in their host galaxies. IMBHs accreting gas from the surrounding medium may shine as “mini-quasars” at redshifts as high as $z = 20$, with dramatic effects on the thermodynamics of the inter-galactic medium (IGM) (Kuhlen and Madau, 2005). There are significant uncertainties about this key period in structure formation, from the fate of the first stars (Abel et al., 2002; Bromm and Larson, 2004; Bromm et al., 2002) to the growth of $M > 10^9 M_{\odot}$ black holes from seed black hole precursors in redshift $z > 6$ quasars (Alvarez et al., 2009; Bromm and Loeb, 2003; Madau and Rees, 2001; Milosavljević et al., 2009; see also simulations by Li et al., 2007) to the role of black holes in the reheating and reionisation of the Universe (Madau et al., 2004), to the establishment at early epochs of the currently observed tight correlation between black hole mass and galactic bulge properties (Ferrarese and Ford, 2005; Ferrarese and Merritt, 2000; Gebhardt et al., 2000; Tremaine et al., 2002).

Models of hierarchical structure assembly predict that galaxy-sized dark matter halos will start to be common at redshifts $z = 10\text{--}20$ (see, *e.g.*, Mo and White, 2002, for a summary). This is also the epoch in which stars and galaxies first form in abundance, hence it is the beginning of the nonlinear phase of the Universe. However, electromagnetic observations of the properties and interactions of these early galaxies are extremely challenging, as they are under-luminous dwarfs and, additionally, the surface brightness decreases with increasing redshift as $(1+z)^{-4}$.

Observations of massive black hole coalescences from this epoch will be uniquely powerful in probing the halo mergers required in current models. The central black holes in many early halos are expected to have masses $M \sim 10^4 M_{\odot}\text{--}10^6 M_{\odot}$, corresponding to the redshifted mass range $10^5 M_{\odot} < M(1+z) < 10^7 M_{\odot}$.

LISA will be able to detect MBH mergers in that mass range with large SNR out to a redshift of $z = 20$ and above (Arun et al., 2009). By measuring the rate of these mergers, expected to be tens per year at redshifts $z > 10$ (*e.g.*, Sesana et al., 2004, 2005, 2007), and by characterising their redshift and the mass distributions, LISA will be able to discriminate between classes of structure formation models as well as the different models for the initial mass function of the seeds.

The merger of galaxies and their black holes

When two galaxies collide, the gravitational interactions between their stars and dark matter merge them together in about 10^8 years. If both galaxies contain nuclear black holes, the black holes orbit within the merger remnant, and lose energy because of dynamical friction (Chandrasekhar, 1943a,b,c) and the subsequent ejection of stars intersecting their orbits (Quinlan, 1996; Sesana et al., 2006). Within several orbital periods, the two black holes eject all the stars in their vicinity, and the rate of subsequent shrinking of their orbits is controlled by the inflow of stars and gas from larger radii, and the emission of gravitational radiation (Merritt and Milosavljević, 2005). For black holes with mass smaller than $10^7 M_{\odot}$ gravitational radiation alone will merge the black holes in less than 10^{10} yr (Yu, 2003). In more massive galaxies, the larger pair of black holes can eject all their surrounding stars before the pair is close enough for gravitational radiation to merge them. Then, without a further inflow of stars or gas, the black holes could be left orbiting each other for longer than the Hubble time, remaining at orbital separations of 0.1 pc–1 pc and orbital periods of 10^2 yr– 10^4 yr.

This “orbital hangup” can be overcome if bulges are sufficiently tri-axial, or enough gas that the continuing supply of material for the pair to eject continues to cause the pair’s orbit to shrink (Berczik et al., 2006; Berentzen et al., 2009; Dotti et al., 2007; Escala et al., 2004, 2005; Merritt and Poon, 2004; Perets and Alexander, 2008).

The black holes are eventually driven close enough together that gravitational radiation takes over and merges them on a fairly short timescale. Observational evidence favours prompt mergers even among the massive black holes, as the number of detected pc- and sub-pc binaries is small (see Rodriguez et al., 2006; and Boroson and Lauer, 2009, respectively). If these binaries lived a Hubble time, such detections should be more common (Volonteri et al., 2009). Furthermore, the most compelling explanation for X-shaped and double-double radio galaxies is that they result from reorientation of the black hole spin following a merger (Zier, 2007, and references therein).

LISA observations of merging MBHs represent one of the best opportunities for observing the complex history of galaxy mergers. LISA can determine the binary’s luminosity distance, typically to within several percent. Assuming the standard concordance cosmology, this distance gives us the binary’s redshift. Thus one can deduce the MBH merger rate as a function of z , and so trace the early history of galaxy mergers and the build-up of MBH masses over time (at least for those of about $10^6 M_{\odot}$). Today, the fraction of low-luminosity galaxies with black holes with masses smaller than $10^6 M_{\odot}$ is unknown at all redshifts.

2.3.3. Black hole Spins

No hair and no naked singularities

In GR, astrophysical black holes are predicted to be completely described by exactly two parameters, mass M and spin S . While GR also allows an electric charge, this is quickly shorted out to gravitationally insignificant levels. This simple parametrisation of a black hole is famously known as “black holes have no hair” (see, *e.g.*,

Thorne, 1994) and a spinning black hole ($a_{\bullet} \neq 0$) is known as a *Kerr* black hole whereas the simple non-rotating black hole ($a_{\bullet} = 0$) is known as the *Schwarzschild* black hole.

The total spin angular momentum S is usually specified in terms of the dimensionless angular momentum $a_{\bullet} = S/(GM^2/c)$, or $a_{\bullet} = S/M^2$ in relativists' units where $G = c = 1$. For a specified mass M , a black hole described by GR cannot have $a_{\bullet} > 1$ without showing a naked singularity, *i.e.* one uncloaked by an event horizon, generally assumed to be forbidden by the Cosmic Censorship conjecture.

Predicted spins from formation and growth

Rotating gas clouds and stars typically have $a_{\bullet} > 1$, so black holes that form from their collapse are likely to have a high spin ($a_{\bullet} \geq 0.75$), and much of the initial angular momentum has to be stored in a residual disk. Accretion from that disk could raise a_{\bullet} even more (Gammie et al., 2004; Shapiro and Shibata, 2002), resulting in black holes with spins close to the maximum of $a_{\bullet} = 1$.

However, as discussed above in the context of seed black holes, most of the black holes in galactic nuclei have masses well above likely seed masses. Doubling the mass of a black hole is enough to change a_{\bullet} by of order unity, so the values of a_{\bullet} probably depend more on the growth history than on the original spins of the seeds (Berti and Volonteri, 2008; Gammie et al., 2004; Hughes and Blandford, 2003; King et al., 2008; Volonteri et al., 2005).

However, as discussed above in the context of seed black holes, most of the black holes in galactic nuclei have masses well above likely seed masses. Black hole spins will be therefore determined by the same of combination of accretion and mergers that shaped the mass growth, rather than than by the original spins of the seeds (Berti and Volonteri, 2008; Gammie et al., 2004; Hughes and Blandford, 2003; King et al., 2008; Volonteri et al., 2005), as described below and summarised in Table 2.1.

Gas accretion can either increase or decrease black hole spins, depending on the duration of accretion episodes and on the properties of accretion disks. Regarding the duration of accretion, one possible evolutionary path involves continuous disk accretion of interstellar gas onto the black hole. Doubling the mass of a black hole by this process is enough to change the spin magnitude by of order unity. Accretion can instead occur via random accretion of small packets of less dense material, such as material from tidally disrupted individual stars or molecular gas clouds (Volonteri et al., 2007). In particular, tidal disruptions can be significantly enhanced in a MBH binary during the inspiral of the secondary MBH (Chen et al., 2009). Regarding the physics of accretion disc and transfer of angular momentum, accreting unmagnetised gas in a thin disk with a steady direction of angular momentum drives a black hole to $a = 0.998$ after the accretion has increased its mass by a factor of 2.5 (Thorne, 1974). Magnetised accretion disks are less effective at spinning up black holes, since they also lose angular momentum electromagnetically through disk winds, torques in the region where the gas begins to plunge into the black hole, and through magnetically-mediated extraction directly from the black hole. Simulations suggest that these effects may limit the final spins to $a = 0.9$, in contrast to the $a = 0.998$ of an unmagnetised thin disk (Hawley and Krolik, 2006; Krolik et al., 2005).

Black hole mergers also can contribute in various ways to spin evolution. Merging binary black holes of comparable masses have orbital angular momentum much larger than the maximum allowed for the merged black hole. Recent numerical relativity simulations of the merger of equal mass, non-spinning black holes show that enough angular momentum is radiated through gravitational waves to avoid a naked singularity, and the final steady-state merged black hole has $a = 0.7$ (Pretorius, 2005). Simulations of the mergers of equal-mass rapidly rotating Kerr holes suggest it is unlikely to create a maximally rotating hole in this way; a maximum final value of $a = 0.89$ was produced from two holes with individual spin parameters $S/M^2 = 0.757$ aligned with the orbit (Campanelli et al., 2006c), a statistical approach results in a strongly peaked spin distribution with an average spin of $S/M^2 = 0.73$ (Lousto et al., 2010). By contrast, growing a black hole by accreting small companions (*e.g.* stars or stellar-mass black holes of mass M_c) which fall in on isotropically distributed orbits causes a secular decrease of a . If $M \gg M_c$, the angular momentum is essentially determined by a random walk, and $a_{\bullet} \sim \sqrt{M_c/M} \sim 10^{-3}$. This mechanism of black hole growth is most plausible for lower luminosity AGN and black holes of smaller than $10^7 M_{\odot}$ (Milosavljević et al., 2006), as there is no compelling evidence for the existence of star clusters massive enough to grow $10^8 M_{\odot}$ – $10^9 M_{\odot}$ black holes (Rauch, 1999).

Although massive black holes could form by any combination of these processes, numerical astrophysics

Table 2.1.: *Black hole spin characteristics for different growth scenarios, and representative efficiencies in converting accreted mass into radiation. Here efficiencies are calculated assuming no torque inside the innermost circular orbit, and corrected for the radiation emitted by the disk and swallowed by the hole (Thorne, 1974).*

| black hole spin a_* | thin disk radiation efficiency (corrected for capture by hole) $\epsilon = L_{\text{disk}}/(\dot{M}c^2)$ | growth scenarios |
|--------------------------|--|--|
| 0 | 0.057 | result of isotropic accretion of small bodies |
| 0.7 | 0.133 | result of collapse or equal mass merger |
| 0.9 | 0.151 | approx equilibrium spin in magnetised disk accretion |
| 0.998 | 0.308 | equilibrium spin in unmagnetised disk accretion |
| 1 | 0.4 | maximal rotation before naked singularity appears |

and relativity have shown that these different mechanisms can produce very different distributions of black hole spins, skewing the distribution to high or low spins or spreading it evenly over a wide range of spins.

Thus, the distribution of spins will be strongly diagnostic of the mechanism of black hole growth, and the spins themselves are vital to many models of electromagnetic phenomena: jet formation, jet twists, accretion efficiency, tidal disruption events. LISA observations of MBH mergers will reveal the spin parameters a_* of the merging black holes (BHs) to within 1 % (Arun et al., 2009; Klein et al., 2009; Lang and Hughes, 2006). EMRI detections (see section 2.3.4) should typically reveal the MBH spin a_* to within 0.01 % (Arun et al., 2009; Babak et al., 2010; Barack and Cutler, 2004).

2.3.4. Stellar captures and the dynamics of galactic nuclei

Formation of extreme mass-ratio inspirals (EMRIs)

Some of the most exciting astrophysics with LISA will come from observing the gravitational waves produced by inspirals of stellar-mass compact objects into massive black holes (for an excellent review of the topic see Amaro-Seoane et al., 2007). There is compelling indirect evidence that these inspirals are common throughout the Universe and occur about once per million years in galaxies like the Milky Way (Freitag, 2003; Hopman and Alexander, 2006b). Because the mass ratio for these binaries is typically around 10^5 , these sources are commonly referred to as extreme mass ratio inspirals, or EMRIs.

White dwarfs, neutron stars, and stellar-mass black holes all share the property that they reach the last stable orbit around the MBH before they are tidally disrupted; hence all three types of compact stars can in principle lead to observable EMRI signals. However, BHs, being more massive, are expected to dominate the observed rate for LISA, for two reasons: mass segregation tends to concentrate the heavier compact stars nearer the MBH, and BH inspirals have higher signal-to-noise, and so can be seen within a much larger volume.

Three different mechanisms for the production of EMRIs have been explored in the literature. The oldest and best-understood mechanism is the diffusion of stars in angular-momentum space, due to two-body scattering. Compact stars in the inner 0.01 pc will sometimes diffuse onto very high eccentricity orbits, such that gravitational radiation will then shrink the orbit's semi-major axis and eventually drive the compact star into the MBH.

Important physical effects setting the overall rate for this mechanism are mass segregation, which concentrates the more massive stellar BHs ($M \approx 10 M_\odot$) close to the MBH, and resonant relaxation, which increases the rate of diffusion (Hopman and Alexander, 2006a): the stars in the inner cusp are on nearly periodic orbits around the MBH, so the same two stars will interact with each other repeatedly.

Most LISA detections of EMRIs will come from BH with a mass of approximately $10 M_\odot$ spiralling into MBHs with masses in the range of $10^6 M_\odot - 3 \times 10^6 M_\odot$. The space density of MBHs in this mass range is around $1.7 \times 10^{-3} \text{ Mpc}^{-3}$, and LISA can detect such sources out to $z \sim 1$, corresponding to a co-moving volume of about 200 Gpc^3 . The two-body scattering mechanism discussed above leads to an average rate of observable inspirals in Milky Way-type galaxies of $2.5 \times 10^{-7} \text{ yr}^{-1}$ (Hopman and Alexander, 2006b), which then implies a LISA detection rate of about 85/yr (Gair et al., 2004). Correcting that estimate for “edge effects” (inspirals ending in the first few months of observation do not accumulate enough SNR for detection) and geometry effects

Table 2.2.: This table shows the SNR at a distance of 1 Gpc for systems with a variety of observed masses M and m . Also shown is the maximum redshift at which such a source could be detected, z_{\max} , and the intrinsic masses of the system, $M_i = M/(1 + z_{\max})$ and $m_i = m/(1 + z_{\max})$, that a source at redshift z_{\max} would need to have in order to have apparent red-shifted masses M and m . The SNR were computed assuming the optimal TDI combination of LISA data streams could be constructed for five years of observation. All sources have MBH spin of $S/M^2 = 0.8$, inclination of 45° and eccentricity at plunge of 0.25. The waveforms were computed using a numerical kludge model (Babak et al., 2007; Gair and Glampedakis, 2006) and the LISA response was included using the Synthetic LISA simulator (Vallisneri, 2005). These results were used for computing event rate estimates using the semi-coherent search (Gair et al., 2004). Adapted from Amaro-Seoane et al. (2007).

| M/M_\odot | m/M_\odot | SNR at 1 Gpc | z_{\max} | $M_i/M_\odot(z_{\max})$ | $m_i/M_\odot(z_{\max})$ |
|-------------------|-------------|--------------|------------|-------------------------|-------------------------|
| 3.0×10^5 | 0.6 | 18 | 0.13 | 2.7×10^5 | 0.53 |
| | 10 | 73 | 0.44 | 2.1×10^5 | 6.9 |
| | 100 | 620 | 2.5 | 8.5×10^4 | 29 |
| 1.0×10^6 | 0.6 | 30 | 0.21 | 8.3×10^5 | 0.50 |
| | 10 | 210 | 1.0 | 4.9×10^5 | 4.9 |
| | 100 | 920 | 3.5 | 2.2×10^5 | 22 |
| 3.0×10^6 | 0.6 | 25 | 0.17 | 2.6×10^6 | 0.51 |
| | 10 | 270 | 1.3 | 1.3×10^6 | 4.4 |
| | 100 | 1500 | 5.2 | 4.8×10^5 | 16 |

(EMRIs with unfavourable orientations will not be observable to $z = 1$) leads to a conservative average rate of 50/yr. The uncertainty in this rate is perhaps a factor of 20, as current observational constraints on stellar populations in galactic nuclei are not very strong.

In addition to the two-body scattering mechanism, other proposed channels for EMRIs are tidal disruption of binaries that pass close to the MBH (Chen et al., 2009; Miller et al., 2005) and creation of massive stars (and their rapid evolution into black holes) in the accretion disks surrounding MBHs (Levin, 2007). Either of these channels could lead to a rate of the same order of magnitude as given above for two-body scattering, and this multiplicity of channels gives added confidence that at least one of them will produce a significant detection rate for LISA. Given a reasonable sample of detections, it is possible to infer the relative contributions from the different EMRI channels listed above. Two-body scattering leads to EMRIs that are moderately eccentric and have arbitrary inclination with respect to the MBH spin. In contrast, tidal disruptions of binaries lead to EMRIs that also have arbitrary inclination, but whose eccentricities are very close to zero, as tidal disruption results in orbits with (initially) much larger pericentre than for two body scattering, giving more time for radiation reaction to circularise the orbit before it becomes visible to LISA. Disk formation of EMRIs leads to sources with zero eccentricity and zero inclination (*i.e.*, orbital angular momentum parallel to the MBH's spin angular momentum). The orbital inclination and eccentricity can both be measured with very high accuracy from the LISA data (Barack and Cutler, 2004).

Observations of the Galactic centre

Extensive near-infrared and X-ray observations of the inner parsec of the Galactic centre reveal a remarkably detailed and surprising picture. Components include a $4 \times 10^6 M_\odot$ black hole (Gillessen et al., 2009) embedded in an extended population of old, relaxed stars (Schödel et al., 2007), an isotropic cluster of seemingly normal young hot stars within a few 0.01 pc from the central MBH, very massive young stars orbiting coherently in a disk (Bartko et al., 2009; Levin and Beloborodov, 2003), possibly formed from a fragmenting accretion disk, and a few X-ray point sources (Muno et al., 2005).

The origin, evolution, and physical processes governing this system remain mysterious; *e.g.*, the spin of the central MBH is completely unknown, and the population of dark compact objects around the central MBH is also unknown. Theory predicts that the central parsec harbours on the order of 10^4 stellar black holes that sank there over the Galaxy's lifetime (Alexander and Hopman, 2009; Freitag et al., 2006; Hopman and Alexander, 2006b; Morris, 1993) together with the stellar BHs that are believed to be produced locally by the unusual mode

of massive star formation in a disk. This hypothesised cluster of black holes dominates the dynamics of the inner 0.01 pc of the galaxy, and interacts with gas and stars there. For example, it likely drives rapid resonant relaxation (Rauch and Ingalls, 1998). The existence of such a cluster cannot yet be dynamically confirmed (Ghez et al., 2008b; Mouawad et al., 2005); in general, very little is known empirically about the birth and mass functions of stellar BHs. Given their important role for the dynamics of regions close to the central MBHs, this represents a significant gap in our understanding of galactic nuclei. Conversely, the Galactic centre, which harbours a fraction up to 10^{-3} of all Galactic stellar BHs in only approximately 10^{-10} of the Galactic volume, provides a unique opportunity to study the properties of stellar BHs. In addition, the Galactic centre may contain several intermediate-mass black holes (IMBHs) (Hansen and Milosavljević, 2003; Merritt et al., 2009; Portegies Zwart et al., 2006).

Probing galactic dynamics

The puzzles posed by the centre of our Galaxy and others couple long-standing key questions in stellar dynamics, gas dynamics, star formation and stellar evolution. At the same time, these systems offer exciting prospects for significant progress because of the wealth of data available on complex structures strongly constrained by the extreme environment. In particular, the presence of so many stellar BHs in the vicinities of MBHs in galactic centres makes it possible to uniquely combine the powers of high-precision electromagnetic observations with those of low-frequency gravitational radiation from EMRIs, which will place constraints on the stellar contents and dynamics.

As discussed previously, the net average detection rate for LISA is expected to be about 50/yr (Gair, 2009) with a large uncertainty. Establishing the EMRI rate provides detailed information on conditions in galactic nuclei that is probably not accessible through electromagnetic observation.

The eccentricities and inclinations of EMRIs that can be detected in the gravitational wave band $f > 10^{-4}$ Hz will be signatures of their origin through processes such as two-body scattering (for a recent review see Gair, 2009), tidal separation of binaries (Miller et al., 2005, ; see Figure 2), or settling of stellar-mass black holes via repeated interaction with an accretion disk (Levin, 2007; Miralda-Escudé and Kollmeier, 2005). The effects of tidal separation may already have been seen, as this process is the leading candidate to explain the so-called hypervelocity stars observed escaping from our Galaxy (e.g. Brown et al., 2009). Combining gravitational wave and electromagnetic observations is key to understanding and interpreting stellar populations there.

The discovery of EMRIs will provide unique information about the mass spectrum of stellar-mass black holes in galactic nuclei, in particular their upper mass limit. This is key for understanding the formation of stellar BHs and their relation to their progenitors. The detection of EMRIs will also give the distribution of the spin parameter a_{\bullet} of the MBH with extremely high accuracy ($\Delta a_{\bullet} \sim 10^{-4}$ Barack and Cutler, 2004; Shapiro Key and Cornish, 2010a) as demonstrated in the Mock LISA Data Challenge (MLDC) 3 (Babak et al., 2010). LISA will provide a databank of hundreds or more black hole spins in the low-redshift ($z < 1$) Universe, thus helping to disentangle the formation history of MBHs (Gammie et al., 2004; Hughes and Blandford, 2003; Volonteri et al., 2005).

EMRIs involving low-mass white dwarfs spiralling into SMBH with $M < 10^5 M_{\odot}$ may yield a strong and extended electromagnetic outburst due to the tidal destruction of the white dwarf and subsequent accretion of gas (Sesana et al., 2008).

The detection of the inspiral of an IMBH into a super-massive black hole (SMBH) will give direct evidence for the existence of IMBHs (Miller, 2005) and identify a major dynamical component in galactic centres.

2.4. Confronting General Relativity with Precision Measurements of Strong Gravity

LISA science objectives and investigations relevant to this section

4. Confront General Relativity with observations
 - 4.1 Detect gravitational waves directly and measure their properties precisely
 - 4.2 Test whether the central massive objects in galactic nuclei are the black holes of general relativity
 - 4.3 Make precision tests of dynamical strong-field gravity

Cosmic Vision scientific questions addressed by this section

- 3.3 Matter under extreme conditions

Probe gravity theory in the very strong field environment of black holes and other compact objects, and the state of matter at supra-nuclear energies in neutron stars

The LISA Science Objectives are given in appendix B, the Cosmic Vision scientific questions in appendix A.

2.4.1. Setting the stage

The **General Theory of Relativity (GR)** is a theory of gravity in which gravitational fields are manifested as curvature of spacetime. **GR** has no adjustable parameters other than Newton's gravitational constant and makes solid, specific predictions. While any test can therefore potentially be fatal to its viability, any failure of **GR** can point the way to new physics. Confronting **GR** with experimental measurements, particularly in strong gravitational fields, is therefore an essential enterprise. And despite its great successes, we know that **GR** cannot be the final word on gravity, since it is a classical theory and so must break down at the Planck scale. As yet there is no complete, quantum theory of gravity, and gravitation is not yet unified with the other fundamental fields.

While so far **GR** has passed all the tests to which it has been subjected (Will, 2006), most of these tests have been in the weak-field regime, in which the parameter $\epsilon = v^2/c^2 \sim GM/(Rc^2)$ is much smaller than one. Here v is the typical velocity of orbiting bodies, M their mass, and R their typical separation. For the tests of **GR** that have been carried out in our Solar System, second-order corrections are of order $\epsilon \sim 10^{-8}$, and so to date it has been sufficient to use first-order post-Newtonian (PN) equations. Solar System tests have been completely consistent with **GR** to this order of approximation.

Binary pulsars, which are essentially very stable and accurate clocks with typical orbital velocities $v/c \sim 10^{-3}$, or $\epsilon \sim 10^{-6}$, are excellent laboratories for precision tests of **GR** (Lorimer, 2008). Current observations of several binary pulsars are perfectly consistent with **GR** predictions, as calculated through first PN order. Observations of the first binary pulsar to be discovered, PSR 1913+16, also provided the first astrophysical evidence for gravitational radiation. Loss of energy due to gravitational-wave emission (radiation reaction) causes the binary's orbit to shrink slowly; its period derivative \dot{P} agrees with **GR** predictions to within 0.2%, which is within the error bars (Weisberg and Taylor, 2005). The double pulsar system, PSR J0737-3039 A and B, provides additional tests of **GR** that were not available previously (Kramer et al., 2006). In that system, the orbital period derivative is consistent with **GR** at the 0.3% level, and the Shapiro delay agrees to within 0.05% with the predictions of **GR** (Kramer and Wex, 2009).

However, the orbital gravitational fields in known binary pulsars are not much stronger than those in the Solar System: the semimajor axis of the orbit of PSR 1913+16 is about $1.4 R_{\odot}$. These weak orbital fields limit the ability of binary pulsars to probe nonlinear **GR dynamics**. They do provide important tests of strong-field *static* gravity, as the redshift at the surface of a neutron star is of order 0.2.

LISA observations of coalescing **massive black hole** binaries, or of stellar-mass compact objects spiralling into **MBHs**, will allow us to confront **GR** with precision measurements of physical regimes and phenomena that are not accessible through Solar System or binary pulsar measurements. The merger of comparable-mass **MBH** binaries produces an enormously powerful burst of gravitational radiation, which LISA will be able to measure

with amplitude signal-to-noise as high as several thousand, even at cosmological distances. In the months prior to merger, LISA will detect the gravitational waveform due to the binary’s inspiral; from that inspiral waveform, the masses and spins of the two **MBHs** can be determined to high accuracy. Given these physical parameters, numerical relativity will be able to predict the exact shape of the burst waveform, and this can be compared directly with the observed burst – providing an ideal test of pure **GR** in the highly dynamical, strong-field regime.

Stellar-mass compact objects spiralling into **MBHs** will provide a qualitatively different sort of test, but an equally exquisite one. The compact object travels on a near-geodesic of the spacetime of the **MBH**, and as it spirals in, it effectively maps out the spacetime surrounding the **MBH**. For these **EMRIs**, LISA will typically observe of order 10^5 cycles of inspiral waveform, all of which are emitted as the compact object spirals from 10 horizon radii down to a few horizon radii. Encoded in these waves is an extremely high precision map of the spacetime metric, just outside a rapidly rotating **MBH**. Better opportunities than these for confronting **GR** with actual strong-field observations could hardly be hoped for. One caveat, however, is that LISA observations of **BH-BH** binaries cannot discriminate between **GR** and scalar-tensor theories of gravity. The reason is that black holes do not support scalar fields; *i.e.*, they have no scalar “hair”. Even after LISA flies, the best limits on scalar-tensor theories will come from Solar System and binary pulsar measurements (Esposito-Farèse, 2004).

The strong-field regime of **GR** will quite likely be observed by ground-based gravitational wave detectors several years before LISA flies (*e.g.*, the Advanced **LIGO/VIRGO** detectors should come online around 2015 and **LIGO** and **VIRGO** are expected at that point to observe stellar mass **BH** mergers where the components are of roughly comparable mass). However, even the brightest **BH** mergers that **LIGO** and **VIRGO** will likely observe will still have an amplitude **SNR** about 100 times smaller than the brightest **MBH** mergers that LISA will observe. The precision with which LISA can measure the merger and ringdown waveforms will correspondingly be 100 times better than for ground-based detectors. The situation is similar for **EMRIs**: while ground-based detectors may detect binaries with mass ratios of about 10^{-2} (*e.g.*, a neutron star spiralling into a $100 M_{\odot}$ **BH**), in observations lasting approximately 10^2 to 10^3 cycles, the precision with which the spacetime can be mapped in such cases is at least two orders of magnitude worse than what is achievable with LISA’s **EMRI** sources. Thus LISA will test our understanding of gravity in the most extreme conditions of strong and dynamical fields, and with a precision that is two orders of magnitude better than attainable from the ground.

GR has been extraordinarily fruitful in correctly predicting new physical effects, including gravitational lensing, the gravitational redshift, black holes and gravitational waves. **GR** also provided the overall framework for modern cosmology, including the expansion of the Universe. However, our current understanding of the nonlinear, strong gravity regime of **GR** is quite limited. Exploring gravitational fields in the dynamical, strong-field regime could reveal new objects that are unexpected, but perfectly consistent with **GR**, or even show violations of **GR**.

2.4.2. Testing strong-field gravity: The inspiral, merger, and ringdown of **MBH** binaries

LISA’s strongest sources are expected to be coalescing **MBH** binaries where the components have roughly comparable masses, $0.1 < m_2/m_1 < 1$. The coalescence waveforms will be visible by eye in the data stream, standing up well above the noise, as illustrated in figure 2.7.

The coalescence can be described in three stages: inspiral, merger, and ringdown (Flanagan and Hughes, 1998b) all of which will typically be observable by LISA. The inspiral stage is a relatively slow, adiabatic process in which the **BHs** spiral together on quasi circular orbits. The **BHs** have separations wide enough so that they can be treated as point particles within the **PN** approximation; consequently, in this stage they can be computed analytically, with high-order **PN** expansions. The inspiral is followed by the dynamical merger, in which the **BHs** leave their quasi-circular orbits and plunge together, forming a highly distorted merged **BH**. Here, the **BH** velocities approach $v/c \sim 1/3$, the **PN** approximation breaks down, and the system can only be analysed using numerical relativity simulations of the full Einstein equations. The distorted remnant **BH** settles into a stationary Kerr **BH** as it “rings down” by emitting gravitational radiation.

While numerical relativity is required to tell us the initial state of the distorted **BH**, the evolution of that distortion – its “ringing down” – can be modelled in terms of **BH** perturbation theory. At the end of the ringdown the final black hole is left in a quiescent state, with no residual structure besides its Kerr geometry. Its spacetime metric is then determined fully by its mass and spin, as required by the **BH** “no-hair” theorem.

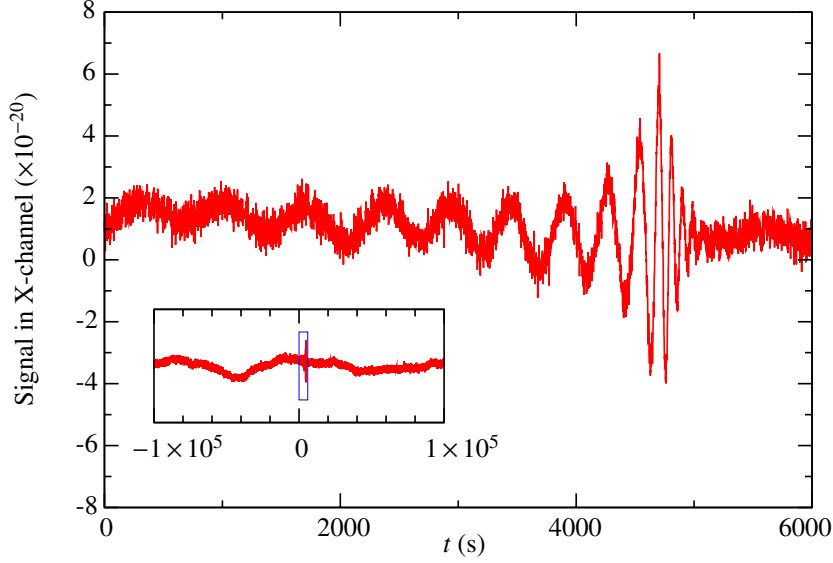


Figure 2.7.: Gravitational wave signal for the final few orbits, plunge, merger and ringdown of an MBH-MBH binary.

For equal-mass MBH binaries with total mass in the range $3 \times 10^5 M_\odot < M(1+z) < 3 \times 10^7 M_\odot$ where z is the cosmological redshift, the three stages have comparable SNR; *i.e.*, within an order of magnitude of each other (see Figure 6 of Flanagan and Hughes, 1998a). From a typical LISA observation of the inspiral part of the signal, it will be possible to determine the physical parameters of the binary to extremely high accuracy. Using these parameters, numerical relativity is able to predict precisely the merger and ringdown waves. The merger and ringdown waveforms will typically have an SNR of 10^2 to 10^3 , so an extremely clean comparison will be possible between the observed waveforms and the predictions of GR.

The inspiral stage: inferring the binary's masses and spins

With orbital velocities v/c typically in the range 0.05 to 0.5, most of the inspiral stage can be well described using high-order PN equations. The inspiral waveform is a chirp: a sinusoid that increases in frequency and amplitude as the BHs spiral together. The part of the inspiral stage that is observable to LISA lasts months to years. More precisely, when the gravitational-wave frequency sweeps past 10^{-4} Hz, the time remaining until merger is approximately

$$t = 1.7 \times 10^8 \text{ s} \left(\frac{0.25}{\eta} \right) \left(\frac{M(1+z)}{2 \times 10^5 M_\odot} \right)^{-5/3} \quad (2.5)$$

where, as above, $M = m_1 + m_2$ is the total mass of the binary and $\eta = m_1 m_2 / M^2$ is the symmetric mass ratio. LISA will observe the last 10^4 to 10^5 gravitational wave (GW) cycles from the inspiral. Since the inspiral signal is quite well understood theoretically, matched filtering can be used to discriminate these inspiral waveforms from the measurement noise, starting more than a year before the final merger, when the total SNR is still small. And because the inspiral waveforms are strong, long lived, and well understood, it is possible from the inspiral alone to determine the system parameters to high accuracy. Both masses can be determined to within a fractional error of about 10^{-3} , and their spins can be measured to within 0.1 % to 1 % (Lang and Hughes, 2006).

The merger stage: spectacular bursts

The inspiral is followed by a dynamical merger that produces a burst of gravitational waves. This is a brief event, comprising a few cycles lasting about $10^3 \text{ s} (M/(10^6 M_\odot))$, yet very energetic: during merger the gravitational wave luminosity is $L_{\text{GW}} \sim 10^{23} L_\odot$, emitting more power than all the stars in the observable Universe. The final merger of MBH-MBH binaries occurs in the very strong-field, highly nonlinear and highly dynamical regime of GR, and is the strongest gravitational wave source that LISA is expected to see. LISA will be able to see the

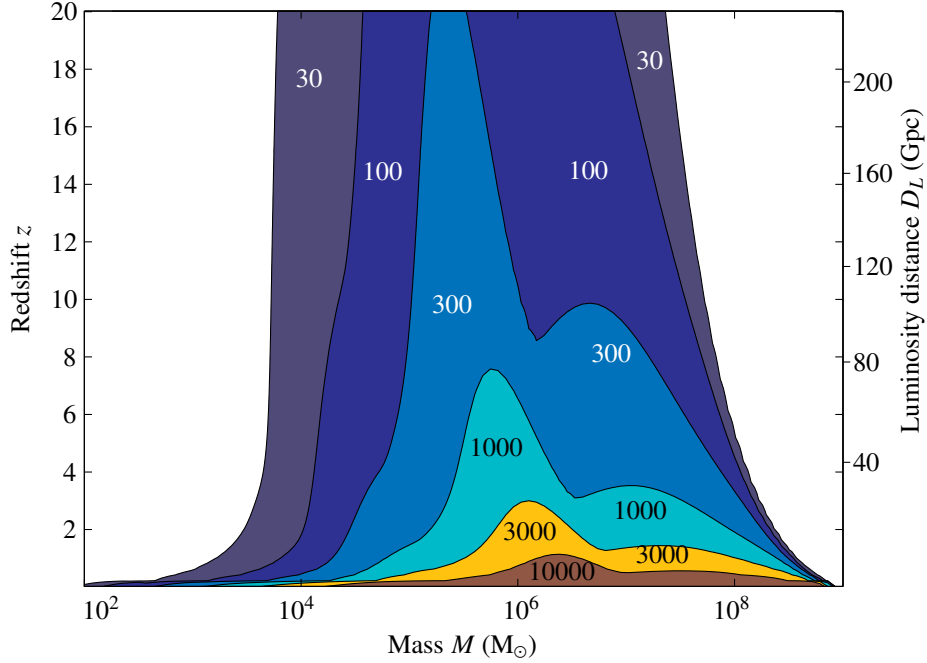


Figure 2.8.: Plot of total signal-to-noise (in one synthetic Michelson) for all three stages of merger, for equal-mass binaries, as a function their total mass and redshift (Baker et al., 2006).

merger of two $10^4 M_{\odot}$ BHs out to redshift $z = 20$, and for mergers of $10^6 M_{\odot}$ BH at $z = 1$ the SNR will be in the thousands (figure 2.8). As mentioned above, LISA observations of the inspiral yield the masses and spins of the MBH components to $\sim 0.1\%$. With these in hand, numerical relativity will make a very specific prediction for the merger and ringdown radiation from the system. Comparison with the waveform that LISA actually observes will allow us to confront the predictions of GR with an ultra-high precision measurement in the fully nonlinear and dynamical regime of strong gravity.

The ringdown stage: black hole spectroscopy

Although numerical relativity waveforms from colliding holes naturally include the ringdown waves, these waves are also well understood analytically. GR predicts, as a consequence of the “no-hair” theorem, that every excited BH emits gravitational waves until it reaches a state characterised entirely by its mass and spin. These ringdown waves consist of a set of superposed BH quasi-normal modes (QNMs), waves with exponentially damped sinusoidal time dependence, plus a far weaker “tail” that decreases as $1/t^6$. The modes are strongly damped as the mode energy is radiated away to infinity, so the final ringdown stage will be brief, lasting a few cycles.

The quasi-normal mode (QNM) of Kerr BHs can be solved by using perturbation theory: the spacetime metric is written as the Kerr metric plus a small perturbation, and Einstein’s equations are expanded to first-order in that perturbation. The solutions can be decomposed into a sum of eigenmodes with complex eigenfrequencies. It was discovered in the 1970s (Chandrasekhar and Detweiler, 1975) that the partial differential equations for the eigenmodes and frequencies of Kerr BHs can be fully separated, so these are known to essentially arbitrary accuracy. While there are a countable infinity of modes (corresponding to the angular order and overtone number of the perturbation from the stationary state), the lowest-order modes are the most readily excited and the most weakly damped; in practise only a few modes are likely to be observed. The frequencies and damping times of these ringdown QNMs are completely determined by the mass and spin angular momentum of the final, merged MBH.

If we can detect at least two different QNMs in a ringdown, the ringdown radiation itself provides a test of strong-field GR and of the hypothesis that the central massive objects in galactic nuclei are really Kerr BHs. The reason is that from two modes one measures four parameters (the frequencies and damping times of both

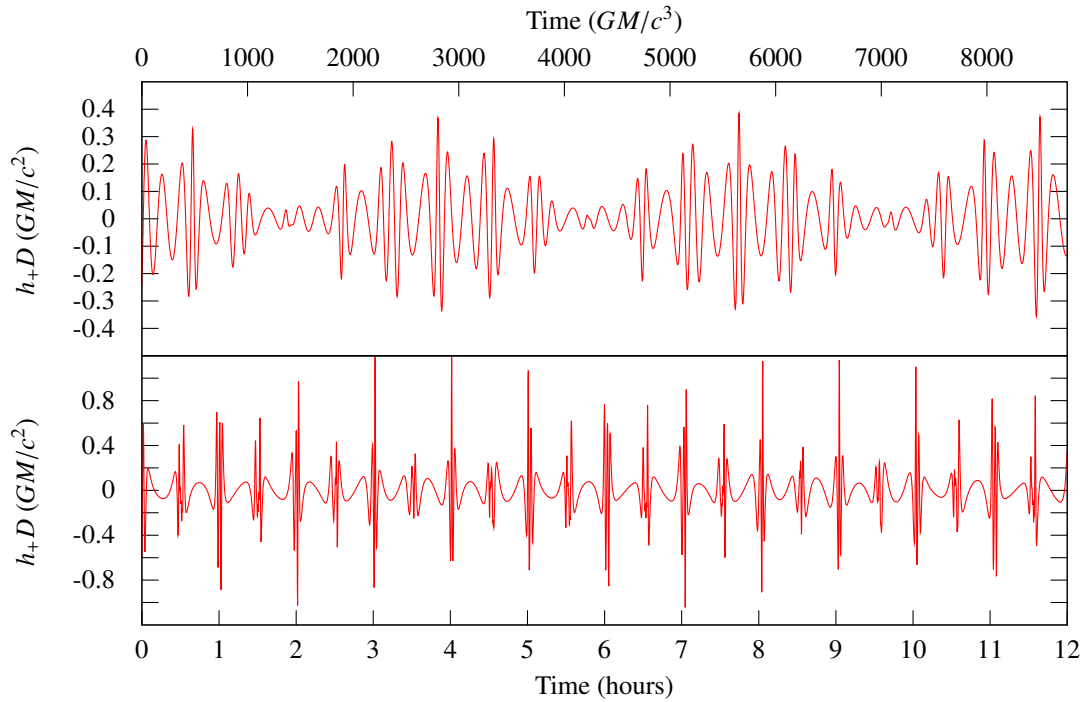


Figure 2.9.: Segments of generic EMRI waveforms (Drasco and Hughes, 2006). These are the plus-polarised waves produced by a test mass orbiting a $10^6 M_{\odot}$ black hole that is spinning at 90% of the maximal rate allowed by general relativity, a distance D from the observer. Top panel: Slightly eccentric and inclined retrograde orbit modestly far from the horizon. Bottom panel: Highly eccentric and inclined prograde orbit much closer to the horizon. The amplitude modulation visible in the top panel is mostly due to Lense-Thirring precession of the orbital plane. The bottom panel's more eccentric orbit produces sharp spikes at each pericentre passage.

modes), which must all be consistent with the *same* mass and spin values (Dreyer et al., 2004). Thus, in the same way that we can identify chemical elements through their spectroscopic fingerprint, so can we uniquely identify a BH (*i.e.*, determine its mass and spin) from the spectrum of its ringdown radiation. On the other hand, if the observed radiation arises from a different source (*e.g.*, a boson star), or if GR does not correctly describe gravity in the extremes of strong fields and dynamical spacetimes, the spectrum would very likely be inconsistent with that predicted by GR for black holes.

Eccentric Massive Black Hole Binaries

It has long been thought that massive black hole binaries will have negligible eccentricity on entering the LISA band due to the circularizing effect of gravitational wave emission. However, recent astrophysical studies have shown that interactions with the surrounding gas or stars can produce and sustain significant orbital eccentricity, and drive the merger close to the LISA band before gravitational wave emission takes over. These systems can enter the LISA band with a measurable eccentricity (Amaro-Seoane et al., 2010; Sesana, 2010). Recent studies have shown that LISA should be able to measure this initial eccentricity to parts in a thousand or better for non-spinning intermediate-mass black hole binaries (BHBs) (Amaro-Seoane et al., 2010) and massive BHBs (Porter and Sesana, 2010) as well as spinning massive BHBs (Shapiro Key and Cornish, 2010b). LISA observations of these systems will provide additional insight into black hole merger models, and provide richly layered signals with which to carry out unique tests of GR.

2.4.3. Extreme mass ratio inspirals: precision probes of Kerr spacetime

EMRIs are expected to be very clean astrophysical systems, except perhaps in the few percent of galaxies containing accreting active galactic nuclei, where interactions with the accretion disk could possibly affect the

EMRI dynamics. Over timescales of order a day, the orbits of the smaller body are essentially geodesics in the spacetime of the **MBH**. On longer timescales, the loss of energy and angular momentum due to gravitational-wave emission causes the smaller body to spiral in; *i.e.*, the geodesic’s “constants” of integration change slowly over time. For LISA’s entire observation time (of years), the orbits are highly relativistic (radius smaller than 10 Schwarzschild radii) and display extreme forms of periastron precession and precession of the orbital plane due to the dragging of inertial frames by the **MBH**’s spin. Figure 2.9 shows two sample waveforms, corresponding to short stretches of time.

For the very large number of **EMRIs**, **GW** cycles that accumulate over a year of LISA observations (about 10^5), a fit of the observed gravitational waves to theoretically calculated templates will be very sensitive to small changes in the systems’ physical parameters. As mentioned above, this sensitivity makes the search computationally challenging, but it allows an extremely accurate determination of the source’s parameters, once an **EMRI** signal is identified. Assuming that **GR** is correct and the central massive object is a **BH**, LISA should be able to determine the mass and spin of the **MBH** to fractional accuracy of about 10^{-5} – 10^{-3} (Barack and Cutler, 2004).

This level of precision suggests that we can use **EMRIs** as a highly precise observational test of the “Kerr-ness” of the central massive object. That is, if we do *not* assume that the larger object is a **BH**, we can use gravitational waves from an **EMRI** to map the spacetime of that object. The spacetime outside a stationary axisymmetric object is fully determined by its mass moments M_l and current multipole moments S_l . Since these moments fully characterise the spacetime, the orbits of the smaller object and the gravitational waves it emits are therefore determined by the multipolar structure of the spacetime. By observing these gravitational waves with LISA we can characterise the spacetime of the central object. Extracting the moments from **EMRI** waves is analogous to geodesy, in which the distribution of the Earth’s mass is determined by studying the orbits of satellites. Black hole geodesy, also known as holiodesy, is very powerful because Kerr **BHs** have a very special multipolar structure. A Kerr **BH** with mass M and spin parameter a (in units with $G = c = 1$) has multipole moments given by

$$M_l + iS_l = (ia)^l M. \quad (2.6)$$

Thus, $M_0 = M$, $S_1 = aM$, and $M_2 = -a^2 M$, and similarly for all other multipole moments; they are all completely determined by the first two moments, the **BH** mass and spin. This is nothing more than the “no-hair” theorem for **BHs**: the properties of a **BH** are entirely determined by its mass and spin.

For inspiraling trajectories that are slightly eccentric and slightly non-equatorial, in principle all the multipole moments are redundantly encoded in the emitted gravitational waves (Ryan, 1995), through the time-evolution of the orbit’s three fundamental frequencies: the fundamental frequencies associated with the r , θ , and ϕ motions (Drasco and Hughes, 2004), or, equivalently, the radial frequency and the two precession frequencies.

The mass quadrupole moment M_2 of a Kerr **BH** can be measured to within $\Delta M_2 \approx 10^{-2}$ – $10^{-4} M^3$ (Barack and Cutler, 2004), along with $\Delta M/M$ and $\Delta S_1/M_2$ to 10^{-5} – 10^{-3} . Any inconsistency with the Kerr relation could signal a failure of **GR**, or the discovery of a new type of compact object, or a surprisingly strong perturbation from some other material or object. For a review of the different hypotheses regarding the nature of the central object see Sopuerta (2010).

Other tests of the Kerr-ness of the central massive object have also been proposed. **EMRI** waves can be used to distinguish definitively between a central **MBH** and a boson star (Kesden et al., 2005). In the **BH** case the **GW** signal “shuts off” shortly after the inspiraling body reaches the last stable orbit (and then plunges through the event horizon), while for a massive boson star, the signal gets prolonged, and its frequency derivative changes sign, as the body enters the boson star and spirals toward its centre.

The above tests take the standard model of the central object and either compare it with a different model (*e.g.*, a boson star) or embed that model in a larger one with extra free parameters (*e.g.*, Kerr, but with arbitrary quadrupole moment), and ask whether the best fit to the data is consistent with Kerr values for the extra parameters. These are all essentially comparison tests. There seems to be no unique or optimum way of constructing such tests – basically because today there is no compelling alternative to **GR** to compare against it. Nevertheless, tests of this sort would be very useful in either cementing confidence in the standard picture, or homing in on discrepancies.

2.4.4. The mass of the graviton

In GR, gravitational waves travel with the speed of light and the graviton is hence massless. Alternative theories with a massive graviton would predict an additional frequency-dependent phase shift of the observed waveform. The dominant effect is at 1 PN order, and would change the PN coefficient ψ_2 to

$$\psi_2 \rightarrow \psi_2 - \frac{128\eta}{3} \frac{\pi^2 DM}{\lambda_g^2(1+z)}, \quad (2.7)$$

where η is again the symmetric mass ratio. This term alters the time of arrival of waves of different frequencies, causing a dispersion, and a corresponding modulation in the wave's phase depending on the Compton wavelength λ_g and the distance D to the binary. Hence, by tracking the phase of the inspiral waves, LISA can put a bound on the graviton's mass to about $\lambda_g > 1.7 \times 10^{20}$ m (or about $m_g < 7.3 \times 10^{-27}$ eV; Will, 1998), as also confirmed by more recent and exhaustive calculations (Berti et al., 2005). This significantly improves on the current Solar System bound on the graviton mass, $m_g < 4 \times 10^{-22}$ eV ($\lambda_g > 3 \times 10^{15}$ m).

2.5. Ultra-Compact Binaries

LISA science objectives and investigations relevant to this section

3. Survey compact stellar-mass binaries and study the structure of the Galaxy
 - 3.1 Elucidate the formation and evolution of Galactic stellar-mass binaries; constrain the diffuse extragalactic foreground
 - 3.2 Determine the spatial distribution of stellar mass binaries in the Milky Way and environs
 - 3.3 Improve our understanding of white dwarfs, their masses, and their interactions in binaries, and enable combined gravitational and electromagnetic observations

The LISA Science Objectives are given in appendix B, the Cosmic Vision scientific questions in appendix A.

2.5.1. Summary

Compact binary stars are double stars in which two compact objects such as white dwarfs and neutron stars, orbit each other with short periods. Binaries with orbital periods below a few hours emit gravitational radiation in the LISA band and are generally referred to as ultra-compact binaries. They have relatively weak gravitational wave signals in comparison to massive black hole binaries, but are numerous in the Galaxy and even the Solar neighbourhood and thus, much closer than MBHs. The prospects for LISA in this area of astrophysics are truly spectacular. Several thousand systems are expected to be detected individually, with their parameters determined to high precision, while the combined signals of the millions of compact binaries in the LISA band will form a well detectable foreground signal. This is in contrast to less than 50 ultra-compact binaries known today. The number of detections will allow to study entire populations of binaries in great detail. This allows to determine not only the properties of this particular population but also to constrain the formation of these binaries and thus many preceding phases in binary evolution. This has a strong bearing on our understanding of many high-energy phenomena in the Universe such as supernova explosions, gamma-ray bursts and X-ray sources as they share parts of the evolution history of the binaries detectable by LISA.

As many of the Galactic sources are rather close (within a few kpc), they will be detectable at high SNR (often larger than 100), allowing detailed studies of individual binaries. For many, the frequency and phase evolution can be studied, enabling the study of the physics of tides and mass transfer in unprecedented detail. The extreme conditions of short orbital periods, strong gravitational fields and high mass-transfer rates are unique in astrophysics.

The LISA measurements will provide different information to what can be deduced from electromagnetic detections. In particular, LISA's capability to determine distances, as well as the fact that the gravitational wave signals are unaffected by interstellar dust provide significant advantages over other detection techniques. Compared to Gaia, LISA will observe a quite different population. Gravitational wave observations allow us to determine the distances to binaries that are right in the Galactic centre rather than to those close to the Sun. The distance determinations will make it possible to map the distribution of many compact binaries in the Galaxy, providing a new method to study Galactic structure. Electromagnetic observations and gravitational wave observations are complementary to one another; dedicated complementary observing programs as well as public data releases will allow simultaneous and follow-up electromagnetic observations of binaries identified by LISA.

A number of guaranteed detectable sources are known to date from electromagnetic observations. Some of these can be used to verify instrument performance by looking for a gravitational signal at twice the orbital period and comparing the signal with expectations. In addition, once LISA has detected several nearby binaries and determined their sky position they can be observed optically thus providing an additional quantitative check on instrument sensitivity.

2.5.2. LISA as a workhorse: thousands of new binaries

Ultra-compact binaries will completely dominate the number of source detections by LISA. Current estimates suggest the numbers of resolved compact binaries that will be detected by LISA to be in the thousands to ten-thousands (Webbink, 2010). The shortest period systems will be the most numerous, the majority having periods less than about 20 minutes. LISA will revolutionise our knowledge of such a population, especially given that ten of the known fifty sources have periods less than twenty minutes. As these systems are relatively short lived and faint, there is no hope to detect such systems in significant numbers by any other means than via gravitational radiation. Their detection will allow us to test different models for the common-envelope phase, a significant uncertainty in our understanding of binary evolution and many high-energy phenomena. The internal statistical accuracy delivered by the sheer number of detected sources will ensure that the common-envelope phase will be put to the most critical test expected in the midterm future of astrophysics.

The outcome of the common envelope phase

Only slightly more than half of the stars in the Universe are single, leaving the other half to be part of a binary, a triple or a higher-order system. On the order of half of the binaries formed with sufficiently small orbital separation, so that the stars will interact during the evolution of the components into giants or super giants. Especially for low-mass stars, the majority of interactions are unstable and will lead to runaway mass transfer. Based on the observed short orbital periods of binaries that have passed this stage it is argued that somehow the companion of the giant ends up inside the giant's outer layers. During that common envelope phase, friction reduces the velocity of the companion, leading to orbital shrinkage and transfer of angular momentum from the orbit into the envelope of the giant. Along with angular momentum, orbital energy is deposited in the envelope, whose matter is then unbound from the giant's core, leading to a very compact binary consisting of the core of the giant and the original companion (Paczynski, 1976).

Virtually all compact binaries and most of the systems giving rise to high-energy phenomena (such as X-ray binaries, relativistic binary pulsars and possibly gamma-ray bursts) have experienced at least one common-envelope phase. Given the importance of this phase in high-energy astrophysics, our understanding of the physics and our ability to predict the outcome of the common-envelope phase are poor. Theoretical progress to understand the phase from first physical principles (*e.g.* Taam and Sandquist, 2000) and the standard formalism described above has been challenged by observational tests.

Comparison of the parameters of the thousands of binaries detected by LISA with model predictions will provide a direct test of the different proposed outcomes of the common-envelope phase and our understanding of the preceding binary evolution in general.

Formation of ultra-compact binaries in globular clusters

Globular clusters have a strong overabundance of bright X-ray sources probably due to dynamical interactions. However, the details of how these interactions lead to the formation of ultra-compact X-ray binaries are poorly understood (Verbunt and Lewin, 2006). In particular it seems that the number of ultra-compact X-ray binaries is enhanced compared to the other Galactic populations. Moreover, it is not apparent whether ultra-compact binaries with white dwarf components are overproduced as well. The angular resolution that can be achieved with LISA is such that globular clusters can be resolved, so that the cluster sources can be distinguished from the Galactic disc sources. This enables LISA to determine the number of ultra-compact binaries in globular clusters and to provide information on the evolution of X-ray binaries in globular clusters.

The foreground of Galactic gravitational waves

At frequencies below a few mHz the number of sources in the Galaxy is so large (6×10^7 to 8×10^7 , see *e.g.* Ruiter et al., 2009) that only a small percentage, the brightest and closest sources, will be *individually* detected. The vast majority will form an unresolved *foreground* signal in the detector, which is quite different from the diffuse extragalactic *background*.

This foreground is often described as an additional noise component, which is misleading for two reasons. The first is that there is a lot of astrophysical information in the foreground. The overall level of the foreground is a measure of the total number of ultra-compact binaries, which gives valuable information given the current uncertainty levels in the normalisation of the population models. The spectral shape of the foreground also contains information about the homogeneity of the sample, as simple models of a steady state with one type of binary predict a very distinct shape. In addition, the geometrical distribution of the sources can be detected by LISA.

Due to the concentration of sources in the Galactic centre and the inhomogeneity of the LISA antenna pattern, the foreground is strongly modulated over the course of a year, with time periods in which the foreground is more than a factor two lower than during other periods (see figure 2.10 and Edlund et al., 2005). The characteristics of the modulation can be used to learn about the distribution of the sources in the Galaxy as the different Galactic components (thin disk, thick disk, halo) contribute differently to the modulation, and their respective amplitude can be used to, for example, set upper limits to the halo population (e.g. Ruiter et al., 2009). For a recent review of the galactic GW foreground, see Nelemans (2009).

The extragalactic ultra-compact binary background

The combined signal of the extragalactic sources, dominated by signals from sources at around redshift of $z = 1$, will provide insight in the cosmic star formation.

While the distance at which LISA can detect *individual* binaries is limited to less than 100 kpc, putting the Large Magellanic Cloud (LMC) and Small Magellanic Cloud (SMC) just within reach, the expected extragalactic background signal is around the limit of the sensitivity of LISA at a few mHz (Farmer and Phinney, 2003). As the predictions for the extragalactic background are greatly hindered by the uncertainties in the binary evolution, the determination of number and distribution of galactic binaries with LISA will help better to constrain these predictions. With that, the detected level of extragalactic background will provide information on the cosmic star formation.

2.5.3. Instrument verification

A subset of the known ultra-compact binaries have been recognised as instrument verification sources, as they should be detected in a few weeks to months and thus can be used to verify the performance of the instrument (Stroeer and Vecchio, 2006). The reliability of the verification binaries has been improved recently by measurements of distances and systems parameters, thus providing predictions of the expected signals with well defined error bars. Their expected monochromatic nature within the LISA mission time prevents astrophysical effects (see section 2.5.5) hampering their detection.

The most promising verification binaries are the shortest-period binaries, HM Cnc (RX J0806.3+1527), V407 Vul and ES Cet. For a decade it has remained unclear if their reported periods were actually orbital periods, but recent results from the Keck telescope on HM Cnc (Roelofs et al., 2010) show conclusively that this system has an orbital period of 5.4 minutes. As V407 Vul has almost identical properties, this implies that this also really is a binary with an orbital period of 9.5 minutes. In some interpretations, these times are the remarkably small orbital periods of binaries in which two white dwarfs are separated by about a quarter of the Earth-Moon distance. A good deal of debate attends the two systems, and several competing theories purport to explain them, ranging from a detached pair of magnetic white dwarfs in which their X-ray emission is produced by induction and an interacting pair of white dwarfs in the so-called direct impact phase (Roelofs et al., 2010), to models in which the observed periods are not orbital periods at all (see Nelemans, 2006). No model is a strong favourite, and LISA will permit understanding the two objects.

Outlook: developments expected in the next decade

Before LISA will fly, there are a number of surveys that will improve our knowledge of ultra-compact binaries in the next decade. One of the major contributions to the increase in the number of known AM CVn systems in the last years has been the Sloan digital sky survey (SDSS), in which twelve new systems have been found.

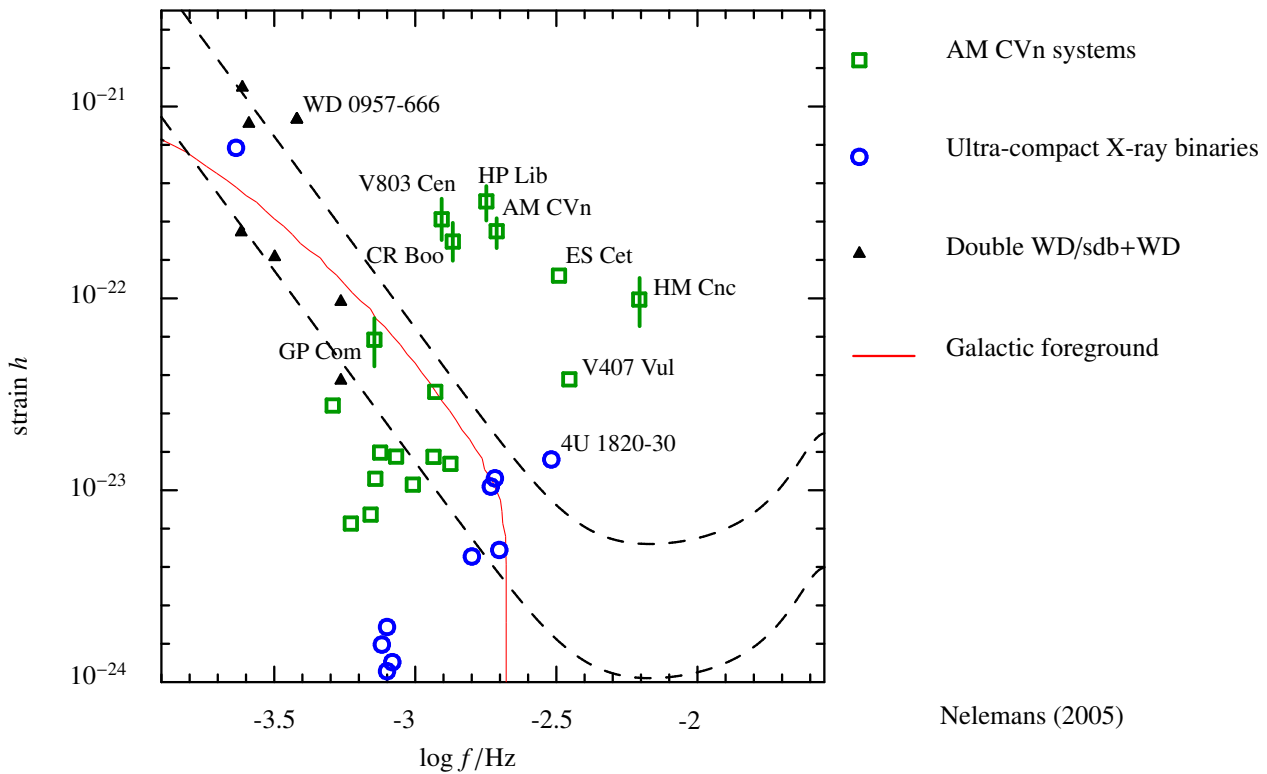


Figure 2.10.: Gravitational wave strain versus frequency for the verification binaries. The upper and lower dashed lines show the design sensitivities of LISA for a SNR of 5 and 1, respectively, in one year of data-collecting (Larson et al., 2000). The solid red line is a population synthesis prediction for the confusion-limited Galactic foreground (Nelemans et al., 2004). Based on Roelofs et al. (2006, 2010)

This number will certainly go up with the ongoing extension of the **Sloan digital sky survey** (SDSS) to lower Galactic latitudes (the SEGUE survey) and the European Galactic Plane Surveys (EGAPS), two surveys that are particularly well designed for finding compact binaries. General variability surveys such as Pan-Starrs, the **Palomar Transient Factory** (PTF) and the future **Large Synoptic Survey Telescope** (LSST) will also find new systems. However, all SDSS systems have relatively long orbital periods (longer than about 30 minutes). Two surveys capable of finding AM CVn stars with periods less than 30 minutes are underway or will start soon: the **Rapid Time Survey** (RATS) and the OmegaWhite survey.

In the future, there are initiatives to find more ultra-compact X-ray binaries both through the continued monitoring of the sky to search for X-ray transients with **Rossi X-Ray Timing Explorer** (RXTE) and other satellites, as well as through dedicated X-ray and optical surveys of the Galactic bulge that are currently in development. With these developments, the number of verification sources available for LISA will be several tens allowing detailed tests of the performance of the instrument.

2.5.4. Studying the astrophysics of compact binaries using LISA

Although the effect of gravitational radiation on the orbit will dominate the evolution of the binaries detected by LISA, additional physical processes will cause strong deviations from the simple point-mass approximation. The two most important interactions that occur are tides – when at least one of the stars in a binary system is not in corotation with the orbital motion or when the orbit is eccentric – and mass transfer. Because many binaries will be easily detected, these interactions do not hamper their discovery, but instead will allow tests of the physics underlying these deviations. By providing a completely complementary approach, gravitational wave measurements are optimal to the study of short period systems in contrast to the current bias towards bright electromagnetic systems and events.

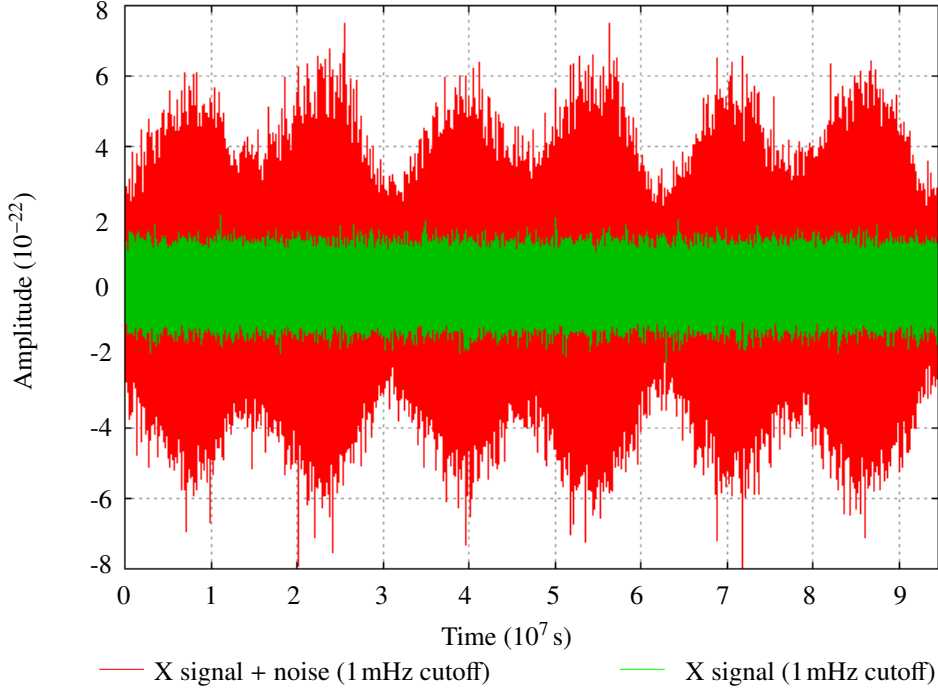


Figure 2.11.: *Level of the Galactic gravitational wave foreground as function of time, showing the yearly change. Adapted from Edlund et al. (2005).*

Physics of tidal interaction

LISA measurements of individual short-period binaries will give a wealth of information on the physics of tides and the stability of the mass transfer. For detached systems with little or no interaction, the frequency evolution is well understood. The strain amplitude h , the frequency f and its derivatives are connected by

$$h \propto \mathcal{M}^{5/3} f^{2/3} D^{-1} \quad \text{with} \quad \mathcal{M} = \frac{(m_1 m_2)^{3/5}}{(m_1 + m_2)^{1/5}} \quad (2.8)$$

$$\dot{f} \propto \mathcal{M}^{5/3} f^{11/3} \quad (2.9)$$

$$\ddot{f} = \frac{11}{3} \frac{\dot{f}}{f} \quad (2.10)$$

where \mathcal{M} is the chirp mass, m_1, m_2 the masses of the binary constituents and D the distance. Thus the measurement of h, f, \dot{f} provides chirp mass and distance; the additional measurement of \ddot{f} gives a direct test of the dominance of gravitational wave radiation in the frequency evolution. Tidal interaction between white dwarfs in detached systems before the onset of mass transfer will give rise to distinct deviations of the frequency evolution as compared to systems with no or little tidal interaction. The strength of the tidal interaction is virtually unknown, with estimates ranging over many orders of magnitude (Marsh et al., 2004). Knowledge of the strength of the tides is important not only for understanding the physics of tides in general and of white dwarf interiors, but has important consequences for the tidal heating (and possibly optical observability) of LISA sources and the stability of mass transfer between white dwarfs (Racine et al., 2007). Short-term variations in the secular evolution of the systems experiencing mass transfer will change the frequency evolution, but are likely to be rare and will not prevent the detection of these systems (Stroeer and Nelemans, 2009).

Physics of mass-transfer stability

Detached ultra-compact binaries will evolve to shorter and shorter periods due to the angular momentum loss through gravitational wave radiation. At sufficiently short orbital period (a few minutes) one of the stars becomes larger than its Roche lobe – the equipotential surface that crosses the minimum of the potential between the two

stars – and material “leaks” out of the potential well of one star upon the other star. Depending on the difference between the change of the radius of this star and the Roche lobe upon mass transfer, there may be positive or negative feedback, leading to either limited, stable mass transfer, or a runaway mass-transfer instability.

For double white dwarfs and white dwarf-neutron star binaries the stability of the ensuing mass transfer has important consequences, for the number of detectable sources, as well as for a number of open astrophysical questions. The stable systems will form interacting binaries, AM CVn systems or ultra-compact X-ray binaries, that can be detected through their GW emissions. LISA will detect a number of double white dwarfs and AM CVn systems that are so close to the onset of mass transfer that the stability of the mass transfer can be tested directly by comparing their numbers. In addition, LISA will detect several ultra-compact X-ray binaries at the very early stages of mass transfer, providing a test of the mass transfer stability in these systems as well.

For AM CVn systems, a major uncertainty in the mass-transfer stability is again the tidal interaction between the two white dwarfs. Most likely the mass transfer will proceed via the direct impact configuration: due to the proximity of the two stars, the mass transfer stream lands directly on the surface of the accreting white dwarf, rather than wrapping around the accreting stars and interacting with itself to form a flat accretion disk in the plane of the orbit (Webbink, 1984). The stability of the mass transfer depends critically on the tidal interaction between the two white dwarfs (Marsh et al., 2004): In the absence of any tidal interaction, there will be additional angular momentum loss from the orbit due to the transfer of angular momentum from the orbit to the accreting star which will consequently spin up. This is different from cases where the accretion is via a disc for which most of the angular momentum generally is stored in the disc and eventually via very efficient tidal interaction put back into the orbit. Efficient tidal coupling between the accreting star and the companion has the ability to return the angular momentum back to the orbit (see D’Souza et al., 2006; Racine et al., 2007), thus reducing the magnitude of the spin-up.

The difference between efficient and inefficient tidal coupling is rather dramatic: the fraction of double white dwarfs estimated to survive the onset of mass transfer can drop from about 20 % to 0.2 % (Nelemans et al., 2001) depending on assumptions about the tidal coupling. This difference is easily measurable with LISA.

For ultra-compact X-ray binaries, the stability issue is completely different. At the onset, the mass transfer is orders of magnitude above the Eddington limit for a neutron star (the mass transfer rate at which the potential energy liberated in the accretion can couple to the infalling gas to blow it away). For normal stars and white dwarfs, this would likely lead to a complete merger of the system, but the enormous amount of energy liberated when matter is falling into the very deep potential well of a neutron star allows matter to be dumped on it at rates up to a thousand times the Eddington limit if the white dwarf has a low mass (see Yungelson et al., 2002). This allows the formation of ultra-compact X-ray binaries from white dwarf-neutron star pairs. LISA will unambiguously test this prediction by detecting several tens of ultra-compact X-ray binaries with periods between 5 and 20 minutes.

Double white dwarf mergers

The 80 % to 99.8 % of the double white dwarfs that experience run-away mass transfer and merger give rise to quite spectacular phenomena. Although it is not expected that LISA will witness the actual merger of a double white dwarf, it will certainly detect the shortest-period binaries known, expected at a period of about two minutes and give an extremely good estimate of their merger rate. Mergers of double white dwarfs have been proposed as progenitors of single subdwarf O and B stars, R Corona Borealis stars and maybe all massive white dwarfs (e.g. Webbink, 1984). In addition, the merger of a sufficiently massive double white dwarf can be a trigger for type Ia supernova events (see Pakmor et al., 2010). Alternatively, if the merger does not lead to an explosion, a (rapidly spinning) neutron star will be formed. This is one possible way to form isolated millisecond radio pulsars as well as magnetars, which have been proposed as sites for short gamma-ray bursts (e.g. Levan et al., 2006). LISA will be able to put strong constraints on these hypotheses. By measuring (chirp) masses and coalescence times, LISA will directly determine the merger rate for double white dwarfs with different masses which can then be compared with the rates and population of their possible descendants determined by other means.

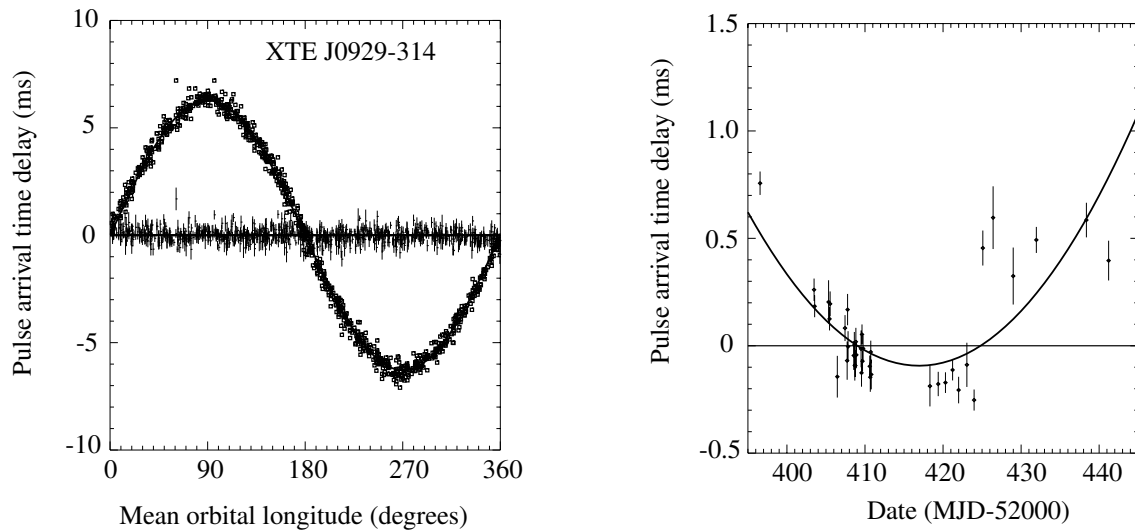


Figure 2.12.: *Imprint of the 40 min orbital period on the arrival times of the X-ray pulsations in the ultra-compact X-ray binary XTE J0929-314. From Galloway et al. (2002).*

Neutron star and black hole binaries

The current observational and theoretical estimates of the formation rate of neutron star binaries predict several tens of neutron star binaries to be detected by LISA (*e.g.* Belczynski et al., 2008; Nelemans et al., 2001). As the systems can be seen throughout the Galaxy, the samples for all these populations will be complete at the shortest periods. Thus, the sample will be independent of selection effects such as those present in radio pulsar surveys and X-ray surveys that pick up only transient X-ray sources. In addition, by the time LISA will fly, Advanced LIGO and Virgo will likely have detected a number of double neutron star mergers from far away galaxies, so these measurements together will test our ability to extrapolate our population models from our own galaxy to the rest of the Universe.

A special situation might arise in the millisecond X-ray pulsars in ultra-compact X-ray binaries. In the last decade, observations of X-ray pulsations from many ultra-compact X-ray binaries have enabled astrophysicists to determine the rotation rate of the neutron star in the binary using the NASA mission RXTE (figure 2.12). As had been expected on theoretical grounds, neutron stars are spinning rapidly several hundred times per second due to the angular momentum gained from infalling matter. The measurements give credence to the idea that these rapidly spinning neutron stars observed as millisecond radio pulsars are descendants of accreting neutron stars in binary systems (*e.g.* Bhattacharya and van den Heuvel, 1991). However, the exact role of ultra-compact binaries in the formation of these pulsars has yet to be established. The distribution of spin periods discovered in X-ray binaries suggests additional neutron star angular momentum loss on top of the plasma physics interaction between the accretion and magnetic field of the spinning neutron stars (Chakrabarty et al., 2003) which could be due to strong gravitational wave emission (Bildsten, 1998; but see Watts et al., 2008). In that case, ultra-compact X-ray binaries might be the only sources that could be studied simultaneously with LISA and Advanced LIGO, with LISA detecting the orbital period and LIGO detecting the neutron star period.

The number of ultra-compact stellar-mass black hole binaries in the Galaxy is highly uncertain (*e.g.* Belczynski et al., 2002); furthermore, these binaries are likely to be detectable only through their GW emission as they are electromagnetically quiet. LISA will constrain the formation rate estimates and the numbers of neutron star binaries and ultra-compact stellar mass black hole binaries.

2.5.5. New studies of galactic structure with LISA

One of the major capabilities of LISA is that it will determine distances for more than 100 compact binaries by measuring their \dot{f} (equation (2.9)). The ability of LISA to determine distances depends critically on the mission lifetime, as larger life times lead to more accurate \dot{f} measurements. The directional dependence of the Galactic

foreground as well as the directional accuracy for the resolved systems allow a statistical assessment of the contributions of the different Galactic components such as the Galactic bulge (with its bar), the thin and thick disc and especially the Galactic halo.

Galactic halo

The distribution of halo sources will be significantly different from the other Galactic components. The halo population might be enhanced compared to the disc as the formation and evolution of binaries in the halo may have been quite different (Ruiter et al., 2009; Yu and Jeffery, 2010). Such old and metal-poor population can locally be studied only in globular clusters, where the formation and evolution of binaries is generally completely altered by dynamical effects. Two of the known AM CVn systems may belong to the halo. They have very low metal abundances and have anomalous velocities. If true this implies that a large number of AM CVn stars are in the halo, maybe as many as in the rest of the Galaxy. The LISA directional sensitivity will immediately pick up any strong halo population.

Galactic centre and bar

The Galactic centre is one of the most interesting areas of the Galaxy, with a central massive black hole surrounded by a dense assembly of stars with intriguing properties. Dynamical effects, in particular mass segregation, will lead to many interactions close to the central black hole so that wide binaries will become tighter or will be disrupted (for a review see Alexander, 2005). This likely leads to an increase in the number of ultra-compact binaries as well as the possibility of EMRIs (see section 2.3.4). LISA will allow to put much more stringent constraints on these populations than current observations (see *e.g.* Roelofs et al., 2007), which are limited by the sources' electromagnetic faintness, or theoretical predictions, which are limited by our current understanding of the processes leading to compact binary formation.

Another major question about the central region of the Galaxy is the size and orientation of a bar (see Churchwell et al., 2009; Gerhard, 2002; Hamadache et al., 2006). Because ultra-compact binaries are expected to follow closely the mass distribution in the Galaxy, direct measurement of distances and directions to hundreds of ultra-compact binaries in the bulge will put a constraint on the bar, independent of the star count interpretation. LISA will be able to determine the distance and directions to many of the sources and in the galactic centre directly.

Galactic disc scale height and angular momentum

The level and shape of the double white dwarf foreground will provide information on the scale height of the ultra-compact binary population (Benacquista and Holley-Bockelmann, 2006) in the disc of the Galaxy. For many of the resolved sources the LISA measurements will also provide an estimate of their orbital inclination. For the first time, this will give hints on the dynamics of the formation of binaries from interstellar clouds, because the angular momentum vectors of the binaries in a statistical way is related to the overall angular momentum of the Galaxy.

2.6. Precision Cosmology

LISA science objectives and investigations relevant to this section

5. Probe new physics and cosmology with gravitational waves
 - 5.1 Study cosmic expansion history, geometry and dark energy using precise gravitationally calibrated distances in cases where redshifts are measured.

Cosmic Vision scientific questions addressed by this section

- 4.1 The early Universe

Define the physical processes that led to the inflationary phase in the early Universe, during which a drastic expansion supposedly took place.

The LISA Science Objectives are given in appendix B, the Cosmic Vision scientific questions in appendix A.

Precision cosmology characterises the structure and behaviour of the Universe as a whole: its global curvature, its expansion with time, and the behaviour of perturbations. The global curvature of space is a relic of the earliest moments of inflation and carries information about the initial conditions of the Universe; cosmic expansion history tests models of the new physics of dark energy; and cosmological perturbations test the dynamical predictions of GR on the largest scales. More than simply mapping our Universe, precision cosmology explores in detail the behaviour of space, time, matter and energy at the opposite extremes to black holes: the lowest density, the largest scales, and the earliest times. LISA has the potential to make fundamental contributions to precision cosmometry with its ability to provide gravitationally calibrated distances to sources with a 1 % accuracy or better.

For the most powerful tests we seek not only high precision, but also a variety of different techniques that measure global space-time in different ways. Precision measurements of cosmic microwave background (CMB) anisotropies (from COBE, balloon- and ground-based experiments, WMAP (Spergel et al., 2007), and Planck) set the highest standard of quality: CMB now reliably determines certain combinations of cosmological parameters with precision at a level of a few percent. Combining other types of measurements with the CMB data breaks degeneracies in fundamental quantities, increases reliability by controlling systematic errors, probes recent expansion where dark energy dominates, and allows deeper questions to be asked: for example, whether dark energy varies with time or reflects a pathology in the theory of gravity on large scales, rather than a new form of energy.

Improved precision in measurements of cosmological quantities, such as absolute and relative distances, the power spectrum of density fluctuations and the growth of structure, have thus emerged as a top priority of cosmological research. Over the next decade several large programs are being carried forward with this goal (Albrecht et al., 2006). Each of the proposed techniques has complementary strengths, weaknesses, sources of systematic errors and physical and astronomical assumptions, and thus it is prudent to pursue a balanced programme of many approaches,

A special challenge is calibration of the large-scale cosmos to absolute (ultimately, laboratory) standards of length or time. Such measurements allow globally-measured quantities, such as CMB angles and galaxy redshifts, to be connected to locally-measured quantities, such as the temperature of the cosmic microwave background, cosmic chronometers, and element abundances. Traditionally this absolute calibration employs a cosmic distance ladder, using direct geometrical parallax measurements of nearby stars to calibrate indirect measures for larger distances, in a series of steps extending to cosmological scales. This indirect approach adds substantial errors even to the best distance indicators at large distances, such as Type Ia supernovae. Other absolute calibrators are now becoming competitive but present major challenges in systematic reliability and precision, and require a variety of assumptions – again, requiring multiple approaches for a robust result.

One of the most important sources of error in constraining global parameters at present is the determination of the absolute cosmic distance scale at low redshift, the Hubble constant H_0 . This is not well constrained by CMB measurements, which provide an absolute ruler at high redshift, the sound horizon size at recombination

$r_S = (147.8 \pm 2.6)$ Mpc. The **CMB** data confine models to a narrow degeneracy line, well approximated by $\Omega_k = -0.3040 + 0.4067\Omega_\Lambda$ (Spergel et al., 2007) but do not distinguish well between points along this line. A precise measure of absolute distance, even at low redshift, narrows the allowed region to a small interval on this line. With the **HST** Key Project estimates of H_0 , **Wilkinson Microwave Anisotropy Probe** (WMAP) yields $\Omega_k = 0.003 \pm 0.015$, with the error dominated by H_0 .

The best distance ladder estimate for the Hubble constant $H_0 = (74.2 \pm 3.6)$ km s⁻¹ Mpc⁻¹ (Riess et al., 2009), still has an uncertainty of about 5%. The possibility of systematic errors in this value cannot be completely ruled out, as perhaps suggested by other different **HST** estimates, $H_0 = (62.3 \pm 1.3_{\text{random}} \pm 5.0_{\text{systematic}}$ km s⁻¹ Mpc⁻¹) (Sandage et al., 2006), and by recent evidence of a low value of $H_0 \approx 61$ km s⁻¹ Mpc⁻¹ from independent Cepheid calibration via eclipsing binaries (Bonanos et al., 2006). Other absolute calibration techniques include gravitational lens time delays, and Sunyaev-Zel'dovich observations of hot gas in galaxy clusters. So far the systematic errors in these techniques have prevented reliable precision at better than the ten percent level.

A new promising technique now emerging uses very long baseline radio observations of proper motions of distant megamasers in disk galaxies. Currently the formal error from this method, $H_0 = (74 \pm 3_{\text{random}} \pm 6_{\text{systematic}})$ km s⁻¹ Mpc⁻¹ based on one object still tied to Cepheids rather than distant Hubble flow (Macri et al., 2006), is comparable to the error of the ladder estimate. As more objects are observed in the coming decade, the megamaser technique may achieve a precision at the few percent level at sufficiently large distances so that Cepheids or other secondary calibrators will be unnecessary.

The baryonic acoustic oscillation (BAO) technique also provides an absolute calibration, based on the known physics of the dark matter/baryon-radiation plasma system around recombination. Currently it offers precision at the 4% level (Eisenstein et al., 2005), with prospects for improvement from a larger sample size. This calibration depends on precise understanding of the matter/radiation energy ratio, largely constrained by **CMB**.

LISA will add a unique and complementary new tool: absolutely calibrated distances determined by measuring the waves generated by massive binary black hole inspiral. Previous sections provide detailed discussion of these waves; for our purpose here, the main point to note is that measurement of these inspiral waves makes it possible to directly determine the luminosity distance to a source with a precision that can be as good as 0.1%. The main drawbacks of this tool relative to other techniques are firstly the uncertain number of events and their redshift distribution, including the uncertain fraction of those events for which an optical counterpart can be found; and secondly the influence of weak lensing, which amplifies or de-amplifies the signal, and so is an additional source of distance error. These are discussed below. On the other hand the intrinsic precision may be higher than any other technique, possibly in some respects even better than the **CMB**, and it brings an absolute physical calibration based on gravity alone, unlike any other technique. Even with a small number of events, the unique features of black hole binary inspirals – their reliable absolute calibration, inherent precision, and large range in redshifts (compared with other techniques) – introduce a new capability that promises to make all other precision measurements more robust and informative.

2.6.1. Absolute cosmology with black hole binaries

The principle of estimating distances from measured waveforms is elegantly simple (Schutz, 1986): the chirping time τ of an inspiral/merger event, together with its orbital frequency ω and strain h , gives an absolute luminosity distance $D \propto c/(\omega^2\tau h)$, with a numerical factor depending on details of the configuration that are precisely determined by the measured waveform.

However, LISA measurements cannot independently determine the redshift of a source. In gravitational wave measurements, the source's intrinsic frequency and chirp time are always measured in combination with cosmic redshift $\omega = \omega_{\text{int}}/(1+z)$, $\tau = (1+z)\tau_{\text{int}}$, *i.e.* the redshift is always degenerate with the source's intrinsic parameters, and cannot be determined from the **GW** data alone. An independent measurement of redshift is therefore needed. This may be accomplished by getting the optical redshift to the host galaxy, for instance by identifying an electromagnetic radiation counterpart to the event (Bloom et al., 2009). Without an identification, it may also be accomplished statistically, by surveying redshifts of galaxies correlated with the host. In reality this promising tool will have limitations. The number and redshift distribution of events that can provide useful distances is uncertain. At large distances, weak gravitational lensing by intervening clustered matter between us and the source introduces significant errors in distance. And depending on the other material present in the

vicinity of the merging holes, it may be difficult to identify the host galaxy electromagnetically.

If a cosmological model is assumed, then a redshift can be inferred self-consistently by requiring agreement between the estimated distance and that predicted from the cosmology. Thus to the extent that cosmological parameters are roughly known, only a certain narrow range of redshift is allowed for the host. Once a host is identified, the precise direction allows a still more precise estimate of distance from LISA. Thus LISA data will be used iteratively and in conjunction with electromagnetic data where these are available, to achieve maximal precision.

Identification of the host galaxy to a merger event can occur in many different ways. For an unusually nearby ($z < 1$) event with large black hole mass and signal-to-noise ratio, the LISA error box in angle and redshift might contain fewer than a thousand candidate galaxies, and the host might be easily identified from large scale optical morphology (such as tidal tails) as the site of a recent galaxy merger. More typically, the error box contains of order ten thousand galaxies, and the merger event may not be associated with a major visible disruption; in many cases the redshift is also very high, making optical identification difficult. On the other hand, models suggest that the same galaxy merger that creates a black hole binary often sends interstellar gas raining into the new galaxy nucleus, and the same gas that helps the two holes dissipate energy and momentum as they sink towards each other also forms a bright infrared nuclear starburst. For large binary mass ratios, and total binary masses at the upper end of the range of expected LISA **BHB** events (more than about $10^6 M_{\odot}$), the starburst is expected to still be active when the merger event occurs (Dotti et al., 2006). Such starbursts will be visible to very high redshift with the **James Webb Space Telescope** (JWST), and observations in the infrared penetrate deeply even into highly obscured nuclei.

An even more distinctive signature to identify the host galaxy may come from responses of the material near the black holes' horizons to the merger event, which can lead to observable time-variable X-ray/UV emission from the galactic nucleus, modulated by the evolution of the potential as the inspiral progresses. In the case of obscured nuclei, the time variations may appear in reprocessed infrared emission. For most LISA-observable **BH** (less than a few million M_{\odot}), gas accretion disks are evacuated during the merger process but then reestablish emission within a few years, causing an “afterglow” – a newly observable X-ray source (Milosavljević and Phinney, 2005). For higher mass **BH**, the interaction of accretion discs as the holes approach each other can lead to observable, variable X-ray precursors to the merger event (Dotti et al., 2006). If the two holes have disks and/or black-hole-spin-powered jet emission, the disrupted disks and jets can show non-thermal signatures that may appear from radio to gamma rays. Recent observations of low-power **AGN**, presumably from low mass **BH**, suggest that such evidence may not be at all rare or unusual. Only a tiny fraction (much smaller than $\sim 10^{-10}$) of the variable gravitational energy of the system needs to appear as a variable electromagnetic signal to be clearly visible.

It has also been demonstrated that at redshifts $0 < z < 0.5$, precise and unbiased statistical information about host redshifts can be obtained from galaxy catalogs in the vicinity of the events, so specific individual host galaxy identifications are not needed. The technique is based on the assumption that the **BHB** host galaxies are correlated with other galaxies. The direction and distance information from a **BHB** waveform fit provides a 3D-“error box” for the location of the host galaxy. Depending on the redshift and the fit, there are typically hundreds or even thousands of candidate hosts in this region of space. A galaxy redshift survey in the angular error box allows identification of candidate host galaxies and a 3D-map of their distribution. These galaxies are then allowed to “vote” on where the true host redshift is. Because the galaxies are significantly clustered in the cosmic web, the distribution of their redshifts is highly nonuniform within the box. The error in the estimated source redshift is not eliminated, but is significantly reduced by adding this information from the actual spatial galaxy distribution in the direction of a source. A simple version of the technique was shown to yield a high precision estimate of Hubble’s constant using mock catalogs based on **SDSS** redshift data (MacLeod and Hogan, 2008).

At redshifts significantly less than unity, the relevant inspiral events consist of a compact stellar mass or **IMBH** captured by a massive black hole in a galactic nucleus. These events will be extremely large mass ratio inspirals (see section on **EMRIs**). The **SNR** and per-event precision for these events are not as high as for binaries of comparable mass, but are still good enough (a few percent per event, possibly for hundreds of events) for precision measurement of H_0 . Even if electromagnetic counterparts for **EMRIs** are not found, adequate redshift

calibration for a large sample might be obtained statistically from galaxy surveys in the LISA error boxes.

By measuring the inspiral waves, particularly in the case where binaries are of comparable mass, LISA will pinpoint many events to better than a degree (in some cases, much better). LISA will also be able to predict the time of merger well in advance (often, hours to weeks), allowing searches for precursors and afterglows, as well as emission associated with the moment of the merger itself. In general, finding and studying electromagnetic signatures from an active inspiral/merger nucleus requires deep imaging over a wide (about a degree) field, in multiple wavebands. The time variable signatures require sampling on a timescale as long as intervals of years, down to a time resolution scale as short as the 1000 second orbital period. Fortunately, such capability is being created in many bands, including arrays of large aperture infrared telescopes, extremely capable optical systems such as **LSST** (which will image galaxies to $z > 1$, in a field four degrees across, in less than a minute), extremely wide angle radio interferometry (being demonstrated in systems such as the **Allen Telescope Array (ATA)**), and new capabilities in space from the infrared (**JWST**) to gamma rays (Fermi gamma-ray space telescope).

Limitations

LISA electromagnetic counterpart sources may provide a rich field of study, with many identifiable hosts and counterparts. LISA sources have possible electromagnetic counterparts over a wide variety of wavebands and timescales: potentially, an exploratory bonanza providing access to new phenomena over a huge range of scales. On the other hand given our ignorance about the processes in galactic nuclei associated with massive black holes and their mergers, it is also possible that the observable electromagnetic signatures may be very rare, in which case precision cosmology with these sources will be impractical.

Another important source of uncertainty is the rate of events, as discussed in Section 2.3. Standard galaxy formation theory suggests that the first black holes formed from the first massive stars, in the first baryonic collapses at redshifts of order $z \sim 20$. Subsequent hierarchical clustering of halos led to mergers of holes on successively larger scales, eventually forming the population of massive black holes found today in galactic nuclei. Detailed models of this process (Sesana et al., 2004; Volonteri, 2006) predict that LISA will see many dozens of massive black hole merger events per year, spread over a range of masses from 10^4 to 10^7 solar masses and a range of redshifts from 1 to 20. On the other hand a more conservative model for the formation of the massive black holes, based only on observed populations of massive black holes, and allowing them to grow as much as possible via accretion rather than mergers, can produce rates an order of magnitude smaller. The total rate and redshift distribution make a big difference in LISA's capability for precision cosmology. Similarly, the rate of **EMRIs** is highly uncertain (covering a similar range of possible rates), because of required extrapolation to nuclear stellar populations in galaxies where we have very limited information at present.

The most important practical limit on precision of distance measurements at high redshift comes from gravitational lensing, which can magnify and brighten an object, or de-magnify it relative to the mean for a given cosmology, and thus bias its inferred distance. Because high precision is the goal, even small-amplitude modulation by weak lensing is a concern. This effect must be controlled at high redshift by using a statistical sample, as is done for example with supernova distance indicators. The overall precision thus depends on the **BHB** redshift distribution and event rates.

Impact of LISA/BHB distances: Examples

Since the **BHB** technique yields independent and physically calibrated absolute distances it complements other techniques of precision cosmology, many of which yield relative distances only, and all of which use different assumptions with radically different systematic errors and biases from **BHBs**.

The potential contribution of **BHB** to precision cosmology has not yet been evaluated as thoroughly as other tools, and is subject to the above uncertainties, some of which will not be resolved until LISA flies. Nevertheless it is useful to cite several benchmark examples of potential impact:

- Since most lines of sight to $z < 1$ are nearly empty of dark matter, lensing errors are relatively small; typical distance errors from weak lensing at $z = 1$ are about 3 % (Kocsis et al., 2006). A few massive inspiral events, or a large number of **EMRI** events, at redshift less than or of order unity may lead to a reliable measurement of the Hubble constant H_0 to better than 1 %, about a factor of five improvement over current techniques.

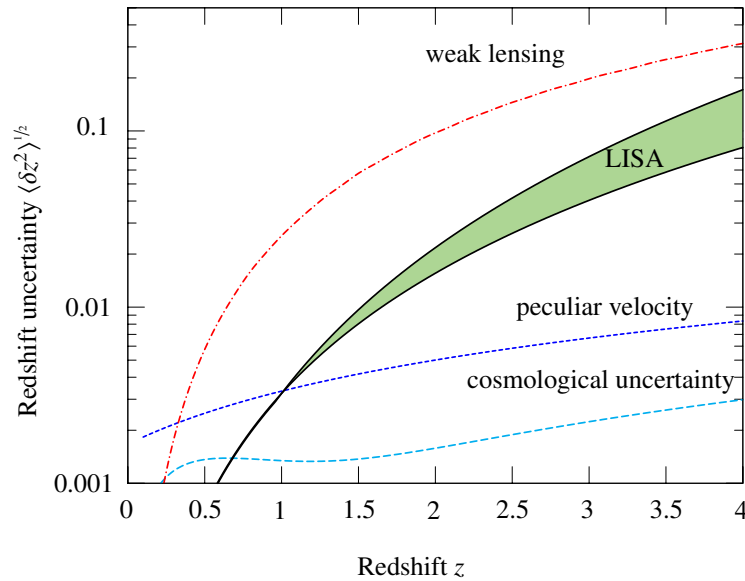


Figure 2.13.: Contribution of various error sources to the uncertainty in redshift $\langle \delta z^2 \rangle^{1/2}$. The errors are dominated by weak lensing (red, dot-dashed) above a redshift of $z = 0.3$, reducing the intrinsic accuracy of LISA of 0.3% at $z = 3$ to about 3%. Cosmological uncertainties (cyan, long dashed) and peculiar velocities (blue, dashed) cause substantially smaller errors (adapted from Kocsis et al., 2006).

Absolute gravitational calibration adds unique information even if other techniques attain comparable formal precision with different assumptions.

- Calibration of the absolute distance scale, in combination with **CMB** measurements, and a definite scaling law for the dark energy $w(a)$, allows a determination of w with high precision (Eisenstein and White, 2004; Hu, 2005). With Planck-quality **CMB** data alone, calibration of the Hubble constant at 2% precision achieves w accuracy of better than 3% (Olling, 2007). Similarly, a one percent constraint on absolute distance, combined with the **CMB** data, yields 10^{-3} error on global curvature Ω_k (Knox, 2006); in this respect the constraints are similar to those obtainable in the future from **baryonic acoustic oscillation (BAO)** (Eisenstein et al., 2005). With both techniques (*i.e.*, LISA and **BAO** together), a new tight constraint can be derived on the density of any invisible relativistic species or “dark radiation” that affects the **BAO** calibration.
- LISA/**BHB** distances are also useful at moderate z (of order 2 to 3) if the **BHB** sample is large enough for fitting to a lensing amplification model. Even with conservative assumptions about lensing noise, a sample of 100 LISA/**BHB** events provides precision comparable to a sample of approximately 3000 SN Ia distances at comparable redshift (Dalal et al., 2006).
- The considerable number of events from higher redshift, out to $z = 20$, will provide measurements of black hole mergers as a function of distance, and measurements of integrated weak lensing along multiple lines of sight to high redshift. The galaxy counterparts of these sources will be infrared galaxies, many of them in very early stages of assembly, and many of them potentially observable with **JWST**. LISA’s observations will complement the revolutionary **JWST** views of early structure and galaxy formation, adding detailed information about the early growth of nuclear regions, massive black holes, and dark matter density fluctuations at high redshift.

2.7. New Physics and the Early Universe

LISA science objectives and investigations relevant to this section

5. Probe new physics and cosmology with gravitational waves
 - 5.2 Measure the spectrum of, or set bounds on, cosmological backgrounds.
 - 5.3 Search for burst events from cosmic string cusps.
 - 5.4 Search for unforeseen sources of gravitational waves

Cosmic Vision scientific questions addressed by this section

- 3.2 The gravitational wave Universe
Make a key step toward detecting the gravitational radiation background generated at the Big Bang
- 4.1 The early Universe
Define the physical processes that led to the inflationary phase in the early Universe, during which a drastic expansion supposedly took place.

The LISA Science Objectives are given in appendix B, the Cosmic Vision scientific questions in appendix A.

Gravitational waves penetrate all of cosmic history, and LISA explores scales, epochs, and new physical effects not accessible in any other way (figure 2.14). A detectable gravitational wave background in the LISA band is predicted by a number of new physical ideas for early cosmological evolution (Hogan, 2006a; Maggiore, 2000). Two important mechanisms for generating stochastic backgrounds are phase transitions in the early Universe and cosmic strings.

Many types of new physics predict first-order phase transitions resulting in bubble nucleation and growth, and subsequent bubble collisions and turbulence. The cosmic expansion rate at a temperature T of about $1 \text{ TeV}/k_B$, corresponding to an apparent horizon size of about $c/H = ca/\dot{a} \approx 1 \text{ mm}$ at that time, is redshifted now to a frequency

$$f_0 = \dot{a}(t) \approx 10^{-4} \text{ Hz} \sqrt{H(t) \times \frac{1 \text{ mm}}{c}} \approx 10^{-4} \text{ Hz} \left(\frac{k_B T}{1 \text{ TeV}} \right) . \quad (2.11)$$

Thus, LISA's frequency band of about 0.1 mHz to 100 mHz today corresponds to the horizon at and beyond the Terascale frontier of fundamental physics. This allows LISA to probe bulk motions at times about 3×10^{-18} to 3×10^{-10} seconds after the Big Bang, a period not directly accessible with any other technique. Taking a typical broad spectrum into account, LISA has the sensitivity to detect cosmological backgrounds caused by new phase transitions from 0.1 TeV to 1000 TeV, if more than a modest fraction of about 10^{-7} of the energy density is converted to gravitational radiation in LISA's band (figure 2.15).

Fundamental string theory, the subject of intense theoretical study as a unified framework for all particles and forces of nature, also predicts the possibility of new fundamental objects called cosmic superstrings, stretched to astronomical size by the cosmic expansion, that lose energy principally through gravitational radiation with a very broad and uniquely identifiable spectrum. LISA will be our most sensitive probe for these objects by many orders of magnitude and so offers the possibility of detecting direct evidence of fundamental strings.

First-order cosmological phase transitions: Bulk motion from bubble nucleation, cavitation, collisions, turbulence

Abundant evidence suggests that the physical vacuum was not always in its current state, but once had a significantly higher free energy. This idea is fundamental and general: it underlies symmetry breaking in theories such as the Standard Model and its supersymmetric extensions, and cosmological models including almost all versions of inflation. Common to all these schemes is the feature that a cold, nearly uniform free energy contained in the original (“false”) vacuum is liberated in a phase transition to a final (“true”) vacuum, and eventually converted into thermal energy of radiation and hot plasma.

In many theories the conversion between vacuum states corresponds to a first-order phase transition. In an expanding universe this leads to a cataclysmic process. After supercooling below the critical temperature for the transition, a thermal or quantum jump across an energy barrier leads to the formation of bubbles of the new phase at widely separated nucleation sites. The bubbles rapidly expand and collide. The internal energy is thus converted to organised flows of mass-energy, whose bulk kinetic energy eventually dissipates via turbulence and finally thermalises. The initial bubble collision and subsequent turbulent cascade lead to relativistic flows and acceleration of matter that radiate gravitational waves on a scale not far below the horizon scale (Dolgov et al., 2002; Hogan, 1986; Kosowsky et al., 2002; Witten, 1984).

Dynamics of warped sub-millimetre extra dimensions

A “theory of everything” based on quantum superstrings requires many, as yet invisible, extra dimensions for mathematical consistency. The sizes of the dimensions, their shapes, and how they are stabilised are unknown. If they exist, gravity can penetrate into them, so they must be small or highly “warped” – with sizes or radii of curvature below the sub-millimetre scale limits set by direct laboratory tests of the gravitational inverse-square law. The scales probed by Standard Model particles and fields are much smaller than this, but fields other than gravity might be confined to a 3-dimensional subspace or “brane” living in a larger dimensional space.

Since the Hubble length at the Terascale is about a millimetre, the current threshold where possible new effects of extra dimensions might appear happens to be about the same in the laboratory gravity, particle/field, and cosmological realms *i.e.*, laboratory gravity experiments, accelerator physics, and LISA cosmology converge on the same new regime in very different ways. It is even possible that new properties of gravity on this scale are related to cosmic dark energy, whose energy density is about $(0.1 \text{ mm})^{-4}$ in particle physics units.

The dynamics associated with the stabilisation of extra dimensions at a certain size or warp radius might introduce a source of free internal energy released coherently on a “mesoscopic”, *i.e.* sub-millimetre to nanometre scale, leading to a detectable background (Hogan, 2000; Randall and Servant, 2007). If the extra dimensions are much smaller than the Hubble length when the stabilisation occurs, the behaviour of the extra dimensions is nearly equivalent to scalar field behaviour as viewed in conventional 3-dimensional space, with effects similar to the phase transitions just discussed (figure 2.15). Brane condensation also introduces a new kind of mechanism for generating gravitational waves: motion and curvature of our Standard Model brane in the extra dimensions. LISA’s high frequency limit at 1000 TeV corresponds to direct probes of extra dimensions as small as 10^{-9} m.

Terascale inflationary reheating

Inflation represents an extraordinarily coherent behaviour of an energetic scalar field that is nearly uniform across the observable Universe. After inflation, the internal potential energy of this field is converted into a thermal mix of relativistic particles, in a process known as “reheating”. The reheating temperature might be as cool as 1 TeV, especially in some brane-world models where the Planck scale is itself not far above the Terascale.

There is no reason to assume a quiet, orderly reheating process: the decay of the inflaton energy may be violently unstable. In many scenarios, the conversion begins with macroscopically coherent but inhomogeneous motions that eventually cascade to microscopic scales. Quantum coherent processes such as “preheating” transform the energy into coherent classical motions that, like the phase transitions discussed above, generate backgrounds on the order of 10^{-3} of the thermal plasma density (Easter and Lim, 2006; Felder and Kofman, 2007; Khlebnikov and Tkachev, 1997). As with these transitions, the characteristic frequency of the background matches the LISA band if the final reheating occurred at 0.1 TeV to 1000 TeV.

Exotic inflationary quantum vacuum fluctuations

The amplification of quantum vacuum fluctuations during inflation leads to a background of primordial gravitational waves. An optimistic estimate of this background in the case of conventional inflation limits these to less than about 10^{-10} of the CMB energy density, far below LISA’s sensitivity; in many inflation models it is much less (Chongchitnan and Efstathiou, 2006). However, some unconventional versions of inflation, particularly pre-Big-Bang or bouncing brane scenarios, predict possibly detectable backgrounds in the LISA band (see *e.g.*

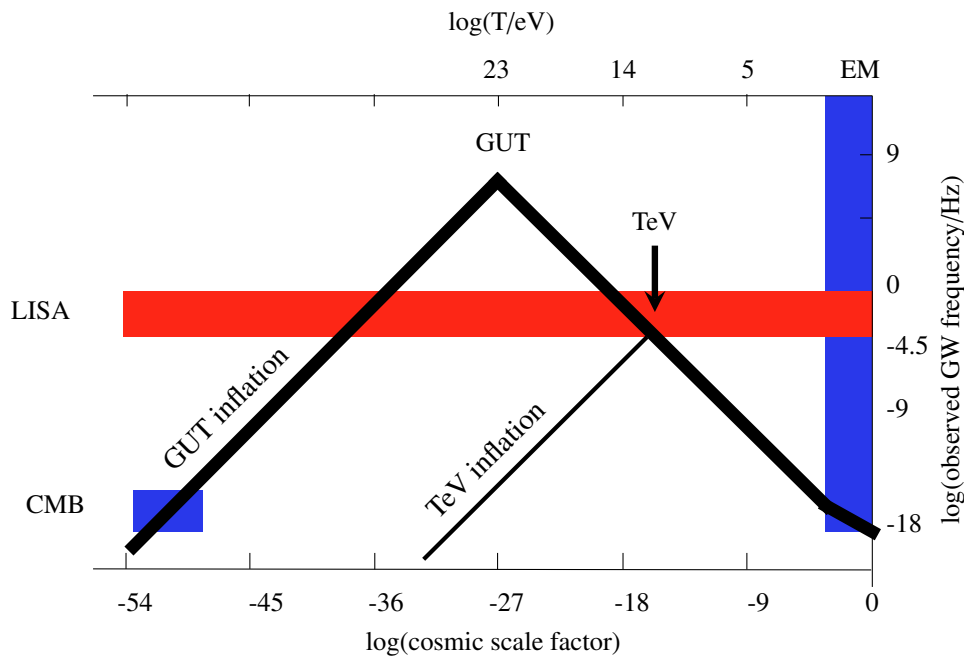


Figure 2.14.: The observed (redshifted) frequency of wave-generating phenomena is shown as a function of cosmic scale factor a , with the present epoch at the right. The redshifted Hubble rate (horizon scale) is shown in black for a standard Grand Unified Theory (GUT) and a lower temperature Terascale (TeV) inflationary cosmology. Blue regions are accessible to electromagnetic (EM) observations: the Universe since recombination (right box) and CMB fluctuations (left box). The red bar shows the range of cosmic history accessible through LISA, from processes within the horizon up to about 1000 TeV, as well as inflation different from CMB observations.

Brustein et al., 1995; Buonanno, 2003; Buonanno et al., 1997). Although some key parameters remain unknown, which limits the predictive power of these models, they are significantly constrained by gravitational wave backgrounds. If such a background is detected, its spectrum also contains information about the Universe at the time perturbations “re-enter” the horizon (the second horizon intersection in figure 2.14).

2.7.1. Backgrounds, bursts, and harmonic notes from cosmic strings

String theory is a leading candidate for a fundamental theory unifying all of physics: both the quantum fields of the Standard Model, and the spacetime dynamics of general relativity. Models of physics and cosmology based on string theory, as well as their field-theory counterparts, often predict the cosmological formation of cosmic superstrings (Polchinski, 2005): thin quasi-stable relativistic strings that form after inflation and are stretched to enormous length by the cosmic expansion. In equivalent field-theory language, cosmic strings arise from certain types of phase transitions, and stable relics of the high-energy phase persist as topological defects: in the form of one-dimensional strings that resemble flux tubes or trapped vortex lines.

The primordial network of strings spawns isolated, oscillating loops that ultimately radiate almost all of their energy into gravitational waves. Their gravitational radiation is mainly governed by a single dimensionless parameter $G\mu/c^4$ reflecting the fundamental physics of the strings, where μ is the energy per unit length, or tension. This number is known to be very small ($\sim 10^{-10}$), as current limits on gravitational wave backgrounds already indicate that if cosmic strings existed, they must be so light that they would have no observable effects apart from their gravitational radiation.

Figure 2.15 includes predicted stochastic background spectra (Hogan, 2006b) from strings for two values of $G\mu/c^4$ spanning a range of scenarios motivated by brane world inflation. (These estimates are plotted for a “large loop” scenario where newly formed loops are about 10% of the horizon size.) The spectrum from cosmic strings is distinguishably different from that of phase transitions or any other predicted source: it has nearly constant energy per logarithmic frequency interval over many decades at high frequencies, including the range

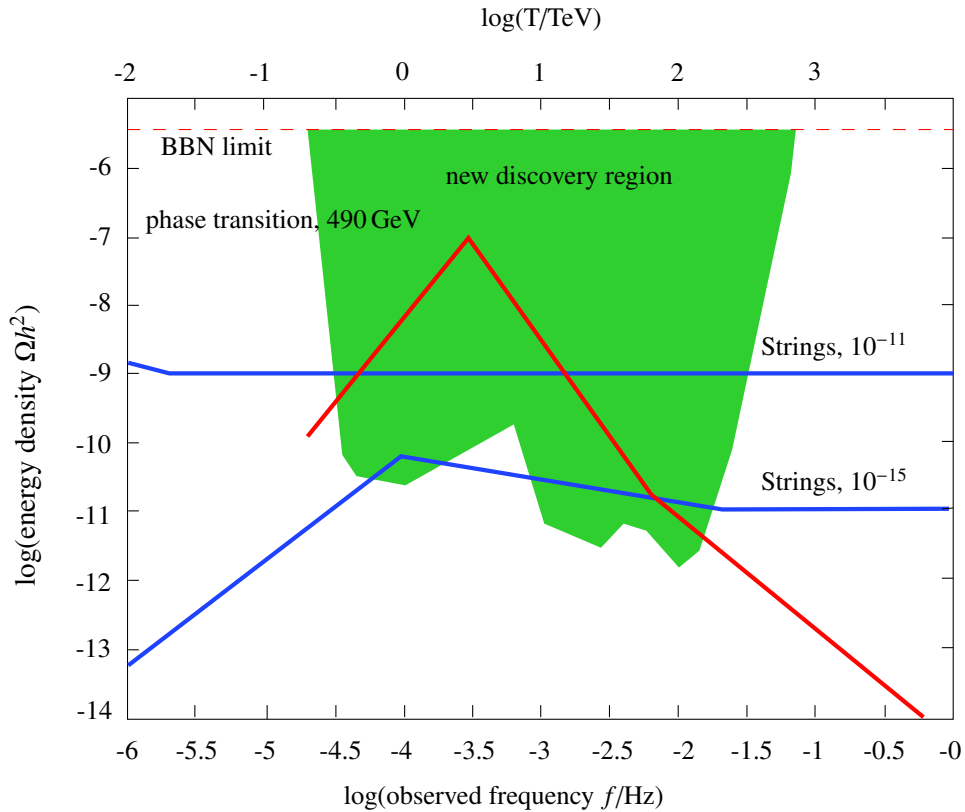


Figure 2.15.: Gravitational wave background energy density in units of the critical density for $h_0 = 1$. The new discovery region for LISA. LISA’s sensitivity extends about seven orders of magnitude below the energy density of thermal radiation, and six orders of magnitude below current limits from Big Bang nucleosynthesis (BBN). The background spectrum from cosmic superstrings (Hogan, 2006b) is shown for two values of string tension, $G\mu/c^4 = 10^{-11}$ and 10^{-15} . A model spectrum is shown from a first order phase transition of warped extra dimensions (Randall and Servant, 2007), which is typical of strongly first order transition spectra. Top axis is labelled with the temperature of the Universe when waves of the specified observed frequency were at the size of the cosmological horizon.

where LISA is able to observe it, and falls off at low frequencies since large string loops are rare and radiate slowly. LISA’s sensitivity in terms of $G\mu/c^4$ is about five orders of magnitude deeper than even the best possible future sensitivity from pulsar timing (about $G\mu/c^4 \sim 10^{-10}$).

If the strings are not too much lighter than $G\mu/c^4 \sim 10^{-10}$, occasional distinctive bursts might be seen from loops that happen to beam gravitational waves in our direction from “cusp catastrophes”, where a momentary event produces a sharply bent bit of string moving at nearly the speed of light (Damour and Vilenkin, 2005; Siemens et al., 2006). These rare events, if they are intense enough to stand out above the background, are recognisable from their universal waveform, which derives just from the geometry of the cusps.

Another possibility opens up for very light strings. String loops emit gravitational waves in a perfect harmonic series of extremely narrow gravitational wave “spectral lines,” unlike any ordinary astrophysical source. For light strings, surviving loops have a size that puts their fundamental or low-order harmonic modes into the detection band of LISA. In this case, line radiation from individual nearby loops in our Galactic halo would appear above the background. Such signals would provide not just a stochastic background but a sample of detailed loop waveforms for study, a rich source of detailed information about these exotic objects.

Although individual burst events, if detected, gave the clearest signature of a string source, the first detectable sign of a superstring loop population is likely their integrated stochastic background as shown in figure 2.15 (Hogan, 2006b).

3. Scientific Requirements

3.1. Science Requirements Overview

LISA will be the first space-borne gravitational wave detector, which means that some of the functional and performance requirements for the science instrument are somewhat uncommon. A gravitational wave detector based on laser interferometry and undisturbed, free-falling test masses is characterised by parameters different from those characterising common space science instruments such as telescopes, spectrographs and cameras. The requirements described here are the product of a considerable effort to create a clear, robust and verifiable interface between the science and the engineering teams.

The LISA mission concept has been stable for over ten years. Over the same time period, the science objectives have matured substantially, but the derived performance requirements remain unchanged. This chapter summarises the logical flow from science objectives, to science investigations, to observation requirements, to the instrument sensitivity model (ISM), to top-level performance requirements, and their flow-down to instrument performance.

The set of observation requirements quantitatively specifies the observation performance that is necessary for a particular source type to carry out the science investigations and to realise the science objectives. However, the observation requirements do not unambiguously define the instrument performance; many different detectors with equally different performances are, in principle, able to meet the observation requirements. Therefore, the choice was made to show that the observation requirements are met by a specifically chosen instrument performance, the **ISM**. The **ISM** has been shown to meet all of the observation requirements. It is based on an analytic description of a gravitational wave detector employing laser interferometry for displacement measurements, free-falling test masses, unique orbits that approximately preserve a constellation of three spacecraft in an equilateral triangle, and a laser frequency noise cancellation scheme that mimics Michelson's "white-light fringe" condition. The **ISM**, in effect, has nominal performance requirements for the instrument built-in. The engineering team has to verify that the design for the LISA mission allows to meet, or to exceed, the performance of the **ISM**.

The next section of this chapter describes the underlying LISA concept that is the foundation of the requirements flow-down. The concept section is followed by sections describing the rationale of the science requirements, the science objectives and investigations, the observation requirements, the **ISM**, the top-level performance requirements and the performance requirements flowed down to the major instrument systems. This chapter can only summarise the science requirements and their flow-down to instrument performance. More extensive descriptions and supporting analyses are found in the following documents:

- *LISA Science Requirements Document* (**LISA-ScRD-066**)
- *Mission Requirement Document* (**MRD**)
- *LISA Measurement Requirements Flowdown Guide* (**LISA-MSE-TN-0001**)
- *System Design Specification* (**LISA-ASD-RS-5001**)
- *Payload Design Specification* (**LISA-ASD-RS-3001**)
- *LISA Measurement Performance* (**LISA-ASD-TN-1002**)
- *Requirement Breakdown* (**LISA-ASD-TN-5001**)

3.2. The LISA concept

The description of the LISA mission concept begins with what is to be measured and the general concept for measuring it. The design concept is chosen to extract maximal information about astrophysical sources to answer questions about astrophysics and to test fundamental physics. Notional values of some top-level design parameters used here are not a prescription for these parameters, but rather are suggestive of the approximate order of magnitude intrinsic to the underlying concept.

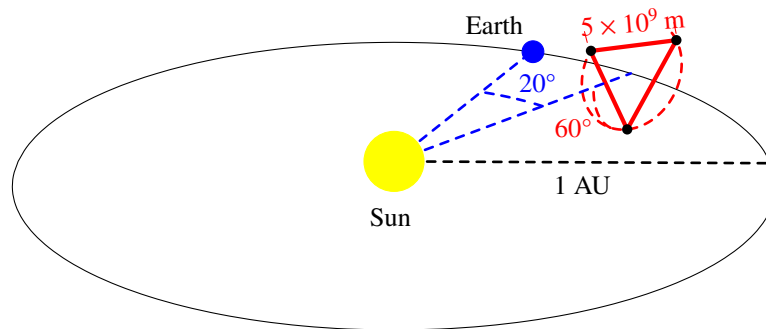


Figure 3.1.: *The LISA orbits: The constellation trails Earth by about 20° (or 5×10^{10} km) and is inclined by 60° with respect to the ecliptic. Separation between the S/C is 5×10^9 km.*

The LISA concept for directly detecting the oscillating strain in spacetime caused by gravitational waves shares the scheme used in all laser interferometer-based gravitational wave detectors: the passage of the wave is detected by measuring the time-varying changes of optical pathlength between free-falling mirrors.

Gravitational wave detectors based on laser interferometers measure the change in length (δL) directly. The strain ($\delta L/L$) produced by the sources accessible with LISA (see chapter 2) may be as small as 10^{-24} . This argues simultaneously for a measurement length L as large as possible and long integration times, the primary impetus for a space-borne detector millions of kilometres long. Interferometry is the only measurement system known that can operate over these distances and with the required sensitivity.

“Free-falling” or inertial masses are, by definition, undisturbed by forces other than gravitation. To achieve free-fall conditions, the detector must be located in a very quiet environment to avoid disturbances to the test masses causing time-varying movements that in turn could be confused with the apparent displacements caused by gravitational radiation. Space can provide a very stable, benign environment if careful design choices for science instrumentation, spacecraft and orbits are made. An interferometer-based gravitational wave detectors requires two basic functions: undisturbed masses to act as the endpoints of the baselines and a measurement system to monitor changes in the lengths of these baselines. The residual disturbances of the masses must be sufficiently small such that the resulting motions are less than the apparent length changes associated with gravitational waves to be detected. Likewise, the measurement system must be able to detect these apparent length changes.

3.2.1. LISA design concept

LISA’s measurement arms are defined by three identical spacecraft orbiting the Sun (figure 3.1) in a triangular constellation. The first key feature of the LISA concept is a set of three orbits that maintain a near-equilateral triangular formation of spacecraft at an approximately constant distance from the Earth for about ten years without station-keeping. The spacecraft at the corners of the triangle house two free-falling “test masses” that define the endpoints of the arms as well as interferometry equipment for measuring changes in the length of these arms. (figure 3.2). Ideally, the distance between the test masses does not depend on the noise in the position of the spacecraft.

For practical reasons, this measurement is broken up into three distinct parts: the measurement between the spacecraft, *i.e.* between the optical benches that are fixed to the spacecraft, and the measurement between each of the test masses and its respective optical bench (see figure 3.3). By combining the three measurements, the measurement of the distance between the test masses is reconstructed and kept insensitive to the noise in the position of the spacecraft with respect to the test masses. As detector noise is generally negligible in LISA, there is no significant noise impact of this measurement partition.

A second key feature of the LISA concept is that the test masses are protected from disturbances as much as possible by careful design and “drag-free” operation. To establish drag-free operation, a housing around the test mass senses the relative position of test mass and spacecraft, and a control system commands the spacecraft’s thrusters to follow the free-falling mass. Drag-free operation reduces time-varying disturbances to the test

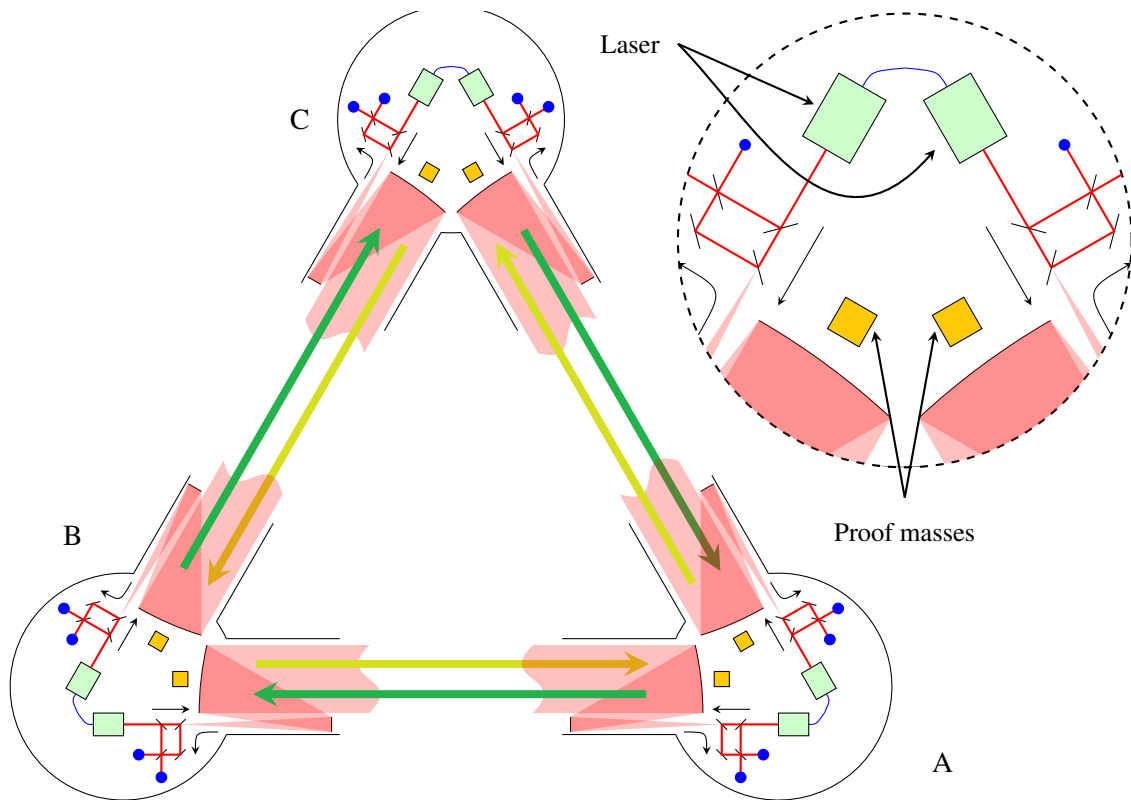


Figure 3.2.: A constellation of three identical LISA spacecraft constitutes the science instrument. There are six identical, send/receive laser ranging terminals (two per S/C) with associated test masses and a comparison of signals at each apex. The sketch leaves out the test mass interferometers for clarity.

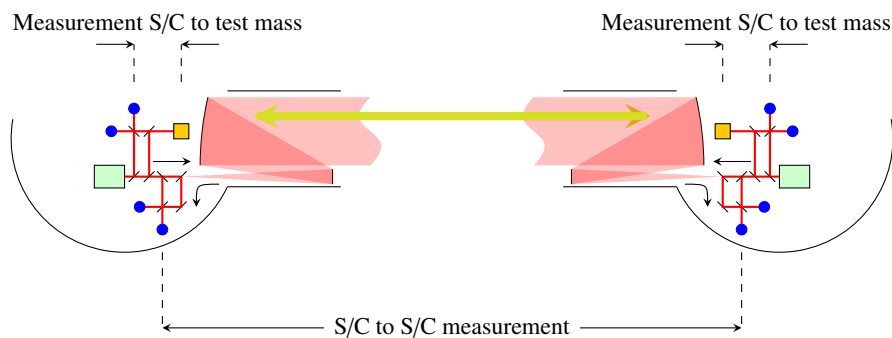


Figure 3.3.: Partition of the LISA measurement. Each measurement between two test masses is broken up into three different measurements: two between the respective test mass and the spacecraft and one between the two spacecraft. As the noise in the measurement is dominated by the shot noise in the S/C-S/C measurement, the noise penalty for the partitioning of the measurement is negligible. The blue (solid) dots indicate where the interferometric measurements are taken.

masses caused by force gradients arising in a spacecraft that is moving with respect to the test masses. The amplitude spectral density of the residual acceleration of the test mass characterises the disturbance reduction, the first basic function of the science instrument.

An additional benefit of the LISA orbits is the constant sun-angle of 30° with respect to the normal to the top of the spacecraft, thereby resulting in an extremely stable thermal environment within, minimising thermal disturbances on the spacecraft.

The third key feature, the distance measuring system, is a continuous interferometric laser ranging scheme, similar to that used for radar-tracking of spacecraft. As the direct reflection of laser light, such as in a normal Michelson interferometer, is not feasible due to the large distance between the spacecraft, lasers at each end of each arm operate in a “transponder” mode. A laser beam is sent out from one spacecraft to a distant one. The laser in the distant spacecraft is then phase-locked to the incoming beam thus returning a high-power phase replica. The returned beam is received by the first spacecraft and beat against the local laser. Variants of this basic scheme are repeated for all the arms. In addition, the phases of the two lasers situated on one spacecraft and serving different arms are compared. The set of phase measurements together with some auxiliary modulation then allows to determine optical path difference changes, laser frequency noise, and clock noise. The amplitude spectral density of the displacement noise characterises the performance of the measurement system, the second basic function of the science instrument.

LISA achieves the requisite $10^{-20} / \sqrt{\text{Hz}}$ strain sensitivity (which allows to detect a strain of about 10^{-24} in a 3-year measurement with an SNR of 1), in part, through a phase resolution of about $5 \mu\text{cycle} / \sqrt{\text{Hz}}$ with $1 \mu\text{m}$ wavelength light, resulting in a displacement sensitivity of $50 \times 10^{-12} \text{ m} / \sqrt{\text{Hz}}$ over a path length of $5 \times 10^9 \text{ m}$. The achievable reductions of disturbances on test masses and the achievable displacement sensitivities by the laser ranging system yield a useful measurement bandwidth in the frequency regime of 10^{-5} Hz to 1 Hz . (The requirement is 10^{-4} Hz to 1 Hz ; the goal is $3 \times 10^{-5} \text{ Hz}$ to 1 Hz .)

3.2.2. Science requirements rationale

The most important consideration that affects LISA science requirements is the complex interaction of many different source waveforms with the instrumental sensitivity curve. All gravitational wave detectors have usable sensitivity only over some limited frequency band. Some gravitational wave sources generate signals in a narrow fixed frequency band; others chirp upwards in frequency during an inspiral. The particular waveform can be a very complicated function of masses, redshifts, spins, etc. Where lots of different kinds of sources are present – as is the case with LISA – changes in the instrumental sensitivity curve have different consequences for the signal-to-noise ratio (SNR) depending on the source type and on the individual source parameters. The complexity is even greater when considering how well the astrophysical parameters of the source can be determined with a given instrumental sensitivity, since information on each parameter accumulates at different rates during the integration. Consequently, there is no unique inversion from available instrumental sensitivity to accessible science. Therefore, a *forward* calculation of the SNR, or the uncertainty in estimation of astrophysical parameters for the different sources, given a certain ISM, has been performed. To do astrophysics with gravitational wave observations, it is best to characterise a gravitational wave detector in terms of how well astrophysical parameters of the source, such as mass or luminosity distance, can be determined. Hence, for a particular source of interest, the effectiveness of a detector design can be evaluated in terms of the uncertainty of a given parameter, such as the luminosity distance, which is frequently the source parameter that is most difficult to determine. With this insight, the LISA science requirements were organised around the following rationale:

1. The science objectives were taken from the *LISA Science Requirements Document (LISA-ScRD-066)*. They are given in chapter B for reference.
2. For each science objective, science investigations necessary to reach that objective were mapped out.
3. For each science investigation, observations were developed with quantitative requirements on the astrophysical parameters to be measured.
4. An ISM and a model of the astrophysical noise, coming from the close white-dwarf binary background, were assumed.
5. The ability of the model instrument to perform the required observations is then validated by calculating the parameter uncertainty from waveforms of anticipated sources with the instrument sensitivity model.

The following sections trace this rationale in some detail. The *LISA Science Requirements Document (LISA-ScRD-066)* is a much more extensive treatise on the subject.

3.3. Observation Requirements

The LISA science objectives and investigations were introduced and motivated with the scientific context in section 2.2. The objectives are the formal statement of the mission’s scientific purpose; the investigations are the research needed to fulfil these objectives.

For each science investigation, one or more observation requirements are defined. The observation requirements are stated (table 3.1) in terms of observable quantities necessary for the science investigation and the precision with which they must be measured, using formal requirements language. These requirements are explained and justified in chapter 5 of the *LISA Science Requirements Document (LISA-ScRD-066)*.

Table 3.1.: *LISA Science Investigations and Associated Observation Requirements*

| Science Investigation | Observation requirements |
|--|--|
| SR 1.1 Trace the formation, growth, and merger history of IMBHs and MBHs out to redshift $z = 15$ | OR 1.1 LISA shall have the capability to detect the mergers of IMBHs and MBHs with masses in the range $300 M_{\odot} < M_2 < M_1 < 3 \times 10^4 M_{\odot}$ with $M_2/M_1 > 1/100$, out to redshift $z = 15$, with sufficient SNR to enable determination of MBH masses, the spin of the larger MBH , and the luminosity distance to the binary. |
| SR 1.2 Determine the merger history of MBHs with masses of $10^5 M_{\odot} - 3 \times 10^5 M_{\odot}$ from the era of the earliest known quasars, $z \sim 6$. | OR 1.2 LISA shall have the capability to detect the mergers of IMBHs and MBHs with masses in the range $10^4 M_{\odot} < M_2 < M_1 < 3 \times 10^5 M_{\odot}$, out to redshift $z = 16$, with sufficient SNR to enable determination of MBH masses, the spin of the larger massive black hole (MBH), and the luminosity distance to the binary. |
| SR 1.3 Determine the merger history of MBHs with masses between $3 \times 10^5 M_{\odot}$ and $10^7 M_{\odot}$ at later epochs, $z < 6$. | OR 1.3 LISA shall have the capability to detect the mergers of MBHs with masses in the range $3 \times 10^5 M_{\odot} < M_1 < 10^7 M_{\odot}$ and $10^3 M_{\odot} < M_2 < M_1$, at redshifts $z < 6$. LISA shall detect such systems with sufficient SNR to enable determination of MBH masses, the spin of the larger MBH , and the luminosity distance to the binary. |
| SR 2.1 Characterise the immediate environment of MBHs in $z < 1$ galactic nuclei from EMRI capture signals. | OR 2.1 LISA shall have the capability to detect gravitational waves emitted during the last year of inspiral for a stellar-mass compact object ($M_2 \sim 5 M_{\odot} \dots 100 M_{\odot}$) orbiting a massive black hole (with $M_1 \sim 10^5 M_{\odot} \dots \text{few} \times 10^6 M_{\odot}$) at $z = 1$ with SNR > 30 (averaged over source locations and orientations) |
| SR 2.2 Study intermediate-mass black holes from their capture signals. | OR 2.2 LISA shall have the capability to detect gravitational waves emitted by a $10^3 M_{\odot} - 10^4 M_{\odot}$ intermediate-mass black hole (IMBH) spiralling into an MBH with mass M in the range $3 \times 10^5 M_{\odot} - 10^6 M_{\odot}$ out to $z = 3$ (with SNR ~ 30). LISA shall maintain this detection capability for a three year observing period. |
| SR 2.3 Improve our understanding of stars and gas in the vicinity of galactic black holes using coordinated gravitational and electromagnetic observations. | OR 2.3 LISA shall be capable of providing advance warning and localisation of mergers of $5 \times 10^5 M_{\odot}$ to $3 \times 10^6 M_{\odot}$ black holes at $z = 1$ with an accuracy of less than 15 square degrees one week before merger. LISA shall be capable of localising the source direction to better than 1 square degree within one week after merger, and with uncertainties of less than 1 % in the luminosity distance for black holes at $z = 1$ with component masses in the range $10^5 M_{\odot} \leq M(1+z) \leq 10^6 M_{\odot}$ and mass ratio $M_1/M_2 > 3$. LISA shall have the capability to measure distance to extreme mass-ratio inspiral (EMRI) or intermediate mass-ratio inspiral (IMRI) sources with SNR > 50 to 3 % or better with a sky position better than 5 square degrees. |

continued on next page

continued from previous page

| Science Investigation | Observation requirements |
|--|---|
| <p>SR 3.1 Elucidate the formation and evolution of Galactic stellar-mass binaries; constrain the diffuse extragalactic foreground.</p> | <p>OR 3.1.1 LISA shall have the capability to detect at least 1000 binaries at $\text{SNR} > 10$ with orbital periods shorter than approximately six hours and determine their period. LISA shall maintain this detection capability for at least one year.</p> <p>OR 3.1.2 LISA shall have the capability to measure the spectral amplitude and frequency dependency of the unresolved Galactic foreground below 1 mHz and constrain the spectral amplitude of the unresolved extragalactic foreground in the frequency region 2 mHz to 5 mHz. LISA shall maintain this detection capability for at least one year.</p> |
| <p>SR 3.2 Determine the spatial distribution of stellar mass binaries in the Milky Way and environs.</p> | <p>OR 3.2.1 LISA shall have the capability to: determine the position of at least a hundred sources with better than a square degree angular resolution and the frequency derivative to a fractional uncertainty of 10 %</p> <p>OR 3.2.2 LISA shall measure the first two moments of the distribution of the Galactic unresolved foreground.</p> <p>OR 3.2.3 LISA shall measure the distance to 10 % for the binaries for which an EM counterpart is available. LISA shall maintain this detection capability for at least two years.</p> |
| <p>SR 3.3 Improve our understanding of white dwarfs, their masses, and their interactions in binaries and enable combined gravitational and electromagnetic observations.</p> | <p>OR 3.3 LISA shall have the capability to measure the second frequency derivative of binary systems with gravitational wave frequencies above 20 mHz to 10 % and their sky location to better than 0.1 square degree. LISA shall maintain this detection capability for at least five years.</p> |
| <p>SR 4.1 Detect gravitational waves directly and measure their properties precisely.</p> | <p>OR 4.1.1 LISA shall have capability to detect and study three or more optically observable verification binaries between 1 mHz and 10 mHz with $\text{SNR} > 20$ in two years of mission lifetime.</p> <p>OR 4.1.2 LISA shall be capable of observing the gravitational waves from at least 50 % of all $z \sim 2$ coalescing binary systems consisting of compact objects with masses between $10^5 M_\odot$ and $10^6 M_\odot$ and mass ratios between 1 : 1 and 1 : 3. LISA shall detect these systems with $\text{SNR} \geq 5$ in each of five equal logarithmic frequency bands between 0.03 mHz (or the lowest observed frequency) and the highest inspiral frequency.</p> |
| <p>SR 4.2 Test whether the central massive objects in galactic nuclei are the black holes of GR.</p> | <p>OR 4.2 LISA shall have the capability to detect gravitational waves emitted during the last year of inspiral for a $10 M_\odot$ black hole orbiting a $3 \times 10^5 M_\odot$ to $3 \times 10^6 M_\odot$ black hole at 1 Gpc with $\text{SNR} > 30$. LISA shall have a science mission duration with adequate observation time for EMRIs to sweep over a range of r/M to map space-time, and to provide a good sample of events.</p> |
| <p>SR 4.3 Perform precision tests of dynamical strong-field gravity.</p> | <p>OR 4.3 Observe the merger and ring-down radiation from all $1 \times 10^5 M_\odot$ to $1 \times 10^6 M_\odot$ black holes formed from approximately equal mass, $M_1 < 3M_2$, mergers to $z \leq 8$, measuring the mass and spin parameters, M and a, of the final black hole to $0.1M$. This will include essentially all systems with these masses as the rates are expected to be vanishingly small for higher redshifts (a $z < 5$ requirement, for example, would also include almost all likely events.).</p> |
| <p>SR 5.1 Study the expansion history of the Universe using gravitationally calibrated distances to merger events (in cases where redshifts can be measured).</p> | <p>OR 5.1.1 LISA shall be capable of providing sky localisation of 3.5° (not squared degrees) or better, for MBH mergers with component masses in the range $10^5 M_\odot$ to $10^6 M_\odot$ at $z \leq 2$. For a large fraction of these, LISA shall be capable of attaining sub-3.5° resolution at least 6 hours before the merger. LISA shall also be capable of determining the luminosity distance to these mergers better than 5 %</p> <p>OR 5.1.2 LISA shall have the capability to provide sky location of 10 square degrees or better, and luminosity-distance measurements to 3 % or better, for EMRI or IMRI binary sources with $\text{SNR} > 50$.</p> |

continued on next page

continued from previous page

| Science Investigation | Observation requirements |
|---|---|
| SR 5.2 Measure the spectrum of cosmological backgrounds, or set upper limits on them | OR 5.2 LISA shall be capable of detecting or setting an upper limit on the spectrum of a stochastic gravitational wave background in the 10^{-4} Hz – 10^{-1} Hz band. |
| SR 5.3 Search for gravitational wave (GW) bursts from cosmic-string cusps | OR 5.3 LISA shall be capable of detecting gravitational wave bursts from cosmic (super-)strings, or of setting cosmologically interesting upper limits on the loops. |
| SR 6.1 Search for unforeseen sources of gravitational waves | OR 6.1 LISA shall be sensitive over discovery space for unforeseen effects (<i>e.g.</i> even at frequencies where we cannot predict likely signals from known classes of astrophysical sources). LISA shall allow for reliable separation of real strain signals from instrumental and environmental artifacts. |

3.4. Instrument Sensitivity Model

As described above, the **instrument sensitivity model (ISM)** is the central constituent of the science requirements, as it connects the science objectives with the astrophysical information obtainable with LISA.

The **ISM** combines an instrument noise model with the antenna's transfer function and serves two main purposes: the engineering team can derive performance requirements for the elements of the flight and ground systems, and the science team can validate the **ISM** against the observation requirements. The following subsections describe the **ISM**, the instrument noise model, the instrument transfer function, the **ISM** validation and the noise model validation.

3.4.1. ISM Description

The noise model for the LISA instrument calculates the strain noise amplitude spectral density (ASD) $\sqrt{S_h(f)} = \tilde{h}(f) = 2\delta\tilde{L}(f)/L$ as the product of several terms:

$$\tilde{h}(f) = \sqrt{5} \frac{2}{\sqrt{3}} T(f) \frac{\sqrt{S_{\delta x, \text{IMS}}(f) + S_{\delta x, \text{DRS}}(f)}}{L} \quad (3.1)$$

where the measurement band is defined from 0.03 mHz to 1 Hz. This frequency range corresponds to the *goal*, whereas the *requirement* is for a smaller frequency band of 10^{-4} Hz to 1 Hz.

The crucial difference between the *requirement* and the *goal* lies in the testing and verification procedures: Performances are fully tested and verified against the *requirements*, whereas *goals* are observed only in terms of design and analysis, *i.e.* the mission design must allow for measurements over the wider frequency band. The distinction between goals and requirements is made to prevent excessive efforts on testing and verification, in particular at low frequencies.

The first term in equation (3.1), $\sqrt{5}$, results from averaging the antenna response over the full sky. The second term, $1/\sin(60^\circ) = 2/\sqrt{3}$, accounts for the projection effect of the equilateral triangular geometry of the detector onto the response of the optimum detector, which is an L-shaped Michelson interferometer. The sensitivity function $T(f)$, described in section 3.4.2, represents the conversion of single-link position uncertainty into the detector strain response, including the finite light travel time of the arm and time-delay interferometry (TDI), using the response of the Michelson X variable. The terms $\delta x_{\text{IMS}}(f)$, $\delta x_{\text{DRS}}(f)$, (or $S_{\delta x, \text{IMS}}(f)$ and $S_{\delta x, \text{DRS}}(f)$, respectively) and L are the power spectral density of the displacement noise from the measuring system, the power spectral density of the displacement noise from spurious accelerations on the test masses and the arm length of the interferometer, respectively. It must be noted that the noise contributions of the interferometric measurement system (IMS) and the disturbance reduction system (DRS) comprise not only some physical model of the noise, but also frequency-dependent factors to allow for a balanced allocation of the noise contributions. The LISA sensitivity model is plotted in figure 3.4.

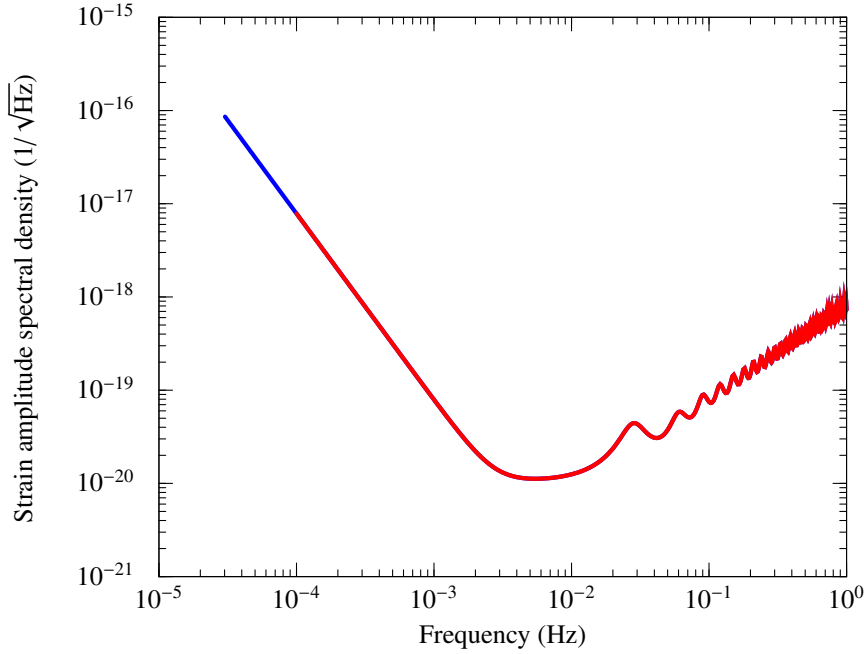


Figure 3.4.: *LISA Sensitivity Curve.* The strain amplitude spectral density of the Instrument Sensitivity Model is plotted. The required measurement bandwidth extends from 0.1 mHz to 1 Hz (red line), and as a goal is extended down to 0.03 mHz and up to 1 Hz (blue lines).

3.4.2. Instrument sensitivity function

The instrument sensitivity function $T(f)$ in section 3.4.1 describes the instrument's sensitivity due to the response to gravitational waves of different frequencies. Traditionally, transfer functions describe the response of a detector to an external stimulus, here gravitational waves. The sensitivity function is the *inverse* of the normal transfer function, as it describes the sensitivity rather than the response, *i.e.* how small the signal is allowed to be while still distinguishable from the noise. As LISA's response to gravitational waves depends in a complex way on the position of the source in the sky, the polarisation of the wave and its frequency, the sensitivity is conventionally averaged over all possible sky locations and polarisations. The instrument transfer function, as discussed in *e.g.* Schilling (1997) or Larson et al. (2000), is often written containing all the effects of the averaging, but it is clear that any transfer function can always be normalised to equal 1 at a given frequency and the remaining numerical factor be absorbed in the instrument sensitivity.

The choice made in this document is to normalise the sensitivity function at low frequencies, where it shows a flat frequency dependence, *i.e.* LISA's response does not depend on the frequency of the gravitational wave if that frequency is low enough. For high frequencies ($f > c/(2L)$), where L is the arm length, the response of LISA decreases and the sensitivity transfer function therefore increases. When the arm length L is an integer multiple of half of the wavelength of the gravitational wave, the effect of the wave on that arm vanishes. So only an effective arm length L_{eff} is affected by the gravitational wave, where L_{eff} is defined such that

$$L_{\text{eff}} = L - n \frac{\lambda_g}{2} \quad (3.2)$$

and n is chosen so that

$$n \frac{\lambda_g}{2} < L \leq (n + 1) \frac{\lambda_g}{2} \quad (3.3)$$

holds. The higher the frequency of the gravitational wave, and consequently the shorter its wavelength, the smaller the effective arm length becomes and the smaller the absolute change of the effective arm length becomes.

So, in general, a decrease proportional to $1/f$ of the response (and an increase proportional to f of the sensitivity) should be expected, with a transition between the constant part at low frequencies and the high

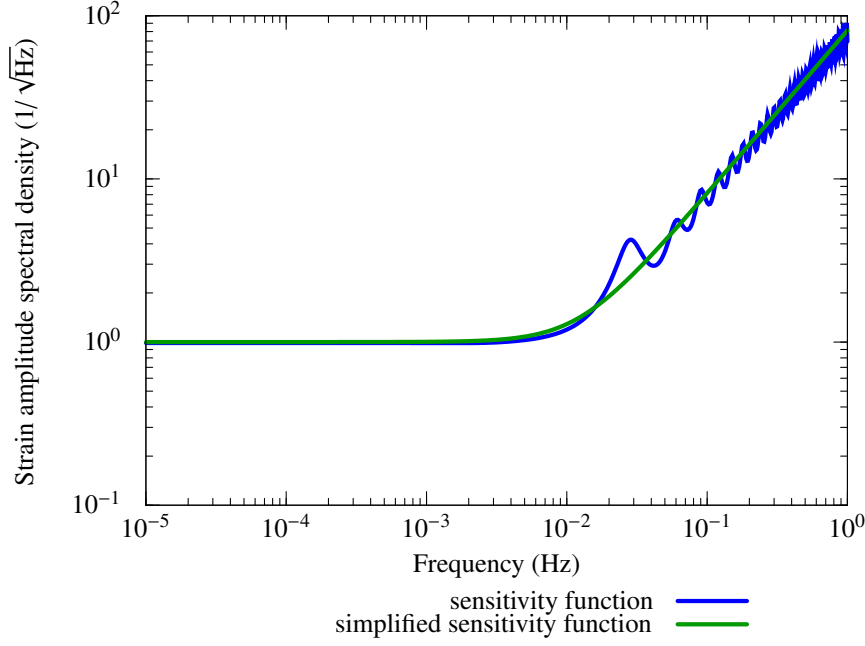


Figure 3.5.: Instrument sensitivity function and its simplified version (see equation (3.4)), relating the sensitivity of the instrument to a normalised gravitational wave strain to the frequency.

frequency decline at $f_0 = c/(2L)$. Furthermore, at frequencies where the wavelength of the gravitational wave is an exact integer multiple of the arm length, the effect in this arm vanishes, and in an interferometer with two identical arms, the overall effect vanishes, which would cause the sensitivity function to diverge. As gravitational waves from sources at different sky positions but same frequency have different angles of incidence on LISA, their effective wavelength, *i.e.* the wavelength projected on the arm, differs. This removes the divergence of the sensitivity function, however, it still increases by about a factor of 2 at these frequencies. Unfortunately, there is no simple analytic model of the instrument sensitivity function that accurately displays all its features. A numerical representation of the sensitivity function is plotted in figure 3.5. If the more complex structure at higher frequencies is not of interest, the following approximation can be used

$$T(f) \approx \sqrt{1 + \left(\frac{f}{af_0}\right)^2} \quad (3.4)$$

where $f_0 = c/(2L) = 30$ mHz and $a = 0.41$, leading to a corner frequency of about 12 mHz.

3.4.3. Instrument Noise Model

The single-link equivalent position uncertainty $\tilde{\delta x}_{\text{single-link}}(f)$ is expressed as an ASD which is the root of the sum of two terms – the displacement noise of the IMS, and the acceleration noise of the DRS, which is responsible for minimising the residual acceleration of the test masses:

$$\tilde{\delta x}_{\text{single-link}}(f) = \sqrt{S_{\delta x, \text{IMS}}(f) + S_{\delta x, \text{DRS}}(f)} \quad (3.5)$$

For each of the terms exists a *budget*, *i.e.*, the amount of noise permitted so that the science requirements can be fulfilled and an *allocation*, *i.e.* the amount of noise that a certain subsystem is foreseen to contribute, which differs from the budget by the system margin. In the following, the budget is given, the subsequent allocations, *i.e.* budget minus margin, are listed in table 3.3 and table 3.4.

The displacement noise amplitude spectral density $\tilde{\delta x}_{\text{IMS}}(f)$ for the uncertainty in the DRS is calculated from

an amplitude spectral density for the residual *acceleration* on each test mass

$$\tilde{\delta}a_{\text{DRS}}(f) = \Delta a_0 \times 10^{-15} \text{ m/s}^2/\sqrt{\text{Hz}} \times \sqrt{1 + \left(\frac{f}{f_H}\right)^4} \sqrt{1 + \frac{f_L}{f}} \quad \text{for } 3 \times 10^{-5} \text{ Hz} \leq f \leq 1 \text{ Hz} \quad (3.6)$$

with $\Delta a_0 = 3$, $f_L = 0.1$ mHz, and $f_H = 8$ mHz. The noise model of the acceleration contains a ‘‘reddening’’ factor $\sqrt{1 + f_L/f}$ to allow for noise sources at lower frequencies. The origin of that precautionary term lies with the fact that low frequency behaviour can only be assessed with extreme difficulties during ground demonstration, testing and verification. The factor $\sqrt{1 + (f/f_H)^4}$ relaxes the requirement to higher frequencies above f_H , as the sensitivity of LISA is reduced to higher frequencies anyway. The equivalent displacement noise amplitude spectral density is then given by:

$$\tilde{\delta}x_{\text{DRS}}(f) = 2 \frac{\tilde{\delta}a_{\text{DRS}}(f)}{(2\pi f)^2} \quad \text{for } 3 \times 10^{-5} \text{ Hz} \leq f \leq 1 \text{ Hz} \quad (3.7)$$

where the factor of two accounts for the presence of four test masses in the measurement of the difference in length of two arms, and the $1/(2\pi f)^2$ is the conversion from acceleration to position in Fourier space.

The displacement noise amplitude spectral density $\tilde{\delta}x_{\text{IMS}}(f)$ resulting from the uncertainty in the **IMS** is given by:

$$\tilde{\delta}x_{\text{IMS}}(f) = \Delta x_0 \times 10^{-12} \text{ m}/\sqrt{\text{Hz}} \times \sqrt{1 + \left(\frac{f_0}{f}\right)^4} \quad \text{for } 3 \times 10^{-5} \text{ Hz} \leq f \leq 1 \text{ Hz} \quad (3.8)$$

with $\Delta x_0 = 18$ and $f_0 = 2.8$ mHz. A sizable contribution to that noise is made up by shot-noise, whose (frequency independent) contribution is

$$\tilde{\delta}x_{\text{SN}}(f) = \sqrt{\frac{\hbar c}{2\pi} \frac{\lambda}{P_{\text{avail}}}} = 7 \text{ pm}/\sqrt{\text{Hz}} \sqrt{\frac{100 \text{ pW}}{P_{\text{avail}}}} \quad (3.9)$$

As the equivalent **DRS** displacement noise starts to dominate at lower frequencies, it allows us to relax the **IMS** displacement noise model below f_0 with $\sqrt{1 + (f_0/f)^4}$

3.4.4. **ISM** validation

The **instrument sensitivity model** is the core of the baseline requirements derived from the mission science. Since the observation requirements cannot be inverted for the required instrument performance, it is necessary to calculate the instrument performance with the **ISM** to verify that the observation requirements can be met. The process of verifying that the **ISM** will in fact enable the required observations is generically summarised in this section. This section is not intended to provide all technical details of the calculation, but rather give a sense of the undertaking. An extensive literature on the gravitational wave emission, propagation and detection has developed over the last thirty years. The desired products are predictions of the **SNR** in the detector and the uncertainty of source parameters extracted from the data, ideally the full posterior probability density functions (PDFs) for the chosen parameters. The number of extractable source parameters depends on the specific source, but may be as large as seventeen. Examples of parameters that might be extracted from the full waveform of a chirping binary are polar location (θ), azimuthal location (ϕ), inclination (i), polarisation (ψ), initial orbital phase (ϕ_o), coalescence time (t_c), luminosity distance (D_L), spin vectors (\vec{s}_1, \vec{s}_2) of both compact objects, chirp mass (M_c), and reduced mass (μ).

Generically, the process involves computing waveforms for the source of interest, taking account of the relative orientation and separation of the source and the detector, invoking the response of the detector with both astrophysical and instrumental noise, and taking into account the estimation of the many parameters in the signal. The **ISM** enters this process as the instrument response and noise.

This general process differs from source to source with assumptions and methodologies appropriate to the source being considered. A good example of this process for binary black holes in many of the observation

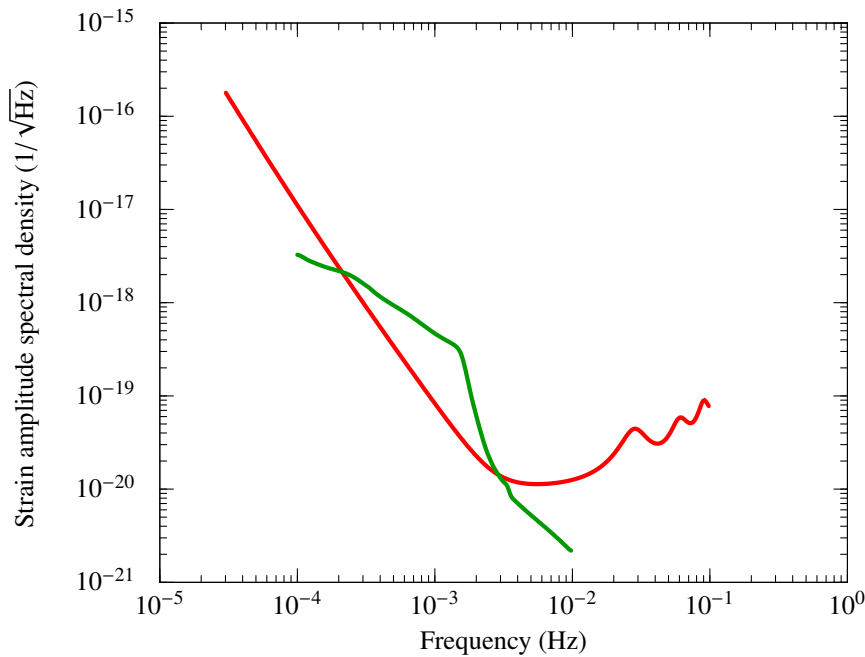


Figure 3.6.: *Standard instrument sensitivity model and binary confusion noise. The red curve is the product of the standard instrument noise model given above multiplied by the instrument transfer function shown in figure 3.5. The blue curve is the expected confusion noise threshold from galactic and extragalactic binaries.*

requirements is Lang and Hughes (2006). The **LISA International Science Team** (LIST) has carried out extensive calculations (Arun et al., 2009) to validate each observation requirement. The Science Requirement Document (**LISA-ScRD-066**) reviews the supporting calculations for each requirement.

Many considerations enter into the details of this process. For example where binaries are concerned, the mass ratios, redshift, spin and precession effects, merger and ring- down signals, sky and polarisation averaging, orbital eccentricity all affect choices in how the calculations are done. Background and burst detection pivots on still other considerations. The following assumptions are made for the calculations supporting the **LISA-ScRD-066**:

- Unless noted, only a single interferometer is used in the calculation. This is taken to add some redundancy against the risk of partial failure. Aside from conservative rate calculations, no other margin is carried in the science requirements.
- Both galactic and extragalactic binaries of compact stellar mass objects will be so numerous as to give confusion noise background at some level. Consequently, a complete noise model for the detection and parameter estimation process must include the astrophysical noise; figure 3.6 illustrates a typical model of the galactic confusion noise backgrounds relative to the **ISM** from section 3.4.1
- In all cases, the **ISM** is assumed to have no useful sensitivity below 0.03 mHz.
- Except where specific sources are known, these calculations usually average over sky position and orientation.

3.4.5. Noise Model validation

In LISA, requirements are closely connected to noise models. Complete and accurate noise models inform the allocation of requirements; the designer must know what can be achieved and judge the comparative difficulty of achieving different aspects of performance to balance competing requirements. So, while the previous subsection described how the performance of the **ISM** satisfies the science requirements, this subsection will address how the LISA Project will ensure that a realisable LISA instrument can meet or exceed the **ISM** performance.

The design of the LISA concept started with models for residual acceleration noise and displacement noise before a sensitivity curve or science requirements were formulated. The **ISM** is an allocation of residual acceleration noise and displacement noise informed by these detailed noise models. The flow-down of performance requirements (Tables 3.3 and 3.4) is also based on these detailed noise models. These models must

be demonstrably correct and complete. Their calculation must be correct to much better than the associated contingency, and no substantive effect must be missed.

This situation demands disciplined maintenance of noise models and current best estimates (CBEs) of effects and, most importantly, experimental validation wherever possible. As described below, laboratory measurements and results from the **LISA Pathfinder** (LPF) test campaigns are being used to validate the instrument noise model. LPF flight results will be an important, in some cases crucial, contribution.

In the frequency band of roughly 0.3 mHz to 3 mHz, the natural confusion foreground of gravitational waves from close binaries of compact stars in the Milky Way will dominate the instrumental noise (see figure 3.6). The origin of that astrophysical noise model is described in the last part of this section.

Laboratory Tests

High-level contributions to the displacement noise model are shown in table 3.3. They are explained in more detail in the *LISA Measurement Requirements Flowdown Guide* (LISA-MSE-TN-0001). The values given in the table are CBEs based on various combinations of measurements and calculations.

By mid-2010, most of the CBEs in table 3.3 have some basis in laboratory measurement. For example, the residual laser frequency error is a critical performance parameter for LISA; the final laser frequency noise must be reduced by nearly 11 orders of magnitude over the natural laser frequency noise. The CBE is validated by a demonstration of laser frequency prestabilisation in a candidate master oscillator laser, a measurement of frequency noise added by a candidate fibre amplifier and a system level demonstration of laser frequency noise suppression by application of TDI to data taken with a TRL 5 LISA phasemeter in a testbed simulating two LISA spacecraft (de Vine et al., 2010). The system level demonstration of the phase measurement sets substantial limits on unanticipated contributions to the displacement noise.

There are laboratory measurements in progress on pointing errors, telescope path-length stability, photoreceiver errors, residual laser frequency noise, residual clock frequency noise and phasemeter noise. Some laboratory measurements relevant to shot-noise (e.g., optical system efficiency) and experience-based estimates have already been made, and three independent models of scattered light are roughly in agreement.

High-level contributions to the residual acceleration noise model are shown in table 3.4 and are explained in more detail in the *LISA Measurement Requirements Flowdown Guide* (LISA-MSE-TN-0001). Comprehensive measurements of the contributions to the residual acceleration budget are more difficult. Most of the laboratory work has been done as part of the LPF development and testing, and is described in part in chapter 4. The torsion pendulum is the preferred tool to measure very small spurious forces in the 1 g laboratory environment. In addition to the LPF work, there have been several measurements of various thermal, pressure and electrostatic effects with specialised torsion pendulums. These measurements confirm the analytic models of these effects, and they rule out unanticipated forces as large as the allocation for “Miscellaneous Small Effects”.

LISA Pathfinder

LISA Pathfinder (LPF) contributes to the validation of the displacement and acceleration noise models in two ways: through validation during future flight operations and through extensive ground-test campaigns in the past and present development phase.

One of the top-level goals of LPF is to validate the acceleration noise model in a high-fidelity flight environment. The flight system incorporates an extensive set of environmental stimuli, actuators, and sensors that can be used to measure the response of the test mass to various disturbances. The master test plan foresees an extensive testing campaign to validate the error model. This ultimate validation awaits flight operations in 2013.

The development of the gravitational reference sensor (GRS) and interferometer for LPF has included an extensive campaign of test and verification on the ground. The status of the LPF flight hardware can be found in *The LISA Pathfinder Mission* (S2-EST-RP-1087). The results of the LPF ground testing of displacement noise and acceleration noise are too voluminous to include here.

The requirements on the LPF’s Optical Metrology System (OMS) differ from those on the LISA IMS; hence, the OMS noise model is not the same as the IMS noise model. However, the tests performed on the flight model of the LPF “X1” interferometer demonstrate that the requirements on the LISA local interferometer, i.e., the

Table 3.2.: Principal Science Requirements

| Quantity | Summary | Details |
|--|---|---|
| Measurement band | 0.1 mHz to 0.1 Hz | |
| Operational lifetime | 5 years | |
| Nominal arm length | 5×10^9 m | |
| Single link IMS displacement noise ASD | 18×10^{-12} m/ $\sqrt{\text{Hz}}$ at 3 mHz | $\tilde{\delta x}_{\text{IMS}}(f) = \Delta x_0 \times 10^{-12} \text{ m}/\sqrt{\text{Hz}} \times \sqrt{1 + (f_0/f)^4}$ for $\Delta x_0 = 18$ and $f_0 = 2.8$ mHz |
| Single test mass DRS acceleration noise ASD | 3×10^{-15} m/s ² / $\sqrt{\text{Hz}}$ at 3 mHz | $\tilde{\delta a}_{\text{DRS}}(f) = \Delta a_0 \times 10^{-15} \text{ m/s}^2/\sqrt{\text{Hz}} \times \sqrt{1 + (f/f_H)^4} \sqrt{1 + f_L/f}$ for $\Delta a_0 = 3$, $f_L = 0.1$ mHz, and $f_H = 8$ mHz |
| Strain ASD | 24×10^{-12} m/ $\sqrt{\text{Hz}}$ at 3 mHz | $\tilde{h}(f) = 2 \sqrt{5} T(f)/(L \sqrt{3}) \times \sqrt{S_{\delta x, \text{IMS}}(f) + S_{\delta x, \text{DRS}}(f)}$, where $T(f)$ is the sensitivity function representing the LISA sensitivity to a normalised gravitational wave strain |

interferometer between optical bench and test mass, can be fulfilled. This validates the optical bench pathlength stability contribution in table 3.3 and excludes unanticipated noise sources in the LISA local interferometer.

The **LPF GRS** is designed to meet the acceleration noise requirements of the LISA **GRS**. However, in the interest of cost containment, **LPF** requirements are relaxed an order of magnitude in both amplitude spectral density (3×10^{-14} m/s²/ $\sqrt{\text{Hz}}$) and frequency (1 mHz. . . 100 mHz). In general, **LPF** ground-testing with torsion pendulums and hollow test masses has shown that the spurious forces in table 3.4 associated with surface effects (e.g., thermal effects, pressure effects, patch fields) are as described by the error model. One exception was found: The residual gas pressure in the test mass housing gave rise to drag forces being applied to the test mass as the test mass moved ever so slightly with respect to the housing. This effect can be accommodated in **LPF** with unused margin. It will be remedied in LISA by a more stringent residual-gas requirement, achieved by venting to space. This illustrates the value of a vigorous validation programme based on both ground and in-flight measurements.

Astrophysical noise

The noise model for the astrophysical contribution from galactic binaries is not easily validated. The model in figure 3.6 is typical of those derived from Bender and Hils (1997). Since these binaries are faint, not enough have been observed electromagnetically to reliably establish their numbers, and hence the confusion level, from observations alone. Consequently, the confusion level is derived from population synthesis models, with some constraints from observations. There are reasons to believe that the model in figure 3.6 is a factor 3 to 10 too high, resulting in a conservative noise estimate. Observations made before LISA launches may provide much stronger constraints on the confusion noise level.

3.5. Performance Requirements

Table 3.2 provides the details of the principal science requirements. These requirements are derived from the **ISM** and the ensemble of observation requirements. The **ISM** – by virtue of being an analytical performance model of the LISA concept – can naturally be decomposed into performance requirements on the **IMS** and requirements on the **DRS**. Table 3.3 provides a flow-down of the noise budget to individual subsystems of the **IMS**, starting with the overall **IMS** displacement noise of 18 pm/ $\sqrt{\text{Hz}}$. Table 3.4 provides a flow-down of the **DRS** noise budget to individual components arising in the instrument and spacecraft (S/C), starting with the overall **DRS** acceleration noise of 3×10^{-15} m/s²/ $\sqrt{\text{Hz}}$. See the *LISA Measurement Requirements Flowdown Guide (LISA-MSE-TN-0001)* for additional details.

Contingency in science performance is contained in two places. The amplitude spectral density allocations for displacement noise and acceleration noise both include 35 % margin over the total subsystems budgets (see tables 3.3 and 3.4), held by Mission Systems Engineering. In addition, the science requirements are based on the

Table 3.3.: Summary of IMS Subsystem Noise Allocations

| Effect | Total per group | Sub-allocation | Comments |
|---------------------------------------|---|----------------|-----------------------|
| | $\times 10^{-12} \text{ m}/\sqrt{\text{Hz}} \sqrt{1 + (2.8 \text{ mHz}/f)^4}$ | | |
| Total IMS error/noise budget | 18 | | |
| Total of subsystem allocations | 11.7 | | RSS of subsystems |
| Subsystem allocations | | | |
| Shot noise | 7.7 | | 100 pW received power |
| Pathlength noise | 7 | | |
| Pointing errors | | 5.3 | |
| Telescope pathlength stability | | 1 | |
| Optical bench pathlength stability | | 4.5 | |
| Measurement noise | 5.4 | | RSS |
| Photoreceiver errors | | 3 | |
| Residual laser frequency noise | | 2 | |
| Residual clock frequency noise | | 2 | |
| Phasemeter noise | | 1 | |
| Intensity noise | | 1 | |
| Phase reconstruction | | 1 | |
| Stray light | | 2 | |

Table 3.4.: Summary of DRS Subsystem Noise Allocations

| Effect | Total per group | Sub-allocation | Comments |
|--|--|----------------|-------------------|
| | $\times 10^{-16} \text{ m/s}^2/\sqrt{\text{Hz}} \sqrt{1 + (f/8 \text{ mHz})^4} \sqrt{1 + 0.1 \text{ mHz}/f}$ | | |
| Total acceleration noise budget | 30 | | |
| Total of subsystem allocations | 19.5 | | RSS of subsystems |
| Electrostatics | | 12.0 | |
| Brownian | | 9.1 | |
| S/C magnetic | | 7.0 | |
| S/C coupling | | 6.0 | |
| S/C cross-coupling | | 4.5 | |
| Thermal | | 4.0 | |
| Interplanetary magnetic | | 4.0 | |
| Misc small effects | | 4.0 | |

assumption that only four of the six links are working. Six links are required in the design and delivery, but only four are required to operate for the mission lifetime. Six links operating for the baseline lifetime are a goal. The extra two links give better performance that varies from source to source, but is generally a factor of $\sqrt{2}$ increase in SNR.

The joint ESA/NASA project team has investigated possibilities for reducing the complexity of the mission and for savings and descopes, and the LIST evaluated the consequences for the science products. The current LISA baseline is nearly optimal in the sense that changes in the baseline architecture would cause the science return to drop precipitously while incurring only modest savings (Stebbins, 2009).

4. Payload

The top-level requirement for the LISA payload is that it has to enable gravitational wave (GW) detection at low frequencies with the strain sensitivities shown in table 4.1.

The values are given in terms of a spectral density of the gravitational strain measurement, where the strain sensitivity h is a measure for the gravitational wave amplitude and is proportional to the relative arm length change: $h = 2\delta L/L$. Here, L is the arm-length expressed in m and δL the arm-length variation in $\text{m}/\sqrt{\text{Hz}}$. At high frequency, the sensitivity is dominated by the LISA interferometric measurement system (IMS) that has to provide an absolute accuracy in the range of $10 \text{ pm}/\sqrt{\text{Hz}}$ for a single arm laser link. At low frequencies, the disturbance reduction system (DRS) dominates the sensitivity. The equivalent displacement noise corresponds to an acceleration noise of $3 \times 10^{-15} \text{ m/s}^2/\sqrt{\text{Hz}}$.

The accurate determination of arm length variations is complicated by the fact that the shape of the formation triangle undergoes residual seasonal changes which cannot be completely removed by orbit optimisation. These changes not only affect the nominal 60° between the lines of sight, but also the so called point-ahead angle, which describes the offset between received and transmitted beam for each individual spacecraft (S/C). This offset is required to account for the comparatively long travel time $L/c \approx 16.7 \text{ s}$ of the laser light to the respective remote S/C.

The combination of picometre resolution, a transmission path of $5 \times 10^6 \text{ km}$ and the need for active elements in the optical science chain makes the physical realisation of the LISA metrology system extremely challenging and has severe implications for the design of all associated subsystems:

Laser Metrology System Measurement noise and the required distance between S/C imposes stringent requirements on the laser-interferometer system, which will have to exhibit very high stability, reliability and power efficiency.

Thermal Control Both the measurement system and the test masses must be protected from thermal noise and gradients that could swamp the signal from gravitational waves. The thermal environment of the payload must be extremely stable, and thus requires that the payload is thermally decoupled from the S/C.

Structural and Mechanical A very stiff and stable structure will be required such that mHz-level disturbances are avoided. This could preclude or limit the use and operations of mechanical components that will introduce mHz-level noise, such as mechanically steered antennas on the communication subsystem.

Propulsion System Reaction propulsion systems obviously produce vibration when they operate: a system must be used that is essentially vibration-free, and produces smooth thrust levels in a force range compatible with the goal of drag-free control for the S/C (*i.e.* capable of compensating, at a minimum, solar-radiation pressure on the S/C structure). Field-emission electric propulsion (FEEP) is the only propulsion concept

Table 4.1.: LISA measurement sensitivity requirements (see chapter 3), design sensitivity, and allocation to the DRS and IMS (adapted from LISA-ASD-BR-5002). The design sensitivity shows a margin of at least 25 % with respect to the requirements. Note that the numbers at $30 \mu\text{Hz}$ refer to a goal.

| Frequency (mHz) | Sensitivity ($1/\sqrt{\text{Hz}}$) | | Displacement ($\text{pm}/\sqrt{\text{Hz}}$) | | |
|--------------------|--------------------------------------|-----------------------|---|---------|--------|
| | required | designed | single link | DRS | IMS |
| 0.03 | 1.9×10^{-16} | 1.2×10^{-16} | 232 453 | 231 323 | 22 900 |
| 0.1 | 1.2×10^{-17} | 6.3×10^{-18} | 12 147 | 11 971 | 2062 |
| 1 | 9.1×10^{-20} | 7.2×10^{-20} | 138 | 136 | 23.8 |
| 5 | 1.1×10^{-20} | 6.0×10^{-21} | 10.7 | 5.0 | 9.5 |
| 10 | 1.2×10^{-20} | 6.2×10^{-21} | 9.3 | 1.1 | 9.3 |
| 100 | 7.7×10^{-20} | 4.0×10^{-20} | 9.4 | 0.0 | 9.4 |
| 1000 | 7.6×10^{-19} | 3.7×10^{-19} | 8.9 | 0.0 | 8.9 |

compatible with the requirements on the thrust level and the noise constraints for LISA.

Electromagnetic The measurement instrumentation and test masses must be shielded from EMC disturbances: this leads to the requirement for extremely strict policing of the electrical and magnetic components of the S/C, and the EMC environment due to the natural space environment and secondary effects such as charging.

Gravitational The gravitational environment of the test masses must be carefully considered: this includes the direct gravity gradient forces due to relative movement between the test masses. Additionally, the self-gravity environment of the S/C must be carefully analysed and designed to ensure that the summed gravity field at the test masses does not interfere with the GW measurement. Additionally displacement of S/C elements (such as mechanically steered antennas) will have to be carefully analysed to assess their impact on the self-gravity field of the S/C.

Test Mass Control Although the test masses are essentially free-flying, there are two on each S/C. This fact, coupled with the requirement that they maintain their orientation with respect to the line of sight (LOS) of the telescopes means that a certain degree of test mass control is necessary, as the S/C cannot accommodate two free-flying objects at once. The test mass control is provided through electrostatic actuation from the test mass cage.

Autonomy The spacecraft must possess a substantial degree of autonomy due to the frequent periods where communication with the ground segment is not possible. This autonomy extends to the ability to communicate with the other S/C in the constellation, and perform autonomous science operations. This requirement for autonomy and operations within a constellation heavily influences the subsequent choice of the data-handling architecture selected for the S/C.

This chapter gives only a brief overview of the LISA payload design, for a full description, please refer to *Payload Preliminary Design Description (LISA-ASD-DD-3001)*.

4.1. Optical System

The optical system of LISA contains all the optical components that are needed for the interferometry and the required support. More specifically, each spacecraft houses one *optical assembly* (figure 4.1, lower row) that consists of two units (figure 4.1, upper row), each consisting of the *optical bench*, the *telescope*, and the *gravitational reference sensor* as well as the associated mounting structures.

The optical bench is mounted parallel to the primary mirror of the telescope, requiring a non-planar beam path, where the light from the optical bench to the telescope has to be directed “up” to the telescope. Whereas the gravitational reference sensor (GRS) is mounted behind the optical bench such that the light from the optical bench to the GRS has to pass through the optical bench (“down”), also resulting in a non-planar beam path.

4.1.1. Optical bench

The main function of the optical bench is to direct the various laser beams to the relevant positions in 3-dimensional space, to bring beams together for interference, and provide stable mechanical support to the electro-optical components such as photodiodes and CCD sensors without adding any significant noise to the measurement path (figure 4.4). The primary optical bench requirement is that the pathlength noise induced by the components on the optical bench should not exceed $1 \text{ pm}/\sqrt{\text{Hz}}$ at frequencies above 3 mHz.

The optical bench is constructed using the same techniques employed in the construction of the optical bench for the LISA Pathfinder technology package (LTP) experiment on board *LISA Pathfinder* (LPF) (Braxmaier et al., 2004; Killow et al., 2006; Middleton et al., 2006). The optical bench is constructed from a block of Zerodur ceramic glass with a diameter of approximately 560 mm, with fused silica mirrors and beamsplitters bonded to the bench using hydroxy catalysis bonding (Elliffe et al., 2005), a technology first developed for the GP-B mission (Gwo, 1998; Turneure et al., 2003). This technology has found broad applications in ground-based gravitational wave detectors (Amico et al., 2002; Smith et al., 2003) as well as in LPF (Elliffe et al., 2005) due to its excellent properties regarding dimensional stability of the components and rigidity and durability of the bond itself.

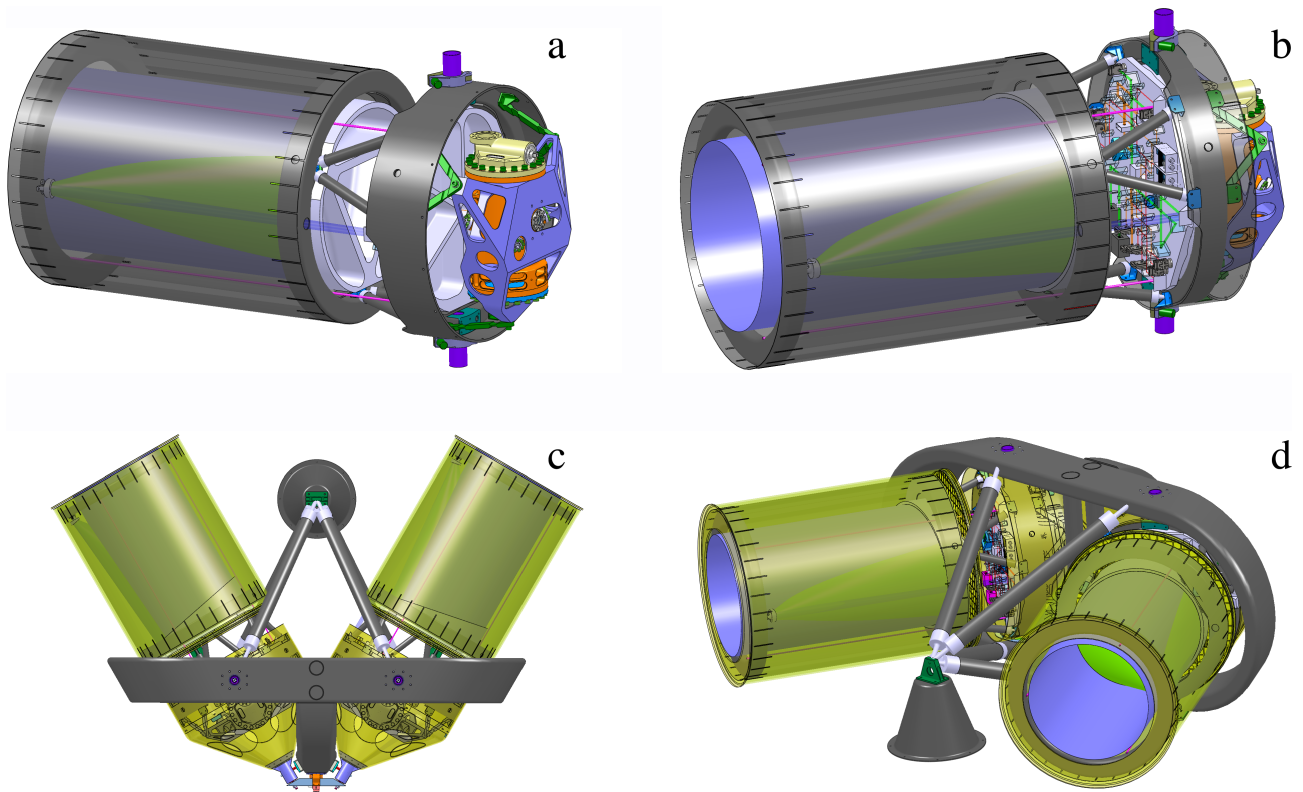


Figure 4.1.: *Optical assembly. Telescope with optical bench attached (upper row). The optical bench is orthogonal to the telescope axis with the optical components facing the back of the primary mirror of the telescope (panel a). The gravitational reference sensor is attached behind the optical bench (panel b) to a support ring also holding the optical bench. A support structure takes the two sub-units (lower row), forming the optical assembly. The angle between the two telescopes is nominally 60° , but can be varied by $\pm 1.5^\circ$ using the optical assembly tracking mechanism (panel c)*

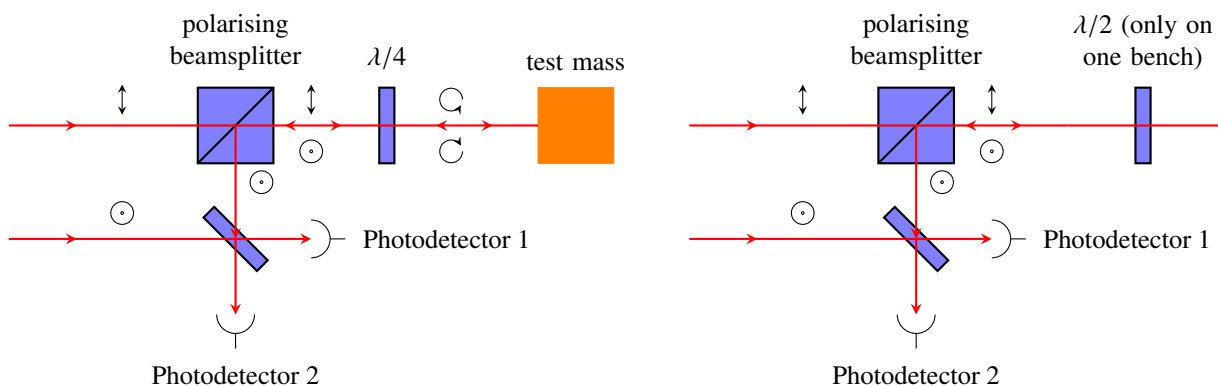


Figure 4.2.: *Separation of incoming and outgoing beam through polarisation in the test mass interferometer (left panel) and in the send/receive path of the telescope (right panel). The test mass interferometer employs a quarter-wave plate to rotate the polarisation, in the send/receive path only one optical bench has a half-wave plate.*

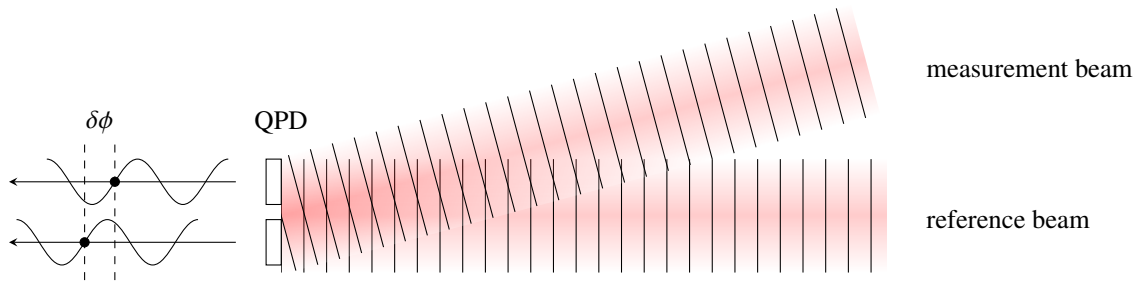


Figure 4.3.: *Differential wavefront sensing. The angle between reference beam and measurement beam causes a phaseshift $\delta\phi$ between the signals in the different quadrants of the QPD.*

While Zerodur has the advantage of a very low coefficient of thermal expansion (CTE) of about 2×10^{-8} , it is quite brittle, and care has to be taken to restrict the mechanical load on the bench by an appropriate design of the surrounding structure. The necessary expertise has been developed during the construction of the optical bench for **LTP**. The few differences between the construction of the optical bench for LISA with respect to the optical bench for **LPF** lie in the use of polarising components for LISA (requiring mounting technology for the different optical materials), and in the inclusion of mechanisms on the optical bench such as the point-ahead actuator. In addition, LISA requires non-planar optical paths, as the telescope and the **GRS** are placed “above” and “below” the optical bench.

Interferometric measurement techniques

The interferometric measurements in LISA are based on heterodyne interferometry, where two laser beams with respective frequencies ν_0 and $\nu_0 + \Delta\nu$ are combined to yield a beat note with the frequency $\Delta\nu$, the phase of which is then detected. Measurements of longitudinal displacements can be performed by directing the combined light on a single element photo detector, whereas for the measurements of angular displacements, *differential wavefront sensing* (Heinzel et al., 2003) is needed. Here, the quadrant photodetector (QPD) and the differential phase between the signals from the different quadrants is used to determine the angle of the wavefront arriving at the photodiode (see figure 4.3). In practise, taking the sum of the signals from the **QPDs** is used to emulate a single element photodetector so that one photodetector can measure both angular displacements and the longitudinal displacement simultaneously.

All the interferometers on the optical bench (science, test mass, reference, point ahead mechanism, and optical truss) are read out by two photodetectors, located at the output ports of the combination beamsplitters, providing redundancy and an increase of the signal-to-noise ratio by a factor of $\sqrt{2}$ in the nominal case, *i.e.* with both detectors working.

Science interferometer

The science interferometer (figure 4.4, panel d) measures the distance between optical benches (*i.e.* **S/C**) located at opposing ends of a constellation arm. The primary laser associated to that optical bench (depicted in red in figure 4.4, panels a and d) provides the reference beam (or local oscillator) for the science interferometer, hence part of the light is split off after the beam expander and its polarisation rotated by 90° , via a half-wave plate, to match the polarisation of the received beam. The light received from the far spacecraft (≈ 280 pW) enters through the telescope and is directed to the optical bench via the telescope back optics, directly to the science interferometer, where about 100 pW reach each detector.

While the optical benches are designed to be as identical as possible, the polarisation multiplexing scheme causes a slight difference, as one of the optical benches on a spacecraft will have a half-wave plate in the transmit/receive path whereas the other does not. An alternative scheme with the beam in free space being either

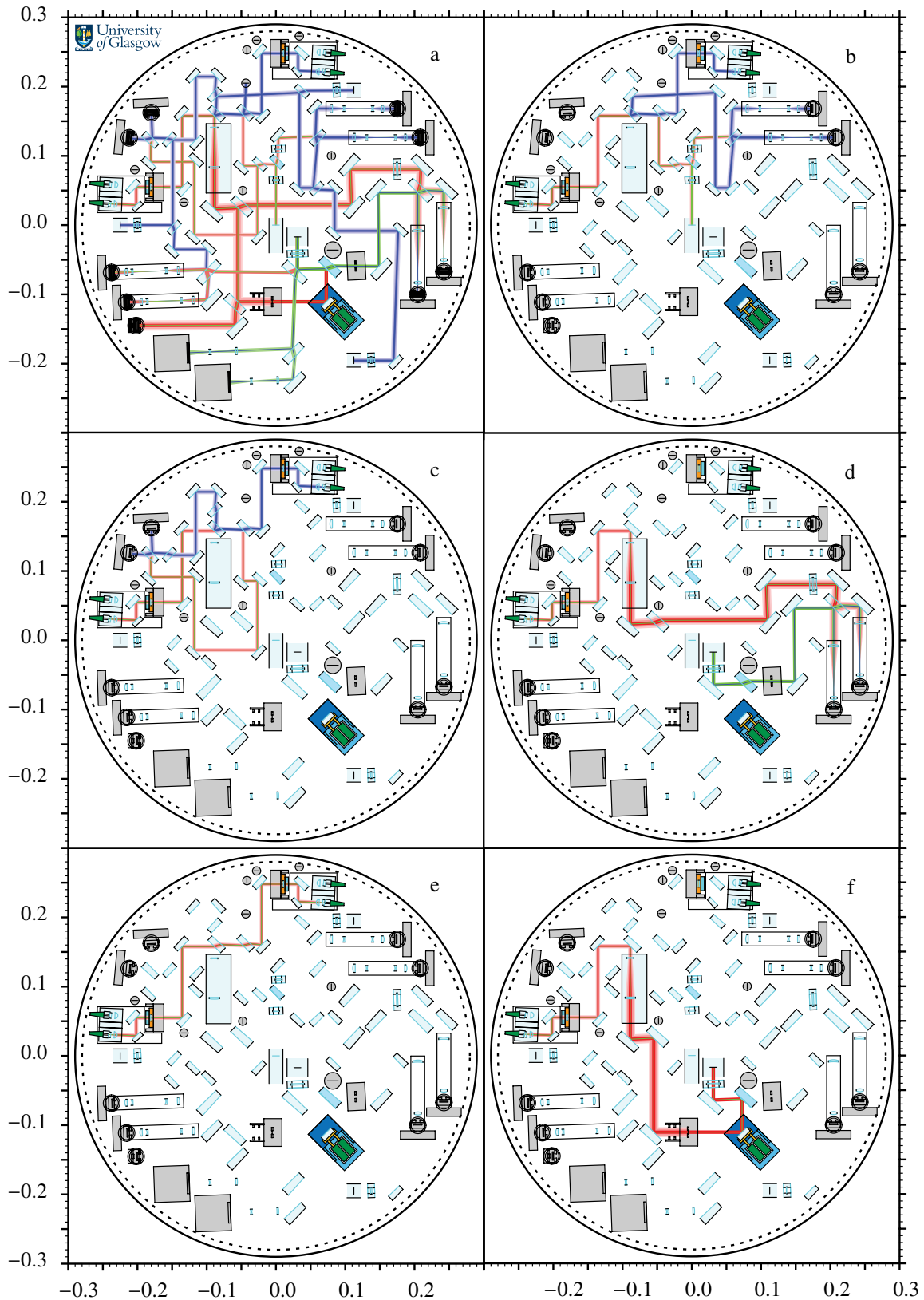


Figure 4.4.: *Optical bench design with all the light beams drawn (panel a); the test mass interferometer with the local oscillator (blue) and the light sampling the position of the test mass passing through the OB (orange) (panel b); only the reference interferometer with the light from the two different lasers (panel c); only the science interferometer with the local oscillator (red) and the beam received from the other S/C (green, panel d); passing the light from one laser to the other optical bench (panel e); and the light transmitted to the other S/C via the telescope, passing through the beam expander and through the OB (panel f).*

circularly polarised or under 45° is under investigation.

Test mass interferometer

The test mass interferometer is used to determine the position of the test mass of the GRS with respect to the optical bench. The measurements from the test mass interferometers on the transmitting and the receiving optical bench are combined with measurements from the science interferometer to perform the measurement of the distance between the free-falling test masses. Thus, the test mass interferometer provides an integral part of the science measurement; its performance will be demonstrated on LPF.

For the test mass interferometer, the reference beam is taken from the secondary laser (blue in figure 4.4, panel b) and the measurement beam (orange) from the primary laser. The measurement beam is directed through the optical bench to the test mass situated in the gravitational reference sensor at the backside of the optical bench. The test mass acts as a mirror and reflects the measurement beam back to the optical bench. Separation of the beam going to the test mass and the reflected beam is again done through polarisation. This scheme is different from the setup used in LTP which relies on a geometrical separation of the two beams (Heinzel et al., 2003). In LISA, an additional quarter-wave plate is therefore needed that is passed twice by the light, effectively resulting in a rotation of the polarisation by 90° . Another half-wave plate rotates the polarisation of the measurement beam back by 90° to coincide with the polarisation of the reference beam and allow the beams to interfere. The impact of these additional polarising components on the pathlength stability has been experimentally checked and found to be negligible (Dehne et al., 2009).

The test mass interferometer provides information on both longitudinal movement of the test mass with respect to the optical bench (and hence the spacecraft) and rotation through differential wavefront sensing. The readout of the test mass interferometer will therefore be used to feed into the control law of the DRS, augmenting the signals from the capacitive readout (see section 4.4).

Reference Interferometer

The reference interferometer (figure 4.4, panel c) provides information on the frequency noise of the primary laser with respect to the secondary laser and its output signal of this interferometer is used to provide an error signal for the phase-locking of the primary and the secondary laser. It also provides a phase reference for the other interferometers, thus allowing to cancel disturbances that do not originate on the optical bench, *e.g.* in the fibres that deliver the laser beams.

Optical truss

The optical truss interferometry is a method to assess the stability of the telescope structure (see section 4.1.2) on orbit. The interferometers consist of three pick-off mirrors separated by 120° on the mounting structure of the secondary mirror of the telescope, each using a sample of the outgoing light for a measurement beam. A beamsplitter and photo detector are co-located with the sampling mirror, while the reference beam is taken from the secondary laser on the optical bench. Taking the measurements at three points allows to reconstruct the alignment of the wavefront of the outgoing light as is needed for diagnosis and correction in post-processing.

Point-ahead angle mechanism

The point-ahead angle mechanism (PAAM) compensates for the angle between the transmitted and received beams. The angle between the beams is due to the fact that the velocity of the far spacecraft has a component perpendicular to the line of sight, *i.e.* the far spacecraft appears to move sideways. This component changes amplitude and direction over the course of time, causing a time-varying angle between transmitted and received beam. Any constant angle could be taken out by a pre-launch alignment process, however, the variation in the angle makes an on-orbit mechanism necessary, as a varying angle between the measurement beam and the local oscillator degrades the contrast on the photo detectors.

The breathing angle can be decomposed into two components, projected into the plane of the constellation (γ_{\parallel}) and perpendicular to it (γ_{\perp}). Most of the constant angle of about $3.32 \mu\text{rad}$ is in the plane of the constellation,

Table 4.2.: Requirements on the point-ahead angle mechanism (PAAM).

| | Requirement |
|-------------------------------|---|
| Dynamical range | $\pm 700 \mu\text{rad}$ |
| Optical path-length stability | $3 \text{ pm}/\sqrt{\text{Hz}} \times \sqrt{1 + \left(\frac{3 \text{ mHz}}{f}\right)^4}$ |
| Angular stability | $16 \text{ nrad}/\sqrt{\text{Hz}} \times \sqrt{1 + \left(\frac{3 \text{ mHz}}{f}\right)^4}$ |

whereas most of the variation (but very little offset) is out of the plane and amounts to about $\pm 6 \mu\text{rad}$ over the course of one year, which, after the magnification of the telescope, equates to $\approx 480 \mu\text{rad}$ on the optical bench. The in-plane offset is taken care of by pre-launch alignment and the in-plane variation is small enough (of orders nrad) to not cause discernible loss of contrast. The out-of-plane component, however, requires on-orbit correction. It is worthwhile noting that due to the fact that the optical bench itself is perpendicular to the plane of the constellation, the out-of-plane angle γ_{\perp} actually lies *in* the plane of the optical bench, so that the necessary correction keeps the optical path planar. As the angle depends only on the orbital dynamics of the constellation, it can be predicted with high accuracy and the necessary commands for the PAAM can be uploaded to the spacecraft well in advance, so that no closed-loop controller is foreseen. However, should it be necessary, such a closed loop controller can be implemented by evaluating the wavefront at the receiving spacecraft and the orientation of both sending and receiving spacecraft.

Situated on the optical bench, the PAAM is exposed to the full magnification of the telescope ($\times 80$), so that the range of the point-ahead mechanism needs to be $\pm 480 \mu\text{rad}$ for the nominal case or $\pm 700 \mu\text{rad}$ including margin. Furthermore, the PAAM is unavoidably in the optical path of the science interferometer, so it has to fulfil stringent requirements (see table 4.2) on the path-length noise it introduces; the optical path-length noise has to be smaller than $3 \text{ pm}/\sqrt{\text{Hz}}$ for frequencies above 3 mHz. The angular jitter noise of the mechanism is required to be smaller than $16 \text{ nrad}/\sqrt{\text{Hz}}$ for frequencies above 3 mHz. Here, the telescope magnification works in favour of a less stringent requirement, as the angular jitter of the transmitted beam is reduced by the telescope magnification. The point-ahead angle and the optical path-length error are monitored through dedicated metrology on the optical bench, allowing to implement a local control of the PAAM.

The solutions currently developed for the PAAM both depend on monolithic designs (Haberland hinge (Haberland, 1981) and bending flexures, respectively) that have no freely rotating axis but translate elastic deformation of thin blades into a rotation. This allows to achieve very little friction and hysteresis for the rotation while keeping a high stiffness in the other degrees of freedom. Both designs have demonstrated compliance with the requirements and have been successfully tested.

4.1.2. Telescope

The telescope foreseen for LISA is an off-axis telescope with a 40 cm aperture, a mechanical length of about 60 cm, and a field of view of $\pm 7 \mu\text{rad}$ out-of-plane and $\pm 4 \mu\text{rad}$ in plane in which the most stringent wavefront requirements have to be met. With an off-axis telescope, the requirements on stray light are easier to achieve than for a telescope with a secondary mirror in normal incidence. Additionally, the off-axis design has the advantage of not blocking part of the incoming light, thus allowing more light for the measurement process and resulting in less wavefront distortion.

The size of the telescope's aperture is determined by the amount of light power needed to achieve a given sensitivity, as its size determines both the widening of the beam due to diffraction and the amount of laser power collected from the received beam. As a rough guideline, the displacement noise due to shot noise for a telescope with diameter D , a laser with power P_0 , wavelength λ and "optical efficiency" ϵ (*i.e.* the ratio between the power sent out by the telescope and the power delivered to the optical bench), and a distance between the S/C of L is

Table 4.3.: Main requirements on the telescope. The full field of view is required for acquisition. The wavefront quality is required only for the smaller field of view in the science mode.

| Characteristics | Requirement |
|-------------------------------------|--|
| Aperture | 40 cm |
| Optical efficiency | ≥ 0.853 |
| Field of view | |
| acquisition mode | 400 μ rad full angle |
| science mode (out of plane) | $\pm 7 \mu$ rad |
| (in plane) | $\pm 4.2 \mu$ rad in-plane |
| Optical pathlength stability | $1 \text{ pm}/\sqrt{\text{Hz}} \times \sqrt{1 + \left(\frac{3 \text{ mHz}}{f}\right)^4}$ |
| Magnification | 80 |
| Far-field wavefront quality | $\lambda/20$ |

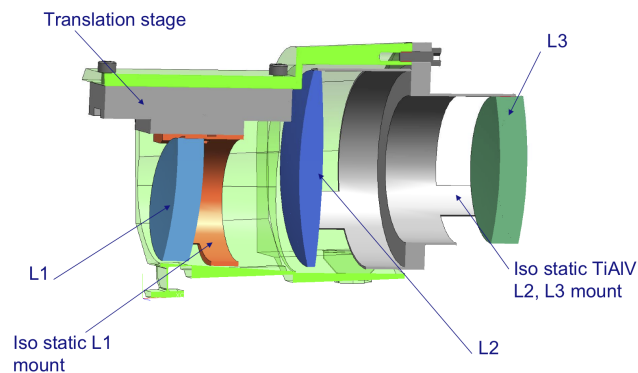
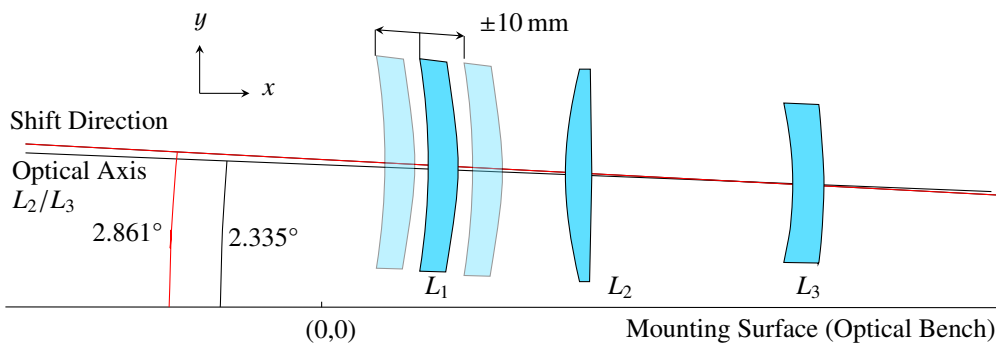


Figure 4.5.: Upper panel: Refocusing mechanism, industrial concept (EADS Astrium). Lower panel: Design of Refocusing mechanism (TNO)

given by

$$\widetilde{x}_{\text{SN}} = 8 \times 10^{-12} \left(\frac{\lambda}{1064 \text{ nm}} \right)^{\frac{3}{2}} \left(\frac{0.25 \text{ W}}{\epsilon} \frac{1.2 \text{ W}}{P_0} \right)^{\frac{1}{2}} \left(\frac{L}{5 \times 10^9 \text{ m}} \right) \left(\frac{0.4 \text{ m}}{D} \right)^2 \text{ m}/\sqrt{\text{Hz}} \quad (4.1)$$

A diameter of 40 cm results in an equivalent pathlength noise due to shot-noise of about $8 \text{ pm}/\sqrt{\text{Hz}}$, the dominating contribution to the noise budget at frequencies above 3 mHz.

With a magnification of the telescope of 80 and a diameter of the outgoing beam of 400 mm, the input beam to the telescope has a diameter of 5 mm. A beam expander, situated on the optical bench (figure 4.4), matches the typical beam diameter on the optical bench (1 mm) to the diameter required by the telescope. Equally important as the telescope's ability to gather light is the quality of the wavefront leaving the telescope. An ideal, perfectly spherical wavefront with its centre at the position of the test mass would render the measurement of the optical pathlength insensitive to any pointing jitter of the sending spacecraft. Any deviation from such an ideal wavefront, however, will translate a spacecraft jitter into an equivalent pathlength noise. As the wavefront errors depend critically on the position of the beam waist with respect to the telescope, the telescope can be refocused on orbit by adjusting the position of two lenses in the telescope "back-optics". Additionally, the back-optics images the exit pupil of the telescope to the test mass, the photodetectors of the science interferometers and the PAAM, minimising the effect of spacecraft rotation on the science measurement.

An additional complication arises from the fact that the telescopes for LISA form part of the interferometric path of the science interferometer. Any change in optical pathlength between, *e.g.*, the primary and secondary mirror, directly contributes to noise degrading the science signal. To reduce the impact of any geometrical distortions, the optical truss interferometry (see section 4.1.1) can be used to directly measure the wavefront and phase of the outgoing beam for later correction in post-processing.

4.1.3. Optical assembly tracking mechanism

In addition to the time variation of the angle between the received and the transmitted beams, the angle between the two telescopes on board one spacecraft changes over time as well. Nominally 60° , it varies by about 1.5° over the course of a year due to orbital mechanics. To compensate for that variation, a mechanism that changes the angle between the two telescopes is required, the so-called optical assembly tracking mechanism (OATM), as can be seen in the lower left of figure 4.1, connecting the rear ends of the two single assemblies. The OATM acts upon the complete assembly of GRS, optical bench and telescope, rotating the assembly around an axis perpendicular to the plane of the constellation. This way, the OATM is *not* part of the optical path of an interferometer, therefore requiring much less care with regard to introducing translations in addition to rotations. The angular jitter contributes to the spacecraft pointing jitter which is controlled to a few nrad/ $\sqrt{\text{Hz}}$ by the DFACS system.

4.2. Laser System

The detailed specifications for the laser subsystem can be found in *Laser subsystem specification (LISA-ASD-RS-3400)*.

The laser system currently envisaged for LISA makes use of the Master Oscillator Fibre Power Amplifier (MOFPA) approach (Weßels et al., 2002; Zawischa et al., 1999). For LISA, the low-power master oscillator is largely identical to the laser used by the LTP experiment on board LPF (McNamara et al., 2008), a Nd:YAG non-planar ring oscillator (NPRO) pumped by an internally redundant, fibre-coupled arrangement of laser diodes. The LTP laser is manufactured by Tesat GmbH (Bartelt-Berger et al., 2001), emitting 40 mW of 1064 nm light and has been used in a similar configuration as proposed for LISA on board the TerraSAR-X and N-Fire satellites (Lange and Smutny, 2004; Roth and Werninghaus, 2006; Sodnik et al., 2006).

The light of the NPRO passes an optical isolator to suppress optical feedback and is coupled into two optical single-mode fibres, the smaller fraction of the light is taken to be used for prestabilisation purposes, the larger fraction fed into a fibre-based electro-optical modulator (EOM) that imprints phase modulation sidebands used for clock-transfer and ranging. From there, it enters a double-clad fibre amplifier, pumped by a redundant array

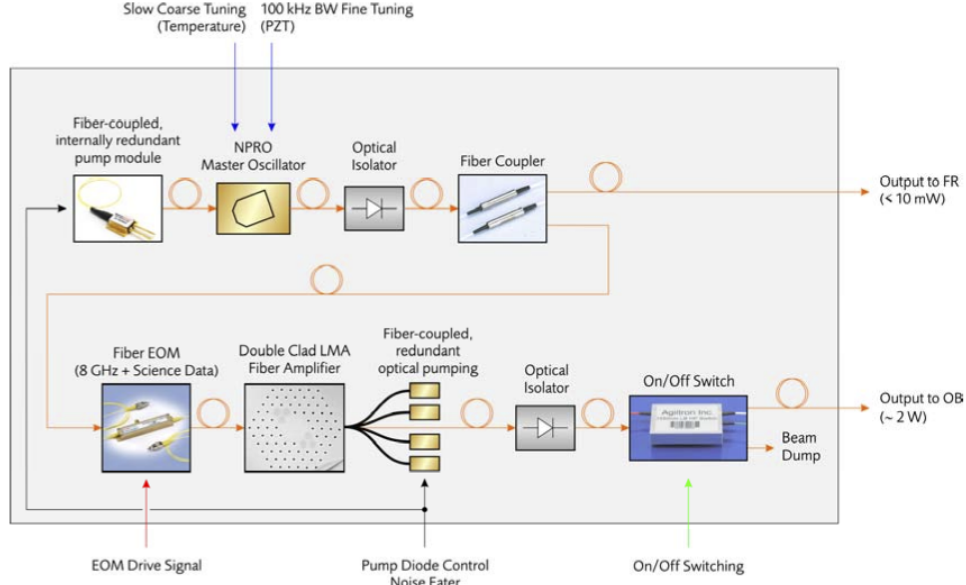


Figure 4.6.: Baseline architecture for the laser system. The output of a diode-pumped NPRO laser (~ 50 mW) is amplified by a double-clad fibre amplifier to the required 2 W. A fibre-coupled EOM imprints communication signals on the low-power light to avoid thermal stress or damage to the EOM. Courtesy of EADS Astrium.

of fibre-coupled laser diodes, bringing the laser power up to the required 2 W. After passing another optical isolator and an on/off switch controlled by the spacecraft computer, the light is then delivered via an optical fibre directly to the optical bench (figure 4.6).

The laser system is fully redundant, providing two identical, assemblies that feed into a fibre switcher on the optical bench that in the case of a laser failure will be used to switch over to the redundant laser without compromising the alignment on the optical bench.

As polarisation encoding is used in LISA to distinguish transmitted from received light (see 4.2), the light entering the optical bench needs to be linearly polarised. This is ensured by a polariser as the first component on the optical bench. To avoid unnecessary stray-light, 98 % of the light power arriving on the optical bench needs to be in the linear polarisation transmitted by the polariser.

The position of the test masses is read out interferometrically in the test mass interferometer, using the test masses as a mirror. Thus, the requirement on the permissible acceleration noise for the test masses leads to a requirement on the power stability of the laser, as a variation in laser power δP causes a variation in radiation pressure on the test masses and therefore a variation in the acceleration δa

$$\delta a = \frac{2\delta P}{mc} \quad (4.2)$$

Consequently, the relative intensity noise (RIN) $\widetilde{\delta P}/P$ for the laser has to be smaller than $10^{-3}/\sqrt{\text{Hz}}$ in the LISA band, given the allocated acceleration noise of $\widetilde{\delta a} = 3.4 \times 10^{-16} \text{ m/s}^2/\sqrt{\text{Hz}}$ and an absolute power of $100 \mu\text{W}$ for the readout of the test mass. A summary of the requirements on the laser at end-of-life is given in table 4.4.

4.2.1. Laser frequency noise suppression

Frequency stabilisation of the lasers is a vital part of the LISA measurement scheme. As in any interferometric length measurement, a frequency noise $\delta \nu$ causes an equivalent noise in the length measurement δx that is proportional to the difference of optical pathlength ΔL and the fractional frequency noise.

$$\delta x = \Delta L \frac{\delta \nu}{\nu} \quad (4.3)$$

Table 4.4.: Laser requirements, specified at end-of-life.

| Requirement | |
|---------------------------------------|---|
| Wavelength | 1064.5 nm |
| Output power (EOL) delivered to OB | 2 W 1.2 W |
| Polarisation | linear, containing more than 98 % of optical power in main polarisation |
| Fractional power stability | $10^{-3} / \sqrt{\text{Hz}}$ in the LISA band |

Table 4.5.: Frequency stabilisation requirements

| Stabilisation stage | Performance after stabilisation in Hz/ $\sqrt{\text{Hz}}$ |
|---------------------|---|
| Free running | $\frac{10^4}{f}$ |
| Pre-stabilisation | $\frac{280}{f} \times \sqrt{1 + \left(\frac{2.8 \text{ mHz}}{f}\right)^4}$ |
| Arm locking | $0.3 \times \sqrt{1 + \left(\frac{2.8 \text{ mHz}}{f}\right)^4}$ |
| TDI | $4 \times 10^{-7} \times \sqrt{1 + \left(\frac{2.8 \text{ mHz}}{f}\right)^4}$ |

The difference in optical pathlength in LISA can be as large as $\Delta L = 10^8$ m due to the orbital motion of the spacecraft, and the equivalent pathlength noise contribution allocated to frequency noise is around $\tilde{\delta}x = 0.4 \text{ pm}/\sqrt{\text{Hz}}$ at 3 mHz. This results in a required frequency stability of $\tilde{\delta}\nu = 1.2 \times 10^{-6} \text{ Hz}/\sqrt{\text{Hz}}$ at 3 mHz. Starting from a free-running laser that has a typical frequency noise of $\tilde{\delta}\nu_{\text{free}} = 3 \text{ MHz}/\sqrt{\text{Hz}}$ at 3 mHz, such a reduction of frequency noise by about 12 orders of magnitude is difficult to achieve in a single step.

Therefore, a three-level approach has been chosen for LISA. First, a pre-stabilisation of the free-running laser to a level of $280 \text{ Hz}/\sqrt{\text{Hz}}$, then a stabilisation of the laser to the LISA arms, and finally the post-processing stage as a last step.

Prestabilisation

The prestabilisation is the first stage of the frequency stabilisation scheme for LISA. It requires a local frequency reference, such as a cavity (Livas et al., 2007; Mueller et al., 2005; Thorpe et al., 2008), a molecular resonance (Argence et al., 2010; Leonhardt and Camp, 2006; Leonhardt et al., 2006) or a dedicated heterodyne interferometer with unequal arms, much like the one employed in the LPF (Heinzl et al., 2006; Wand et al., 2006).

Laser stabilisation to a cavity using a variety of techniques, most prominently RF-sideband locking, has been demonstrated to well beyond the required stability for LISA (see e.g. Notcutt et al. (2005) for a demonstration of a stability of $\tilde{\delta}\nu = 1 \text{ Hz}/\sqrt{\text{Hz}}$ for frequencies above 1 Hz) at frequencies somewhat higher than the LISA frequency band. In the LISA frequency band, thermally driven changes of the cavity length are a major contributor to the residual frequency noise. As the thermal environment for LISA will be exceptionally stable, this is mainly a problem for laboratory-based demonstration or verification experiments, as these need sophisticated thermal insulation to reach an equivalent stability. Using multiple-stage insulation systems, a frequency stability of $\tilde{\delta}\nu = 30 \text{ Hz}/\sqrt{\text{Hz}}$ at 3 mHz has been demonstrated at NASA's Goddard Space Flight Center (GSFC) (Mueller et al., 2005). The cavities used in this experiment underwent environmental testing and the stated performance has been reached before and after the testing cycle.

The stabilisation of a frequency-doubled Nd:YAG laser to a hyperfine absorption line of the I_2 molecule has a long history as well. Typically used for comparing absolute frequencies in metrology (Hong et al., 1998; Nevsky et al., 2001), iodine stabilisation has been employed in ground-based gravitational wave detectors (Musha et al.,

2000) and is currently under investigation for applications in LISA (Leonhardt and Camp, 2006; Leonhardt et al., 2006; Mondin et al., 2004). where frequency stability of around $10 \text{ Hz}/\sqrt{\text{Hz}}$ to $100 \text{ Hz}/\sqrt{\text{Hz}}$ in the frequency range of 1 mHz to 100 mHz has been demonstrated in tabletop experiments (Leonhardt et al., 2006; Musha et al., 2000). In contrast to the stabilisation on a cavity resonance, stabilisation on a molecular line provides an absolute frequency reference; the drawback is some added complexity due to the need of frequency-doubled light and gas cell. Recently, a frequency-doubling system has been qualified for space application in the framework of the technology development for the SIM mission (Chang et al., 2007), greatly reducing the impact of frequency doubling on the technology development for LISA.

Heterodyne interferometry, as opposed to the “homodyne” stabilisation schemes described above, does not require a tuning of the laser to the reference, as it provides an error signal largely independent of the common-mode frequency of the light used. The drawbacks are the need for two light fields, separated by the heterodyne frequency and the comparatively low sensitivity. The use of a heterodyne interferometer with optical paths deliberately chosen to be unequal has been proposed for LISA, using a scheme much like the frequency interferometer in the LTP experiment on board LPF.

Arm-locking

The second stage of the frequency stabilisation scheme uses the interferometer arms of LISA as a frequency reference. By design, the fractional stability of the arms in the frequency range of around 1 mHz is on the order of $\delta x/L \sim 10^{-21}/\sqrt{\text{Hz}}$ as it has to fulfil the science requirements for LISA.

Arm-locking therefore makes use of this stability and derives an error signal from the phase-difference of the local laser and the received light. As the received light is phase-locked to the local laser at the remote spacecraft, it can be regarded to carry a replica of the noise of the local laser delayed by one full round-trip time $\tau = 33 \text{ s}$ (Sheard et al., 2003). After choosing a suitable control law, the noise is suppressed at frequencies f smaller than the corresponding round-trip frequency $f_0 = 1/\tau = 30 \text{ mHz}$ but causes significant amplification of the noise at integer multiples of f_0 (Sylvestre, 2004) as well as a long decay time for the initial conditions. A more elaborate implementation of arm-locking (Herz, 2005) uses the phase-differences from the two arms in sum and difference to suppress the noise spiking. The main advantage of the arm-locking scheme is the additional suppression of the laser frequency noise. The only additional functionality required is a tunable frequency reference, as the sensors for the required phase measurements and the actuators for setting the laser frequency are already present. The control law is fully implemented in software and requires no additional resources.

A proof-of-concept implementation in hardware uses RF signals instead of light and a 300 m coaxial cable to simulate the LISA arm (García Marín et al., 2005) and shows the feasibility of unity gain frequencies above the inverse of the delay time ($\tau = 1.6 \mu\text{s}$) as well as the predicted amplification of the noise and the “ringing” after lock acquisition. Similar experiments, using light in optical fibres ($L = 10 \text{ km}$, $\tau = 100 \mu\text{s}$) and purely electronical delays (Thorpe et al., 2006) yield comparable results.

Time delay interferometry

The third stage of the frequency stabilisation scheme, time-delay interferometry (TDI), does not reduce the laser frequency noise *in situ*, but rather suppresses the effects of laser frequency noise in a post-processing stage. In contrast to standard interferometers, where the light from the two arms is combined optically and the phase of the individual light impinging on the recombining beamsplitter is not known, in LISA each incoming light field is combined optically with a reference beam individually, so that the phase of the incoming light is separately measured and recorded. This allows to make use of correlations in the frequency noise and to remove the frequency noise down to the level of the measurement accuracy provided for the individual phase measurements by algebraically combining phase measurements delayed by multiples of the light travel time between the spacecraft to the so called *TDI variables*. The ability to use the individual phase measurements in post-processing does *not* depend on the actual values of the measurements. This means that TDI is not in any way restricted by arm-locking (or does in any way restrict arm-locking, for that matter) (Shaddock et al., 2004).

The first implementation of the algorithm was based in the frequency domain and dealt with a much simplified constellation (Giampieri et al., 1996). Such a frequency-domain based implementation is difficult to generalise

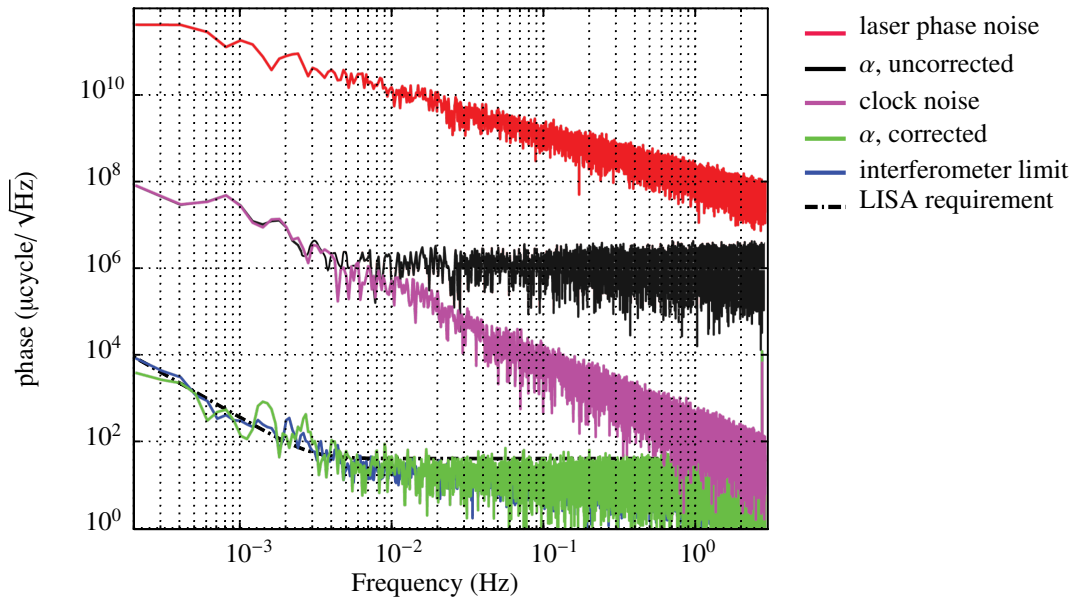


Figure 4.7.: Displacement measurements of the LISA interferometry test bed, showing injected laser phase noise (red); interpolated and clock noise corrected Sagnac TDI variable α (green), demonstrating phase noise cancellation by about 9 orders-of-magnitude, down to the interferometer noise floor (blue). Note: $1\ \mu\text{cycle} \approx 1\ \text{pm}$ displacement equivalent. Adapted from de Vine et al. (2010).

to the case of changing arm-length differences and more complex interferometric schemes. Subsequent implementations of the algorithm have therefore been based in the time-domain and include signals from all three spacecraft (Armstrong et al., 1999; Tinto and Armstrong, 1999). The simple time-domain implementation of the TDI algorithm (“first generation TDI”) using only phase measurement data delayed by the respective distances between the spacecraft cancels the frequency noise *exactly* only for fixed inter-spacecraft distances (much like the algorithm in the frequency domain) and requires an initial frequency noise of the lasers not larger than $5\ \text{Hz}/\sqrt{\text{Hz}}$ (Cornish and Hellings, 2003). Further refinements of the algorithm (“second generation TDI”) allow to deal with changing arm-lengths as well (Shaddock et al., 2003; Tinto et al., 2002) by using phase measurement data that are delayed by multiples of the inter-spacecraft distances. Using TDI with changing arm-lengths requires in addition the ability to perform phase measurements at arbitrary times to accommodate for the fact that the travel time of the light between the spacecraft will not only be different for each arm, but also changing over time. This additional complication can be overcome by oversampling and subsequent high-precision interpolation (Shaddock et al., 2004) of the phase measurements.

A rigorous algebraic approach to the mathematics of TDI progressed as well from considering a purely static constellation (Dhurandhar et al., 2002) to coping with changing arm-lengths (Nayak and Vinet, 2004) and a fully relativistic treatment of the optical links (Dhurandhar, 2009). The set of TDI variables forms a complete set of interferometric observables, so that any interferometric combination can be retrieved by linearly combining suitable TDI variables (Dhurandhar et al., 2002). Furthermore, suitably chosen linear combinations of TDI variables correspond to optimal statistical inference (Romano and Woan, 2006). An in-depth review of the current state-of-the-art techniques and the mathematical understanding of the algorithm has been conducted by Dhurandhar and Tinto (2005).

A full experimental demonstration of TDI poses some difficulties, mainly because of the need to provide sufficient, or at least representative, time delays between the data streams. Two main experimental routes have been explored in the past and have proceeded to demonstrate the full performance of TDI. One experimental approach uses electronic delays of the measured signal to emulate the optical delay. Starting with a delay of 2 s and later 16 s a reduction of the laser phase noise to within a factor of two of the requirements in the LISA bandwidth (see figure 4.8) has been shown (Cruz et al., 2006; Cruz et al., 2006; Mitryk et al., 2010). Another approach employs an all-optical setup, using smaller delays of order 10 ns. With this technique, de Vine et al. (2010) achieved a reduction of the laser frequency noise to the LISA requirements (see figure 4.7).

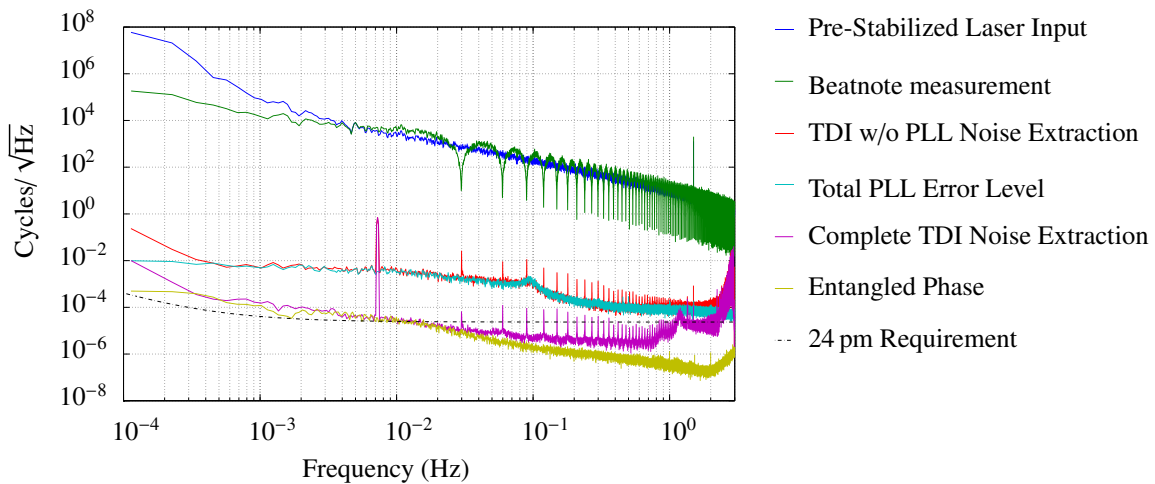


Figure 4.8.: *TDI Simulation results showing the laser input noise level with the applied ranging tone (blue), the sensor signals' spectral analysis with zeros at frequencies of $nc/(2L)$ (green), the TDI noise cancellation both with (purple) and without (red) the PLL noise extraction compared with the PM noise (yellow) and PLL noise (cyan) respectively. Adapted from Mitryk et al. (2010).*

4.3. Phase measurement

The phasemeter for LISA is one of the few payload items that can claim no or very little heritage from LPF. The main reason lies with the fact that LPF uses a constant and relatively low heterodyne frequency of 1.6 kHz to 2 kHz (Heinzel et al., 2003, 2004, 2006) in its interferometers, whereas the heterodyne frequency for LISA is much higher due to the relative motion of the spacecraft and the resulting Doppler effect. The requirement for the LISA phasemeter calls for a maximum admissible frequency heterodyne frequency of 15 MHz and for a frequency rate of change up to 1 Hz/s. Additionally, the phasemeter must be compatible with data transfer and ranging tones on the laser link between the spacecraft as well as with the transmission of the clock signal, none of which are present on LISA Pathfinder. Furthermore, the LISA phasemeter requires significantly more independent channels than the LPF phasemeter, as LISA has a much larger number of photoreceivers, most of them quadrant diodes. In the current baseline architecture, LISA requires 58 phasemeter channels, not counting redundancy.

The phasemeter architecture foreseen for LISA is based on a digital phase locked loop (DPLL) as sketched in figure 4.9. The signal from the photoreceiver passes through an analog anti-alias filter and is then digitised at 50 MHz. The digitisation frequency has to be chosen high enough to exceed the Nyquist frequency for the highest occurring beat note in the system. The signal is then multiplied with a local oscillator whose frequency is made to track the signal frequency. The low-pass filtered output of this multiplication is directly proportional to the *phase* difference between signal and local oscillator and is used as an error signal to drive the frequency and phase of the local oscillator to be the same as for the signal. The DPLL needs to update the local oscillator quickly enough (~ 0.1 ms) to follow the frequency changes occurring in LISA. For performance reasons, these operations are implemented in a field-programmable gate array (FPGA), and all operations are based on integer arithmetic. Residual tracking errors are corrected by evaluating the information in the two quadratures of the error signal in a floating point processor and combine them with the local oscillator phase. Further filtering of the signal yields the output at a rate of 100 Hz for recording. A more detailed insight into the principle of operation of the phasemeter including initial results on simulated data is given in (Shaddock et al., 2006).

4.3.1. Clock noise removal

An ultra-stable oscillator (USO) is required onboard to trigger the analog-to-digital converters (ADCs) in the phasemeter, assigning timestamps to all measurements, and for providing offset frequencies for laser phase locking. Because of phase noise limitations for available space-qualified USOs, the USO phase noise must be measured. Current USOs have a stability (Allan standard deviation) of 1×10^{-13} to 2×10^{-13} for periods of

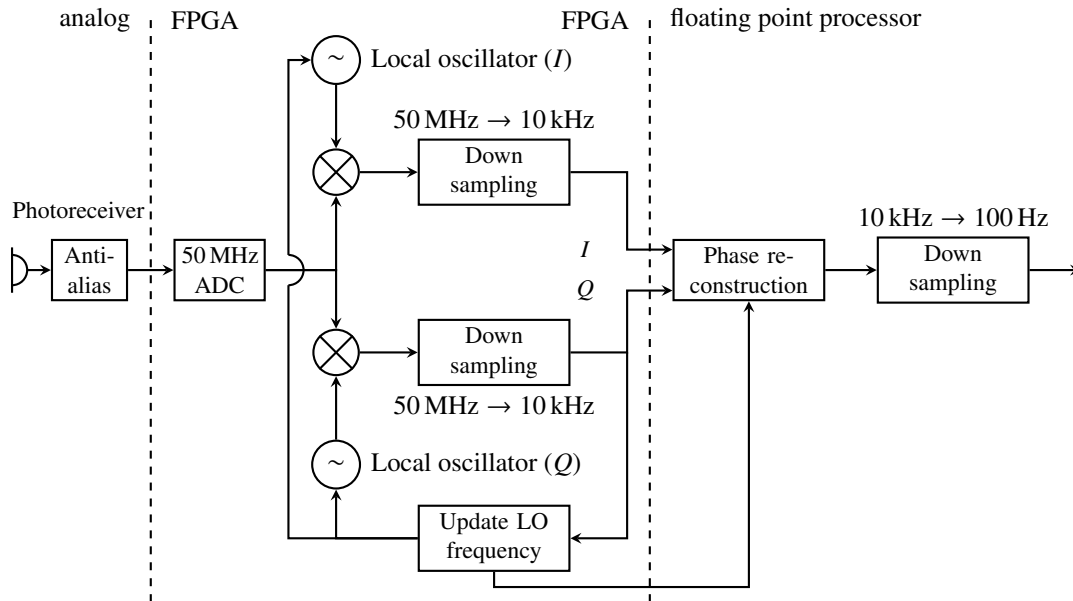


Figure 4.9.: Block diagram of the LISA phasemeter. Signals from the photodetector pass an analogue anti-alias filter before digitisation in a 50 MHz analog-to-digital converter (ADC) and further processing to determine phase and frequency, based on integer arithmetic in a field-programmable gate array (FPGA). A phase reconstruction algorithm to correct residual tracking errors is implemented in a floating point processor and feeds back to the local oscillator.

1 s to 1000 s. At 1 mHz, this corresponds to a fractional frequency noise level of about $7 \times 10^{-12} / \sqrt{\text{Hz}}$.

To remove the clock phase (*i.e.* USO) noise, the absolute distance between the spacecraft to about 1 m, and the clock offset between spacecraft to a few ns. These measurements are performed by applying two different phase modulations on the laser link. To measure the clock noise, the phase noise of each of the three spacecraft master clocks is multiplied by an integer factor and modulated as high frequency (GHz) phase modulation sidebands onto each laser link using 10 % of the light power. After interference between local and incoming lasers, the phase measurement of the resulting sideband-to-sideband beat note contains the amplified clock noise information necessary to remove the clock noise by TDI. Absolute inter-spacecraft distances are determined with a pseudo-random noise (PRN) phase modulation on each laser carrier using 0.1 % to 1 % of the light power. The distance is measured via correlation of the demodulated carrier phase with a local copy of the original PRN code. An important benefit of such a modulation is the possibility of additional data encoding on top of the PRN codes to enable inter-spacecraft communication. A direct measurement of the clock offsets between the three spacecraft to a few nanoseconds is an automatic by-product of this technique.

4.4. Disturbance Reduction System

The DRS of LISA is one of the main components of the mission. Whereas the IMS allows to measure the distance between the test masses to picometer accuracy, the DRS is responsible to render these measurements meaningful, as it ensures that the test masses follow gravitational orbits as much as possible, *i.e.* experience as small an acceleration as possible. Thus, the DRS consists of the GRS and its ancillary structures, and the drag-free attitude control system (DFACS). While the latter is not, in a strict sense, part of the payload, the main components of the DFACS will be discussed in this section: the micro-newton propulsion system that is used to provide the thrust for the fine attitude and position control of the spacecraft, and the control law that takes the data from the gravitational reference sensor and controls the micro-newton thrusters such as to keep the spacecraft centred on the test mass while keeping alignment of the telescopes to each other.

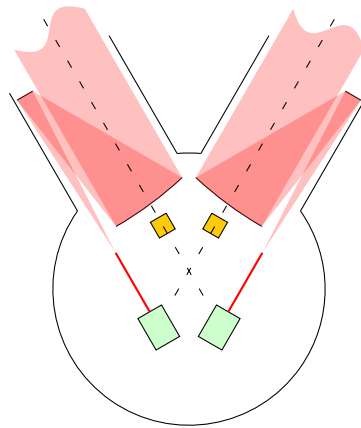


Figure 4.10.: Position and orientation of the two test masses (dark grey) in the spacecraft. The sensitive axes of the sensors are indicated with the dashed lines and are aligned with the direction to the far spacecraft.

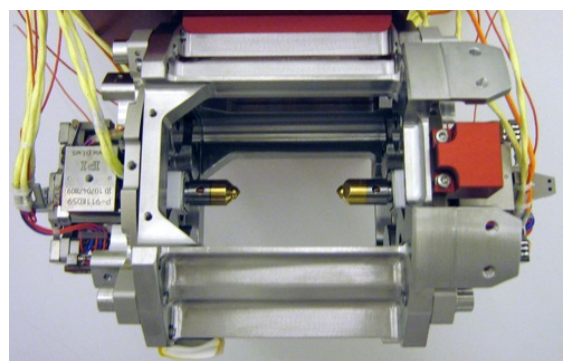
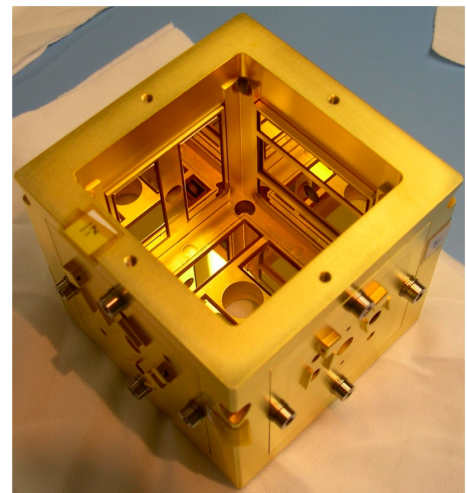
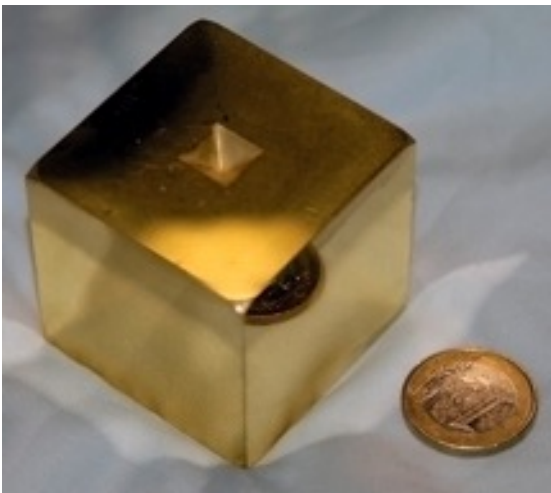


Figure 4.11.: Upper left: *LISA Pathfinder* test mass made of a mono-phasic alloy of 73 % gold and 27 % platinum, coated with gold. The inverted prism-like impression at the centre of the top face takes the plunger of the caging system and allows centering of the test mass, the chamfered corners accept the fingers of the launch lock. Edges are chamfered to prevent damage during caging. Upper Right: Electrode Housing. Lower left: Schematic drawing of the bottom half of the caging mechanism, with the central plunger in the centre and the four hydraulically actuated fingers that grab onto the corners of the test mass. Lower right: Flight model of the Grabbing, Positioning, and Release Mechanism (GPRM) of the caging mechanism assembly (side view) with both plungers visible.

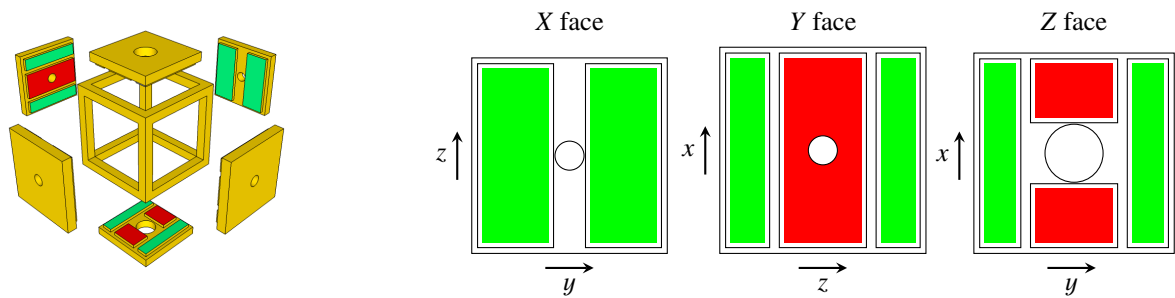


Figure 4.12.: Left: Exploded schematic view of the electrode housing, showing the structure of the electrode housing and the electrodes mounted on the inner faces. Right: Placement of the electrodes onto the inner surfaces of the electrode housing. Control electrodes are given in green (light grey), injection electrodes in red (dark grey). The central holes in the X- and Y-faces admit the laser, the central hole in the Z face admits the plunger. The electrodes differ slightly in overall size on the different faces.

4.4.1. Principle of operation

The main objective of the **DRS** is to maintain the free fall of a test mass that serves as nominal reference point for the measurement of the inter-spacecraft distance. To keep the test mass in free fall, the **DRS** measures the position and orientation of the test mass with respect to the spacecraft, applies a control law and commands micro-newton thrusters such that the test mass remains in its nominal position with respect to the spacecraft. Situated inside the spacecraft, the test mass is shielded from the external effects, such as solar radiation pressure and (to a certain degree) the interplanetary magnetic field. In addition, the spacecraft architecture has to ensure that the forces on the test mass are as small as possible, requiring special design precautions regarding the mass distribution, the thermal balance and the magnetic cleanliness. Each spacecraft has two **GRSs**, each mounted in the line of sight of the corresponding telescope (see figure 4.1, upper right panel), behind the optical bench. The *sensitive axis* of the **DRS** denotes the axis aligned with the line of sight to the telescope and consequently to the test mass in the remote spacecraft (see figure 4.10). As LISA employs two test masses per spacecraft, it is impossible to keep both of them in free fall condition in all degrees of freedom and ensure at the same time that the test masses stay close to their nominal position. However, it is sufficient to maintain free fall in the direction of the sensitive axes which can be achieved by controlling the “non-sensitive” degrees of freedom of the test masses and the position and attitude of the spacecraft. The measurement of the test mass position is provided by a capacitive readout system, augmented in the sensitive axes by the measurement provided by the test mass interferometer.

The **DRS** can claim substantial heritage from LISA Pathfinder, as the gravitational reference sensor will be identical and the micro-Newton thrusters and the control law will be similar, requiring adaptation to the larger mass of the LISA spacecraft and the different geometry of the test mass arrangement. Similarly, lifetime requirements for the propulsion system are more stringent as LISA’s nominal design life-time is 5 years compared to the 11 months of LISA Pathfinder.

4.4.2. Environmental requirements

As gravitational forces cannot be shielded, the mass distribution of the spacecraft can cause significant disturbances on the test mass, both through direct gravitation as well as through gravity gradients. To be able to compensate both mass imbalance and gravity gradient, the mass distribution on the spacecraft has to be known accurately enough to be able to use the correct amount of compensation mass in the correct position. On ground, a measurement of the self-gravity is not feasible to the precision necessary for LISA, verification of the self-gravity relies on analyses. Such analyses on self-gravity and the design of compensation masses has been successfully performed on LISA Pathfinder (Armano et al., 2005; Brandt et al., 2005) and the corresponding analysis tools have been developed for LISA (Merkowitz et al., 2004, 2005).

Of similar importance is the magnetic cleanliness of the spacecraft, as magnetic fields can cause a non-gravitational acceleration of the test mass coupling to its non-zero magnetic susceptibility. In addition, they create an acceleration noise as soon as the test mass carries an electric charge. As neither the magnetic susceptibility of the test mass nor its electric charge can be controlled to be precisely zero, strict magnetic cleanliness has to be enacted, requiring the use of only non-magnetic materials in the vicinity of the **GRS**.

Temperature fluctuations at the **GRS** have the potential to cause acceleration noise, as they will cause a time varying gas pressure in the electrode housing leading to varying radiometer effect. The thermal variations allowed are at the level of 10^{-5} K/ $\sqrt{\text{Hz}}$.

4.4.3. Gravitational Reference Sensor

The **GRS** forms a crucial part of the LISA mission and is one of the major components of the **DRS**, providing it with the data necessary to keep the spacecraft in a (nearly) gravitational orbit. The **GRS** includes the test mass (figure 4.11, upper left), enclosed in a housing (figure 4.11, upper right) that contains the electrodes needed for the capacitive readout of the test mass position. The electrodes are arranged in such a way that all relevant degrees of freedom can be capacitively measured (Carbone et al., 2003; Stanga et al., 2006; Weber et al., 2002). The **GRS** further contains the launch lock mechanism (figure 4.11, lower row) and the charge control system.

Forcing of the test mass to control its orientation and position in the non-sensitive directions is achieved by applying additional **AC** voltages to the electrodes; the unavoidable cross-coupling of the actuation from non-sensitive directions into the sensitive directions has to be as small as possible (on the order of 10^{-3}) to avoid “leakage” into the sensitive axis that causes acceleration noise of the test mass. Knowledge of the correct cross-coupling coefficients and an effective diagonalisation of the control matrix is an important task during on-orbit commissioning of the instrument.

Other important noise sources in the **GRS** to consider include the electrostatic coupling between the test mass and the housing (and ultimately the spacecraft) due to the capacitive sensing, the *stiffness* of the sensor that feeds the noise of the micro-newton thrusters back into the **GRS** (Carbone et al., 2005); forces induced by thermal gradients, such as thermal radiation pressure, or asymmetric outgassing (Carbone et al., 2007a); random charging processes (Shaul et al., 2004, 2005); and gas damping.

The patch field effect, caused by spatial (and temporal) variation of the work function, can be a major source of noise to drag-free sensors (Everitt et al., 2008). The work function of the test mass contributes to stray **DC** electrostatic fields that couple to the time-varying charge of the surrounding electrode housing (and vice versa), introducing both forcing and sensing noise. A technique to measure the stray **DC** field imbalances has been proposed (Weber et al., 2007) and experimentally verified (Carbone et al., 2003) that simulates a sinusoidally varying charge on the test mass by applying a dither voltage to selected electrodes. Using this method, the average bias voltage that results from the spatial variation of the work function can be suppressed by a factor of about 100 by applying a **DC** compensation voltage, resulting in a reduction of the respective acceleration noise to levels negligible for LISA.

The **GRS** is a direct heritage from the **LTP** experiment on LISA Pathfinder; a detailed review on the working principle of the **GRS** can be found in (Dolesi et al., 2003). An extensive ground-testing campaign evaluating the performance and the noise sources on in the **GRS** employing a low-frequency torsion pendulum is under way and results and more detailed descriptions of noise sources and their effect can be found in (Carbone et al., 2003, 2005, 2006; Hueller et al., 2005); requirements on the sensor and the environmental conditions are summarised in table 4.6. The current status of the **GRS** subsystem on **LPF** can be found in *The LISA Pathfinder Mission* (S2-EST-RP-1087).

Test mass and housing

The test mass is a cube made of an alloy of about 73 % gold and 27 % platinum with a mass of 1.96 kg and dimension 46 mm \times 46 mm \times 46 mm. The mixing ratio of the two metals is chosen such that the magnetic susceptibility χ can be made very small (Budworth et al., 1960; Silvestri et al., 2003). As the susceptibility depends on the mixing ratio and the manufacturing process, a small residual magnetic susceptibility of $\chi \approx -2 \times 10^{-5}$ remains in the test mass, requiring a certain amount of magnetic cleanliness of the whole spacecraft

Table 4.6.: Summary of the environmental and performance requirements on the DRS

| Condition | Requirement |
|--|--|
| Acceleration | |
| DC | $3 \times 10^{-9} \text{ m/s}^2$ |
| residual variation | $3 \times 10^{-15} \text{ m/s}^2 / \sqrt{\text{Hz}}$ |
| Capacitive readout noise | |
| Displacement (sensitive axis) | $1.8 \text{ nm} / \sqrt{\text{Hz}}$ |
| Displacement (non-sensitive axes) | $3.0 \text{ nm} / \sqrt{\text{Hz}}$ |
| Rotation | $200 \text{ nrad} / \sqrt{\text{Hz}}$ |
| Forcing noise | |
| Sensitive axis | $2 \times 10^{-15} \text{ m/s}^2 / \sqrt{\text{Hz}}$ |
| Non-sensitive axes | $3 \times 10^{-14} \text{ m/s}^2 / \sqrt{\text{Hz}}$ |
| Rotation | $7.3 \times 10^{-13} \text{ rad/s}^2 / \sqrt{\text{Hz}}$ |
| Thermal variation across sensor | $10^{-5} \text{ K} / \sqrt{\text{Hz}}$ |
| Magnetic field | |
| DC field | $4 \times 10^{-6} \text{ T}$ |
| DC gradient | 10^{-6} T/m |
| Variation | $72 \times 10^{-9} \text{ T} / \sqrt{\text{Hz}}$ |
| Variation of gradient | $25 \times 10^{-9} \text{ T/m} / \sqrt{\text{Hz}}$ |
| Charge on test mass | 10^7 electron charge |
| Absolute position of test mass inside electrode housing | $1.5 \times 10^{-9} \text{ m} / \sqrt{\text{Hz}} \times \sqrt{1 + \left(\frac{8 \text{ mHz}}{f}\right)^4}$ |

that prohibits the use of ferro-magnetic materials in the vicinity of the **GRS**. The surface of the test mass is coated with a thin layer of gold that provides reflectivity for the laser light of the local interferometer. In addition gold proves to be the material of choice to minimise the patch field effect.

The test mass is surrounded by a housing that contains the electrodes for the capacitive sensing and actuation. The housing is slightly larger than the test mass, with the gap between the test mass and the electrodes measuring between 3 mm and 4 mm, providing a further reduction of the patch field effect, as the noise forces decrease with the distance. An additional benefit of the large gaps is a reduction of the dissipation due to gas flow around the test mass. The electrode housing admits the fingers and the plunger of the launch lock and repositioning mechanism (see section 4.4.3) in the Z faces and the laser of the test mass interferometer through a hole in the X face. The electrodes are made from a gold-coated sapphire substrate, surrounded by a molybdenum guard ring; the electrode housing structure is also manufactured from molybdenum.

The physical properties of test mass and housing are summarised in table 4.7.

Capacitive sensing

The capacitive sensing of the test mass position is designed to provide a measurement of the test mass position in the sensitive axis with noise levels of $1.8 \text{ nm} / \sqrt{\text{Hz}}$, while at the same time minimise the back-action on the test mass. Six opposing pairs of electrodes form a differential capacitive-inductive bridge with a resonance frequency of about $\omega_0 = 2\pi \times 100 \text{ kHz}$. Combinations of the obtained signals yield all relevant displacement and rotation measurements. In order to apply the **AC** bias to the test mass, injection electrodes are placed on the $+Z$ and $-Z$ as well as on the $+Y$ and $-Y$ surfaces of the electrode housing (figure 4.12). The capacitive sensing achieves a sensitivity of $2 \text{ nm} / \sqrt{\text{Hz}}$ in displacement and $200 \text{ nrad} / \sqrt{\text{Hz}}$ in rotation (Carbone et al., 2007b) in ground tests, matching or exceeding the requirements for LISA.

The details of the sensor design and a detailed discussion of the noise can be found in Cavalleri et al. (2001).

Table 4.7.: Summary of the physical parameters of the test mass and the housing.

| Element | Property |
|---------------------------|--------------------------------------|
| Test mass | |
| Size | 46 mm × 46 mm × 46 mm |
| Material | gold-coated AuPt (73 % Au, 27 % Pt) |
| Mass | 1.96 kg |
| Magnetic susceptibility | $ \chi \leq 2 \times 10^{-5}$ |
| Housing | |
| Material | gold-coated molybdenum |
| Gaps Electrodes/Test mass | 4 mm (x), 2.9 mm (y), 3.5 mm (z) |
| Electrodes | |
| Material | gold-coated sapphire |
| Size and Arrangement | see figure 4.12 |

Launch lock and repositioning

The relatively large gaps make it necessary that the test mass is held during launch by the *caging mechanism* to avoid damage to the test mass or the electrode housing due to the vibrations during launch. The caging mechanism comprises three actuators: a launch lock; a grabbing/positioning actuator; and the release mechanism. The launch lock consists of eight hydraulically actuated fingers that connect to the eight corners of the cubical test mass, each pushing with a force of 1200 N to keep the test mass securely in place (see figure 4.11, lower left panel for a drawing of the caging mechanism).

Releasing the test mass from the launch lock requires to break the adhesion present between the fingers and the surface of the test mass. The necessary force to break the adhesion can be up to 10 N per finger (on the order of 1 % of the load), so that without a way to push the test mass off the fingers, it would remain stuck to the launch lock. In addition, the residual momentum of the test mass after release needs to be smaller than 10^{-5} Ns for the electro-static actuator to be able to slow down and centre the test mass in the electrode housing. To overcome the adhesion between the fingers and the test mass, two piezo-driven plungers, acting centrally on the +Z and -Z surface of the test mass, respectively, are used to push the test mass off the fingers. The Z surfaces of the test mass have inverted pyramidal indentations to allow for an auto-centring and auto-aligning of the test mass during engagement of the plungers (see figure 4.11, upper left panel). As the plungers push with up to 40 N into the indentations, an adhesion force of about 0.5 N will have to be overcome when attempting to retract the plungers. For that purpose, the plungers accommodate a release tip at their end (much like a retractable ball-point pen) that can be pushed out by a piezo-electric element to deliver the necessary force. The remaining adhesion, still too large to be overcome by the electro-static actuator (Benedetti et al., 2006), is then broken using the inertia of the test mass by quickly retracting the plungers, leaving the test mass with residual momentum below the specified 10^{-5} Ns. After launch, only the plungers are employed to grab and position the test mass during spacecraft safe mode or any other circumstance that makes it necessary to re-position the test mass.

The breaking of the adhesion between plungers and test mass has been the topic of intense ground-based testing, showing the feasibility of a test mass release within the required limits of the transferred momentum (Bortoluzzi et al., 2009).

Vacuum system

It is a peculiarity of LISA (and LPPF) that despite the fact that the mission will operate in interplanetary space, it needs to carry a vacuum system. The residual gas pressure within the spacecraft due to outgassing is too high for the GRS to tolerate, as it creates spurious noise due to the radiometric effect (Carbone et al., 2007a) and through gas damping. Therefore, a vacuum system (figure 4.13), pumped by a getter pump and encapsulating the test mass, the electrode housing and ancillary structures is foreseen, maintaining a pressure of 10^{-8} mbar. Due to the criticality of ferro-magnetic materials close to the test masses, this vacuum system has been made entirely from titanium. During the transfer orbit phase, a gate valve connecting the vacuum enclosure to a pipe leading to

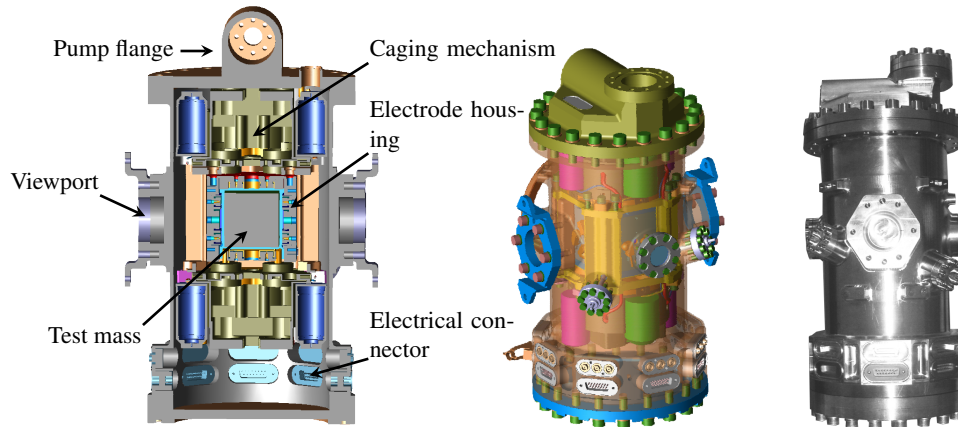


Figure 4.13.: *Left: Schematic drawing of the vacuum housing of the inertial sensor of LISA Pathfinder. Centre: Schematic drawing, external view. Right: Flight model of the vacuum housing for the inertial sensor of LISA. The inertial sensor for LISA is foreseen to be identical to the sensor used in LISA Pathfinder.*

the outside of the spacecraft will be opened, allowing the vacuum enclosure to vent to space, maintaining the internal pressure at, or below, the required 10^{-8} mbar.

Charge control system

As forcing of the test mass depends to a large degree on electrostatic forces, the electric charge of the test mass has to be controlled as any fluctuation in the charge of the test mass will give rise to a fluctuation in force, hence acceleration noise. Charging of the test mass occurs mainly when secondary particles created by interaction of either protons or α -particles from cosmic radiation with the spacecraft materials hit the test mass (Jafry and Sumner, 1997; Sumner et al., 2004). The charging rates incurred are on the order of 50 e/s. A standard way to discharge test masses in similar setups is to connect a thin wire of conductive material to the test mass (Touboul et al., 1996), however, such a mechanical connection introduces spurious accelerations and proves to be too noisy for the LISA requirements. Another well proven way to remove surface charge is through the photo-electric effect. In the case of LISA, UV light will be used to irradiate test mass and electrode housing, removing surface charges from electrodes and test mass. The charge control system for LISA is based on the heritage from LISA Pathfinder (Schulte et al., 2006), which itself is based on the charge control system flown on the GP-B mission, and whose functionality and performance has been demonstrated (Wass et al., 2006). The LISA Pathfinder charge control system consists of six mercury discharge lamps, producing UV light at 254 nm coupled into optical fibres and brought to the test mass (2 lamps) and electrode housing (1 lamp). An identical setup controls the charge of the second test mass, bringing the number of lamps up to the total of six. Due to the reflectivity of both the electrodes and the test mass, light shone on any surface will eventually reach most of the other surfaces as well and release electrons, so that the discharge rate is determined by the net current between electrodes and test mass. The polarity of the discharge is determined by the digitally controlled output power of the UV lamps received by the test mass and the electrode housing, respectively, and can be further controlled by applying bias voltages to the electrodes. Operationally, the discharging can occur episodically or continuously, depending on the observed charge rate. Both methods will be demonstrated during the LISA Pathfinder mission. The charge itself is measured by applying an AC voltage to the electrodes and measuring the ensuing displacement of the test mass (Schulte et al., 2006; Sumner et al., 2004). For LISA the development of UV LED (Sun et al., 2006) opens the possibility to replace the mercury discharge lamps with LED requiring less power and having less mass.

4.4.4. Micro-newton thrusters

The micro-newton thrusters are a key technology for LISA, as they are providing the fine attitude and position control for the drag free flight. LISA will employ three clusters of four thrusters each, situated on the outside

Table 4.8.: Summary of the micro-Newton thruster requirements.

| | Requirement |
|-------------------|--|
| Minimum thrust | 0.3 μN |
| Maximum thrust | 100 μN |
| Thrust resolution | 0.3 μN |
| Thrust noise | $0.1 \mu\text{N}/\sqrt{\text{Hz}} \times \sqrt{1 + \left(\frac{10\text{mHz}}{f}\right)^4}$ |
| Lifetime | 55 000 hours |
| Specific impulse | 4000 s |
| Total impulse | 8300 Ns per thruster |

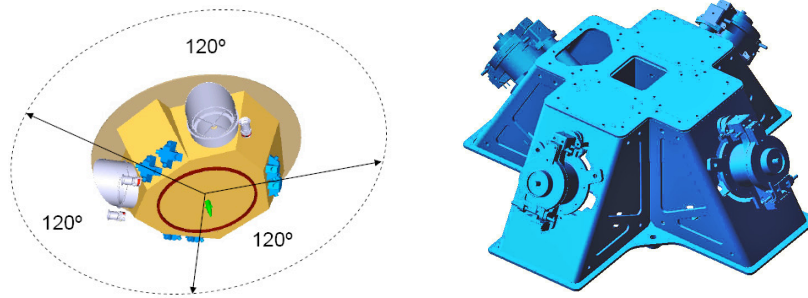


Figure 4.14.: Left panel: Geometrical layout of the micro-newton thrusters on the LISA spacecraft. Right panel: FEFP cluster module geometry (EADS Astrium)

of the spacecraft, separated by 120° (see figure 4.14, allowing the control of all degrees of freedom of the spacecraft. The thrusters are controlled by the DRS and operate continuously during science operation. The main thrust is used to counteract the solar radiation pressure that amounts to about $10 \mu\text{N}$ per relevant thruster, the largest external force on the spacecraft. The thrust noise is required to be smaller than $0.1 \mu\text{N}$ peak-peak at high frequencies (relaxing to lower frequencies, see table 4.8) in order to keep the motion of the spacecraft with respect to the test masses as small as possible.

Two different propulsion systems currently meet the LISA requirements on thrust and thrust noise, both based on field emission ionisation of the propellant: a colloid micro-newton thruster (CMNT) developed in the US and the European FEFP. Both thruster systems will be flown on LPF (McNamara et al., 2008; S2-EST-RP-1087) to demonstrate the technology and to assess the on-orbit performance. The US CMNT uses a colloidal liquid as the propellant. Small droplets of the colloid are ionised through field emission, accelerated in an electrical field and ejected from the thruster. The thrust is over a wide range proportional to the acceleration voltage and can be controlled with the required precision. The CMNT has shown a capability of $15 \mu\text{N}$ thrust with a noise well below the requirement and has successfully passed a 3400 hour life time test. The ESA FEFP development programme advanced two different technologies, based on indium (Fehringer et al., 1998; Genovese et al., 2004; Ruedenauer et al., 1997; Steiger et al., 2000; Tajmar et al., 2004) and caesium (Marcuccio et al., 1998) with different geometrical setups for the field emission. The advantage over the CMNT lies in the much higher specific impulse of the FEFP, as single ions instead of charged droplets are accelerated and ejected, yielding a better charge-to-mass ratio. In the In-FEFPs capillary forces push the indium to the tip of a needle where it is ionised, whereas the Cs-FEFPs employ a narrow slit in which the caesium then forms narrow cusps due to the electric field, emitting ions from the tip of the cusps, producing higher thrust than the In-FEFPs due to the multiple emitters. The Cs-FEFPs have been chosen as the baseline technology to fly on LISA Pathfinder and have demonstrated the required thrust, noise and resolution and have performed endurance testing with a total impulse in excess of 800 Ns in over 3000 hours of operation.

While the currently demonstrated lifetime and total impulse of both micro-newton thruster systems is sufficient for LPF, a higher lifetime and total impulse has to be demonstrated for LISA. The additional life-time testing is part of ESA's technology development programme for LISA.

5. Mission Design

5.1. Overview

All three LISA spacecraft will be launched at once with a single **EELV**-class launcher (Atlas V), directly into an Earth escape trajectory with a ΔV of approximately 1 km/s. In order to reach the final operational orbit, each science spacecraft is equipped with an additional propulsion module (P/M) which is separated when the target orbit is obtained after approximately 14 months. The P/M are designed to form the launch stack, isolating the spacecraft (S/C) from the quasi-static load at launch. Figure 5.1 depicts the launch stack configuration and illustrates the science spacecraft and the propulsion module.

The space segment consists of two distinct elements: the **S/C** which carries the payload, and the **P/M** which is responsible for delivering the **S/C** to the selected orbit. Following final orbit acquisition the elements are separated to ensure that no disturbances generated by the **P/M** will affect the payload.

5.2. Spacecraft Design

The basic structure of the **S/C** is an irregular octagon, consisting of radial panels splaying from a central cylinder to the outer panelling (see figure 5.2). A very stable carbon composite is employed, avoiding flexible appendages on the spacecraft that could have natural frequencies in the mHz range. The gravitational reference sensors (GRSs) are separated as far as possible from other equipment to simplify gravitational compensation. To further ensure disturbance minimisation, extremely stable thermal control is required, with no active thermal elements able to induce mHz disturbances at the payload interface. This requirement drives the payload thermal environment to be well decoupled both from solar radiation and in turn from the **S/C** structure itself. A sunshield is provided to protect the spacecraft from the Sun, and the thermally benign carbon composite structure is coupled with radiators to provide passive thermal control. Field-emission electric propulsion (FEEP) microthrusters are employed to provide the required fine control for the attitude and orbit control system (AOCS).

The **S/C** contains the payload, the micro-propulsion and the attitude and orbital control system, and power, thermal and communication subsystems to support the mission. The inertial sensor core assemblies are each mounted in a dedicated cylindrical housing to isolate them from the rest of the **S/C** structure. The payload electronics and spacecraft equipments are accommodated away from the test mass (TM) locations to minimise their contributions to gravitational, thermal and magnetic noise at the **TM** locations. The **FEEP** micro-propulsion assemblies are arranged on the outer panels to provide fully redundant control of six degrees of freedom

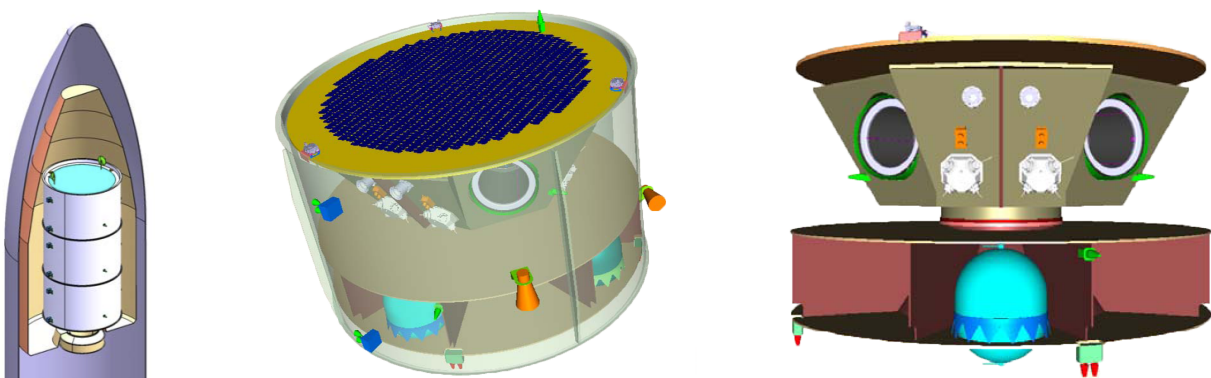


Figure 5.1.: *Launch stack, propulsion module and spacecraft composite, and S/C-P/M composite with external shroud removed*

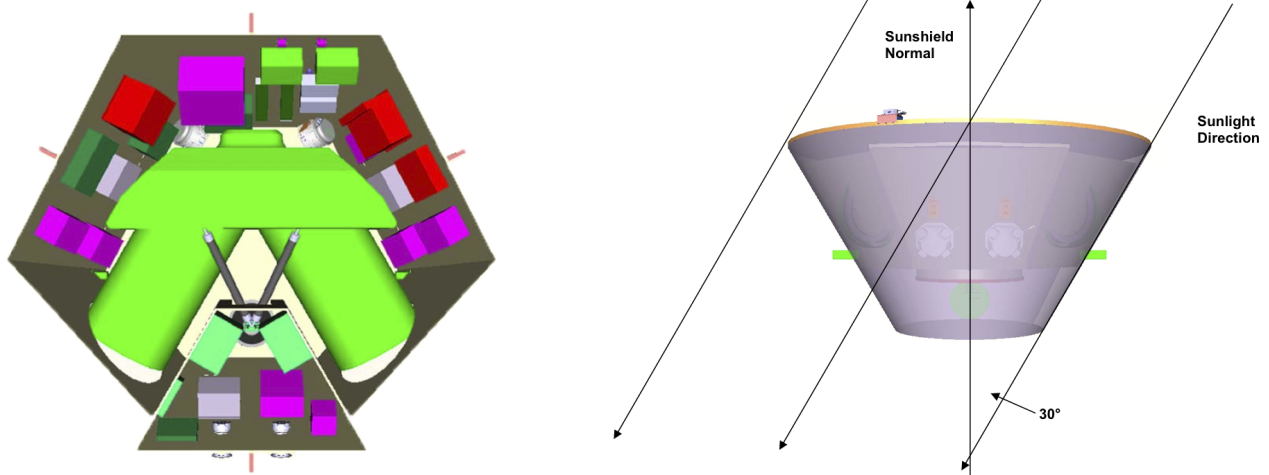


Figure 5.2.: Left: *S/C interior with sunshield removed*. Right: *Sunshield protects all parts of the S/C from direct sunlight*. (EADS Astrium)

(DOFs) and to avoid plume impingement onto the *S/C* structure. The key design features of the *S/C* are briefly described below, a more detailed description can be found in *Preliminary Propulsion Module Design Description (LISA-ASU-DD-4002)*:

Structure A very stable CFRP/aluminium structure is used to avoid inducing structural disturbances in the mHz frequency range, along with a thermal design and operational attitude that ensures a very high degree of thermal stability throughout the operational phase. To this end the structure of the *S/C* has been designed such that no *S/C* unit or structural element behind the sunshield is exposed to the Sun at any time in the nominal attitude.

Interface to Ground Segment The current baseline foresees the Deep Space Network (DSN) to provide the interface between the ground station (GS) and the *S/C*, once on orbit. To minimise the number of antenna pointing events, a contact schedule is proposed which cycles the link with the GS through each *S/C* in the constellation (LISA-ASU-TN-4003).

Communications The large spacecraft range and medium size ground antenna requires the use of data compression, together with a high-gain antenna (HGA) and high-power RF amplifier to achieve the required data rates. The use of a HGA requires regular repointing of the antenna, which, while likely to interrupt the science mode, should allow the laser-lock to be maintained, so that no re-acquisition will be necessary.

Payload location The sensitive axis of the GRS lies as near to perpendicular to the sun vector as possible, which is the axis of greatest disturbance. The payload is located so that the TMs are close to the spacecraft centre of mass (CoM) to minimise propellant consumption in drag-free mode (the magnitude of gravitational compensation required is proportional to the mismatch between TM and *S/C* CoM). The GRS is separated as far as possible from other equipment to simplify gravitational compensation. There are no unknown masses close enough to the TM to induce uncompensated DC gravitational forces that exceed the capability of the electrostatic suspension.

AOCS and FDIR The *S/C* AOCS consists of attitude sensors (star trackers, inertial measurement units, Sun sensors) and actuators (micropropulsion system). During nominal science mode and drag-free operations, the payload controls the AOCS. In any other spacecraft mode, the *S/C* will have full control over its AOCS. Transition between modes, *e.g.* in response to an anomaly or fault, will be controlled by the *S/C*.

Separation Subsystem The separation function between the *S/C* and P/M is performed by a motorised light band (MLB). This mechanism provides a low shock, debris-free, easily reset, low tip-off separation; factors which are crucial for the LISA mission. A detailed analysis of the separation system is provided in *Separation Analysis (LISA-ASU-TN-4002)*.

Spacecraft autonomy is based on a fail-operational principle, supported by a robust sun-pointing safe mode. The spacecraft is designed to be single point failure tolerant. The following features are included in the spacecraft redundancy design.

- The on-board computer (OBC) is fully internally redundant
- The solar array includes a redundant string
- The power control and distribution unit (PCDU) controller is redundant
- Three sun sensors are used in a majority voting configuration
- At least six skewed gyro axes are used to allow fault detection and isolation
- The X-band communication system is fully redundant including two transponders and traveling-wave tube amplifiers (TWTAs). A single HGA for nominal communication is regarded a non-credible single failure. Back-up communications are provided by three omni-directional antennas
- Six clusters of FEETPs, three prime and three redundant, are included in the current design.

5.3. Propulsion module design

The P/M is designed to provide the spacecraft with the manoeuvrability to reach the science orbit. The P/M supports the communication during the 14 months cruise phase and is jettisoned upon arrival at the science orbits. For a full description of the P/M preliminary design, refer to *Preliminary Propulsion Module Design Description (LISA-ASU-DD-4002)*.

The accommodation of the LISA propulsion system is within an independent module that separates from the S/C after orbit insertion. It is configured to meet the volume constraints of the baseline launch vehicle (Atlas V), providing the necessary propellant capacity and propulsive capability. Because the P/M fully encapsulates the S/C, in order to fulfil the mission the P/M must also accommodate several elements from other subsystems, such as the AOCS/Propulsion units (autonomous star trackers, thrusters), the telecommand/telemetry units (antennas), and thermal units (radiators, heaters), along with the electrical harness required for their operation. The selection of the P/M design is driven by the need to provide the environment, protection, and services required by the S/C during assembly, integration, verification, and testing (AIVT); Launch and Early Operations Phase (LEOP); and transfer (including separation). Most critically, protection is required during launch. Furthermore, the P/M design must take into account the dimensions and geometry of the S/C and it must provide adequate mounting points for the equipments required to perform AOCS; telemetry, tracking, and command (TT&C); thermal and separation functions.

5.3.1. Structural Concept

The P/M structural concept has been designed primarily to isolate S/C and payload from the launch environment. The P/M primary structure is an outer cylindrical shroud, which acts as the primary load path for the stack, transmitting the entire stack load down to the launch vehicle adaptor (LVA). In this way the S/C and the payload are completely protected from the load of the elements in the stack above.

The P/M structure inside the primary *outer cylindrical shroud* can be considered as composed of two separate parts: the lower section which houses the propellant and pressurant tanks, and the upper cylindrical section which accommodates the S/C. In order to transmit the load from S/C mass to the outer cylinder efficiently, the S/C is attached to the P/M via a *clamp-band* located at an interface plane between the S/C floor panel and the *central frustum* of the P/M, thus avoiding any attachment passing through the S/C sunshield, which would interfere with the solar array mounting. This circular interface load is then propagated to the P/M outer cylinder. First down through the *central frustum*, and then through *radial shear panels*, the *upper floor panel* and *lower floor panel*. The conical shape of the frustum helps to transmit the axial loads at the diameter of the clamp-band interface towards the outer cylinder; the ideal structure would be a frustum angled out to the cylinder, but the requirement to accommodate four propellant tanks around the central frustum precludes this. An additional small *pressurant tank radial panel* is included as a mounting point for the pressurant tank.

The *upper floor panel* serves to laterally constrain the clamp-band interface between the S/C and P/M, and also separates the lower section of the P/M from the area that accommodates the S/C. This provides a unit-free, contaminant-free accommodation for the S/C. The *lower floor panel* provides additional lateral stiffness, and also includes cutouts to make room for the AOCS thrusters, and the skirt-mounted propellant tanks.

The structural design of each P/M is identical, although it could be tailored according to its position within the

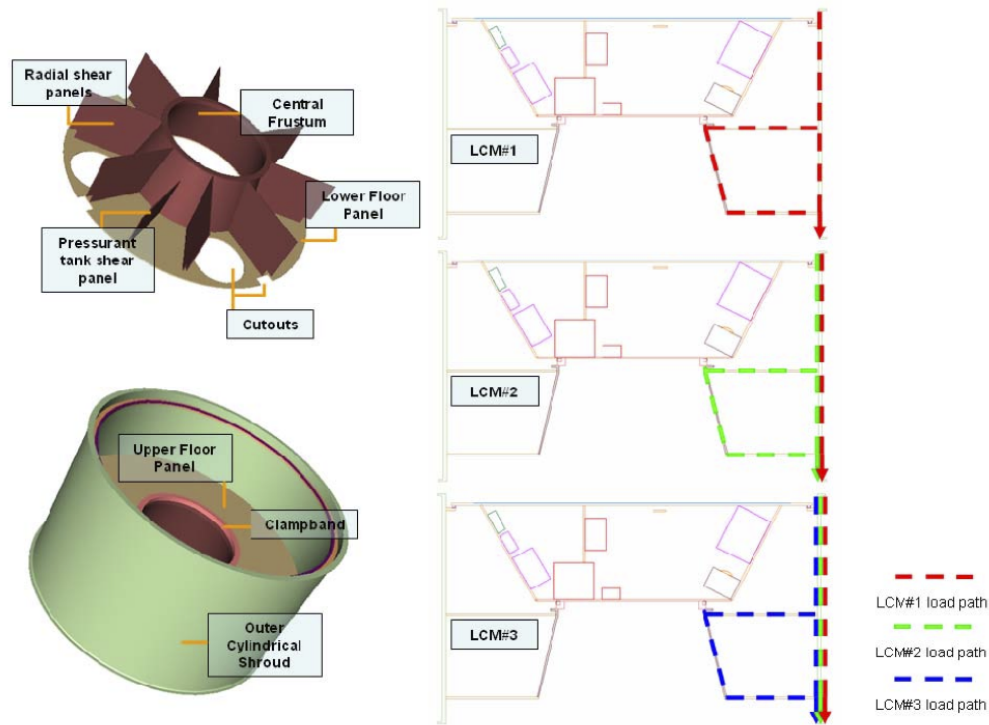


Figure 5.3.: Left: *P/M structural elements*. Right: *Load-paths within the stack*

stack; identical structural design for the three *P/M* entails significant cost savings during production and also testing. The *P/M* is mainly constructed from aluminium honeycomb cores layered with skins of pseudo-isotropic carbon fibre reinforced plastic (CFRP). The conical frustum is filament-wound CFRP.

The structural elements and the resulting load paths are shown in figure 5.3.

5.3.2. Separation Subsystem

The selection and analysis of the separation events for the LISA mission are detailed in *Separation Analysis (LISA-ASU-TN-4002)*. The LISA mission involves a total of six separation events, not including the launch phase but including separation of the stack from the *LVA* (see figure 5.4). Each of these six events is mission critical and constitutes a single point of failure for the entire mission. As a consequence, selection of suitable separation technologies is crucial.

The separation mechanism must allow safe separation between the *S/C* and *P/M* such that the *S/C* does not impact upon the *P/M* cylinder walls, which completely enclose the *S/C*. This requires in turn very low tip-off rates and/or high spin rates to provide stability along the separation axis (and also implies the additional requirement that the principal axis of inertia on both the *S/C* and *P/M* is in the $+z$ direction). Furthermore the *S/C* must not tumble post-separation such that the telescopes are exposed to sunlight. The very low thrust levels provided by the *FEEPs* imply a very long period required to detumble, and this provides an additional reason to adopt a spin separation. The separation mechanism must result in the *P/M* retiring to a safe distance from the *S/C* after the separation manoeuvre is completed. This implies the ability to impart a relative velocity that ensures that the subsequent *P/M* orbit does not intersect with the *S/C* orbit. The *S/C* will provide commands and power to the *P/M* throughout the mated period, and therefore an electrical connection must exist between *S/C* and *P/M*, capable of providing not only power to the *P/M*, but also telemetry and telecommand. This connection must be separable. Given the proximity of the telescope heads to both separation interfaces (especially the separation plane between two *P/M*), any debris generation by the separation event is to be avoided. The separation mechanism must also allow safe separation at a *S/C* spin rate that is equal to or lower than any spin-rate limitations imposed by the functional elements of the *S/C* that are susceptible to acceleration forces, e.g. *FEEP* units.

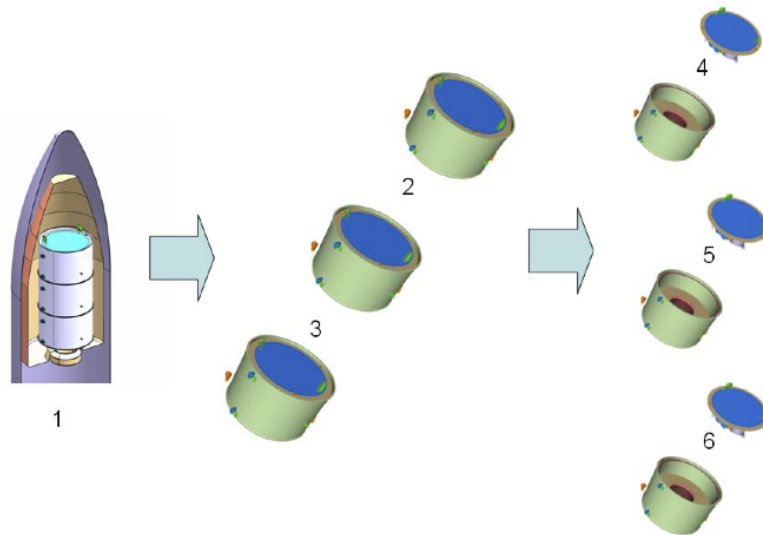


Figure 5.4.: The LISA mission undergoes six mission critical separation events. First, each S/C-P/M composite separates from the launch stack, commencing the cruise phase. At the end of the cruise phase, each composite separates into spacecraft and propulsion module.

5.4. Mission Analysis

For a complete description of the Mission Analysis work conducted, please refer to *Mission Analysis (LISA-ASU-TN-4001)*.

5.4.1. Overview

The different operational phases of the LISA mission are

- Launch and Early Operations Phase (LEOP)
- Cruise Phase
- Commissioning Phase
- Acquisition Phase
- Constellation Commissioning Phase
- Operational Phase
- Decommissioning Phase.

These in turn are separated into a number of sub-phases and specific mission events as defined in the Mission Requirement Document (MRD).

The spacecraft composite stack (LCM) will be launched on an Atlas V into a parking orbit, the final launcher burn will inject the composite stack into an escape orbit, with a low escape velocity in the range of $C_3 = 0.5 \text{ km}^2/\text{s}^2$. The composite spacecraft are then released from the stack individually.

Transfer to the final science orbits takes about 14 months. During this time, a chemical propulsion system will provide manoeuvrability to the spacecraft/propulsion-module (S/C-P/M) composites.

5.4.2. Launch and Early Operations Phase

The LEOP operations consist of those essential activities that are necessary to configure the spacecraft for cruise after separation from the launcher (where this cannot be done prior to launch) and to monitor the health of the composite spacecraft systems. Following separation, each launch composite will acquire a basic sun-pointing attitude using its sun sensors. The final configuration actions for the LEOP phase are to switch on the star trackers, upload the inertial pointing guidance and command the AOCS to an inertial pointing mode.

During the LEOP phase, communication between the ground segment and the S/C uses conventional omnidirectional antennas to provide coverage for any spacecraft attitude. This will be provided by two low-gain

Table 5.1.: Required Δv , actual transfer time Δt and initial mass for each of the spacecraft. The transfer time is constrained to not exceed 14 months, thus reducing the performance to a final mass of 1121 kg.

| S/C | Δv (m/s) | Δt (days) | initial mass (kg) | final mass (kg) |
|-----|------------------|-------------------|-------------------|-----------------|
| 1 | 899 | 426 | 1493 | 1121 |
| 2 | 1009 | 426 | 1546 | 1121 |
| 3 | 752 | 423 | 1424 | 1121 |

antennas (LGAs) which are mounted on the outer shroud of the propulsion module, and optimised to give a maximum field of view.

5.4.3. Transfer

During the 14 month transfer phase, starting from launcher separation, the **S/C-P/M** composites are travelling toward the target orbits, using a chemical propulsion system for manoeuvring. During the transfer an out-of-plane manoeuvre is needed in order to set up the required inclination.

As fuel-optimal transfers take more than 14 months to reach the operational orbits, constraining the transfer to 14 months reduces the performance somewhat so that only 1121 kg per **S/C** can be inserted into the final orbit, 40 kg less than in the optimal case. The details of the time-constrained transfer are presented in table 5.1.

5.4.4. Separation from Propulsion Module

The separation phase is very challenging in the LISA mission. The complex dynamics during the spinning separation and the uncertainties involved in the dynamic characteristics of the separation system (or mechanism) require special attention, as a failure during separation could result in an unrecoverable mission failure.

The approach of the analysis carried out in *Mission Analysis (LISA-ASU-TN-4001)* relies on the definitions of safe nutation zones, significantly simplifying the analysis. In addition, some idealisations are assumed. The most significant one is that the composite spacecraft's z -axis is its major principal inertia axis and it remains the same for the science spacecraft and its carrier after separation. This assumption actually can be taken as a design requirement for structure and propulsion system as well as overall spacecraft mass distribution at system level to ensure the assumption is met as closely as possible. If the z -axis is not a principal inertia axis, an extra nutation will develop which cannot be reduced just by increasing the spin rate. Thus, the safe separation zones would be eroded.

The separation impulses are the other key parameters that have considerable effect on the separation collision avoidance. To date, only the rotational impulses are considered. The translational impulses are not explicitly considered but included in the tolerance space between the safe separation zones. Generally, the separation impulses should be as low as possible except in the separation direction. The requirements on the separation system can be derived from the definitions of the safe separation zones and the spin rate damping requirements. The analysis approach can be seen as a stationary one, which virtually ignores the axial motions of the separating bodies. A transient analysis taking into account full aspects of the rigid-body dynamics will give an accurate picture about the separation process. This may improve the requirements on the definitions of the safe separation zones and on the limits for off-axis and tip-off impulses of the separation system.

The spin damping time for the science spacecraft is mostly driven by its angular momentum after separation. However, better **AOCS** design with quicker response time and shorter processing delay could help reduce the spin damping time. This time reduction gained from the improved **AOCS** performance will relax the requirements on the separation system if both the spin rate prior to separation and spin damping time are conditioned.

5.4.5. Science orbit

Orbit selection for the LISA mission is influenced by a number of drivers: the requirement for a benign environment for the payload; non-gravitational perturbations should be minimised to allow accurate micro-propulsion control; the thermal character of the orbit should be stable to avoid widely varying or sudden thermal

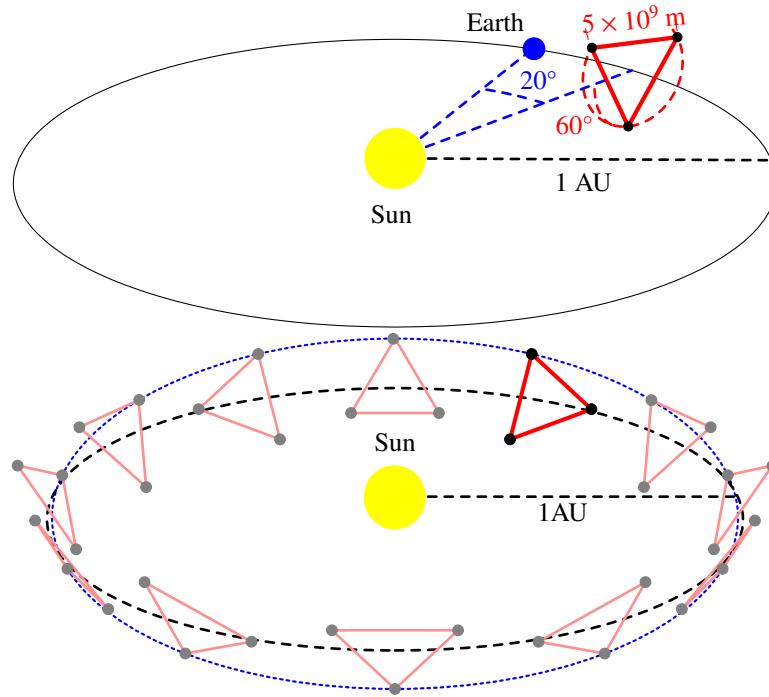


Figure 5.5.: *LISA Science Orbit.* The three spacecraft form an equilateral triangle with 5×10^6 km armlength, inclined by 60° with respect to the ecliptic. The constellation trails the Earth by about 20° and orbits the Sun in a distance of about 1 AU. The exact constellation parameters are optimised so that a mission duration of up to 10 years is feasible without exceeding the requirements on relative velocities and Doppler shift.

Table 5.2.: *Main parameters and constraints of the constellation for a typical science orbits.*

| Parameter | nominal value | actual value/deviation |
|---------------------|--------------------|---|
| Arm length | 5×10^6 km | $\delta L_{\max} = 45.55 \times 10^3$ km $\delta L_{\min} = -49.16 \times 10^3$ km |
| Relative velocities | 0 m/s | $\delta v_{\max} = 12.53$ m/s |
| Trailing angle | 20.00° | $\Phi_{\max} = 22.40^\circ$ $\Phi_{\min} = 18.16^\circ$ |
| Inner angle | 60° | $\alpha_{\max} = 60.81^\circ$ $\alpha_{\min} = 59.20^\circ$ |

shocks; the orbit must allow a quasi-static equilateral triangular constellation with arm lengths of 5×10^6 km to be maintained without active maintenance; distance from the Earth must be accounted for by the communications subsystem design.

The baseline LISA orbits for the three LISA S/C are Heliocentric Earth Trailing Orbits (HETOs), providing a good compromise between the orbit drivers. In their HETO constellation, the three S/C form a constellation with a plane of rotation that is inclined by 60° to the ecliptic (see figure 5.5). Nominally, that would lead to orbits with identical eccentricity $e = 0.009648$ and inclination of $i = 0.967541^\circ$. However, the influence of Earth, Moon and the large planets results in slightly perturbed orbital parameters (see table 5.3).

The optimisation process has taken into account the MRD requirements for range and range rate. It has also aimed to minimise the maximum angular excursion from the basic equilateral triangle solution. The target is a peak to peak value of no more than 3° (*i.e.* $\pm 1.5^\circ$) for each spacecraft. In addition a perturbing acceleration has been added to account for the mass distribution of the science spacecraft. It should be possible to limit this effect to an acceleration of 1×10^{-9} m/s², on each sciencecraft, which means that in the worst-case scenario the relative acceleration between two science-craft will be 2×10^{-9} m/s². Table 5.4 summarises the results obtained. Including the perturbation in the optimisation process results in the possibility of withstanding accelerations of

Table 5.3.: Initial orbital elements of the spacecraft for a typical science orbit

| | S/C 1 | S/C 2 | S/C 3 | nominal |
|-------------------|-------------|--------------|-------------|-----------|
| a (AU) | 0.998 789 | 0.998 810 | 0.998 795 | 1.0000 |
| e | 0.017 304 | 0.011 264 | 0.006 340 | 0.009 648 |
| i (degree) | 0.954 356 | 0.958 878 | 0.960 360 | 0.957 541 |
| Ω (degree) | 89.031 646 | -150.710 906 | -31.007 554 | — |
| ω (degree) | 278.424 821 | 226.006 930 | 324.381 855 | 270 |
| M (degree) | -25.606 033 | -93.436 417 | 48.475 876 | — |

Table 5.4.: Results for optimisation assuming different levels of perturbation; armlength 5×10^6 km, Earth offset 21° , perturbation acting on S/C 2 in the direction towards S/C 1 (positive acceleration values) and in the direction away from S/C 1 (negative acceleration values).

| perturbing acceleration (m/s^2) | angular excursion (degree) | $\max \dot{r}_{12}$ (m/s) | $\max \dot{r}_{13}$ (m/s) | $\max \dot{r}_{23}$ (m/s) |
|---|-------------------------------|------------------------------|------------------------------|------------------------------|
| 0 | 1.64 | 14.95 | 15.77 | 11.69 |
| 1×10^{-8} | 1.52 | 15.41 | 20.75 | 14.64 |
| 3×10^{-8} | 1.67 | 12.14 | 20.68 | 11.56 |
| 5×10^{-8} | 2.13 | 22.24 | 26.81 | 26.05 |
| 1×10^{-7} | 3.32 | 40.07 | 26.38 | 38.91 |
| -1×10^{-8} | 1.63 | 19.36 | 22.86 | 16.90 |
| -3×10^{-8} | 2.13 | 21.26 | 23.65 | 19.44 |
| -5×10^{-8} | 2.59 | 34.67 | 27.61 | 23.63 |
| -1×10^{-7} | 4.21 | 52.77 | 28.39 | 43.57 |

up to $5 \times 10^{-8} \text{ m s}^{-2}$ without exceeding the 3° maximum angular deviation requirement.

5.5. Mission budgets

5.5.1. Mass budget

The total available launch mass is limited by the capabilities of the foreseen launcher, Atlas V, whose relevant mass capability (including launch vehicle adaptor) for the “551” series is 6200 kg.

A detailed breakdown of the mass budget can be found in *System Budgets (LISA-ASU-BR-5001)*; in here, we report only an abridged mass budget, summarised in table 5.5.

Table 5.5.: Mass budget

| Subsystem | Mass per unit (kg) | Units | Total mass (kg) |
|-----------------------------|--------------------|-------|-----------------|
| Sciencecraft Bus | 345.3 | 3 | 1035.9 |
| Payload | 282.1 | 3 | 846.3 |
| Propulsion Module | 364.1 | 3 | 1092.1 |
| composite mass, no margin | | | 2974.3 |
| margin and contingency | | | 1132.1 |
| composite mass incl. margin | | | 4106.4 |
| Launch adaptor | 194 | 1 | 203.7 |
| Propellant | | | 1838.6 |
| Total mass | | | 6155 |

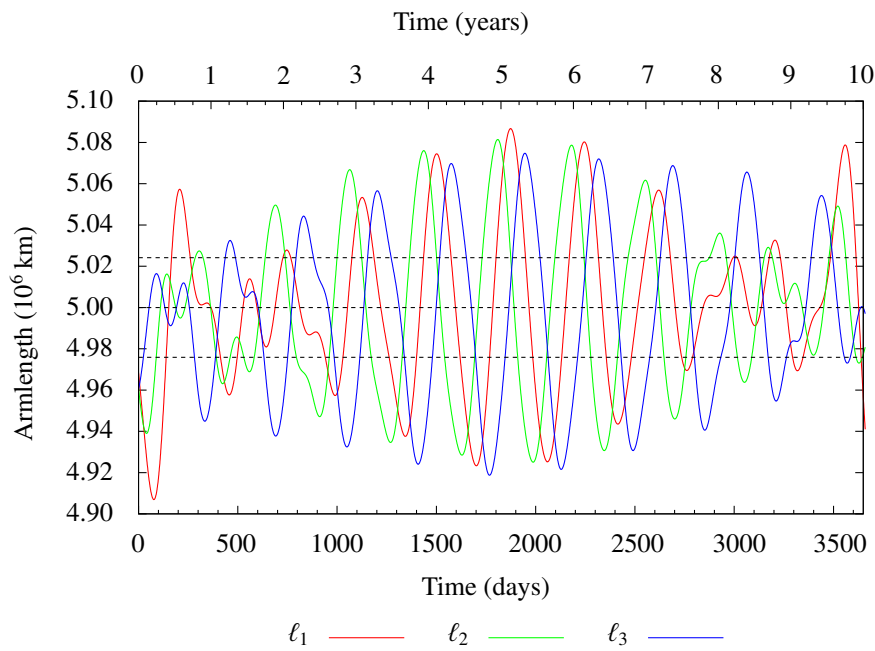


Figure 5.6.: Variation in inter-S/C distance for a 10-year mission duration. Notional armlength is 5×10^6 km, variations are within $\pm 10^5$ km, or 2%. Earth offset is between 17° and 22° . The dashed line indicates the “natural” oscillation without gravitational disturbances from Earth, Moon and the planets.

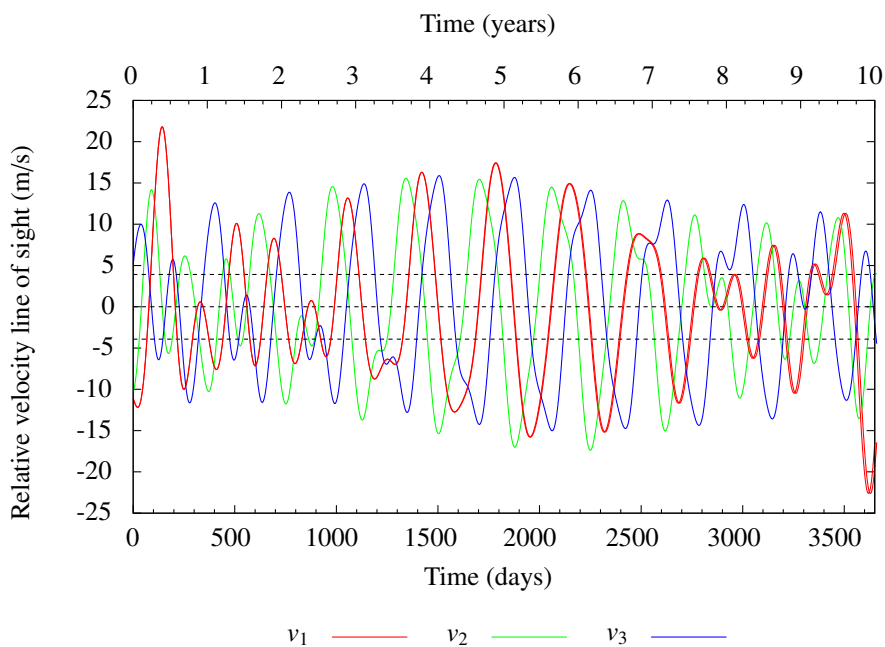


Figure 5.7.: Variation in the velocity in line-of-sight between the satellites for a 10-year mission. This variation determines the dopplershift between received and emitted beam. For the wavelength chosen for LISA, 1 m/s corresponds to 1 MHz Doppler shift. The dashed line indicates the “natural” oscillation without gravitational disturbances from Earth, Moon and the planets.

Table 5.6.: Required propellant loads for a selection of launch dates. 25 November is the overall worst case for a leading constellation target orbit, 10 April is the worst case trailing target constellation

| | Launch Date | v_{∞} m/s | S/C-P/M Δv (m/s) | | | total | S/C-P/M Mass (kg) | | |
|----------|-------------|---------------------|--------------------------|------|------|-------|-------------------|--------|--------|
| | | | 1 | 2 | 3 | | 1 | 2 | 3 |
| trailing | 23 February | 707 | 983 | 984 | 879 | 2846 | 549.23 | 548.61 | 486.05 |
| | 10 April | 633 | 896 | 899 | 1109 | 2904 | 627.44 | 497.91 | 496.12 |
| | 28 May | 659 | 885 | 918 | 938 | 2741 | 521.27 | 509.25 | 489.60 |
| | 01 July | 649 | 887 | 1062 | 832 | 2781 | 597.64 | 490.78 | 458.49 |
| leading | 24 August | 707 | 816 | 999 | 853 | 2668 | 558.44 | 470.75 | 449.21 |
| | 10 October | 713 | 1001 | 984 | 863 | 2848 | 559.67 | 549.23 | 476.62 |
| | 25 November | 661 | 931 | 1013 | 984 | 2928 | 567.08 | 549.23 | 517.05 |
| | 20 January | 653 | 907 | 1020 | 838 | 2765 | 571.41 | 502.68 | 461.98 |

Table 5.7.: Propellant budget for the operational phase.

| | |
|-----------------------------------|----------|
| Total impulse per thruster | 4500 Ns |
| Propellant mass per thruster | 0.064 kg |
| Propellant mass for 12 thrusters | 0.768 kg |
| Propellant mass for redundant set | 0.768 kg |
| Total mass | 1.536 kg |

5.5.2. Propellant budget

The baseline design propellant system for the transfer is a bi-propellant chemical propulsion system. The propulsion module has been designed to provide 1100 m/s of ΔV_2 . However the actual required ΔV for each spacecraft composite stack (LCM) for a particular transfer is typically substantially less than this amount. Table 5.6 shows the required propellant loads for the various transfers as calculated using the dry mass of the LCM including the 30 % system margin. No margin is placed on the calculated fuel mass.

In accordance with the MRD, no station keeping manoeuvres are performed during the operational lifetime. The ΔV budget for the science spacecraft accounts for initial attitude acquisition, constellation acquisition, and drag free control. The FEPP propulsion subsystem is installed on the Science Spacecraft to provide the high accuracy attitude control and the initial acquisition. The propellant requirements for the 10 year extended lifetime have been calculated based on a total impulse of 4500 Ns for each thruster and a minimum specific impulse of $I_{sp} = 4000$ s for the FEPP. Table 5.7 summarises the propellant requirements for the operational phase.

5.5.3. Power budget

The power budget has been compiled based on consumption numbers from similar projects including LISA Pathfinder (LPF). A system margin of 25 % has been applied on all power estimates except those of the thermal subsystem (effectively heaters); as the consumption of other units increases, the required heater power is expected to decrease, and hence adding a margin to both entries would be overly conservative.

The power consumption for the FEPP micro-propulsion has been assessed based upon the latest results and measurements from LPF, assuming a mean thrust of 50 μ N each on a full set of twelve thrusters. Harness losses are included and internal switching distribution of the power subsystem equipments is also incorporated into the budget calculation. Mission (*i.e.* launch date, orbit altitude, etc.), seasonal and ageing criteria impact on the power required and have been taken into account when producing the overall system budget.

Table 5.8 summarises the detailed power budgets for the operational phase and the transfer phase. Science mode and safe mode are the most significant modes for the power system, they form the base for the sizing estimates for both the solar panel surface area requirements and the battery sizing requirements.

The size of the battery is driven by the energy requirements during the early part of the LEOP, whereas the solar array size is determined by the operational power requirements of about 1 kW.

Table 5.8.: Power budgets, for the operational phase (nominal science mode and safe mode) and the transfer phase. The system margin of 25 % is applied to all contributions save the thermal control.

| Subsystem | Power consumption (W) | | | | | |
|-----------------------|-----------------------|--------------|----------------|----------------------|-----------------------|---------------------------|
| | Operational Phase | | Transfer Phase | | | |
| | Safe Mode | Science Mode | Pre-launch | Launch to separation | normal mode, downlink | firing chemical thrusters |
| Data Handling | 43 | 43 | 43 | 43 | 43 | 43 |
| Power | 10 | 10 | 10 | 10 | 10 | 10 |
| AOCS | 10.7 | 10.7 | 0 | 0 | 49.4 | 49.4 |
| X-band comm. | 30 | 150 | 30 | 30 | 130 | 130 |
| Thermal control | 336.7 | 136 | 0 | 0 | 112 | 112 |
| Micropropulsion | 143.4 | 143.4 | 0.6 | 0.6 | 0.6 | 0.6 |
| Payload | 0 | 277.3 | 0 | 0 | 0 | 0 |
| S/C total | 573.8 | 770.4 | 83.6 | 83.6 | 345 | 345 |
| P/M total | — | — | 0 | 0 | 115 | 147 |
| Composite total | 573.8 | 770.4 | 83.6 | 83.6 | 460 | 492 |
| Losses | 45.9 | 61.63 | 6.69 | 6.69 | 36.8 | 39.36 |
| Subtotal (w/o margin) | 619.7 | 832.03 | 90.29 | 90.29 | 496.8 | 531.36 |
| 25 % margin | 70.75 | 174.01 | 22.57 | 22.57 | 77.28 | 85.29 |
| Total | 690.46 | 1006.04 | 112.86 | 112.86 | 574.08 | 617.28 |

Table 5.9.: Battery sizing for LEOP phases

| Phase | Power demand (W) | Time (h) |
|----------------------------|------------------|----------|
| Pre-launch | 120 | 1 |
| Sun acquisition | 400 | 1 |
| Battery sizing | | |
| Energy required (Wh) | 520 | |
| Discharge efficiency | 90 % | |
| Max Depth of Discharge | 90 % | |
| Battery size required (Wh) | 642 | |
| Battery mass (kg) | 5.58 | |

The power output of the current science spacecraft solar array is scaled for distance, area, and lifetime effects from the latest test data for the 3G cells used on LPF to ensure that the requirement ($P > 650$ W at end-of-life (EOL)) is met. The current plan is to use RWE 3G 150-8040 solar cells of 28 % efficiency. These have been qualified through the ARTES 3 programme (between ESA/RWE) but require delta qualification to cover the LPF environment; once this has occurred, it implies automatic qualification for the very similar LISA environment. Differences in the operational parameters for the solar array between LPF and LISA are the angle toward the Sun (30° instead of 0°), the distance to the Sun (1.01 AU instead of 0.99 AU) and the foreseen degradation at EOL (0.89 instead of 0.93). The required solar array size for LISA is therefore given by:

$$A = 2.8 \text{ m}^2 \times \left(\frac{1006 \text{ W}}{650 \text{ W}} \right) \times \left(\frac{1.01 \text{ AU}}{0.99 \text{ AU}} \right)^2 \times \frac{1}{\cos 30^\circ} \times \frac{0.93}{0.89} = 5.4 \text{ m}^2 \quad (5.1)$$

The baseline solar array panel has an area of about 8 m^2 , so that a 5.4 m^2 solar array can be easily accommodated.

Table 5.10.: RF link budgets (up- and downlink) for the nominal and emergency scenarios in the operational phase

| Parameter | Operational phase | | | |
|-----------------------|-------------------|--------|-----------|--------|
| | nominal | | emergency | |
| | downlink | uplink | downlink | uplink |
| Data rate (kbps) | 217.8 | 2.2 | 0.055 | 0.055 |
| S/C-Antenna gain (dB) | 31.01 | 29.62 | -2.00 | -2.00 |
| SNR receiver (dB) | 3.08 | 34.33 | 7.65 | 18.49 |
| required SNR | 0.08 | 9.60 | 0.08 | 9.60 |
| Margin (dB) | 3.00 | 24.73 | 7.57 | 8.89 |

5.5.4. RF link budgets

The communication between the spacecraft and ground station during the operational phase uses HGA (+30 dB gain) on the spacecraft and the 34 m-DSN for up- and downlink in the nominal scenario. In the case of an emergency, communication is conducted via the omnidirectional LGA (-2 dB antenna gain) on the spacecraft and the 70 m-DSN on ground. The maximum distance between spacecraft and the ground station is assumed to be 69.5×10^6 km, the data generation rate per spacecraft during science operation is 11 kbps. The main characteristics of the communication scenarios in the operational phase are given in table 5.10.

During the transfer phase, the communication ability changes due to the changing distance between the spacecraft and the ground station. Communication is conducted via the 34 m-DSN and omnidirectional antennas on the S/C-P/M-composite. Upon arrival at the science orbits, the spacecraft can handle data rates for downlink and uplink are about 0.5 kbps and 1 kbps, respectively, through the omnidirectional antennas of the P/M. The theoretical rates during LEOP exceed 10 Gbps; actual rates during that phase are limited by the data handling capabilities of the S/C.

6. Mission Operations

6.1. Introduction

Science operation for LISA is assumed to be conducted jointly with representatives of both agencies in the Science Operation Centre (SOC), sharing the responsibility for the science products of the mission and the archiving of the data and the science products. The ESA share will be under the responsibility of the European Space Astronomy Centre in Madrid, Spain (ESAC). Each agency is assumed to build up a data centre and an archiving team according to their established processes. For the European data centre, an Announcement of Opportunity (AO) for nationally funded development, implementation, and operation is proposed. In the current baseline for the ground segment for LISA it is foreseen that the mission operations and the communications will be conducted via NASA's Deep Space Network (DSN).

The consolidation of the science products is under the responsibility of the SOC, and while different data processing pipelines are foreseen (though not enforced) only one set of consolidated data products will be put into the archive. Each archiving team is then responsible for maintaining and operating a local copy of the archive and providing a freely and publicly accessible interface.

The guiding principle for publication of the data products is to enable the scientific community to re-do any analysis of the data, starting from the Level 0 products to Level 3 products. It is therefore required to not limit the publication to the data, but to also make available the algorithms, the software, and the models used for processing the data as well as ensuring that the data processing history for any data published is traceable and retrievable. All data products will be public, the associated software under an open source license and no proprietary period is foreseen. The data centres will make the data available in regular intervals, *e.g.* 3 months (to be defined).

Raw data streams (Level 0) Level 0 data are the raw data streams necessary to obtain the basic time-delay interferometry (TDI) data streams and the relevant data streams of the gravitational reference sensor (GRS), the interferometric measurement system (IMS) and the science housekeeping. The Level 0 data contain all the data from each of the phase-meter channels, all the data from the GRS, and the complete science and payload housekeeping data. In addition, Level 0 data contain the software and the models used to produce Level 1 data from Level 0 data, in particular the full dynamical model of the GRS as well as the phase-meter algorithms.

Basic data streams (Level 1) Level 1 data are the data streams necessary to obtain the fully calibrated and corrected TDI data streams. The Level 1 data consist of the basic TDI data streams plus the relevant data streams of the GRS, the IMS, and the science housekeeping that are needed to correct the basic data streams for spurious accelerations, environmental and geometric effects. These data streams might include *e.g.* temperature, magnetic field, orientation of the test masses, accumulated charge, and any information on the effective optical pathlength. In addition, Level 1 data contain the software and the models used to produce Level 2 data from Level 1 data.

Processed data streams (Level 2) Level 2 data are the fully processed data streams that are needed to isolate individual gravitational wave signals using parametrised source models or other data analysis techniques. The Level 2 data consist of fully calibrated and corrected TDI data streams, augmented by the spacecraft ephemerides and data streams that contain the current best estimates for catalogued signals (Level 3) that can be used, *e.g.* to subtract the known signals prior to further data analysis. In addition, Level 2 data contain the software and the models used to produce Level 3 data from Level 2 data, in particular the software for modelling the instrument response to gravitational waves and the current best estimate for the noise spectra of the instrument.

Source catalogue (Level 3) One of the main products will be the publication of a source catalogue, containing the identified sources, their physical and astrophysical parameters (including confidence intervals or

Table 6.1.: *LISA Operations Characteristics*

| Metric | Comment |
|---|--------------------------------------|
| Number of spacecraft | 3 |
| DSN pass frequency | 1 every other day |
| On-board data storage per spacecraft | 5 GB |
| Recorded data per day per spacecraft | 432 Mb (5 kbps for 24 h) |
| Total mission data for 3 spacecraft | 2.4 Tb |
| Time required to down link 6 days' data | 8 h at 90 kbps |
| Frequency of required commanding | Once every six days |
| Number of Ops shifts per day | 1 |
| High gain antenna slews | 2 slews per spacecraft every 12 days |
| Ephemeris loads | Once every six days |
| Number of Manoeuvres | |
| Deterministic Manoeuvres | 3 per spacecraft |
| Trajectory Correction Manoeuvres | 5 per spacecraft |

probability density functions), potential electro-magnetic counterparts, as well as their strain time series $h(t)$. It will be updated regularly until it includes all the results obtained by the mission.

Additional products Although not the main scientific product of the LISA mission, the measured performance and the physics model of the inertial sensor can be useful for future space missions. Therefore, the respective data will be made available in a form yet to be determined.

6.2. Mission Phases

The operational phase of the LISA mission can be broken up into the following phases

Launch and early operations phase This phase covers the first 30 days after launch. The activities include all the launch-related activities leading to the separation of the three spacecraft on their trajectories.

Cruise phase This phase covers the 14-month period during which the three spacecraft move away from the Earth to their respective operational orbits. The major cruise activities are the spacecraft manoeuvres that are required to change the spacecraft trajectory.

Commissioning phase This phase covers the three-month period to achieve the science mode configuration required for science operations. Key activities include acquisition, drag-free testing, and instrument calibration.

Calibration phase This phase covers a three-month period during which the characteristics of the instrument will be established. The activities performed in this phase can be fully or partly repeated during the science operations phase as needed.

Science operations phase This phase covers the nominal five-year period during which science data are collected. Activities for this phase include the generation of science data products, health monitoring of the spacecraft and instrument, and the planning and execution of downlinks every other day with one spacecraft.

Post-operational phase This phase covers the period after the Science Operations Phase comes to an end. During this phase, the main activities are in the data centres and the data archive. The duration of this phase is at least two years.

Archive phase During the Archive phase support will be provided to the scientific community for the usage of the LISA data products. It is foreseen that the LISA archive will continue to be operated beyond the end of the Archive phase.

A mission timeline is given in figure 6.1 showing placement of the spacecraft manoeuvres for each of the three spacecraft.

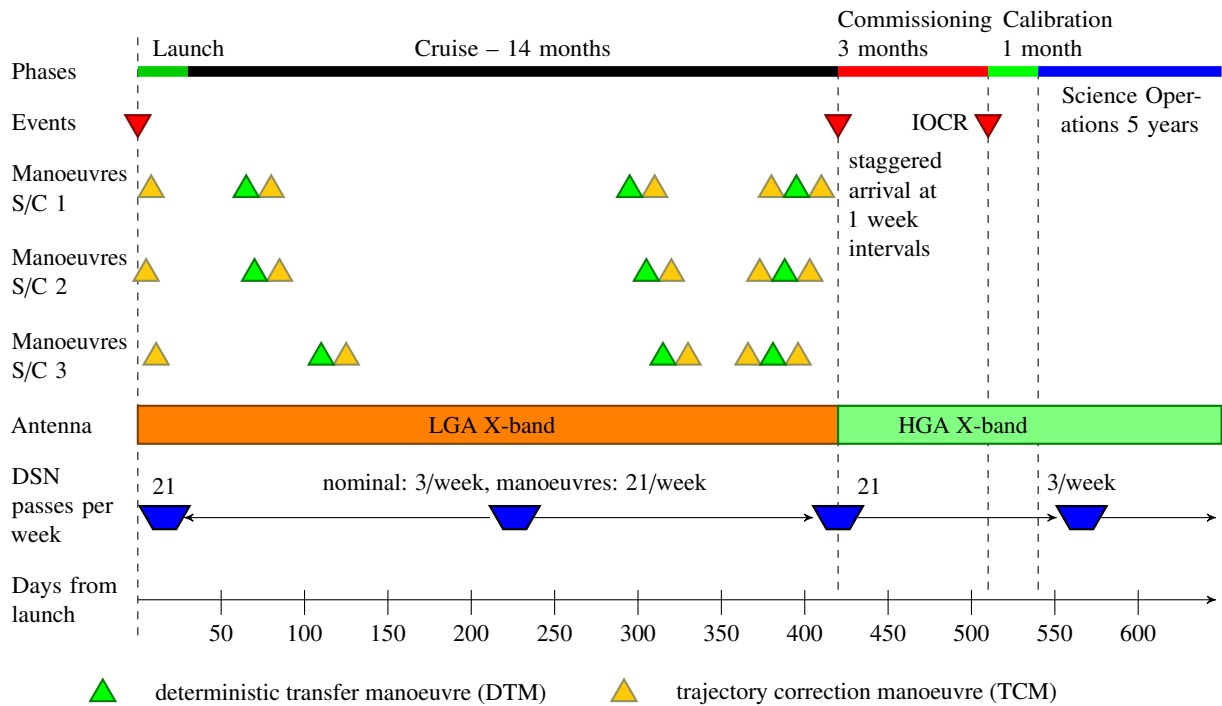


Figure 6.1.: Mission timeline as relevant for MOC activities. The science operations phase is shown not to scale and the post-operations phase is left out completely, as it has no impact on the mission operation.

6.2.1. Launch and Early Operations Phase

The Launch and Early Operations Phase (LEOP) contains the following critical activities.

Launch An expendable launch vehicle (ELV) will launch the entire stack (the three integrated spacecraft) from **Kennedy Space Center** (KSC) into a heliocentric orbit with a period of a few weeks longer than a year, so that after one orbit the spacecraft constellation will be 20° behind the Earth.

Spacecraft separation Separation of the stack from the second stage of the ELV will occur approximately five minutes after the injection burn. Ten minutes after separation of the stack the three spacecraft will separate from each other with $1 \text{ m/s } \Delta v$. After an appropriate interval, allowing for sufficient separation between spacecraft, each spacecraft will use thrusters located on the propulsion module to orient its solar cells to the Sun. The spacecraft battery is sized to allow for approximately three hours of operation prior to sun acquisition, although nominal acquisition will occur as early as inside one hour.

Deep Space Network (DSN) acquisition After separation from the launch vehicle or alternatively after a ground station comes into view approximately an hour after launch, each spacecraft will maintain continuous communications with the ground using omnidirectional antennas to allow initial orbit determination and to downlink engineering status data. After the spacecraft power levels are sufficient, each spacecraft will perform an initial functional checkout. Continuous communications will be maintained until the end of the Launch Phase to allow daily orbit determination updates.

Near-Earth trajectory correction manoeuvres Five, eight, and eleven days after launch respectively, trajectory correction manoeuvres (TCMs) will be performed by one of the spacecraft to correct launch errors. Because liquid rocket injection errors are expected to be small, these TCMs should be less than 10 m/s . These TCMs will also allow calibration of the spacecraft thrusters that will be used for the deterministic transfer manoeuvres.

6.2.2. Cruise Phase

During the cruise phase the following activities take place.

Spacecraft health monitoring During the majority of the cruise phase the spacecraft are in a sun-pointing

attitude with minimal active operations. Engineering telemetry is collected during this time and formulated into packets for storage and transmission to the ground at the next communication window. The spacecraft health monitoring telemetry will include spacecraft attitude, propulsion module thruster usage, solar array output, and temperature monitoring. It is unlikely that much payload commissioning can be performed during the cruise phase. However there is plenty of time if useful functional checks can be done that are compatible with the cruise configuration.

Manoeuvre design and execution The major cruise activities for the spacecraft are the planning and execution of eight manoeuvres per spacecraft over a 14-month time period. Each of the spacecraft will require three large deterministic transfer manoeuvres (DTMs) to transfer from launch to its respective operations orbit that establishes the triangular configuration. Fortunately these manoeuvres may be designed to occur at different times to smooth out the operations team workload. Each of these DTMs will require a correction manoeuvre one week afterwards to compensate for execution errors.

Operations orbit delivery At the end of the cruise phase each spacecraft performs the final DTM which establishes the operational orbit for the next 5 years. The cruise trajectories are designed to provide staggered arrivals with a two week separation. This final DTM for each spacecraft will be preceded by a correction manoeuvre seven days earlier to correct any position delivery error. An additional final cleanup manoeuvre will be scheduled for two weeks after the DTM, adjusting the spacecraft velocity so that the period of the achieved orbit will preserve the stability of the triangular configuration for the mission duration. Final delivery of each spacecraft is accomplished by separation of the propulsion module using a spring mechanism to impart a 3 cm/s separation velocity. The delivery target for each spacecraft is rendezvous with a point on its respective operations orbit within 500 km in position and 0.1 m/s in velocity and with an achieved heliocentric period within 38 s of nominal.

DSN passes Communications during most of the interplanetary transfer will be a pass weekly for each spacecraft with Doppler and range data being taken for orbit determination. This will be increased to daily passes starting one week before the first two DTMs and two weeks before the final DTM for each spacecraft; the daily passes will continue for each spacecraft until one week after the last TCM for each DTM.

6.2.3. Commissioning Phase

In the commissioning phase, the overall mission performance will be tested. The commissioning phase ends with a formal in-orbit commissioning review (IOCR) and responsibility of the mission will be handed over from the project manager to the mission manager. During the commissioning phase the following activities take place.

Drag-free attitude control system (DFACS) commissioning DFACS commissioning starts upon reaching the operational orbits. The test masses will be uncaged and the spacecraft attitude and orbit control system (AOCS) will be handed over to the DFACS control. The performance of the DFACS will be established and a number of commissioning procedures will be initiated, such as test on magnetic and thermal disturbances, actuation noise and parasitic stiffness. These tests will be derived from the previous experiences with the LISA Pathfinder (LPF) operations. DFACS commissioning requires intense ground support, both in commanding for the commissioning procedures and in instrument operations. Upon completion of DFACS commissioning, each spacecraft can be put in autonomous drag-free mode and the test mass interferometry has been established.

Laser commissioning The commissioning of the laser system includes establishing the necessary laser power and the required amplitude and frequency noise.

Acquisition During acquisition, the three spacecraft are brought to a science mode configuration and all laser links between the three spacecraft are established. Acquisition of the laser links between the spacecraft will make use of a collaborative strategy. The coarse pointing of the spacecraft is established through star trackers. The outgoing laser of the first spacecraft is then scanned in a slow spiral pattern over the pointing uncertainty cone. The remote (second) spacecraft signals the reception of light to ground control which then commands the first spacecraft to return to the sending direction corresponding to the time of reception (corrected for run-time delays), establishing the link from spacecraft (S/C) 1 to S/C 2. The second spacecraft now enters the spiral search procedure, establishing the link from S/C 2 to S/C 1 in the same way. The links between S/C 2 and S/C 3, and S/C 1 and S/C 3, respectively, are established in

a similar way. The main task of ground operations during the acquisition phase is to provide relative position and velocity information of all spacecraft to each of the three spacecraft and to command the commissioning procedure. Upon completion of the acquisition, each spacecraft receives laser light from each other spacecraft, and the *S/C–S/C* interferometry is established.

Measurement system commissioning With both the test mass interferometry and the inter-spacecraft interferometry established, the commissioning of the measurement system commences. This includes the commissioning of the phase measurement system, establishing clock transfer, data transfer and ranging, as well as the commissioning of the *TDI* procedure. The latter is a ground based activity, demonstrating the necessary corrections for laser frequency noise to verify the required sensitivity.

DSN passes Communications during this phase will be required for up to eight hours for each spacecraft.

This phase is complete when all spacecraft and payload functions have been checked in the operational mode and the *IOCR* has been successfully completed.

6.2.4. Calibration phase

During the calibration phase, final instrument characterisation and calibrations are performed. This includes:

Far-field characterisation The characterisation of the far-field quality of the received laser beam can be done only after the laser links are fully established and the measurement system is fully functional. Assessing the beam quality will require actuation of the spacecraft and of payload mechanisms.

Phase-centre characterisation The characterisation of the phase-centre requires actuation of the test masses and of the spacecraft to minimise the coupling between spacecraft jitter and length measurement.

Determination of instrument noise levels The noise levels of the instruments depend on the precise operational parameters and need to be assessed to optimise the science return.

DSN passes Communications during this phase will be required for up to eight hours for each spacecraft.

This phase is complete when the instrument calibration data are fully retrieved. Any of the activities required in this phase may need to be repeated either periodically in routine science operation or after incidents that are likely to change the calibration data (*e.g.* spacecraft safe-mode or loss of laser link).

6.2.5. Science Operations Phase

During the science operations phase the following activities take place.

Data Collection Collection of the science data (main, and auxiliary) will continue until end of mission.

Communications planning Nominal communication is scheduled every second day to one of the spacecraft. The nominal communication schedule will be superseded by an extended communication schedule in case of an upcoming merger event. Extended communication requires complete download from *all* spacecraft six days, four days, two days, and six hours before the merger event. The communications planning is performed by the Operations Planning Team.

Preliminary noise analysis The science data undergo a preliminary noise analysis to ensure data integrity. The preliminary noise analysis is performed by the Data Analysis Team.

Data validity monitoring and maintenance The validity of the data is monitored by the Instrument Operations Team using the instrument health data received from the Mission Operations Centre (MOC) and the preliminary noise analysis. Invalid data will be flagged.

Announcements of upcoming merger events Notices of transient events are published (and updated) through standard astronomy alert services (*e.g.* *The Astronomer's Telegram*). The responsibility for these notices lies with the Transient Event Coordination Committee (TECC).

Science product generation The science products, as described in section 6.1, are generated by the Data Centres.

Archiving The science data products, including the related code will be archived by the Data Archiving Team.

Decommissioning At the end of the science operations phase decommissioning activities are performed by which the the spacecraft is placed in a well determined passive state. All systems will be powered off.

6.2.6. Post-operations Phase

During the post-operations phase, the collection of science data and the mission operations has ceased, with the only activities in the data centres, the **SOC** and the data archive. The following activities are still performed:

Science Product Generation Generation of science products continues to make full use of the data collected
Archiving The science data products, including the related code will be archived in the data archive.

6.3. Mission Operations Elements

6.3.1. Deep Space Network

The **DSN** will provide command uplink, telemetry reception, and navigation services to the LISA mission. Specific services that are provided are

- Prior to launch, supporting the design and development of the spacecraft telecommunications hardware, the mission operations system, and the operations concept
- Providing a simulator for verifying compatibility of the flight hardware during integration and test
- Receiving requests for contacts, files and command sequences from the **MOC**
- Transmitting commands and files to the three spacecraft
- Scheduling passes with the network of 34-meter antennas, reconciling competing demands from other users
- Delivering tracking and navigation data, de-commutated telemetry, and event logs back to the **MOC**

6.3.2. Flight Operations

Spacecraft and instrument operations will be conducted at the **Mission Operations Centre (MOC)**. The key operations functions are described next.

Mission Control Team The Mission Control Team has the basic responsibility of monitoring and controlling the spacecraft. Specific activities include

- Radiate commands to all three spacecraft
- Monitor spacecraft engineering telemetry
- Perform real-time analysis and characterisations of performance parameters
- Contribute to definition and correction of spacecraft anomalies

Data Management Team The Data Management Team is responsible for the processing, storage and distribution of spacecraft and instrument data. Specific duties include

- Create channelised engineering telemetry for real time monitoring
- Remove spacecraft headers from raw telemetry received from **DSN** to create Level 0 products
- Deliver Level 0 products to Spacecraft Team and Instrument Operations Team
- Locally archive raw telemetry and Level 0 products

Spacecraft Team The analysis of spacecraft performance and health and the planning of future spacecraft activities are performed by the spacecraft team. Detailed activities include

- Monitor, analyse and characterise spacecraft health including thermal, telecommunications, consumables such as propellant, and flight software
- Identify anomalous conditions and work their resolution
- Participate in command generation
- Coordinate with the Navigation Operations Team on spacecraft manoeuvres
- Operate flight testbeds

Navigation Operations Team The Navigation Operations Team is responsible for those functions required to deliver the three spacecraft from launch into their final operations orbit. After the operations orbit is achieved the propulsion module is dropped off since additional manoeuvres are not required. Activities include

- Perform trajectory analysis
- Perform orbit determination
- Design cruise phase manoeuvres

- Create manoeuvre commands for incorporation into command sequences

Mission Planning Team The Mission Planning Team plays a lead coordination role in the planning and organising of mission activities. Specific activities include

- Provide high level integration of mission resources required for activity execution
- Plan use scenarios with other teams
- Design operational procedures
- Support development of flight operations plan
- Develop contingency plans
- Interface with Science Centre to coordinate observation strategies
- Work out telemetry return priority schemes

Sequence Integration Team The Sequence Integration Team develops and integrates the sequence of commands to control spacecraft and instrument activities. Specific activities include

- Receive and integrate commands from Spacecraft Operations Team and Instrument Operations team into command sequences
- Test command sequences in project testbed prior to uplink
- Prepare predictions of spacecraft state after command execution for comparison against real time telemetry results

DSN Scheduler It is necessary that mission operations, represented by the **DSN** scheduler, participate in the **DSN** allocation process to ensure that critical **DSN** resources are available to the Project. The **DSN** scheduler does the following.

- Schedule **DSN** antenna resources to meet project needs
- Resolve conflicts in antenna coverage requirements between LISA and other projects
- Maintain accurate allocation files of scheduled resources and distribute to other operations teams

6.4. Science Operations Elements

6.4.1. Science Operation Centre

The **SOC** will coordinate the development of the science operations ground segment and its operations to optimise the scientific return of the LISA mission.

During operation, it generates Level 1 data products from the Level 0 data products that are received from the **MOC**. It will also perform the planning and the coordination for the extended communication in the case of upcoming transient events. The extended communication schedule ensures that information on the sky position of the upcoming mergers can be assessed by the Data Centres (section 6.4.2).

In many cases, the precise time of occurrence of a transient event can be determined many weeks or even months before the event to within about a second. The error bars on the sky position collapse only in the last few hours to within a size that can be usefully covered with electro-magnetic telescopes. The extended data schedule therefore foresees download periods of six days, four days, two days and six hours before the transient event (see figure 6.3).

The activities of the **SOC** include

Science planning **SOC** is the unique point of contact with **MOC** on matters relevant for the payload uplink chain. This includes:

- Planning the instrument operations requests to update the configuration of the instruments
- Planning the calibration activities
- Planning the extended Ground Station communication in case of upcoming merger events

Instrument operations The **SOC** will be responsible for the instrument operations related activities. This includes:

- Calibration of the instruments in-flight and monitoring of their calibration throughout operations
- Maintenance of up-to-date instrument calibration files to be used in the data processing
- Monitoring instrument operations and triggering the updates of their configuration

Data processing The **SOC** is responsible for the generation of the Level 1 data products. This includes:

- Ingestion of the Level 0 data from **MOC**

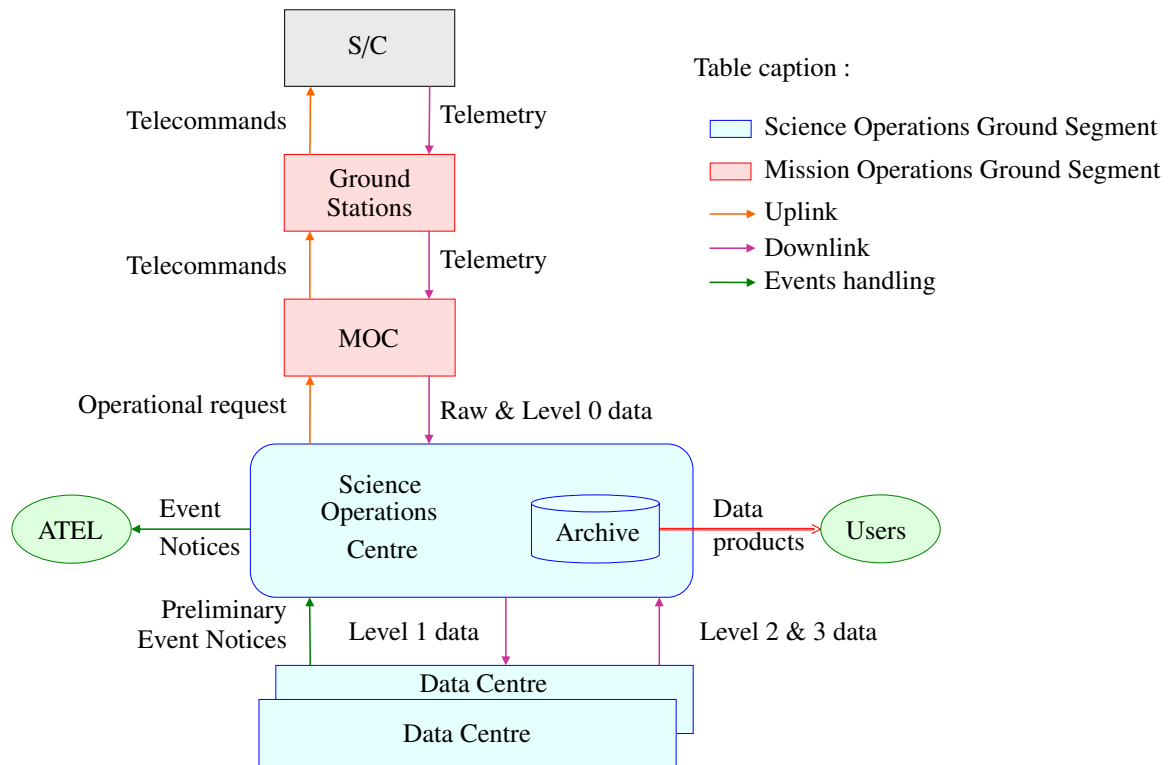


Figure 6.2.: Overview of the LISA Ground Segment including the data flow between the various elements of the Ground Segment. Data flows from S/C through MOC and SOC to the data centres (black). The data centres and the SOC issue data products (blue) that are archived and are accessible to the users. Merger Event Notices are issued by the SOC that receives preliminary event notices by the data centres.

- Quick-Look Analysis of the data to confirm that the Level 0 data are fine
- Level 1 data products are generated by a data processing pipeline
- Transfer of the Level 1 data to the Data Centres

Archive data quality Since it is likely to have two archives in different locations (one in Europe and one in the US) it is important to ensure that the higher level products being made available to the scientific community via these two archives are consistent. The high level products generated by the Data Centres will be consolidated before they are issued to the Archives.

Transient events consolidation The preliminary transient event notices received from the Data Centres have to be consolidated to ensure their quality and prepared for publication. This includes:

- Reception of the preliminary event notices from the Data Centres
- Assessment of the preliminary event notices
- Notification of the authorised transient notice using the established channels in astronomy
- To provide the detailed transient parameters to the science planning

6.4.2. Data centres

The task of the Data Centres is to generate and provide the main science products to the SOC. The expected number of Data Centres is at least two, one in Europe and one in the US. The European Data Centre is assumed to be developed and operated under national funds. Their activities include:

- Receiving Level 1 data from the SOC
- Creating Level 2 and Level 3 science products
- Performing quality analyses of the science data products
- Producing periodic releases of science data products to the SOC. A release period of three months is foreseen
- Supporting the quality analysis of the science data products
- Performing the data analysis required to generate event notices for upcoming transient events

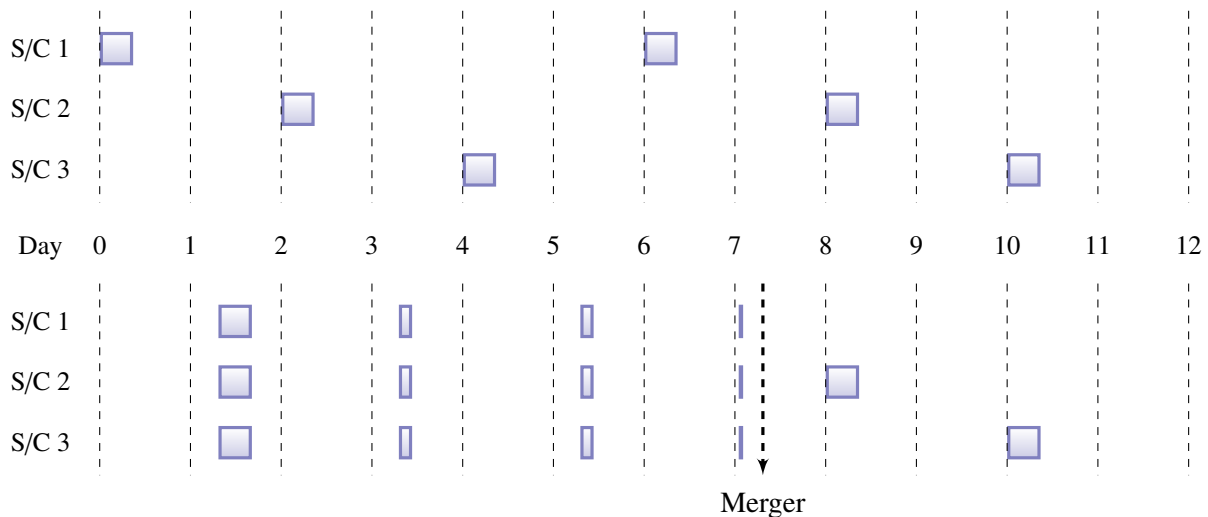


Figure 6.3.: *Communication schedule. In nominal communications (upper half), the constellation is contacted every second day for eight hours, iterating through the three spacecraft, resulting in a six day sequence for each spacecraft. In extended communications (lower half), each spacecraft is contacted six days, four days, two days and six hours before a merger event, after which the nominal schedule continues.*

- Producing preliminary event notices containing all the relevant parameters of the transient event
- Passing preliminary event notices to the **SOC**
- Providing interface with Guest Investigators, where applicable

6.4.3. Data Archive

The data archive is the primary repository for all the science data products of all levels. The data archive is freely and publicly accessible and provides standard interfaces to the data (web browser, ftp, etc.). The data are available in standard formats (*e.g.* HDF, FITS, XML), the associated software is available in open source.

Two data archives are currently foreseen, one in Europe and one in the US. Both archives will contain identical data products. Development of user interfaces, however, will be under the responsibility of the local data archives. Their activities include:

- Development, operation and maintenance of the archive system
- Populate the archive with the data products (Level 0 from the **MOC**, Level 1 from the **SOC** and subsequent levels from the Data Centres).
- Providing free and public access to the archive

6.5. Data Analysis

As LISA does not have the ability for dedicated observational campaigns but observes all the sky all the time, the extraction of the science from the data requires a special effort. As stated above, the current planning foresees an **AO** for the data analysis pipeline. In this section, the current state of the data analysis preparation, the methods and techniques, and the general principles will be summarised.

6.5.1. General principles

The basis for the LISA data analysis are the Level 2 data products, *i.e.* the fully calibrated and corrected **TDI** data streams, augmented by the spacecraft ephemerides. The goal of the data analysis is to determine the astrophysical parameters of the sources of the various gravitational wave (GW) signals in the data stream; more generally, the output of the data analysis is a probability density function (PDF) for the source parameters, encoding not only the most likely value, but the full probabilistic information.

While the problem is well defined and well understood in principle, the large number of parameters per source, *e.g.* 14 for extreme mass-ratio inspirals (EMRIs) or 17 for black hole binaries, and the even larger number of potential sources (tens of millions Galactic binaries) in the data stream makes an exhaustive search of the parameter space impossible. Consequently, the identification of sources in the data stream is limited to only the brightest ones with a high signal-to-noise ratio (SNR) that are well “separated” in the parameter space. Typically, an $\text{SNR} > 5$ is assumed as a threshold for detectability, but higher SNR can be required if the signal is not well modelled. But even then the number of identifiable sources is in the tens of thousands.

The largest number of these are Galactic binaries, which have a relatively simple signal structure (see section 2.5) – an almost monochromatic signal with only a very small frequency change over the lifetime of LISA. Signals from massive black hole binaries (MBHBs) have a more complex signal structure but are much less numerous (tens to hundreds) and have an SNR of up to 10^4 . The most complex signals are emitted by EMRIs, which have a relatively low SNR of about 100 or less.

Almost all of the detection algorithms for *known* sources rely on *matched filtering*, a correlation of a signal template $q(\vec{p}, t)$ depending on parameters \vec{p} with the data stream $s(t)$, weighted by the inverse of the spectral density of the noise $S_n(f)$:

$$\langle q(\vec{p}, t), s(t) \rangle = \int \frac{\tilde{q}(f)\tilde{s}(f)^* + \tilde{q}(f)^*\tilde{s}(f)}{S_n(f)} df \quad (6.1)$$

where $\tilde{s}(f)$ and $\tilde{q}(f)$ are the Fourier transforms of $s(t)$ and $q(\vec{p}, t)$, respectively. Finding the parameters \vec{p}_0 for a given source is then reduced to maximising $\langle q(\vec{p}, t), s(t) \rangle$ with respect to \vec{p} using the proper waveform q for the source. The *effective* SNR is then given by that maximum,

$$\text{SNR} = \langle q(\vec{p}_0, t), s(t) \rangle \quad (6.2)$$

The keys to the LISA data analysis are therefore fast and reliable search algorithms and high-fidelity waveform templates that allow to have the SNR to be as close as possible to the *true* SNR $\langle Q(\vec{p}_0, t), s(t) \rangle$ where $Q(\vec{p}_0, t)$ describes the source’s waveform perfectly.

Searching the data stream for unknown, or just unmodeled, signals such as GW bursts makes use of methods that do not use templates, but rather search for excess power or use maximum-likelihood methods, such as the coherent waveburst pipeline currently in use for LIGO (Klimenko et al., 2008).

It should be noted that some aspects of instrument characterisation and noise identification will be performed at the stage of Level 2 products, *i.e.* during the data analysis. This requires interaction between the data centres and the SOC as foreseen in section 6.4.

6.5.2. Templates

The generation of high-fidelity templates varies in difficulty with the different sources. The templates for the signals from galactic binaries are by far the easiest to obtain, as they consist of a sinusoidal with a weakly time-dependent frequency:

$$\begin{aligned} A &= \frac{2}{D_L} (\pi f)^{2/3} \mathcal{M}^{5/3} & \phi(t) &= 2\pi(ft + \frac{\dot{f}t^2}{2}) \\ h_+ &= A(1 + \cos^2 \iota) \cos(\phi(t) + \phi_0) & h_\times &= -2A \cos \iota \sin(\phi(t) + \phi_0) \end{aligned} \quad (6.3)$$

where D_L is the luminosity distance, f the frequency, ι the inclination of the binary’s orbit with respect to the direction to the Solar System barycenter (SSB), and \mathcal{M} the chirp mass.

The templates for the MBHB are somewhat more complicated. During the inspiralling phase, they can be described sufficiently well using, *e.g.*, post-Newtonian (PN)-approximation, and the signal can be calculated by integrating the resulting differential equations (Lang and Hughes, 2006). The signal during coalescing and the ringdown can be calculated only through numerical relativity (NR). Fortunately, NR has made significant progress in the last decade (Baker et al., 2006, 2007a,b, 2008; Buonanno et al., 2007b; Campanelli et al., 2006a,b; Pretorius, 2005), so that waveforms from coalescing MBHB and the ringdown phase are available. The two

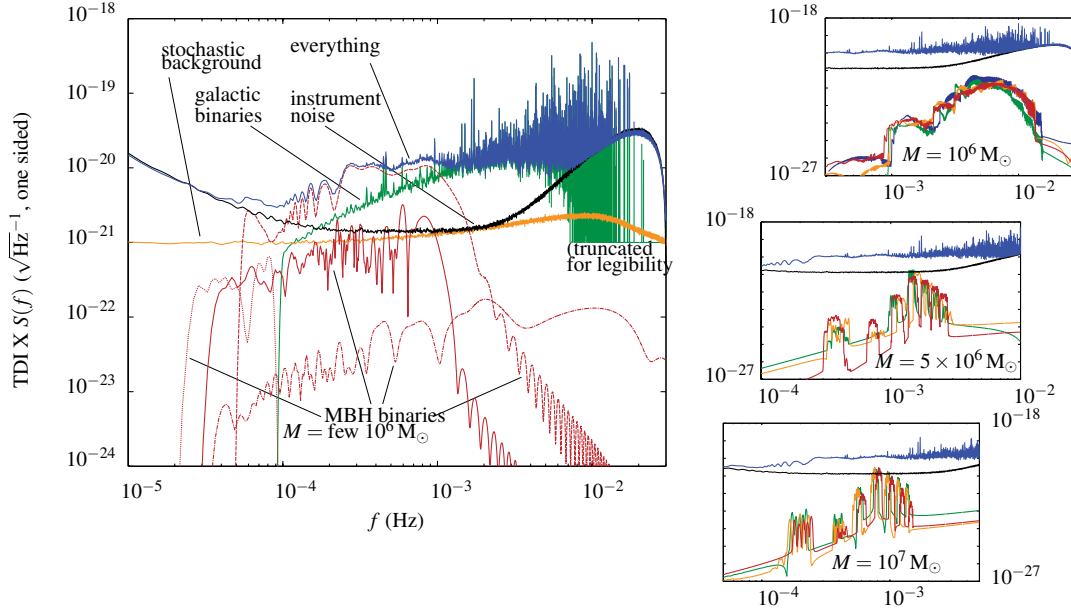


Figure 6.4.: A graphic representation of a Round 4 training dataset. This particular realisation includes more than 60 million chirping Galactic binaries, 4 MBH binaries, 9 EMRIs, 15 cosmic-string bursts, an isotropic stochastic background, and of course instrument noise.

different phases can be combined to provide a continuous waveform from early inspiral to ringdown (Baker et al., 2007c; Buonanno et al., 2007a; Campanelli et al., 2009).

The templates for the EMRIs are even more complex. While they can in principle be calculated directly, it is computationally far too expensive to do so for the needs of LISA data analysis. Therefore, so called “kludge” waveforms are used (Babak et al., 2007) that approximate the “real” waveforms sufficiently well to allow detection.

6.5.3. Algorithms

The algorithms that are currently used to search for the optimal source parameters and to calculate the posterior PDF range from straight-forward optimisers to elaborated statistical and genetic algorithms.

Methods employed include time-frequency searches (Brown et al., 2007; Gair and Jones, 2007; Gair and Wen, 2005; Gair et al., 2008b), Markov-chain Monte Carlo (MCMC) searches (Christensen and Meyer, 1998; Christensen et al., 2004; Cornish and Crowder, 2005; Cornish and Porter, 2006; Crowder and Cornish, 2007; Stroer et al., 2006; Trias et al., 2008) and its variants, such as reversible jump Markov-chain Monte Carlo (MCMC) (Stroer and Veitch, 2009), and parallel tempered MCMC (Key and Cornish, 2009; Littenberg and Cornish, 2010) as well as a combination of simulated annealing and MCMC (Cornish and Porter, 2007a,b,c; Gair et al., 2008a).

Furthermore, nested sampling (Feroz et al., 2010; Gair et al., 2010) and its extension MultiNest (Feroz et al., 2009) as well as genetic algorithms (Crowder et al., 2006; Petiteau et al., 2010), and combinations of these algorithms are used (Gair and Porter, 2009).

Owing to the complexity of the LISA data, it is highly likely that there is no single “optimal” algorithm but that a combination of different search strategies and parameter extraction algorithms will have to be employed.

6.5.4. Mock LISA Data Challenge

The data-analysis for LISA is challenging and has been perceived in the past as a potentially insurmountable problem for the mission. In response to that, the Mock LISA Data Challenge (MLDC) had been proposed and discussed at meetings organised by the US and European LISA Project that were attended by a broad cross section of the international gravitational-wave community. The challenges are meant to be blind tests, but

Table 6.2.: Characteristics of the different rounds of the MLDC

| | MLDC 1 | MLDC 2 | MLDC 1b | MLDC 3 | MLDC 4 |
|-----------------------|---|---|---|--|--|
| Galactic Binaries | Verification binaries, isolated systems | Galaxy with 3×10^6 binaries | Verification binaries, isolated systems | Galaxy with 6×10^7 chirping binaries | Galaxy with 6×10^7 chirping binaries |
| MBHB | Isolated systems | 4–6 systems over simulated Galaxy and EMRI signals | Isolated systems | 4–6 spinning systems, over simulated Galaxy and EMRI signals | 4–6 spinning, precessing systems, extended to low mass, over simulated Galaxy and EMRI signals |
| EMRI | | 4–6 isolated systems, over simulated Galaxy and MBH signals | Isolated systems | 5 signals all in one set, weaker signals | 3 frequency bands, expected 2 EMRI per band (Poisson statistics) |
| Bursts | | | | Cosmic string cusps | Cosmic string cusps (20 expected, Poisson statistics) |
| Stochastic background | | | | Isotropic | Isotropic |
| Participants | 40 | 39 | 25 | 27 | |
| Institutions | 10 | 13 | 10 | 15 | |

not really a contest and serve the dual purposes of fostering the development of LISA data analysis tools and capabilities, and of demonstrating the technical readiness already achieved by the gravitational-wave community in being able to distill a rich science payoff from the data.

The MLDC Task force has been working since 2006 to formulate challenge problems of maximum efficacy, to establish criteria for the evaluation of the analyses, to develop standard models of the LISA mission (orbit, noises) and of the LISA sources (waveforms, parametrisation), to provide computing tools such as LISA response simulators, source waveform generators, and a Mock Data Challenge file format, and more generally to provide any technical support necessary to the challengers, including moderated discussion forums and a software repository. The challenges involve the distribution of several data-sets, encoded in a simple standard format, and containing combinations of realistic simulated LISA noise with the signals from one or more LISA gravitational-wave sources of parameters unknown to the challenge participants. The first round of challenges focused on parameter estimation for examples of several sources in otherwise clean noise. Subsequent challenge data-sets have addressed increasingly ambitious data-analysis problems. Round 2, completed in 2007, focused on the global analysis problem. A re-issue of challenge 1, called Round 1B, also ran in 2007 to provide an easy opportunity for new groups to develop analysis codes. A similar challenge, Round 1C, oriented toward students of gravitational-wave astronomy, is ongoing. Round 3, with new sources and source models finished in Spring 2009 (see table 6.2). The current challenge Round 4 returns to the global analysis problem. While the third round of the MLDC was focused on increasing the complexity and variety of GW sources, this current iteration is devoted to the global-fit problem of detecting and analysing sources of different types superposed in the LISA data. All sources classes (*i.e.* galactic binaries, EMRIs, MBHB, cosmic-string bursts and stochastic background) are included, with a larger numbers of EMRIs and cosmic-string bursts and larger parameter ranges for massive black hole (MBH) binaries and EMRIs than in previous rounds (see figure 6.4). The different rounds, their challenges, sources and parameter constraints are described in a series of papers (Arnaud et al., 2007a,b; Arnaud et al., 2006a,b; Babak et al., 2008a,b, 2010).

7. Management

The LISA mission is a proposed joint European and US scientific venture. Agreements on how to proceed in the formulation phase have been documented in the “Formulation Phase Agreement” of August 2004, signed by ESA and NASA Headquarters. NASA and ESA project offices were established in 2001 as a result of a Letter of Agreement (LoA) signed between the two agencies. Since then the combined LISA team has been working closely together to:

- Mature the science requirements
- Define and trade-off mission concepts
- Advance the selected mission concept to a mature mission architecture
- Identify and advance the necessary technologies required for the mission success

Thanks to the stability of the mission science requirements and the stability of the resulting mission concept, the LISA project has made tremendous progress towards maturing the mission architecture and technology development and towards achieving the above objectives. The team has initiated lower level trades for defining sub-system architectures and developing sub-system requirements.

The working agreement of 2004 defines preliminary division of responsibilities between NASA and ESA for the purpose of the formulation phase as well as parallel activities for the purpose of risk reduction, *e.g.*, the micro-newton thrusters.

Before entering the implementation phase, the agencies will negotiate actual roles and responsibilities, documented in an Memorandum of Understanding (MoU).

In order to assess the full implications (including cost and schedule) of the mission ESA has conducted the industrial study with the assumption of being the mission lead. The System Specification has therefore been compiled to cover the whole mission and the Sub-system Specifications have been prepared for all the major sub-systems.

7.1. Procurement strategy

As the integrated scientific complement is of critical importance to the mission, it is proposed to be funded by the agencies and to be the object of the main industrial procurement contract. Member States support has so far been fruitfully used in support of technology development activities and is planned to be used later in support of data analysis. National groups (*e.g.*, in Germany, France, UK and Italy, amongst others) are already actively involved, under the coordination of ESA, in the development of data analysis algorithms and methodologies that will be later used for the processing of scientific data and possibly their archiving with an organization structure that will be defined later.

A. Cosmic Vision Science Questions

Here we give for reference the science questions defined in *Cosmic Vision: Space Science for Europe 2015–2025* for the Cosmic Vision programme.

1. What are the conditions for planet formation and the emergence of life?
 - 1.1 From gas and dust to stars and planets
Map the birth of stars and planets by peering into the highly obscured cocoons where they form
 - 1.2 From exo-planets to biomarkers
Search for planets around stars other than the Sun, looking for biomarkers in their atmospheres, and image them
 - 1.3 Life and habitability in the Solar System
Explore in situ the surface and subsurface of the solid bodies in the Solar System most likely to host – or have hosted – life
Explore the environmental conditions that makes life possible
2. How does the Solar System work?
 - 2.1 From the Sun to the edge of the Solar System
Study the plasma and magnetic field environment around the Earth and around Jupiter, over the Sun's poles, and out to the heliopause where the solar wind meets the interstellar medium
 - 2.2 The giant planets and their environments
In situ studies of Jupiter, its atmosphere, internal structure and satellites
 - 2.3 Asteroids and other small bodies
Obtain direct laboratory information by analysing samples from a Near-Earth Object
3. What are the fundamental physical laws of the Universe?
 - 3.1 Explore the limits of contemporary physics
Use stable and weightless environment of space to search for tiny deviations from the standard model of fundamental interactions
 - 3.2 The gravitational wave Universe
Make a key step toward detecting the gravitational radiation background generated at the Big Bang
 - 3.3 Matter under extreme conditions
Probe gravity theory in the very strong field environment of black holes and other compact objects, and the state of matter at supra-nuclear energies in neutron stars
4. How did the Universe originate and what is it made of?
 - 4.1 The early Universe
Define the physical processes that led to the inflationary phase in the early Universe, during which a drastic expansion supposedly took place.
Investigate the nature and origin of the Dark Energy that is accelerating the expansion of the Universe
 - 4.2 The Universe taking shape
Find the very first gravitationally-bound structures that were assembled in the Universe – precursors to today's galaxies, groups and clusters of galaxies – and trace their evolution to the current epoch
 - 4.3 The evolving violent Universe
Trace the formation and evolution of the supermassive black holes at galaxy centres – in relation to galaxy and star formation – and trace the life cycles of matter in the Universe along its history

B. LISA Science Objectives

Here we give for reference the science objectives for LISA as defined in *LISA Science Requirements Document*.

1. Trace the formation, growth, and merger history of massive black holes
 - 1.1 Trace the formation, growth, and merger history of **IMBHs** and **MBHs** out to redshift $z = 15$
 - 1.2 Determine the merger history of **MBHs** with masses of $10^4 M_{\odot} - 3 \times 10^5 M_{\odot}$ from the era of the earliest known quasars, $z \sim 6$
 - 1.3 Determine the merger history of **MBHs** with masses between $3 \times 10^5 M_{\odot}$ and $10^7 M_{\odot}$ at later epochs, $z < 6$
2. Explore stellar populations and dynamics in galactic nuclei
 - 2.1 Characterise the immediate environment of **MBHs** in $z < 1$ galactic nuclei from **EMRI** capture signals
 - 2.2 Study intermediate-mass black holes from their capture signals
 - 2.3 Improve our understanding of stars and gas in the vicinity of Galactic black holes using coordinated gravitational and electromagnetic observations
3. Survey compact stellar-mass binaries and study the structure of the Galaxy
 - 3.1 Elucidate the formation and evolution of Galactic stellar-mass binaries; constrain the diffuse extra-galactic foreground
 - 3.2 Determine the spatial distribution of stellar mass binaries in the Milky Way and environs
 - 3.3 Improve our understanding of white dwarfs, their masses, and their interactions in binaries, and enable combined gravitational and electromagnetic observations
4. Confront General Relativity with observations
 - 4.1 Detect gravitational waves directly and measure their properties precisely
 - 4.2 Test whether the central massive objects in galactic nuclei are the black holes of general relativity
 - 4.3 Make precision tests of dynamical strong-field gravity
5. Probe new physics and cosmology with gravitational waves
 - 5.1 Study cosmic expansion history, geometry and dark energy using precise gravitationally calibrated distances in cases where redshifts are measured
 - 5.2 Measure the spectrum of, or set bounds on, cosmological backgrounds
 - 5.3 Search for burst events from cosmic string cusps
 - 5.4 Search for unforeseen sources of gravitational waves

Acronyms

- MRD** Mission Requirement Document.
LISA-ScRD-066 Science Requirement Document.
AC alternating current; *fig* referring to oscillating processes or entities.
ADC analog-to-digital converter.
AGN active galactic nuclei.
AIVT assembly, integration, verification, and testing.
AM CVn class of cataclysmic variable stars.
AO Announcement of Opportunity.
AOCS attitude and orbit control system.
ASD amplitude spectral density.
AST autonomous star tracker.
ATA **Allen Telescope Array**.
BAO baryonic acoustic oscillation.
BH black hole.
BHB black hole binary.
CBE current best estimate.
CCD charge-coupled device.
CDM cold dark matter.
CFRP carbon fibre reinforced plastic.
CMB cosmic microwave background.
CMNT colloid micro-newton thruster.
COBE **COsmic Background Explorer**.
CoM centre of mass.
CTE coefficient of thermal expansion.
DC direct current; *fig* referring to quasi-static processes or quasi-constant entities.
DFACS drag-free attitude control system.
DOF degree of freedom.
DPLL digital phase locked loop.
DRS disturbance reduction system.
DSN Deep Space Network.
DTM deterministic transfer manoeuvre.
EELV evolved expendable launch vehicle.
EGAPS European Galactic Plane Surveys.
ELV expendable launch vehicle.
EM electro-magnetic.
EMC electro-magnetic compatibility.
EMRI extreme mass-ratio inspiral.
EOL end-of-life.
EOM electro-optical modulator.
ESA European Space Agency.
ESAC European Space Astronomy Centre in Madrid, Spain.
FDIR failure detection, isolation, and recovery.
FEED field-emission electric propulsion.
FPAG Fundamental Physics Advisory Group.
FPGA field-programmable gate array.
GR General Theory of Relativity.
GRS gravitational reference sensor.
GS ground station.
GSFC Goddard Space Flight Center.
GW gravitational wave.
HETO Heliocentric Earth Trailing Orbit.
HGA high-gain antenna.
HST **Hubble Space Telescope**.
IGM inter-galactic medium.
IMBH intermediate-mass black hole.
IMF initial mass function.
IMRI intermediate mass-ratio inspiral.
IMS interferometric measurement system.
IOCR in-orbit commissioning review.
ISM instrument sensitivity model.
JILA **Joint Institute for Laboratory Astrophysics**.
JWST **James Webb Space Telescope**.
KSC **Kennedy Space Center**.
LAGOS Laser Antenna for Gravitational-radiation Observation in Space.
LCM spacecraft composite stack.
LED light-emitting diode.
LEOP Launch and Early Operations Phase.
LGA low-gain antenna.
LIGO **Laser Interferometer Gravitational Wave Observatory**.
LIST **LISA International Science Team**.
LMC Large Magellanic Cloud.
LoA Letter of Agreement.
LOS line of sight.
LPF **LISA Pathfinder**.
LSST **Large Synoptic Survey Telescope**.
LTP LISA Pathfinder technology package.
LVA launch vehicle adaptor.
MBH massive black hole.
MBHB massive black hole binary.
MCMC Markov-chain Monte Carlo.
MLB motorised light band.
MLDC **Mock LISA Data Challenge**.
MOC Mission Operations Centre.
MOFPA Master Oscillator Fibre Power Amplifier.
MoU Memorandum of Understanding.
NASA **National Aeronautic and Space Administration**.
NPRO non-planar ring oscillator.
NR numerical relativity.
OATM optical assembly tracking mechanism.
OBC on-board computer.
OMS Optical Metrology System.
P/M propulsion module.
PAAM point-ahead angle mechanism.
PCDU power control and distribution unit.
PDF probability density function.
PN post-Newtonian.
PTF **Palomar Transient Factory**.
QNM quasi-normal mode.
QPD quadrant photodetector.
RATS Rapid Time Survey.
RF radio frequency.
RIN relative intensity noise.
RSS root sum square.
RXTE **Rossi X-Ray Timing Explorer**.
S/C spacecraft.

S/C-P/M spacecraft/propulsion-module.
SDSS Sloan digital sky survey.
SIM Space Interferometry Mission.
SMBH super-massive black hole.
SMC Small Magellanic Cloud.
SNR signal-to-noise ratio.
SOC Science Operation Centre.
SSB Solar System barycenter.
TC/TM telecommand/telemetry.
TCM trajectory correction manoeuvre.

TDI time-delay interferometry.
TECC Transient Event Coordination Committee.
TM test mass, *often proof mass*.
TRL Technology Readiness Level.
TT&C telemetry, tracking, and command.
TWTA traveling-wave tube amplifier.
USO ultra-stable oscillator.
UV ultra-violet.
WMAP Wilkinson Microwave Anisotropy Probe.

Bibliography

Scientific References

- Abel, T et al. (Jan. 2002). *Science* **295**, pp. 93–98.  
- Albrecht, A et al. (Sept. 2006). ArXiv Astrophysics e-prints. 
- Alexander, T (Nov. 2005). *Phys. Rep.* **419**, pp. 65–142.  
- Alexander, T and C Hopman (June 2009). *ApJ* **697**, pp. 1861–1869.  
- Aller, MC and D Richstone (Dec. 2002). *AJ* **124**, pp. 3035–3041.  
- Alvarez, MA et al. (Aug. 2009). *ApJ* **701**, pp. L133–L137.  
- Amaro-Seoane, P et al. (Sept. 2007). *Class. Quantum Grav.* **24**, pp. 113–+.  
- Amaro-Seoane, P et al. (Feb. 2010). *MNRAS* **401**, pp. 2268–2284.  
- Amico, P et al. (2002). *Class. Quantum Grav.* **19** (7), pp. 1669–1674. 
- Argence, B et al. (Apr. 2010). *Phys. Rev. D* **81.8**, pp. 082002–+. 
- Armano, M et al. (2005). *Class. Quantum Grav.* **22** (10), S501–S507. 
- Armstrong, JW et al. (Dec. 1999). *ApJ* **527**, pp. 814–826. 
- Arnaud, KA et al. (Oct. 2007a). *Class. Quantum Grav.* **24**, pp. 551–+.  
- Arnaud, KA et al. (Oct. 2007b). *Class. Quantum Grav.* **24**, pp. 529–+.  
- Arnaud, KA et al. (2006a). *AIP Conf. Series. Vol. 873*, pp. 625–632. 
- (2006b). *AIP Conf. Series. Vol. 873*, pp. 619–624.  
- Arun, KG et al. (May 2009). *Class. Quantum Grav.* **26.9**, pp. 094027–+.  
- Babak, S et al. (Jan. 2007). *Phys. Rev. D* **75.2**, pp. 024005–+.  
- Babak, S et al. (June 2008a). *Class. Quantum Grav.* **25.11**, pp. 114037–+.  
- Babak, S et al. (Sept. 2008b). *Class. Quantum Grav.* **25.18**, pp. 184026–+.  
- Babak, S et al. (Apr. 2010). *Classical and Quantum Gravity* **27.8**, pp. 084009–+.  
- Baker, JG et al. (May 2006). *Phys. Rev. D* **73.10**, pp. 104002–+.  
- Baker, JG et al. (June 2007a). *Phys. Rev. D* **75.12**, pp. 124024–+.  
- Baker, JG et al. (June 2007b). *Class. Quantum Grav.* **24**, pp. 25–+.  
- Baker, JG et al. (Nov. 2007c). *Phys. Rev. Lett.* **99.18**, pp. 181101–+.  
- Baker, JG et al. (Aug. 2008). *Phys. Rev. D* **78.4**, pp. 044046–+.  
- Barack, L and C Cutler (Apr. 2004). *Phys. Rev. D* **69**, 082005 (8), pp. 082005–+.  
- Bartelt-Berger, L et al. (2001). *IEEE Conf. Proceedings*, pp. 580–581. 
- Barth, AJ et al. (Feb. 2005). *ApJ* **619**, pp. L151–L154.  
- Bartko, H et al. (June 2009). *ApJ* **697**, pp. 1741–1763.  
- Begelman, MC et al. (July 2006). *MNRAS* **370**, pp. 289–298.  
- Belczynski, K et al. (June 2002). *ApJ* **572**, pp. 407–431.  
- Belczynski, K et al. (Nov. 2008). ArXiv e-prints. 
- Bell, EF et al. (Nov. 2006). *ApJ* **652**, pp. 270–276.  
- Benacquista, M and K Holley-Bockelmann (July 2006). *ApJ* **645** (1), pp. 589–596.  
- Bender, PL and D Hils (June 1997). *Class. Quantum Grav.* **14**, pp. 1439–1444. 
- Benedetti, M et al. (2006). *Journal of Tribology* **128** (4), pp. 828–840. 
- Berczik, P et al. (May 2006). *ApJ* **642**, pp. L21–L24.  
- Berentzen, I et al. (Apr. 2009). *ApJ* **695**, pp. 455–468.  
- Berti, E and M Volonteri (Sept. 2008). *ApJ* **684**, pp. 822–828.  
- Berti, E et al. (Apr. 2005). *Phys. Rev. D* **71**, 084025 (8), pp. 084025–+.  
- Bhattacharya, D and EPJ van den Heuvel (1991). *Phys. Rep.* **203**, pp. 1–124. 
- Bignami, G et al. (2005). *Cosmic Vision: Space Science for Europe 2015–2025*. Tech. rep. ESA. 

- Bildsten, L (July 1998). ApJ **501**, pp. L89+.
- Bloom, JS et al. (Feb. 2009). ArXiv e-prints.
- Bonanos, AZ et al. (Nov. 2006). ApJ **652**, pp. 313–322.
- Bond, JR et al. (May 1984). ApJ **280**, pp. 825–847.
- Boroson, TA and TR Lauer (Mar. 2009). Nature **458**, pp. 53–55.
- Bortoluzzi, D et al. (May 2009). Class. Quantum Grav. **26**.9, pp. 094011–+.
- Brandt, N et al. (2005). Class. Quantum Grav. **22** (10), S493–S499.
- Brandt, WN and G Hasinger (Sept. 2005). ARA&A **43**, pp. 827–859.
- Braxmaier, C et al. (Sept. 2004). Pp. 164–173.
- Bromm, V and RB Larson (Sept. 2004). ARA&A **42**, pp. 79–118.
- Bromm, V and A Loeb (Oct. 2003). ApJ **596**, pp. 34–46.
- Bromm, V et al. (Jan. 2002). ApJ **564**, pp. 23–51.
- Brown, DA et al. (Oct. 2007). Class. Quantum Grav. **24**, pp. 595–+.
- Brown, WR et al. (Jan. 2009). ApJ **690**, pp. L69–L71.
- Brustein, R et al. (Feb. 1995). Physics Letters B **361**, pp. 45–51.
- Budworth, DW et al. (1960). Proceedings of the Royal Society of London. Series A **257**.1289.
- Buonanno, A (Mar. 2003). ArXiv e-prints.
- Buonanno, A et al. (Mar. 1997). Phys. Rev. D **55**, pp. 3330–3336.
- Buonanno, A et al. (Nov. 2007a). Phys. Rev. D **76**.10, pp. 104049–+.
- Buonanno, A et al. (June 2007b). Phys. Rev. D **75**.12, pp. 124018–+.
- Campanelli, M et al. (Mar. 2006a). Physical Review Letters **96**.11, pp. 111101–+.
- Campanelli, M et al. (Mar. 2006b). Phys. Rev. D **73**.6, pp. 061501–+.
- (Aug. 2006c). Phys. Rev. D **74**.4, pp. 041501–+.
- Campanelli, M et al. (Apr. 2009). Phys. Rev. D **79**.8, pp. 084010–+.
- Carbone, L et al. (Oct. 2003). Phys. Rev. Lett. **91**.15. P. 151101.
- (May 2005). Class. Quantum Grav. **22**.10, pp. 509–+.
- Carbone, L et al. (Nov. 2006). AIP Conf. Series. Vol. 873, pp. 561–565.
- Carbone, L et al. (Nov. 2007a). Phys. Rev. D **76**.10, pp. 102003–21.
- Carbone, L et al. (Feb. 2007b). Phys. Rev. D **75**.4, pp. 042001–6.
- Cavalleri, A et al. (Oct. 2001). Class. Quantum Grav. **18** (19), pp. 4133–4144.
- Chakrabarty, D et al. (July 2003). Nature **424**, pp. 42–44.
- Chandrasekhar, S (Mar. 1943a). ApJ **97**, pp. 255–+.
- (Mar. 1943b). ApJ **97**, pp. 263–+.
- (July 1943c). ApJ **98**, pp. 54–+.
- Chandrasekhar, S and S Detweiler (Aug. 1975). Royal Soc. of London Proc. Series A **344**, pp. 441–452.
- Chang, DH et al. (2007). Proc. SPIE. Vol. 6713, 67130U–13.
- Chen, X et al. (June 2009). ApJ **697**, pp. L149–L152.
- Chongchitnan, S and G Efstathiou (Apr. 2006). Phys. Rev. D **73**.8, pp. 083511–+.
- Christensen, N and R Meyer (Oct. 1998). Phys. Rev. D **58**.8, pp. 082001–+.
- Christensen, N et al. (July 2004). Phys. Rev. D **70**.2, pp. 022001–+.
- Churchwell, E et al. (Mar. 2009). PASP **121**, pp. 213–230.
- Cohen, SH et al. (Mar. 2006). ApJ **639**, pp. 731–739.
- Cornish, NJ and J Crowder (Aug. 2005). Phys. Rev. D **72**, 043005 (4), pp. 043005–+.
- Cornish, NJ and RW Hellings (Nov. 2003). Class. Quantum Grav. **20** (22), pp. 4851–4860.
- Cornish, NJ and TB Littenberg (Oct. 2007). Phys. Rev. D **76**.8, pp. 083006–+.
- Cornish, NJ and EK Porter (Oct. 2006). Class. Quantum Grav. **23**, pp. 761–+.
- (Jan. 2007a). Phys. Rev. D **75**.2, pp. 021301–+.
- (Oct. 2007b). Class. Quantum Grav. **24**, pp. 501–+.
- (Dec. 2007c). Class. Quantum Grav. **24**, pp. 5729–5755.
- Crowder, J and NJ Cornish (Feb. 2007). Phys. Rev. D **75**.4, pp. 043008–+.
- Crowder, J et al. (Mar. 2006). Phys. Rev. D **73** (6), pp. 063011–+.

- Cruz, RJ et al. (Oct. 2006). *Class. Quantum Grav.* **23**, pp. 751–+.
- Cruz, RJ et al. (2006). *AIP Conf. Series*. Vol. 873, pp. 319–325.
- Dalal, N et al. (Sept. 2006). *Phys. Rev. D* **74.6**, 063006, pp. 063006–+.
- Damour, T and A Vilenkin (Mar. 2005). *Phys. Rev. D* **71.6**, pp. 063510–+.
- de Vine, G et al. (May 2010). *Phys. Rev. Lett.* **104.21**, pp. 211103–+.
- Dehne, M et al. (Mar. 2009). *Journal of Physics Conference Series* **154.1**, pp. 012023–+.
- Dhurandhar, SV (Mar. 2009). *Journal of Physics Conference Series* **154.1**, pp. 012047–+.
- Dhurandhar, SV and M Tinto (July 2005). *Living Reviews in Relativity* **8**, pp. 4–+.
- Dhurandhar, SV et al. (May 2002). *Phys. Rev. D* **65** (10), pp. 024015–+.
- Dolesi, R et al. (2003). *Class. Quantum Grav.* **20.10**, S99–S108.
- Dolgov, AD et al. (Nov. 2002). *Phys. Rev. D* **66.10**, pp. 103505–+.
- Dotti, M et al. (Oct. 2006). *MNRAS*, pp. 997–+.
- Dotti, M et al. (Aug. 2007). *MNRAS* **379**, pp. 956–962.
- Drasco, S and SA Hughes (Feb. 2004). *Phys. Rev. D* **69.4**, pp. 044015–+.
- (Jan. 2006). *Phys. Rev. D* **73.2**, 024027, pp. 024027–+.
- Dreyer, O et al. (Feb. 2004). *Class. Quantum Grav.* **21**, pp. 787–803.
- D’Souza, MCR et al. (May 2006). *ApJ* **643**, pp. 381–401.
- Eardley, DM et al. (Nov. 1973). *Phys. Rev. D* **8**, pp. 3308–3321.
- Easther, R and EA Lim (Apr. 2006). *Journal of Cosmology and Astro-Particle Physics* **4**, pp. 10–+.
- Edlund, JA et al. (June 2005). *Phys. Rev. D* **71** (12), pp. 122003–+.
- Einstein, A (1915). *Sitzungsberichte der Königlich Preußischen Akademie der Wissenschaften (Berlin)*. Pp. 844–847.
- Eisenstein, DJ and M White (Nov. 2004). *Phys. Rev. D* **70.10**, pp. 103523–+.
- Eisenstein, DJ et al. (Nov. 2005). *ApJ* **633**, pp. 560–574.
- Elliffe, EJ et al. (2005). *Class. Quantum Grav.* **22.10**, S257–S267.
- Escala, A et al. (June 2004). *ApJ* **607**, pp. 765–777.
- (Sept. 2005). *ApJ* **630**, pp. 152–166.
- Esposito-Farèse, G (Nov. 2004). *AIP Conf. Series*. Vol. 736, pp. 35–52.
- Everitt, CWF et al. (2008). *Class. Quantum Grav.* **25.11**, p. 114002.
- Farmer, AJ and ES Phinney (Dec. 2003). *MNRAS* **346**, pp. 1197–1214.
- Fehring, M et al. (Dec. 1998). *AIP Conf. Series*. Vol. 456, pp. 207–213.
- Felder, GN and L Kofman (Feb. 2007). *Phys. Rev. D* **75.4**, pp. 043518–+.
- Feroz, F et al. (Nov. 2009). *Class. Quantum Grav.* **26.21**, pp. 215003–+.
- Feroz, F et al. (Apr. 2010). *Class. Quantum Grav.* **27.7**, pp. 075010–+.
- Ferrarese, L and H Ford (Feb. 2005). *Space Science Reviews* **116**, pp. 523–624.
- Ferrarese, L and D Merritt (Aug. 2000). *ApJ* **539**, pp. L9–L12.
- Flanagan, ÉÉ and SA Hughes (Apr. 1998a). *Phys. Rev. D* **57**, pp. 4535–4565.
- (Apr. 1998b). *Phys. Rev. D* **57**, pp. 4566–4587.
- (Sept. 2005). *New Journal of Physics* **7**, pp. 204–+.
- Freitag, M (Jan. 2003). *ApJ* **583**, pp. L21–L24.
- Freitag, M et al. (Sept. 2006). *ApJ* **649**, pp. 91–117.
- Gair, JR (May 2009). *Class. Quantum Grav.* **26.9**, pp. 094034–+.
- Gair, JR and K Glampedakis (Mar. 2006). *Phys. Rev. D* **73.6**, pp. 064037–+.
- Gair, JR and G Jones (Mar. 2007). *Class. Quantum Grav.* **24**, pp. 1145–1168.
- Gair, JR and EK Porter (Nov. 2009). *Class. Quantum Grav.* **26.22**, pp. 225004–+.
- Gair, JR and L Wen (Sept. 2005). *Class. Quantum Grav.* **22** (18), S1359–S1371.
- Gair, JR et al. (Oct. 2004). *Class. Quantum Grav.* **21** (20), S1595–S1606.
- Gair, JR et al. (Sept. 2008a). *Class. Quantum Grav.* **25.18**, pp. 184030–+.
- Gair, JR et al. (Sept. 2008b). *Class. Quantum Grav.* **25.18**, pp. 184031–+.
- Gair, JR et al. (May 2010). *Journal of Physics Conference Series* **228.1**, pp. 012010–+.
- Galloway, DK et al. (Sept. 2002). *ApJ* **576**, pp. L137–L140.

- Gammie, CF et al. (Feb. 2004). *ApJ* **602**, pp. 312–319. 
- García Marín, AF et al. (May 2005). *Class. Quantum Grav.* **22**, pp. 235–+. 
- Gebhardt, K et al. (Aug. 2000). *ApJ* **539**, pp. L13–L16. 
- Genovese, A et al. (Oct. 2004). *ESA Special Publication*. Vol. 555. 
- Gerhard, O (2002). *Astronomical Society of the Pacific Conference Series*. Vol. 273, pp. 73–+. 
- Ghez, AM et al. (Dec. 2008a). *ApJ* **689**, pp. 1044–1062. 
- Ghez, AM et al. (July 2008b). *IAU Symposium*. Vol. 248, pp. 52–58. 
- Giamperri, G et al. (1996). *Opt. Commun.* **123**, pp. 669–678. 
- Gillessen, S et al. (Feb. 2009). *ApJ* **692**, pp. 1075–1109. 
- Gilli, R et al. (Feb. 2007). *A&A* **463**, pp. 79–96. 
- Greene, JE and LC Ho (Nov. 2007). *ApJ* **670**, pp. 92–104. 
- Gültekin, K et al. (June 2009). *ApJ* **698**, pp. 198–221. 
- Gwo, DH (Sept. 1998). *Proc. SPIE*. Vol. 3435, pp. 136–142. 
- Haberland, R (Apr. 1981). U.S. Patent No. 4261211. 
- Hamadache, C et al. (July 2006). *A&A* **454**, pp. 185–199. 
- Hansen, BMS and M Milosavljević (Aug. 2003). *ApJ* **593**, pp. L77–L80. 
- Hawley, JF and JH Krolik (Apr. 2006). *ApJ* **641**, pp. 103–116. 
- Heinzl, G et al. (May 2003). *Class. Quantum Grav.* **20** (10), S153–S161. 
- Heinzl, G et al. (Mar. 2004). *Class. Quantum Grav.* **21**, pp. 581–+. 
- Heinzl, G et al. (Mar. 2006). *Journal of Physics Conference Series* **32**, pp. 132–136. 
- Herz, M (Sept. 2005). *Optical Engineering* **44**, pp. 505–+. 
- Hogan, CJ (Feb. 1986). *MNRAS* **218**, pp. 629–636. 
- (Sept. 2000). *Phys. Rev. Lett.* **85**, pp. 2044–2047. 
- (Nov. 2006a). *AIP Conf. Proc.* Vol. 873, pp. 30–40. 
- (Aug. 2006b). *Phys. Rev. D* **74.4**, pp. 043526–+. 
- Hong, FL et al. (Sept. 1998). *Proc. SPIE*. Vol. 3477, pp. 2–10. 
- Hopman, C and T Alexander (July 2006a). *ApJ* **645**, pp. 1152–1163. 
- (July 2006b). *ApJ* **645**, pp. L133–L136. 
- Hu, W (Aug. 2005). *Astronomical Society of the Pacific Conference Series*. Vol. 339, pp. 215–+. 
- Hueller, M et al. (May 2005). *Class. Quantum Grav.* **22**, pp. 521–+. 
- Hughes, SA (Apr. 2002). *MNRAS* **331** (3), pp. 805–816. 
- (Jan. 2003). *Annals of Physics* **303**, pp. 142–178. 
- Hughes, SA and RD Blandford (Mar. 2003). *ApJ* **585**, pp. L101–L104. 
- Hughes, SA (2006). *AIP Conf. Series*. Vol. 873, pp. 13–20. 
- Hulse, RA and HJ Taylor (Sept. 1974). *Bulletin of the American Astronomical Society*. Vol. 6, pp. 453–+. 
- Jafray, Y and TJ Sumner (1997). *Class. Quantum Grav.* **14.6**, pp. 1567–1574. 
- Kesden, M et al. (Feb. 2005). *Phys. Rev. D* **71.4**, 044015, pp. 044015–+. 
- Key, JS and NJ Cornish (Feb. 2009). *Phys. Rev. D* **79.4**, pp. 043014–+. 
- Khlebnikov, S and I Tkachev (July 1997). *Phys. Rev. D* **56**, pp. 653–660. 
- Killow, CJ et al. (2006). *AIP Conf. Series*. Vol. 873, pp. 297–303. 
- King, AR et al. (Apr. 2008). *MNRAS* **385**, pp. 1621–1627. 
- Klein, A et al. (Sept. 2009). *Phys. Rev. D* **80.6**, pp. 064027–+. 
- Klimenko, S et al. (June 2008). *Class. Quantum Grav.* **25.11**, pp. 114029–+. 
- Knox, L (Jan. 2006). *Phys. Rev. D* **73.2**, pp. 023503–+. 
- Kocsis, B et al. (Jan. 2006). *ApJ* **637**, pp. 27–37. 
- Kosowsky, A et al. (July 2002). *Phys. Rev. D* **66.2**, pp. 024030–+. 
- Koushiappas, SM et al. (Oct. 2004). *MNRAS* **354**, pp. 292–304. 
- Kramer, M and N Wex (Apr. 2009). *Class. Quantum Grav.* **26.7**, pp. 073001–+. 
- Kramer, M et al. (Oct. 2006). *Science* **314**, pp. 97–102. 
- Krolik, JH (1999). *Active galactic nuclei: from the central black hole to the galactic environment*. Princeton University Press. 

- Krolik, JH et al. (Apr. 2005). *ApJ* **622**, pp. 1008–1023. 
- Kuhlen, M and P Madau (Nov. 2005). *MNRAS* **363**, pp. 1069–1082. 
- Lang, RN and SA Hughes (Dec. 2006). *Phys. Rev. D* **74**.12, pp. 122001–+.
- Lange, R and B Smutny (Oct. 2004). *IEEE Conf. Proceedings*. Vol. 1, pp. 441–444. 
- Larson, SL et al. (Sept. 2000). *Phys. Rev. D* **62**.6, pp. 062001–+.
- Lauer, TR et al. (June 2007). *ApJ* **662**, pp. 808–834. 
- Leonhardt, V and JB Camp (June 2006). *Applied Optics* **45**.17, pp. 4142–4146. 
- Leonhardt, V et al. (Nov. 2006). Vol. 873, pp. 354–358. 
- Levan, AJ et al. (May 2006). *MNRAS* **368**, pp. L1–L5. 
- Levin, Y (Jan. 2007). *MNRAS* **374**, pp. 515–524. 
- Levin, Y and AM Beloborodov (June 2003). *ApJ* **590**, pp. L33–L36. 
- Li, Y et al. (Aug. 2007). *ApJ* **665**, pp. 187–208. 
- Littenberg, TB and NJ Cornish (Aug. 2010). *ArXiv e-prints*. 
- Livas, JC et al. (Dec. 2007). *Bulletin of the American Astronomical Society*. Vol. 211, p. 990.
- Lorimer, DR (Nov. 2008). *Living Reviews in Relativity* **11**, pp. 8–+.
- Lousto, CO et al. (Apr. 2010). *Phys. Rev. D* **81**.8, pp. 084023–+.
- Lynden-Bell, D (Aug. 1969). *Nature* **223**, pp. 690–694. 
- MacLeod, CL and CJ Hogan (Feb. 2008). *Phys. Rev. D* **77**.4, pp. 043512–+.
- Macri, LM et al. (Dec. 2006). *ApJ* **652**, pp. 1133–1149. 
- Madau, P and MJ Rees (Apr. 2001). *ApJ* **551**, pp. L27–L30. 
- Madau, P et al. (Apr. 2004). *ApJ* **604**, pp. 484–494. 
- Maggiore, M (2000). *Phys. Rep.* **331**, pp. 283–367. 
- Maoz, E (Feb. 1998). *ApJ* **494**, pp. L181+.
- Marconi, A et al. (June 2004). *MNRAS* **351**, pp. 169–185. 
- Marcuccio, S et al. (1998). *Journal of Propulsion and Power* **14**.5, pp. 774–781. 
- Marsh, TR et al. (May 2004). *MNRAS* **350**, pp. 113–128. 
- McNamara, P et al. (2008). *Class. Quantum Grav.* **25**.11, p. 114034. 
- Merkowitz, SM et al. (2004). *Class. Quantum Grav.* **21**.5, S603–S610. 
- Merkowitz, SM et al. (2005). *Class. Quantum Grav.* **22**.10, S395–S402. 
- Merloni, A (Oct. 2004). *MNRAS* **353**, pp. 1035–1047. 
- Merritt, D and M Milosavljević (Nov. 2005). *Living Reviews in Relativity* **8**, pp. 8–+.
- Merritt, D and MY Poon (May 2004). *ApJ* **606**, pp. 788–798. 
- Merritt, D et al. (Mar. 2009). *ApJ* **693**, pp. L35–L38. 
- Middleton, KF et al. (Dec. 2006). *Optical Engineering* **45**.12, pp. 125601–11. 
- Miller, MC (Jan. 2005). *ApJ* **618**, pp. 426–431. 
- Miller, MC et al. (Oct. 2005). *ApJ* **631** (2), pp. L117–L120. 
- Milosavljević, M and ES Phinney (Apr. 2005). *ApJ* **622**, pp. L93–L96. 
- Milosavljević, M et al. (Nov. 2006). *ApJ* **652**, pp. 120–125. 
- Milosavljević, M et al. (May 2009). *ApJ* **696**, pp. L146–L149. 
- Miralda-Escudé, J and JA Kollmeier (Jan. 2005). *ApJ* **619**, pp. 30–40. 
- Mitryk, SJ et al. (Apr. 2010). *Class. Quantum Grav.* **27**.8, pp. 084012–+.
- Mo, HJ and SDM White (Oct. 2002). *MNRAS* **336**, pp. 112–118. 
- Mondin, L et al. (Nov. 2004). *Journal de Physique IV* **119**, pp. 237–238. 
- Morris, M (May 1993). *ApJ* **408**, pp. 496–506. 
- Mouawad, N et al. (Feb. 2005). *Astronomische Nachrichten* **326**, pp. 83–95. 
- Mueller, G et al. (Dec. 2005). *Laser frequency stabilization for LISA*. Technical Report NASA/TM-2005-212794; Rept-2006-00387-1. Goddard Space Flight Center, p. 23. 
- Muno, MP et al. (Apr. 2005). *ApJ* **622**, pp. L113–L116. 
- Musha, M et al. (Sept. 2000). *Optics Communications* **183**.1-4, pp. 165–173. 
- Nayak, KR and JY Vinet (Nov. 2004). *Phys. Rev. D* **70** (10), pp. 102003–+.
- Nelemans, G (2006). *Physics Today* **59**.7, pp. 070000–+.

- Nelemans, G (May 2009). *Class. Quantum Grav.* **26.9**, pp. 094030–+.
- Nelemans, G et al. (Mar. 2001). *A&A* **368**, pp. 939–949.
- Nelemans, G et al. (Mar. 2004). *MNRAS* **349**, pp. 181–192.
- Nevsky, AY et al. (June 2001). *Optics Communications* **192**, pp. 263–272.
- Notcutt, M et al. (July 2005). *Optics Letters* **30.14**, pp. 1815–1817.
- Olling, RP (July 2007). *MNRAS* **378**, pp. 1385–1399.
- Paczynski, B (1976). *IAU Symposium*. Vol. 73, pp. 75–+.
- Pakmor, R et al. (Jan. 2010). *Nature* **463**, pp. 61–64.
- Perets, HB and T Alexander (Apr. 2008). *ApJ* **677**, pp. 146–159.
- Petiteau, A et al. (May 2010). *Phys. Rev. D* **81.10**, pp. 104016–+.
- Polchinski, J (2005). *International Journal of Modern Physics A* **20**, pp. 3413–3415.
- Portegies Zwart, SF et al. (Apr. 2006). *ApJ* **641**, pp. 319–326.
- Porter, EK and A Sesana (May 2010). *ArXiv e-prints*.
- Pretorius, F (Sept. 2005). *Physical Review Letters* **95.12**, pp. 121101–+.
- Quinlan, GD (July 1996). *NewA* **1**, pp. 35–56.
- Racine, É et al. (Sept. 2007). *MNRAS* **380**, pp. 381–398.
- Randall, L and G Servant (May 2007). *Journal of High Energy Physics* **5**, pp. 54–+.
- Rauch, KP (Apr. 1999). *ApJ* **514**, pp. 725–745.
- Rauch, KP and B Ingalls (Oct. 1998). *MNRAS* **299**, pp. 1231–1241.
- Rees, MJ (Oct. 1978). *The Observatory* **98**, pp. 210–223.
- Riess, AG et al. (July 2009). *ApJ* **699**, pp. 539–563.
- Rodriguez, C et al. (July 2006). *ApJ* **646**, pp. 49–60.
- Roelofs, GHA et al. (Sept. 2006). *MNRAS* **371**, pp. 1231–1242.
- Roelofs, GHA et al. (Dec. 2007). *MNRAS* **382**, pp. 685–692.
- Roelofs, GHA et al. (Mar. 2010). *ApJ* **711**, pp. L138–L142.
- Romano, JD and G Woan (May 2006). *Phys. Rev. D* **73** (10), pp. 102001–+.
- Roth, A and R Werninghaus (2006). Pp. 1918–1920.
- Ruedenauer, GF et al. (Aug. 1997). *ESA Special Publication*. Vol. 398, p. 267.
- Ruiter, AJ et al. (Mar. 2009). *ApJ* **693**, pp. 383–387.
- Ryan, FD (Nov. 1995). *Phys. Rev. D* **52**, pp. 5707–5718.
- Salpeter, EE (Aug. 1964). *ApJ* **140**, pp. 796–800.
- Sandage, A et al. (Dec. 2006). *ApJ* **653**, pp. 843–860.
- Schilling, R (June 1997). *Class. Quantum Grav.* **14** (6), pp. 1513–1519.
- Schödel, R et al. (July 2007). *A&A* **469**, pp. 125–146.
- Schulte, M et al. (Nov. 2006). *AIP Conf. Series*. Vol. 873, pp. 165–171.
- Schutz, BF (Sept. 1986). *Nature* **323**, pp. 310–+.
- Sesana, A (Aug. 2010). *ApJ* **719**, pp. 851–864.
- Sesana, A et al. (Aug. 2004). *ApJ* **611**, pp. 623–632.
- (Apr. 2005). *ApJ* **623** (1), pp. 23–30.
- Sesana, A et al. (Nov. 2006). *ApJ* **651**, pp. 392–400.
- Sesana, A et al. (June 2007). *MNRAS* **377**, pp. 1711–1716.
- Sesana, A et al. (Dec. 2008). *MNRAS* **391**, pp. 718–726.
- Sesana, A et al. (May 2009). *Class. Quantum Grav.* **26.9**, pp. 094033–+.
- Shaddock, D et al. (Nov. 2006). *AIP Conf. Series*. Vol. 873, pp. 654–660.
- Shaddock, DA et al. (Sept. 2003). *Phys. Rev. D* **68** (6), pp. 061303–+.
- Shaddock, DA et al. (Oct. 2004). *Phys. Rev. D* **70** (8), pp. 081101–+.
- Shapiro, SL and M Shibata (Oct. 2002). *ApJ* **577**, pp. 904–908.
- Shapiro Key, J and NJ Cornish (June 2010a). *ArXiv e-prints*.
- (June 2010b). *ArXiv e-prints*.
- Shaul, DNA et al. (2004). *Class. Quantum Grav.* **21.5**, S647–S651.
- Shaul, DNA et al. (2005). *Class. Quantum Grav.* **22.10**, S297–S309.

- Sheard, BS et al. (Dec. 2003). *Physics Letters A* **320**, pp. 9–21. 
- Siemens, X et al. (May 2006). *Phys. Rev. D* **73**.10, pp. 105001–+. 
- Silvestri, Z et al. (2003). *Metrologia* **40**.4, pp. 172–176. 
- Smith, JR et al. (2003). *Class. Quantum Grav.* **20**.23, pp. 5039–5047. 
- Sodnik, Z et al. (2006). *IEEE Conf. Proceedings*, pp. 78–79. 
- Soltan, A (July 1982). *MNRAS* **200**, pp. 115–122. 
- Sopuerta, CF (Sept. 2010). *GW Notes* **4**, pp. 3–47. 
- Spergel, DN et al. (June 2007). *ApJS* **170**, pp. 377–408. 
- Stanga, R et al. (Nov. 2006). *AIP Conf. Series. Vol. 873*, pp. 210–214. 
- Stebbins, RT (May 2009). *Class. Quantum Grav.* **26**.9, pp. 094014–+. 
- Steiger, W et al. (Dec. 2000). *ESA Special Publication. Vol. 465*, pp. 475–+. 
- Stroeer, A and G Nelemans (Nov. 2009). *MNRAS* **400**, pp. L24–L28. 
- Stroeer, A and A Vecchio (Oct. 2006). *Class. Quantum Grav.* **23**, pp. 809–+. 
- Stroeer, A and J Veitch (Sept. 2009). *Phys. Rev. D* **80**.6, pp. 064032–+. 
- Stroeer, A et al. (Sept. 2006). *AIP Conf. Series. Vol. 873*, pp. 444–451. 
- Sumner, T et al. (2004). *Class. Quantum Grav.* **21**.5, S597–S602. 
- Sun, KX et al. (Apr. 2006). *Class. Quantum Grav.* **23**, pp. 141–+. 
- Sylvestre, J (Nov. 2004). *Phys. Rev. D* **70**, 102002 (10), pp. 102002–+. 
- Taam, RE and EL Sandquist (2000). *ARA&A* **38**, pp. 113–141. 
- Tajmar, M et al. (2004). *Journal of Propulsion and Power* **20** (2), pp. 211–218.
- Thorne, KS (July 1974). *ApJ* **191**, pp. 507–520. 
- (1987). “Gravitational radiation.” *Three Hundred Years of Gravitation*, pp. 330–458. 
- (1994). *Black holes and time warps: Einstein’s outrageous legacy*. W.W. Norton. 
- Thorpe, JI et al. (2006). *AIP Conf. Series. Vol. 873*, pp. 661–667. 
- Thorpe, JI et al. (Sept. 2008). *Optics Express* **16**, pp. 15980–+. 
- Tinto, M and JW Armstrong (May 1999). *Phys. Rev. D* **59**.10, pp. 102003–+. 
- Tinto, M and SL Larson (May 2005). *Class. Quantum Grav.* **22** (10), S531–S535. 
- Tinto, M et al. (Apr. 2002). *Phys. Rev. D* **65** (8), pp. 082003–+. 
- Toomre, A (1977). Pp. 401–+. 
- Touboul, P et al. (1996). *Class. Quantum Grav.* **13**.11A, A67–A78. 
- Tremaine, S et al. (Aug. 2002). *ApJ* **574**, pp. 740–753. 
- Trias, M et al. (Sept. 2008). *Class. Quantum Grav.* **25**.18, pp. 184028–+. 
- Tundo, E et al. (July 2007). *ApJ* **663**, pp. 53–60. 
- Turneure, JP et al. (Oct. 2003). *Advances in Space Research* **32**.7, pp. 1387–1396. 
- Vallisneri, M (Jan. 2005). *Phys. Rev. D* **71** (2), pp. 022001–+. 
- Verbunt, F and WHG Lewin (Apr. 2006). “Globular cluster X-ray sources”. *Compact stellar X-ray sources*. Cambridge University Press, pp. 341–379. 
- Volonteri, M and MC Begelman (Mar. 2010). ArXiv e-prints. 
- Volonteri, M et al. (Aug. 2003). *ApJ* **593**, pp. 661–666. 
- Volonteri, M et al. (Feb. 2005). *ApJ* **620**, pp. 69–77. 
- Volonteri, M et al. (Nov. 2006). *MNRAS* **373**, pp. 121–127. 
- Volonteri, M et al. (Oct. 2007). *ApJ* **667**, pp. 704–713. 
- Volonteri, M et al. (Sept. 2009). *ApJ* **703**, pp. L86–L89. 
- Volonteri, M (2006). *AIP Conf. Series. Vol. 873*, pp. 61–69. 
- Wand, V et al. (Apr. 2006). *Class. Quantum Grav.* **23**, pp. 159–+. 
- Wass, PJ et al. (Nov. 2006). *AIP Conf. Series. Vol. 873*, pp. 220–224. 
- Watts, AL et al. (Sept. 2008). *MNRAS* **389**, pp. 839–868. 
- Webbink, RF (Feb. 1984). *ApJ* **277**, pp. 355–360. 
- (Nov. 2010). ArXiv e-prints. 
- Weber, WJ et al. (2002). *Class. Quantum Grav.* **19**.7, pp. 1751–1756. 
- Weber, W et al. (2007). *Advances in Space Research* **39**.2, pp. 213–218. 

- Weßels, P et al. (Apr. 2002). *Optics Communications* **205**.1-3, pp. 215–219. 
- Weisberg, JM and JH Taylor (July 2005). *Astronomical Society of the Pacific Conference Series*. Vol. 328, pp. 25–+. 
- Will, CM (Feb. 1998). *Phys. Rev. D* **57**, pp. 2061–2068. 
- (Mar. 2006). *Living Reviews in Relativity* **9**, pp. 3–+. 
- Witten, E (July 1984). *Phys. Rev. D* **30**, pp. 272–285. 
- Yu, Q (May 2003). *Class. Quantum Grav.* **20**, pp. 55–+. 
- Yu, S and CS Jeffery (Oct. 2010). *A&A* **521**, A85+. 
- Yungelson, LR et al. (June 2002). *A&A* **388**, pp. 546–551. 
- Zawischa, I et al. (Apr. 1999). *Optics Letters* **24**.7, pp. 469–471. 
- Zel'dovich, YB and ID Novikov (Oct. 1964). *Soviet Physics Doklady* **9**, pp. 246–+.
- Zier, C (July 2007). *MNRAS* **378**, pp. 1309–1327. 

Project Documents

- LISA-ASD-RS-3400. *Laser subsystem specification*. Tech. rep.
- LISA-ASD-TN-1002. *LISA Measurement Performance*. Technical Note.
- LISA-MSE-TN-0001. *LISA Measurement Requirements Flowdown Guide*. Tech. rep.
- LISA-ScRD-066. *LISA Science Requirements Document*. 5.1. RD.
- LISA-ASU-TN-4003. *LISA Telecommunications Subsystem Design*. Technical Note.
- LISA-ASU-TN-4001. *Mission Analysis*. Technical Note.
- MRD. *Mission Requirement Document*. Requirement Document.
- LISA-ASD-RS-3001. *Payload Design Specification*. Design Specification.
- LISA-ASD-DD-3001. *Payload Preliminary Design Description*. Design Description.
- LISA-ASU-DD-4002. *Preliminary Propulsion Module Design Description*. Design Description.
- LISA-ASD-TN-5001. *Requirement Breakdown*. Tech. rep.
- LISA-ASU-TN-4002. *Separation Analysis*. Technical Note.
- ESA-SCI(2000) 11 (2000). *System and Technology Study Report*. Tech. rep.
- LISA-ASU-BR-5001. *System Budgets*. Budget Report.
- LISA-ASD-RS-5001. *System Design Specification*. Design Specification.
- LISA-ASD-BR-5002. *System Parameters and Error Budgets*. Budget Report.
- S2-EST-RP-1087. *The LISA Pathfinder Mission*. Tech. rep.

Index

- acceleration noise
 - conversion to displacement noise, 56
 - due to cross-coupling, 78
 - due to gas damping, 78
 - due to micro-newton thrusters noise, 78
 - due to temperature fluctuations, 77
 - due to thermal gradients, 78
 - model verification by *LISA Pathfinder* (LPF), 58
 - radiation pressure, 70
 - reddening, 56
 - relaxing at higher frequencies, 56
 - stiffness, 78
- acquisition, 87, 98
- active galactic nuclei, *see* AGN
- adhesion, 80
 - break, 80
- AM CVn, 32, 33, 35, 37
- antenna
 - high-gain, 94
 - omnidirectional, 94
 - transfer function, 53
- apparent horizon size, 43
- archive data quality, 102
- archive phase, 96
- Atlas V, 85
- Atlas V, 83, 87, 90
- baryonic acoustic oscillation, 39
- battery, 92
 - discharge
 - efficiency, 93
 - maximum depth, 93
 - mass, 93
 - size, 93
- Big Bang, 5, 12
- binaries
 - black hole, 36
 - double white dwarf, 35
 - mass transfer, 34
 - mass-transfer stability, 34
 - for X-ray binaries, 35
 - neutron star, 36
 - Roche lobe, 34
 - tidal heating, 34
 - tidal interaction, 35
 - ultra-compact X-ray, 35, 36
- binary
 - compact, *see* compact binaries
- black hole
 - alternatives in galactic centres, 14
- binary
 - eccentricity, 27
 - constraints on growth by accretion, 17
 - correlation between mass and galactic bulge properties, 17
 - correlation between mass and host galaxy, 15
 - Eddington limit, 14
 - electric charge, 18
 - EMRI, 27
 - evolution of early cosmic structure, 17
 - galactic nuclei, 10, 13
 - geodesy, *see* holiodesy
 - growth
 - through gas accretion, 19
 - growth mechanism, 10
 - initial mass function, 16
 - intermediate mass seeds, 16
 - Kerr, 14, 19, 24, 26, 28
 - low mass seeds, 16
 - mass, 18
 - correlation to galaxy luminosity, 15
 - correlation to velocity dispersion, 15
 - estimate, 15
 - maximum spin, 19
 - merger, 9, 25
 - driven by gravitational waves, 18
 - final mass, 26
 - final spin, 26
 - inspiral, 24, 25
 - ringdown, 24
 - multipolar structure, 28
 - name for central mass, 14
 - no hair, 18, *see* no hair theorem
 - reheating and reionisation of the Universe, 17
 - relic in galactic nuclei, 14
 - ringdown, 26
 - spectroscopic fingerprint, 27
 - Schwarzschild, 19
 - seed formation, 16
 - space density, 15
 - spin, 18
 - spin distribution
 - diagnostic for black hole growth, 20
 - spin evolution, 19
 - stellar-mass, 11
 - population in galactic nuclei, 10
 - stellar-mass binaries, 11
- brane, 44
- caging mechanism, 80

- launch lock, 80
- overcoming adhesion, 80
- positioning actuator, 80
- pushing force, 80
- release mechanism, 80
- calibration
 - far field characterisation, 99
 - instrument noise, 99
 - phase-centre characterisation, 99
- calibration phase, 96
- capacitive readout, 66
- capacitive sensing
 - sensitivity, 79
- Chandra X-ray observatory, 14
- charge control system
 - mercury discharge lamps, 81
- charge control system, 81
 - polarity, 81
- chirp mass, 34, 104
- COBE, 38
- commissioning, 87, 96
 - acquisition, 98
 - DFACS, 98
 - Laser, 98
 - measurement system, 99
- commissioning phase, 96
- communication
 - during operational phase, 94
 - during transfer phase, 94
- communications planning, 99
- Compact binaries
 - frequency and phase evolution, 30
- compact binaries, 30
 - common-envelope phase, 31
 - testing models, 31
 - distances, 36
 - resolved, 31
- concordance cosmology, 10
- confusion foreground, 11
- constellation commissioning, 87
- Cosmic Censorship conjecture, 19
- Cosmic Vision, 1
 - scientific questions, 13, 23, 38, 43
- cosmology, 38
- cruise, 87
- cruise phase, 96
- dark energy, 44
- data analysis, 103–107
 - algorithm
 - MultiNest, 105
 - nested sampling, 105
 - Monte-Carlo Markov chain search, *see* Monte-Carlo Markov chain
 - pipeline, 103
 - simulated annealing, 105
 - templates, 104
 - time-frequency search, 105
- data archive, 103
- data centres, 102
- data collection, 99
- data formats, 103
- data processing, 101
- data product, *see* science product
- data validity
 - monitoring, 99
- decommissioning, 87, 99
- detection algorithms
 - for known signals, 104
 - for unmodeled signals, 104
- detection rate
 - black holes, 9
 - EMRI, 11, 20
 - galactic binaries, 11
 - merger events, 10, 16
- detector strain response, 53
- differential wavefront sensing, 64
- displacement noise
 - amplitude spectral density, 55, 56
 - conversion from acceleration noise, 56
 - from residual acceleration, 55
 - from the DRS, 55
 - from the IMS, 56
 - relaxing at lower frequencies, 56
- distance ladder, 38
 - calibration by BAO, 39
 - calibration by Cepheids, 39
 - calibration by gravitational lens time delays, 39
 - calibration by gravitational waves, 39
 - calibration by megamasers, 39
 - calibration by Sunyaev-Zel'dovich, 39
 - estimate, 39
- distance measurement
 - limits from gravitational lensing, 41
- disturbance reduction system
 - heritage, 77
- DSN
 - 34 m, 94
 - 70 m, 94
 - acquisition, 97
 - passes, 98, 99
- dynamical friction, 18
- Eddington limit, 13
 - black holes radiating, 14
 - for a neutron star, 35
- electro-magnetic counterparts, 96
- electrode housing, 78
 - electrodes
 - material, 79
 - gap, 78
 - material, 79
- event rate
 - MBH merger, 41
- extended lifetime, 92
- extreme mass-ratio inspiral, 10

- eccentricity, 11, 22
 - inclination, 22
 - kludge waveforms, 105
 - Lense-Thirring precession, 11
 - periapsis precession, 11
 - precession of orbital plane, 28
 - precession of periapsis, 28
 - production
 - mechanism, 22
 - star formation in accretion disks, 21
 - tidal disruption of binaries, 21
 - two-body scattering, 20
 - signal, 104
 - template, 105
- false vacuum, 43
- frequency stabilisation
 - arm-locking, 72
 - cavity resonance, 71
 - heterodyne interferometry, 72
 - molecular absorption line, 71
 - prestabilisation, 71
 - time-delay interferometry, 72
- fuel-optimal transfers, 88
- Gaia, 30
- Galactic bar, 37
- galactic binaries
 - extragalactic, 11
 - internal physics, 11
 - orbital inclination, 37
 - parameters, 11
 - signal, 104
 - template, 104
 - tidal interaction, 34
 - verification, *see* verification binaries
- Galactic bulge, 37
- galactic bulge
 - tri-axial, 18
- Galactic centre, 21–22, 37
 - dark compact objects, 21
 - observations
 - near-infrared, 21
 - X-ray, 21
- Galactic disc, 37
- Galactic halo, 37
- galaxies
 - constraints on evolution, 10
 - double-double radio, 18
 - growth connected to massive black holes, 10
 - hierarchical mergers, 10
 - merger, 18
 - merger history, 16
 - nuclei
 - stellar-mass black holes, 10
 - X-shaped, 18
- galaxy formation
 - standard theory, 41
- gamma-ray burst, 35
- General Relativity, 5
 - strong-field, 24, 25
 - test
 - central mass in galactic nuclei, 14
 - EMRI, 9, 11, 24, 28
 - gravitational wave polarisation, 6
 - graviton mass, 29
 - massive black hole mergers, 11
 - merger events, 23, 24
 - solar system, 23
 - weak-field regime, 23
- geodesic constants of integration, 28
- global curvature of space, 38
- globular clusters, 31, 37
- goal vs. requirement, 53
- GP-B mission, 62, 81
- gravitational lensing
 - fitting an amplification model, 42
 - weak, 41
- gravitational reference sensor
 - capacitive readout system, 77
 - mounting, 77
 - non-sensitive degrees of freedom, 77
 - sensitive axis, 77
 - test mass interferometer, 77
- gravitational waves
 - as probes for extreme conditions, 5
 - extragalactic background, 31, 32
 - foreground, 30, 31, 37
 - geometrical distribution of sources, 31
 - modulation, 32
 - spectral shape, 31
 - from black holes, 9
 - from capture events, 9
 - from compact binaries, 9
 - from cosmic strings, 43
 - from early Universe, 9, 43
 - from EMRI, 9, 10, 20
 - from first-order phase transition, 43
 - from phase transitions, 12
 - from string loops, 46
 - from strings, 45–46
 - from superstrings, 9, 12
 - from verification binaries, 9
 - generation, 6
 - interferometry, 7
 - mass quadrupole, 6
 - measurement principle, 7
 - oscillations of spacetime, 5
 - polarisation, 6, 7
 - primordial, 44
 - propagation speed, 6
 - property, 5
 - radiated power, 5
 - stochastic background, 12, 43, 44
 - strain, 7
 - wavelength, 6
- graviton

- Compton wavelength, 29
 - mass, 29
- gravity gradient
 - compensation, 77
- ground segment, 100
- ground station
 - emergency, 94
 - nominal, 94
- ground-based detectors
 - LIGO, *see* LIGO
 - Virgo, *see* Virgo
- gyro, 85
- heterodyne interferometry, 64
- hierarchical structure assembly, 17
- heliodesy, 28
- host galaxy
 - identification
 - by starburst, 40
 - by variable EM emission, 40
- housekeeping data
 - payload, 95
 - science, 95
- Hubble constant, 38, 42
- Hubble length, 44
- Hulse-Taylor, *see* pulsar, PSR1913+16
- hydroxy catalysis bonding, 62
- inflation, 43, 44
- inflaton
 - decay, 44
- initial acquisition, 92
- instrument noise
 - allocation, 55
 - budget, 55
 - margin, 55, 59
- instrument noise model, 53
- instrument operations, 101
- instrument sensitivity function, 53, 54
 - high-frequency approximation, 55
 - inverse of transfer function, 54
 - normalisation, 54
- ISM
 - validation, 56
- Keck telescope, 32
- laser
 - fibre amplifier, 69
 - frequency noise
 - free-running, 71
 - frequency stabilisation, 70, *see* frequency stabilisation
 - low-power master oscillator, 69
 - neodymium YAG, 69
 - power stability, 70
 - pump diodes
 - amplifier, 70
 - low-power seed, 69
- launch, 97
- launch and early operations, 87–88
- launch mass, 90
- launch phase, 96
- launch stack, 97
- launch vehicle, 85
- launcher
 - baseline, 90
 - mass capability, 90
 - separation, 88
- LIGO, 7
 - advanced, 24, 36
- LISA
 - all-sky detector, 8
 - angular resolution, 31
 - antenna pattern, 8, 32
 - differences to electro-magnetic observatories, 8
 - directional sensitivity, 37
 - displacement sensitivity, 7
 - distance measurement, 50
 - drag-free operation, 48
 - dynamical range, 8
 - EM counterpart, 39–41
 - formation, 48
 - frequency range, 8
 - ground segment, 95
 - implementation, 7
 - measurement arm, 48
 - measurement concept, 7
 - measuring chirp mass, 35
 - measuring coalescence time, 35
 - mission concept, 47
 - orbits, 48
 - without station-keeping, 48
 - partition of measurement, 48
 - residual acceleration, 50
 - science data stream, 8
 - science objectives, 13, 23, 30, 38, 43
 - science requirements, 50
 - signal-to-noise ratio, 8
 - sources, 8
 - MBH, 9
 - black hole binaries, 36
 - compact binaries, 9, 30
 - EMRI, 9
 - MBH, 18, 24
 - MBH mergers, 16, 20
 - neutron star binaries, 36
 - ultra-compact X-ray binaries, 35
 - verification binaries, 9, 30, 32
 - spacecraft Doppler tracking, 7
 - strain sensitivity, 7
 - transfer function, 53
 - transponder mode, 50
- luminosity distance, 9, 39, 50, 104
- magnetar, 35
- manoeuvre

- design and execution, 98
- inclination changing, 88
- station keeping, 92
- Markov-chain Monte Carlo, 105
 - parallel tempered, 105
 - reversible jump, 105
- mass imbalance
 - compensation, 77
- mass-to-radiation conversion, 14
- massive black hole binary
 - coalescing phase, 104
 - event rate, 41
 - inspiralling phase, 104
 - ringdown phase, 105
 - signal, 104
 - template, 104
- matched filtering, 104
- mercury discharge lamps, 81
- merger
 - afterglow, 41
 - precursor, 41
- Michelson interferometer, 7
- micro-newton propulsion system, 77
- micro-newton thrusters, 81
 - CMNT, 82
 - FEEP, 82
 - caesium, 82
 - indium, 82
- mission phases, 96
- mission timeline, 96
- N-Fire, 69
- naked singularity, 19
- neutron star, 35
 - binaries, 36
- no hair theorem, 24, 26, 28
- noise
 - gravity-gradient, 7
 - seismic, 7
- noise analysis
 - preliminary, 99
- noise model
 - validation, 57
- numerical relativity
 - predictions for merger and ringdown, 26
 - waveforms for ringdown, 26
- observation requirement, 56
- OmegaWhite, 33
- on-board computer
 - redundancy, 84
- open source, 103
- operations, 87
- operations orbit delivery, 98
- optical assembly
 - gravitational reference sensor, *see* gravitational reference sensor
 - optical bench, *see* optical bench
 - telescope, *see* telescope
- optical bench, 62
 - additional half-wave plate, 64
 - construction technique, 62
 - differences to LPF, 64
 - interferometer, 64
 - optical truss, 64
 - point-ahead angle mechanism, 64
 - reference, 64
 - science, 64
 - test mass, 64, 66
 - material, *see* Zerodur
 - mirrors, 62
 - non-planar beam path, 62
 - polarisation, 64
 - polarising components, 64
 - requirement, 62
 - size, 62
- optical system
 - optical assembly, 62
- orbital hangup, 18
- orbits, 88–90
 - eccentricity, 89
 - inclination, 89
 - influence of Earth, 89
 - selection, 88
- Pan-Starrs, 33
- patch field effect, 78
 - measuring, 78
 - reduction, 78
 - suppression, 78
- payload
 - requirement, 61
- payload housekeeping data, 95
- payload subsystem
 - autonomy, 62
 - electromagnetic, 62
 - gravitational, 62
 - laser metrology system, 61
 - mechanical, 61
 - propulsion system, 61
 - structural, 61
 - test mass control, 62
 - thermal control, 61
- perturbation theory, 26
- phase measurement
 - system level demonstration, 58
- phase transition
 - first-order, 44
- Planck, 38, 42
- Planck scale, 23, 44
- point-ahead angle, 66
 - components, 66
- point-ahead angle mechanism
 - angular jitter noise, 67
 - Haberland hinge, 67
 - optical path-length noise, 67
 - requirements, 67

- polarisation encoding, 70
- polarisation multiplexing, 64
- post-operational phase, 96
- posterior PDF, 103
- proof mass, *see* test mass
- propellant system, 92
- propulsion module
 - central frustum, 85
 - clamp band, 85
 - lower floor panel, 85
 - pressurant tank radial panel, 85
 - primary structure, 85
 - radial shear panels, 85
 - upper floor panel, 85
- propulsion system
 - bi-propellant, 92
- protogalaxies, 10
- pulsar
 - binary, 23
 - orbital gravitational fields, 23
 - double, 23
 - Hulse-Taylor, *see* pulsar, PSR1913+16
 - millisecond radio, 36
 - millisecond X-ray, 36
 - PSR 1913+16, 5, 23
 - PSR J0737-3039, 23
 - radio, 35
- quantum vacuum fluctuation
 - amplification of, 44
- quasar, 13, 14
 - mini, 16, 17
- radiation pressure, 13
- safe nutation zones, 88
- Salpeter time, 14
- scalar-tensor theories, 24
- science housekeeping data, 95
- science instrument
 - basic function, 50
- science investigation, 50
- science objectives, 10, 50
- science observation, 50
- science operations phase, 96
- science planning, 101
- science product, 95, 103
 - archiving, 99, 100
 - consolidation, 95
 - generation, 99, 100
 - Level 0, 95
 - Level 1, 95
 - Level 2, 95, 103
 - Level 3, 95
- science requirements, 47
- SEGUE survey, 33
- self-gravity analyses, 77
- separation
 - detumble, 86
 - mechanism, 86
 - separation phase, 88
- Shapiro delay, 23
- shot-noise, 56
- single-link position uncertainty, 53
- solar array
 - power output, 93
- solar array, 92
 - baseline, 93
 - panel size, 93
 - redundancy, 85
- solar cells
 - efficiency, 93
- soliton stars, 15
- source catalogue, 95
- Space Interferometry Mission, 72
- spacecraft
 - AOCS, 84
 - autonomy, 84
 - carbon composite, 83
 - communications, 84
 - ephemerides, 103
 - FDIR, 84
 - health monitoring, 97
 - interface to ground segment, 84
 - magnetic cleanliness, 77
 - payload location, 84
 - redundancy, 84
 - separation, 84, 97
 - structure, 83, 84
 - sunshield, 83
- spacecraft architecture, 77
 - magnetic cleanliness, 77
 - mass distribution, 77
 - thermal balance, 77
- spectral density
 - amplitude, 8
 - power, 8
 - units, 8
- Standard Model, 43
 - fields, 44
 - particles, 44
- star
 - neutron, *see* neutron star
 - population III, 16
 - R Corona Borealis, 35
 - subdwarf, 35
- star formation, 17
- star formation, 32
- starburst, 40
- string theory, 43
- structure formation, 17
- superstrings, 9, 12
- supersymmetry, 43
- symmetric mass ratio, 25, 29
- telescope
 - aperture, 67

- exit pupil, 69
- magnification, 67, 69
- off-axis, 67
- wavefront quality, 69
- temperature fluctuations, 77
- Terascale, 11, 43, 44
- TerraSAR-X, 69
- test mass
 - actuation
 - cross-coupling, 78
 - capacitive sensing, *see* capacitive sensing
 - charging, 81
 - dimension, 78
 - discharging, 81
 - electrostatic coupling, 78
 - free fall, 77
 - forcing, 78
 - magnetic susceptibility, 77, 78
 - residual, 78
 - mass, 78
 - material, 78
 - surface, 78
- theory of everything, 44
 - string theory, 45
- Thomson cross section, 13
- tidal tails, 40
- time-delay interferometry, 72
 - algebraic approach, 73
 - first generation, 73
 - frequency domain, 72
 - second generation, 73
 - time domain, 73
- trajectory correction manoeuvres, 97
- transfer phase, 88
- transient events
 - announcement, 99
 - consolidation, 102
- vacuum
 - false, 43
- verification binaries, 11, 32
 - ES Cet, 32
 - HM Cnc, 32
 - RX J0806.3+1527, *see* HM Cnc
 - V407 Vul, 32
- Virgo, 7, 36
- white dwarfs, 11
- WMAP, 38
- X-band, 85
- X-ray
 - background, 17
- Zerodur, 62
 - CTE, 64